Tabletop production and study of cold radioactive molecules

Thesis by
Chandler Jacob Conn

In Partial Fulfillment of the Requirements for the
Degree of
Doctor of Philosophy

CALIFORNIA INSTITUTE OF TECHNOLOGY
Pasadena, California

2026
Defended May 28, 2026

© 2026

Chandler Jacob Conn
ORCID: 0000-0001-9046-4439

All rights reserved

Acknowledgements

Here, I am presented with the impossible task of trying to properly thank everyone that made this work possible. It truly takes a village to raise a thesis, and the following is an attempt to capture even a fraction of the appreciation that I have for all of those who enriched my life during this PhD.

First, I wish to extend my sincere gratitude to professors Mitchio Okumura, Olivier Doré, and Brad Filippone, for your services as my committee members.

A special acknowledgement is in order for my advisor (and final committee member) Nick Hutzler. Thank you Nick for serving as a wonderful example for what it means to be a scientist, and for being an all-around great person. Your commitment to fostering a broader scientific community is something I wish more people shared. It has been fun watching the lab transition from a relatively new one to an established powerhouse, and I am excited to see how things develop over the next many years. And congratulations on tenure!

It is absolutely not an exaggeration to say that very little of this would have been possible without the support and guidance of Haick Issaian, as well as the rest of Caltech EHS. Haick, your willingness to indulge our wishes of working with open sources of radium is much appreciated, as I can only imagine the many headaches we must have caused. We were lucky to have your experience and expertise behind us throughout every step of the way. Similarly, I would like to acknowledge professor Alyssa Gaiser for all of the help developing our radiochemical handling protocols, and I hope you get to have some In-N-Out soon.

From my time at Northwestern I must thank professor Bill Halperin for taking me

on as a undergraduate researcher in my first year when I barely had a concept for what research meant. My introduction to AMO came under the guidance of professor Brian Odom, to whom I owe a lot for getting me to this position. Brian, if you had not agreed to take me on as a summer student with no funding situation, there is a good chance my trajectory would have looked a lot different, and for that I am eternally grateful. To my postdoc mentors Vincent Carrat and Ivan Antonov, many thanks for indulging my early questions and imparting your wisdom.

Here at Caltech I was blessed with many wonderful labmates. To Arian Jadbabaie and Nick Pilgram, it is so surreal to me now to be in your position when I was looking up to you both with such admiration. For so much of my PhD you were my models for what it meant to be a scientist, and I'd like to believe I carry a little of each of your scientific mannerisms with me. On the other side of the table, I am happy to see that the future of the lab is in good hands with Jonathan, Xukun, and Olivia ringing in the new generation. Yuxi, even though our lab work diverged over time, I feel like we got closer in the last few years, and my hope is that every time you sneeze you know that there is someone out there looking out for you.

I was unbelievably lucky to join the lab at the same time as two other fantastic scientists and humans. Yuiki, even though I will never understand your working schedule, I'm grateful for our shenanigans in the times that we did share. Your sense of humor carried me through the slowest work days and for that I must say thank you, or as they say in Japan: いらっしゃいませ. To Phelan, it has been such a pleasure working so closely alongside you all these years. You have an unmatched ability to keep things pushing forward and there's nobody else I'd rather have in my corner when it seems like all hope is lost. As I'm sure you know, yet I'll put into words anyway, this project would not have happened without you.

For organizational reasons I must mention Madison here, despite the fact she is just as much of a friend as a labmate. Madison, at no point in your first few months with the lab did I have any idea what I was getting into (complimentary). You have grown into one of my closest friends and partners-in-crime; my lab "sister," according to Yuiki. Through you I have met so many wonderful people, which yes does include Huma even though her job seems to be to distract us in the office. There's so much more I could put here, but I will simply say thank you for being such a force for fun and good and someone I'm lucky I got to see so often. No matter what you may think, this is not the last you will see of me[1].

[1] This is a threat.

To the many students and groups whom I have had the pleasure of mentoring—Maya, Taz, Zitian, the HSRC students, and the Warrior Scholar Project participants—you all caught me at various stages of teaching ability, and I appreciate you sticking with me as I learned what it meant to mentor.

Thank you to the Caltech orchestra, particularly the horn section, for providing a much needed respite from the daily grind and allowing me to continue interfacing with a creative outlet.

A good chunk of this thesis was written up in Oregon while house sitting for Tim Steimle. Tim, I greatly value all of the guidance, professional and otherwise, that you have provided me throughout my PhD. Packing up all of those lasers at Notre Dame was a fantastic experience, even if I'm still glad we decided to ship them rather than drive them all the way back.

Being completely objective and unbiased, I would claim that my friends are the best that one could have. Thank you to all of the members of the Free Radicals softball team, who showed up early[2] for every single softball game despite the beatings we sometimes endured. Whenever your life really needs to score some metaphorical runs, remember the froggy chant! A few people graduated way too early for my liking, but still had a profound impact on my experience: Kim and Vince, thank you for the many adventures big and small with the Goofballs, whose existence is largely owed to Kim's crazy agreement to let us crash that trip to Banff, one that ended up being a contender for the most amazing experience ever. Steven, I admire your ability to always have some plan to rally all of David's Disciples together, as I'm sure I would have gone to many fewer puppet shows without you. Brian, thank you for always calling things like you see them, and my hope is that you see yourself as a pleasure to be around in the same way that others (myself included) do.

To the Hormbles youths: I have to thank Zion for always indulging my jokes and giving me the laughs that I so desperately deserve; your payment will be in the mail soon. Nick, you contain multitudes—even though you're not afraid to get a little silly with it sometimes, it is obvious that you are a deeply caring and considerate person. My gift to you is a mental image of a partially tucked-in Djungelskog[3]. Colin, despite how difficult I have been lately, you have tenaciously kept trying to wrench me out to go do things even when my tendency has been to hole myself up at home. Whether a

[2]This never happened.

[3]Funniest thing I ever saw.

hike or trivia, I can always trust in you to show up; thank you for being such a versatile and reliable friend.

To my midwestern sister Michelle, thank you for bringing balance to my life by building me up but also by never being afraid to knock me down a peg when necessary. In a bittersweet way, I am happy for all of the fun times we had within the context of your move, although the fact it meant you had to leave at the end was rude and you should apologize for that. Maybe one day we can get around to playing protobowl like you promised, but until then we must assume that I would win.

I owe Andreas, my longest-lasting Caltech friend, a genuine and sincere acknowledgement, a notion which I'm sure will surprise anyone who knows the two of us. Out of all of my friendships it is yours through which I believe I have grown the most. You always make me laugh and think in ways which nobody else does, and have become a part of my life that I deem irreplaceable. Now, with this thesis out of the way, we can fully devote our lives to our podcasting career.

To Adam, it has been great keeping up with you since your graduation from Caltech. You taught me the true meaning of "work hard, play hard," the former of which I am still working on. I have immensely enjoyed the many chaotic nights and LOTR marathons, but also the chill game nights just keeping up. Of course, it has been lovely to get to know Jane through it all.

Nathan, I am beyond glad that we have been able to keep up our (mostly) weekly calls and that our mediocre performance at University Challenge has stood the test of time. Even when there are gaps in our contact, it is comforting to be able to pick things up like no time was ever lost. It was an honor to be your best man, and wherever things take me after this I hope to be able to spend more of my time with you and Kevie.

Of course, no part of my grad school experience would have been the same if it weren't for Ana. Ana, you have been a constant force for good in my life and I can't imagine things without you. From eating oranges in the Catalinas during COVID, to trips all across the world, we have grown and shared this whole experience together (even if you did beat me to the PhD by over eight months) and I'm happy that you've been by my side throughout it all. You are genuinely one of the nicest, most caring people I could have wished for, and are always ready and willing to do what's necessary for others. Your scientific perseverance is admirable, and I am so excited to see what the future holds. I love you. And to your parents, Paco and Donna, thank you two for all that you have done for me throughout this time—it has not gone unnoticed.

To my family: Mom, dad, despite none of us (myself very much included) having any idea what I was really getting myself into with this PhD, you put your whole support behind me and allowed all of this to be possible. I couldn't have asked for more; even though it comes nowhere close to approximating the gratitude I feel, I would still like to say thank you. This extends to Pa Pa and my expanded immediate family in Tom and Gretchen, as you have each contributed to my development in your own unique way. Finally, to Pa and Grandma Conn, I'm glad that I was able to share the beginning of this process with you, even if we couldn't all be here together at the end.

My last thanks goes out to the birds that I—and, by extension, much of the lab—watched for many hours on the ever-present livestream on my second monitor, notably the Big Bear bald eagles Jackie and Shadow and the Northern Royal Albatrass cam, whose newest chick is slated to be named on the day of my defense. The narrow focus required during a PhD can make the universe feel quite small, but watching these majestic birds grow up provides a necessary reminder that a whole living, breathing world is out there, and that everything we do exists in the context of something much bigger than ourselves.

Abstract

Radioactive molecules have remained severely understudied relative to their stable counterparts, owing to difficulties associated with their radiological hazards and limited material availabilities. Despite this, their relevancy to many fields including nuclear science, chemistry, and astronomy make them attractive prospects for precision investigations. In particular, laser-coolable radioactive molecules containing octupole-deformed nuclei such as radium monohydroxide (RaOH) and radium monofluoride (RaF) promise dramatic sensitivity increases for experiments aiming to measure new physics originating from fundamental symmetry violations. Before they may be used for any of these purposes, however, new tools are needed that allow for their safe and precise study while making them accessible in a university (or similar) setting. In this thesis, we construct a tabletop cryogenic apparatus capable of studying radioactive molecules which we produce in-situ from trace quantities of starting material. We use this apparatus to perform the first spectroscopic observation of a radium-containing polyatomic molecule RaOH and its deuterated isotopologue RaOD, as well as high-resolution spectroscopy of the photon cycling transitions in RaF. To prepare for laser cooling, we develop a protocol to measure the vibrational branching ratios of these exotic species and use it to establish RaF to be among the most laser-coolable molecules known as of yet. We demonstrate the versatility of our approach by producing and detecting over twenty different atoms and molecules, ranging from transuranic radioisotopes to complex asymmetric top molecules. The species-agnostic methodology employed throughout this work allows its application to a wide class of previously ignored radioactive atoms and molecules, and makes them accessible to the many advanced experimental techniques already leveraged in stable systems.

Published Content and Contributions

[1] Chandler J Conn*, Phelan Yu*, Madison I Howard, Yuxi Yang, Chaoqun Zhang, Arian Jadbabaie, Aikaterini Gorou, Alyssa N Gaiser, Timothy C Steimle, and Lan Cheng. "Production and spectroscopy of cold radioactive molecules". In: *arXiv preprint arXiv:2508.08368* (Accepted in *Science* 2026). DOI: 10.48550/arXiv.2508.08368.
C.J.C. participated in the conception of the project, construction of the apparatus, data collection and analysis, and manuscript preparation.

[2] Nicholas R Hutzler, Chandler J Conn, Madison I Howard, Yuxi Yang, and Phelan Yu. *Robust Ablation Production Of Gas-Phase Atoms And Molecules*. U.S. Patent application 19/551,368.
C.J.C. conceived of the patented methods, as well as performed the collection and analysis of the justifying data.

[3] Tianxiang Chen, Chaoqun Zhang, Lan Cheng, Kia Boon Ng, Stephan Malbrunot-Ettenauer, Victor V Flambaum, Zack Lasner, John M Doyle, Phelan Yu, Chandler J Conn, et al. "Relativistic exact two-component coupled-cluster study of molecular sensitivity factors for nuclear Schiff moments". In: *The Journal of Physical Chemistry A* 128.31 (2024), pp. 6540–6554. DOI: 10.1021/acs.jpca.4c02640.
C.J.C. contributed to motivating the study of the molecules contained in this work and aided in review of the manuscript.

[4] Nickolas H Pilgram, Arian Jadbabaie, Chandler J Conn, and Nicholas R Hutzler. "Direct measurement of high-lying vibrational repumping transitions for molecular laser cooling". In: *Physical Review A* 107.6 (2023), p. 062805. DOI: 10.1103/PhysRevA.107.062805.

C.J.C. assisted with data collection and experimental developments to the apparatus employed for this work.

[5] Chaoqun Zhang, Phelan Yu, Chandler J Conn, Nicholas R Hutzler, and Lan Cheng. "Relativistic coupled-cluster calculations of RaOH pertinent to spectroscopic detection and laser cooling". In: *Physical Chemistry Chemical Physics* 25.47 (2023), pp. 32613–32621. DOI: 10.1039/D3CP04040B.
C.J.C. collected supporting data on the molecules examined in this work to motivate their experimental study.

Table of Contents

Acknowledgements . . . iii
Abstract . . . viii
Published Content and Contributions . . . ix
Table of Contents . . . x
List of Illustrations . . . xiv
List of Tables . . . xli
Chapter I: Introduction . . . 1
1.1 Searching for signs of new physics . . . 3
CP-violating observables . . . 5
BSM physics sensitivity factors . . . 11
Radium-containing molecules . . . 15
1.2 Interest from other fields . . . 16
Chapter II: Atomic and molecular structure . . . 19
2.1 Atomic structure . . . 19
2.2 Molecular structure . . . 22
Electronic energy . . . 23
Energy of nuclear motion . . . 25
2.3 Selection rules and laser cooling . . . 31
Chapter III: Radioactivity . . . 34
3.1 Basics and terminology . . . 35

3.2 Dosage . . . 39
3.3 Radium-226 . . . 41
Chapter IV: Tabletop cryogenic apparatus - the Minifridge . . . 44
4.1 Cryostat design . . . 48
4.2 Atom and molecule production . . . 64
4.3 Optical spectroscopy . . . 69
Chapter V: Production and spectroscopy of radium-containing molecules . . . 79
5.1 Radioactive remodel . . . 82
Radiation monitoring and personal dose . . . 85
5.2 Radium ablation targets . . . 87
Drop casting . . . 91
Coffee rings and crystallization . . . 98
5.3 Spectroscopic improvements . . . 108
Radium $^1P_1$ measurement . . . 114
5.4 RaOH . . . 116
Attempts at $\tilde{A} - \tilde{X}$ . . . 121
5.5 RaOD . . . 124
Synthesizing aluminum deuteroxide . . . 125
5.6 RaF . . . 130
5.7 RaCl . . . 133
Chapter VI: Vibrational branching ratios of radium monofluoride . . . 136
6.1 Determining branching ratios of trace isotopes . . . 138
Signal Modeling . . . 139
Light Collection Efficiency . . . 142
6.2 Worked example - RaF $A^2\Pi_{1/2}(v = 0) \rightarrow X\,^2\Sigma^+(v = 0, 1)$ branching 143
6.3 Benchmarking . . . 148
6.4 RaF $A^2\Pi_{1/2}(v = 0) \rightarrow X\,^2\Sigma^+(v = 0, 2)$ branching . . . 154
6.5 RaF $C^2\Sigma^+(v = 0) \rightarrow X\,^2\Sigma^+(v = 0, 1)$ Branching . . . 156
6.6 Results and interpretation . . . 157
Chapter VII: Studies on other atoms and molecules . . . 159
7.1 Barium-containing . . . 159
BaOH . . . 160
BaF . . . 162
7.2 Calcium-containing . . . 163
$CaNH_2$ . . . 164

CaCl & CaI 167
7.3 Uranium oxide 170
7.4 Neptunium 173
Chapter VIII: Magnetic shielding 175
8.1 Shielding in theory 179
8.2 Shielding in reality 183
8.3 Design 185
Degaussing circuit 187
8.4 Simulations 189
Chapter IX: Future prospects 194
Appendix A: Radium SOP 214
A.1 Overview 215
A.2 Summary of Hazards 216
A.3 Target Preparation 217
A.4 Preparation and Installation of Cell and Chamber 221
A.5 Description of the Cryostat 224
A.6 Cell installation 227
A.7 Experimental Operation and Procedures 230
A.8 Cell and Target Disposal 233
A.9 Mitigation of Contamination 237
A.10 Safety Concerns and Potential Failure Modes 239
Appendix B: Cell assembly guide 245
B.1 Gather the cell parts 245
B.2 Assemble the cell 251

List of Illustrations

Number *Page*

1.1 Diagrammatic illustration as to why a permanent EDM would violate T (equivalent to CP) and P symmetries. The color gradient represents the charge distribution of the system, and the circular arrow shows the classical interpretation of its intrinsic angular momentum (spin). Under a time reversal or spatial reflection, the resulting particle is qualitatively different from the one before the operation. 6

1.2 Attempt at interpreting the Schiff moment of an atomic system. Left: Intrinsic EDM of a nucleus with a CP-violating permanent dipole moment. The color represents a possible charge distribution, and the behaviors under T and P reflections are the same as in Figure 1.1. Right: Atomic EDM in this system with electrons (black dots), which rearrange to screen the majority of the bare nuclear charge. Now the dominant contribution to the measured, weaker EDM results from the Schiff moment, diagrammatically represented by the residual (unscreened) nuclear charge distribution. This Schiff moment is related to the underlying charge distribution of the bare nucleus; see [22] for a good discussion. 9

1.3 Illustration of the different types of nuclear deformations. $\beta_\lambda = 0$ for all λ yields a non-deformed, spherical nucleus. A quadrupole deformation $\beta_2 \neq 0$ leads to either prolate or oblate spheroids. $\beta_3 \neq 0$ results in an octupole-deformed pear- or avocado-shaped nucleus. Diagram modified from the one in [37]. 13

2.1 Diagrammatic representation of atomic energy levels under successive orders of perturbation, where the "Bohr atom solution" is the solution to the spinless, nonrelativistic electrostatic Hamiltonian. The atom represented is alkali-like, i.e. having one valence electron, as this is the structure closest to the molecules we study. For the hyperfine splitting, the nucleus was taken to have spin $I = 1/2$; this is absent for atoms with no nuclear spin. Magnitudes for the energy splittings at each order are shown, with values representative of the alkali atoms. $1\ \text{cm}^{-1} \approx \frac{29.98}{c}$ GHz. 21

2.2 Vibrational modes of a linear triatomic molecule, such as RaOH. v_1 and v_3 correspond to stretching between the outer atoms relative to the inner one. Because the bending motion is doubly-degenerate, the true bending mode vibration is a linear combination of the two, which possess an angular momentum. The projection of this angular momentum is given by l, where the states corresponding to $\pm l$ are almost, but importantly not, degenerate. In molecules like RaOH, where the blue atom in the example above is quite heavy and the white is extremely light, the bending motion is more like a gyrating of the light atom about the internuclear axis. 27

2.3 Attempt at visualizing the hierarchies of energies in a molecule, using a system like ^{226}RaF ($I_{Ra} = 0, I_F = 1/2$) as reference. After the spin-orbit splitting, the excited $A\,^2\Pi$ levels are no longer shown to provide room for expanding the ground state levels, although they each contain a ladder of successive states just as for the ground $X\,^2\Sigma^+_{1/2}$. The spin-rotation constant γ is assumed to be greater than 0, otherwise the F_1/F_2 ordering flips. Λ-doubling is not present in the above X state, as it has $\Lambda = 0$, but in other states with $\Lambda > 0$ (such as the excited $A^2\Pi$) it leads to a qualitatively similar level structure to the spin-rotation splitting shown. Hyperfine doublets are caused by interactions with the ^{19}F nuclear spin, further splitting the levels into two; if a spinful isotope of radium was chosen, such as ^{225}Ra ($I = 1/2$), even more hyperfine states would be present. Numbers at the bottom give characteristic values for the energy separation of the levels introduced at each level. Nothing is to scale. 29

2.4 Level diagram depicting photon cycling closure on a $^2\Pi_{1/2} - {}^2\Sigma^+_{1/2}$ transition, such as the $A - X$ band of RaF/RaOH. If two lasers (solid lines) drive the $P_{11}(J'' = 1.5)$ and $Q_{12}(J'' = 0.5)$ transitions from both $N = 1$ spin-rotation levels to the parity-allowed Λ-doubling component of the excited $J' = 1/2$ state, then the only allowable decays (dotted lines) are to the same initial states, allowing for repeated excitation. Colors indicate parity. Adapted from [72], which has many similar diagrams for other types of transitions. 32

3.1 Maximum ranges of beta particles in selected materials. Plot adapted from material in [75]. 36

3.2 Decay chain for ^{226}Ra. Gamma emissions are not shown, but occur most strongly in the beta decays of Pb-214 and Bi-214 and weakly along during the alpha decay of Ra-226 to Rn-222. Decays with vanishingly rare probabilities are not shown. Plot taken from [80]. 38

3.3 Log-scale buildup of radium-226 daughters as a function of elapsed time, starting with a pure 1 mCi (1 mg) sample of radium. At one day, the total activity of the sample is already twice that of the initial sample, and plateaus to around 6 times higher after 10 days. Note that the y-axis is activity and not quantity—to convert to quantity, use Equation 3.1. 42

3.4 Log-scale buildup of radium-225 daughters as a function of elapsed time, starting with a pure 1 mCi (1 mg) sample of radium-225. Compared to radium-226, the shorter half-life of this isotope means that 99% of the initial material has decayed away by 100 days. 43

4.1 Visualization of the rotational state distribution as a function of temperature for a molecule with a similar rotational constant to RaF [84]. Left: Rotational state occupation fraction $P(J)$ as a function of temperature for a few selected values. Right: Number of rotational levels N_J that make up 90% of the total occupied states, quantifying the spread of the molecular population. 45

4.2 Diagrammatic representation of buffer gas cooling of laser-ablated molecules. **a)** The cryogenic cell made of copper is filled with helium gas, which thermalizes with the cell at 4 K. **b)** Pulsed ablation lasers vaporize material off of solid reagent targets which react to form various energetic atoms and molecules. **c)** Elastic and inelastic collisions with the buffer gas cool the ablated species. 47

4.3 Photos of the Minifridge on the optics table from two different angles. Features are easier to see on the rendering, Figures 4.5 and 4.6. Note that the cold head orientation is flipped 180 degrees between this photo and the renderings, but all other components match. 48

4.4 Temperatures of cryostat stages across different thermal cycles. Room temperature corresponds to a reading of 280 K as these diodes are not calibrated for accuracy at high temperatures. For all three plots the 4 K adapter and cell temperatures are within a fraction of a degree and thus the traces are overlapped. Left: Cooldown to 4.2 K from room temperature. The cell reaches its base temperature at just over two hours from the start of cooldown. Center: Warming up to room temperature without heating. After around a day and a half the cryostat is above the dew point, meaning it can be opened without introducing moisture into the system due to condensation. Right: An example of a forced warmup, achieved by driving the 30 K top and 4 K adapter cartridge heaters with 0.5 A. Solid lines are data and dotted lines are fits using a simple model based on Newton's Law of Heating. Data after two hours was modeled rather than taken experimentally as we run the heaters on a timer to mitigate the potential to overheat and damage the system. Because of the lower thermal mass and better conductance, the 4 K stage warms up more quickly. If desired, up to four times more current may be run through the heaters to further expedite the warmup. 49

4.5 Rendering of the full cryostat exterior. Unless significant modifications are being made only three plates need to be removed to perform any task inside the chamber. These plates are visible on the second rendering above: the blank plate, fluorescence window plate, and probe laser window plate. Depending on the access required, removal of only one of these might be possible. In the photos of Figure 4.3, the cold head extends towards the fluorescence detection side, not the ablation side. 51

4.6 Renderings of various stages of disassembly of the Minifridge. Orientation is the same as the left render in 4.5. The leftmost image makes it clear why the 30 K stage was designed in three sections, as the middle plates are completely blocked by the vacuum cube frames and cannot be removed easily. 51

4.7 Finding the optimal helium value via an absorption measurement of the overlapped $Q_{21}(1.5)$ and $R_{22}(0.5)$ lines on the $\tilde{A}\,^2\Pi_{3/2}(000) \leftarrow \tilde{X}\,^2\Sigma^+(000)$ transition in BaOH [98], produced by co-ablating barium metal with aluminum hydroxide powder. Each color above represents a different cumulative amount of helium added. Left: fractional laser absorption versus time after ablation, offset for visibility. The dotted lines represent the zero and one values for each respective trace, corresponding to 0% and 100% laser attenuation due to absorption by the molecules. For example, the 1000 mTorr trace peaks at around 90% absorption. The time traces show that complicated pressure dynamics occur within the cell, perhaps occurring due to acoustic waves or vortices [99]. Right: integrated optical depth of each absorption trace. Pressure values listed are *not* the pressure readings inside the cell, but rather the cumulative readings of the pressures on the gauge attached to the load lock region before adding the helium. For example, the first set of data was taken after filling the load lock with helium until the gauge read 200 mTorr, after which the helium was allowed to flow into the cell. This process was repeated with another 200 mTorr, bringing the total amount of helium added to 400 mTorr, and so forth. This process should be repeated whenever a new type of target is loaded to better understand the helium adsorbing properties and optimal helium levels. Generally, helium densities that yield successful molecule production are on the order of 10^{15} cm^{-3}. 55

4.8 Photo of the heat exchanger thermally anchored to the 30 K adapter plate on the top. VCR connectors are placed on either end of the heat exchanger to facilitate its relocation or removal without the need to drastically alter the rest of the gas lines. 56

4.9 Diagrammatic representation of the Minifridge gas handling manifold before upgrading to work with radioactive samples. This is a simplification of the current gas manifold, which is shown in 5.3. . . 56

4.10 A cutaway rendering and assembly photo of the 30 K stage, explicitly pointing out some of the components described in the text. 80-20 struts were used to raise the Minifridge during assembly so that the bottom plate could be attached. 57

4.11 Temperature of the bottom of the 30 K stage as a function of support bar material and thickness, assuming a 1 W heat load on the bottom. Copper was included as an example high-conductivity material, with a thermal conductivity coefficient of $k \sim 900$. 58
4.12 Cutaway rendering and photo of the cell in the same orientation. Features mentioned in the text are identified. 62
4.13 Photo of the dual-ablation setup employed on the Minifridge. The beam paths are merged using a 1" PBS cube before entering the cell. Each laser path features multiple mirrors to allow for individual steering on the target plate. 64
4.14 Testing the importance of ablation delay for dual-ablation production of YbOH. Yb metal was ablated with a variable delay relative to ablation of $Al(OH)_3$ pressed powder. Top: Absorption fraction of a probe laser driving the ${}^{Q}Q_{11}(1.5)$ line of the $\tilde{A}\,{}^2\Pi_{1/2}(000) \leftarrow \tilde{X}\,{}^2\Sigma^+(000)$ band in YbOH, which is at 17323.6728 cm^{-1} [104]. The OH reagent target was always ablated at $t = 0$. Each color represents a data set taken with a different delay timing. The bottom plot shows the respective integrated absorption signals for each of these delays, with error bars indicating one standard deviation of the integrated values within a data set. Negative delay corresponds to ablation of metal before OH. 65
4.15 Demonstration of chemical enhancement on fluorescence signals for radium monofluoride (RaF). For both traces, we are driving the $C\,{}^2\Sigma^+(0) \leftarrow X\,{}^2\Sigma^+(1)$ transition at 618 nm with a 50 kHz pulsed dye laser and detecting the strong fluorescence at 602 nm. At 3 ms after ablation, a shutter opens allowing roughly 1 W of enhancement light to enter the cell. When the enhancement light is resonant with the radium ${}^1S_0 \rightarrow {}^3P_1$ transition at 13999.357 cm^{-1}, we see an increase in molecular fluorescence, indicating more molecules were formed. 67
4.16 Example target plates. Target materials shown include: hydraulic-pressed powders, pure metals, pieces of sputtering targets, dried radioisotope solutions on gold foil, and radium-painted watch hands, all of which are described throughout this thesis. Details about the radioactive targetry are given in 4.3. 71
4.17 Cut-away diagram showing the methods of optical spectroscopy performed inside a Minifridge cell. Probe lasers may be used for absorption or fluorescence measurements. Reproduced from [84]. 72

4.18 Representative direct DC absorption plots labeled by the type of ablation target. For the atomic signals, the $^1S_0 \rightarrow {}^1P_1$ transition was driven, at 553 nm for barium and 483 nm for radium. YbOH absorption was performed on the main $\tilde{A}\,^2\Pi_{1/2} - \tilde{X}\,^2\Sigma^+$ line at 577 nm. Each plot color is roughly the color of the probe laser, as seen by eye. Note the differences in time scales—we achieved full attenuation of a barium $^1P_1$ probe laser for nearly one third of a second, visible clearly by eye as an extinction of the beam. 73

4.19 Representative fluorescence traces labeled by the molecule being studied. Heights are scaled to account for the different PMT gains used for different wavelengths. For all traces, we were exciting the molecules with our high-repetition rate pulsed dye laser at 50 kHz. To make YbOH, we ablated both ytterbium metal and $Al(OH)_3$ pressed powder, and did not use any chemical enhancement light. We excited the main line at 577 nm and detected the off-diagonal decay to the Yb – O stretch at 595 nm. For RaF, we produced molecules by co-ablation of the radium drop cast target with a CuF_2 pressed powder target in the presence of 1 W of chemical enhancement. For this fluorescence data, we drove the $C\,^2\Sigma^+(0) \leftarrow X\,^2\Sigma^+(0)$ transition at 602 nm and detected the decays down to $X\,^2\Sigma^+(1)$ at 618 nm. The final (green) trace shows the signal when our laser is off resonance of the YbOH transition, where the early time signal is still visible due to ablation glow. Note that the pre-ablation background is greater for the RaF trace than for the YbOH and off-resonant trace; this is due to the increased light leakage of the pulsed dye laser through the PMT filters at the RaF wavelengths. 74

4.20 Laser-induced fluorescence of BaOH observed by a sCMOS camera pointed at the light collection window. Gain has been increased in software to make the fluorescence visible. We probed the $\tilde{A}^2\Pi_{3/2} \leftarrow \tilde{X}\,^2\Sigma^+$ main line at 12043.493 cm^{-1} (830 nm) and observed the decay between these same two states. Optical filtering cut out most of the ablation fluorescence, as demonstrated in the off resonant image. . . 75

4.21 Camera image for a single data shot showing bright streaks of laser scatter off of macroscopic ablation dust. The molecule fluorescence band is visible like in Figure 4.20, but is overwhelmed by the nonresonant laser scatter. Off-diagonal detection with appropriate optical filtering would fix this issue. 75
4.22 Off-diagonal decay in YbOH observed by imaging on a fiber-coupled spectrometer. The strong 577 nm probe light was optically filtered out, allowing for detection of photons from the decay to the ground state Yb – O stretch vibration at 595 nm. 76
4.23 Dispersing the fluorescence from ablation on a fiber-coupled spectrometer. Data was taken in a few configurations of BaOH ablation. Top: Ablating the $Al(OH)_3$ pressed powder co-target but not the barium metal. Middle: Ablating the barium metal but not the co-target. Bottom: Ablating both targets. Broad peaks are found at a significant portion of the visibile spectrum, hinting at the origin of the nonresonant "glow" that we observe. A 532 nm longpass filter was used in front of the fiber coupling side of the spectrometer to filter out the intense ablation laser light. The observed lines correlate quite well with the strong transitions in neutral barium—see [109]. Many of these lines originate from transitions between two excited states, rather than through the ground state. 77
5.1 Visual comparison of the quantities of material we have available to us. Left: photo of the vial containing 1 mg of radium-226 in the form of $^{226}Ra(NO_3)_2$ salt, about 20 – 100 times more material than we use in a single cell. The white speck is smaller than a grain of fine sand and is resting in the tip of the v-vial. Radiation damage has turned the glass brown, obscuring the material. Right: target plate for one of our other sources showing three black Yb + $Yb(OH)_3$ pressed powder targets and a chunk of pure ytterbium metal. Total mass of ytterbium on this singular target plate is just under 1 g—over 1000 times more than the amount of radium we distributed across 30 cells. Photos taken by Phelan Yu and Arian Jadbabaie. 80
5.2 Photos of the cold trap region of the cell gas lines. A styrofoam cup contains the liquid nitrogen. 84

5.3 Updated gas handling manifold for accommodating radioactive material. The red highlighted valve is the normally closed valve. "load" is the load lock volume. Figure inspired by the one made by Nick Hutzler for the radium SOP. 86
5.4 Photos of some of the radium-painted watch hands. Note that they are no longer glowing not because the radium has decayed, but rather because the crystal structure of the zinc sulfide phosphor has degraded after being bombarded by radiation for so many years. 88
5.5 The first ever radium target plate, showing the five radium-painted watch hands epoxied to the plate with Stycast. Before attaching the targets, we electroplated the copper target plate with pure gold (see Section 5.2 for discussion). We also pocketed out two wells, seen on the bottom left and underneath the watch hands. These wells were unused. 89
5.6 Early traces showing resonant absorption of the $^1S_0 \rightarrow {}^3P_1$ transition in ^{226}Ra while ablating radium-painted watch hands. At most, we were able to observe around 0.5% absorption of the 13999.357 cm^{-1} laser light. 90
5.7 Before and after photos showing the ablation of the radium-painted watch hands. Note that the layout is different as this is from the second radium target. The arrow points out a part of the watch hand that appears to have been completely blown out of the frame, potentially contributing to the inconsistent atom signal. 91
5.8 Photo of the glass ampoule containing our 10 μCi sample of radium-226 chloride in 500 μL of solution. The meniscus is visible below the printed label. 92
5.9 Tests of electroplating copper with various metals. Left photo shows the base layer, where we electroplated either 24 K gold, nickel, or 24 K gold onto nickel. All of these were then electroplated with pure gold (which appears as a dull brownish color rather than shiny) and tested with a barium solution. The photos on the right show the degradation of the wells where the solution was added, including a reaction leading to some green crystallization. These tests also show the strong coffee ring formed by these spherical wells. Two of the wells have foils pressed in them which we were also testing at the time. 94

5.10 Photos demonstrating four qualitatively different radiolysis effects on our early targets. On plates with co-targets attached, the radium drop cast target is always in the center. Top left: formation of a crusty blue-green surface layer via the reaction of the radium chloride solution with pure copper. The color indicates the formation of either copper chloride or copper hydroxide. Top right: likely the formation of copper fluoride, owing to our use of a teflon beaker for pre-evaporation of the radium chloride solution, which almost certainly leeched fluoride ions. We believe copper fluoride to be the resultant material because of the lighter green coloration and the fact that this was not observed in tests without the pre-evaporation. Bottom left: similar to the top left, but with a much more crystalline structure, possibly copper hydroxide or chloride again. Bottom right: radiolysis of pure gold foil, likely forming gold chloride (lighter yellow region inside the larger gold circle). 97

5.11 Illustration of the formation of coffee rings in drying droplets. Contact line pinning, a phenomenon which locks the edge of the droplet in place through the evaporation process, leads to a net outward flow within the droplet as the liquid that evaporates near the contact line needs to be continually replaced. This flow results in accumulation of dissolved particles at the edges, leaving behind a ring of material when the droplet fully evaporates. 99

5.12 Photos showing the rhodamine dye tracer test on the various alumina substrates. Starting from the top left, the materials follow the order of Table 5.1 row-wise starting from the top left, except for the very last aerogel which is the hydrophobic variant. Note the visible "coffee ring" made from dye on the nonporous alumina. 102

5.13 Accompanying photos for Table 5.2, showing some of the different concentrations of sucrose and xylitol tested as matrices. Note that, despite their reflective sheen, all of these targets have been drying for a long time and are quite immobile at this point. 105

5.14 Photo of a representative radium target with xylitol. The thick gel (center) is extremely viscous and does not move under the effects of gravity, allowing us to handle it and install it into the cell, where it may remain suspended for weeks without movement. It appears to be wet because of the glare, but has been drying for at least a day. For reference, the diameter of the gold foil is 5/16", made by a hole punch. 107

5.15 Photo of a Yb + $Yb(OH)_3$ pressed powder target that has been removed from one of our other sources. Initially, these targets look like flat pucks (see Figure 5.1). When the ablation laser is steered by hand, as was the case here, the resulting inconsistencies in the ablation locations are immediately visible. Photo from Arian Jadbabaie. 108

5.16 Still from the camera feed we use to align the ablation lasers. The reagent co-targets are clearly discernible, especially with a reference photo of the target. The two ablation laser beams, firing at very low energy so as not to actually ablate any material, are visible. The laser to the right is steered across the edges of the drop cast radium target (center-right, dark oval) to establish the bounds for our automated rastering program. 109

5.17 Traces showing the fast chopping demodulation process on a representative fluorescence signal for RaOH. Top: All PMT data shown. The bump in the lower edge of the data around 1.5 – 2 ms corresponds to ablation glow, which varies significantly from shot-to-shot; if we just integrated this data, the glow would lead to a false signal. Middle: Splitting the raw data into three regimes corresponding to when the probe is on or off, or when the AOM is switching between the two. This switching data is thrown out for the analysis, as the magnitudes in this switching region depend on how the AOM switching is aliased into our data collection, and thus varies shot-to-shot. Bottom: Signal obtained by subtracting the "signal on" trace from an interpolated version of the "signal off" trace. We integrate this subtracted trace to obtain our fluorescence signal for this shot. 111

5.18 Effect of normalization on a set of lines in RaF. The lines shown are the ${}^{P}P_{11}(J'' = 2.5)$ and ${}^{P}Q_{12}(J'' = 1.5)$ transitions in the $C^2\Sigma^+(0) \leftarrow X^2\Sigma^+(0)$ band, where 0 offset in the plots corresponds to 16609.4065 cm^{-1}. Without normalization, the hyperfine doublet (indicated by dotted lines) on the P-branch is not cleanly resolved. The lineshapes are also better defined in the normalized case, leading to more precise fits. For this data, normalization was performed by driving the ${}^{P}Q_{12}(0.5)$ line of the $X - A$ band at roughly 13284.6370 cm^{-1} and collecting the diagonal fluorescence on a second PMT. 113

5.19 Diagrammatic representation of the methods of normalization employed in our work. (a) Atomic normalization on the Ra $^1P_1$ transition. Laser absorption of the 483 nm light is detected on a photodiode, while molecule fluorescence from the chopped CW probe is detected on a PMT. (b) Interspersed pulsed dye and chopped CW normalization. Either laser may be used as the probe or normalization signal depending on the desired resolution of the measurement. (c) CW normalization with only one PMT, achieved by temporally interleaving the two chopped CW beams. (d) CW normalization with two PMTs, where the optical filtering for each PMT only admits the decays from one of the probe transitions. 114

5.20 Uncorrected scan of the ^{226}Ra $^1S_0 \rightarrow ^1P_1$ transition at 483 nm. Fitting this data to a Voigt profile gives a measured line center of 20715.6011(1) cm^{-1}, where values in parenthesis correspond to 1σ fit errors. By accounting for our absolute wavemeter offset we report an updated transition frequency of 20715.6028(1) cm^{-1}. 115

5.21 Saturated absorption (Doppler-free) scan of a few lines in molecular iodine. Green points are data, and dotted lines are the predicted I_2 spectrum from IOSpec5, a program based on measurements in [139]. This frequency range was chosen because our laser was already tuned to the $^1S_0 \rightarrow ^1P_1$ transition in barium at 553 nm. The dotted peaks correspond to the same transition, and the offset between the two is used to calibrate the wavemeter. 117

5.22 Level diagram for RaOH, showing wavelengths of relevancy to this data. Values for the $\tilde{A}$ state are approximate as the main line has not been rigorously identified yet. Numbers separated by – indicate the wavelengths of decays to both (02^n0) states. 118

5.23 Low-resolution survey scan data showing the initial identification of RaOH band. The entire scan, which took one afternoon to perform, is shown in (a), highlighting the region of high fluorescence intensity near 15740 cm^{-1}. Raw data for highlighted points at 15740.5 and 15711.3 cm^{-1} are shown in (b) and (c), respectively, showing the early-time fluorescence due to nonresonant glow. Magenta (blue) points are when the laser is unblocked (blocked) through the cell, and black is the switching region between the two. The modulation frequency is only 1.5 kHz as this data was taken using a mechanical chopper wheel instead of an acousto-optic modulator as in later data. Traces (d)/(e) show the background-subtracted signal of (b)/(c), emphasizing the excess fluorescence present at early time when the laser is resonant and passing through the cell in (b). 119

5.24 High-resolution scan of RaOH $\tilde{C}\,^2\Sigma^+(000) \leftarrow \tilde{X}\,^2\Sigma^+(000)$. Data was normalized using our pulsed dye laser signal to account for production fluctuations. Colored insets show zoom-ins on specific data ranges, emphasizing the good lineshapes with strong SNR. Not all of the range was scanned; once we had located enough lines to accurately predict the progressions, we stopped measuring in regions where no lines were expected so as not to waste our limited material. To see a version of this plot where the rotational branches are explicitly shown, see our publication [84]. 120

5.25 Initial survey scan of the RaOH $\tilde{A} - \tilde{X}$ band near 782 nm. To achieve $\sim$ 30 GHz linewidth in the infrared range, we broadened a Coherent 899 Ti:Sapphire laser according to the methods described in the text. Regions of excess fluorescence were identified around 12782 cm^{-1}, only 16 cm^{-1} away from the predicted value [70]. The plot on the right shows the highest-SNR single shot from the scan. 123

5.26 Medium resolution scan of RaOH $\tilde{A} - \tilde{X}$ near 781 nm. As mentioned in the text, our repeated measurements could not corroborate the excess fluorescence indicated by the low resolution scan, but a number of shots showed signal near 12806 cm^{-1}. The plot on the right shows the highest-SNR single shot from the scan. 124

5.27 Medium-resolution (~ 0.07 cm^{-1}) pulsed dye spectrum identifying the band head and coarse features in RaOD. Black overlaid lines are the predicted spectrum at the recorded linewidth and temperature of 7 K. Red lines are the prediction for RaOH, which we observe because of hydroxide residue in our target materials. The grayed region to the left is believed to be the $\tilde{C}(100) - \tilde{X}(100)$ vibrational overtone in RaOD, which is expected to be redshifted from the main line by ~ 4 cm^{-1} . . 126

5.28 High-resolution spectrum of the low-N region in RaOD, identifying the 31 lines used in the Hamiltonian fit. The $P_2(N'' = 4)$ line was not scanned. The R-branch $N'' = 6$ doublet from this spectrum is enlarged on the right, overlaid by the Voigt profile fits that were used to extract line centers. 126

5.29 Plots showing effects identifying this molecule with RaOD. Left: Histogram of RaOD fluorescence signals while ablating hydroxide and deuteroxide co-targets. A strong line in the RaOD spectrum was probed as the reagent ablation laser was switched between the $Al(OD)_3$ and $Al(OH)_3$ pellets, resulting in a fluorescence signal only when vaporizing the deuterated target. Right: Time trace for representative fluorescence signals when our enhancement laser was on and off resonance with the $^3P_1$ transition at 13999.357 cm^{-1}. In both cases, a mechanical shutter opens at 3 ms to allow the light to enter the cell, showing the signal enhancement achieved when this laser is resonant with the transition in ^{226}Ra. 127

5.30 $Al(OH)_3$ precipitate. 129

5.31 Aluminum deuteroxide powder after drying in the vacuum oven and crushing with mortar and pestle. 130

5.32 ^{2}H magic-angle spinning NMR spectrum confirming synthesis of aluminum deuteroxide powder. The two peaks near ±84 kHz form a Pake doublet corresponding to the $I = -1 \rightarrow 0$ and $I = 0 \rightarrow 1$ transitions in deuterium, which are split into narrow sidebands separated by the magic-angle spinning frequency of 6 kHz. (b) ^{1}H NMR of synthesized $Al(OD)_3$ against commercial $Al(OH)_3$. The integrated signals indicate that the synthesized sample is roughly 5% H instead of D, likely owing to uncontrolled ambient humidity during synthesis. (c) ^{27}Al magic-angle spinning NMR of both samples (offset for visibility), demonstrating structural agreement between the two. This data was taken by Sonjong Hwang, who also greatly assisted with the interpretation. 130

5.33 Level diagram showing the relevant states and transitions in RaF. Arrows indicate driven transitions, which might have also been used for fluorescence detection, and wiggly lines indicate lines only used for fluorescence detection. 131

5.34 Measurement of the low-J lines on the RaF $A - X$ transition. The $P_1(1.5)$ cycling line is isolated enough to establish a clean line center, which we referenced to the potassium D2 transition [144]. The other cycling line ${}^{P}Q_{12}(0.5)$ unfortunately overlaps with the (stronger) $P_1(2.5)$ line, which is the peak around 13284.635 cm^{-1}, as well as a cluster of P_1 lines at around 13284.645 cm^{-1}. The right panel data points show our scan over the potassium D2 line, with the curves below representing the six hyperfine transitions and their relative intensities. The sum of these were used to fit the measured D2 line shape to determine the center frequency and extract a wavemeter offset, which is applied to the RaF data on the left. 132

5.35 Resonant absorption signals for RaF around the $P_1(2.5)$ and ${}^{P}Q_{12}(0.5)$ lines. Using Eq. 5.1, we convert this laser transmission dip into an approximate molecule density, where this number refers to just the density of molecules that are in this exact $N'' = 2$ rotational state. Using the proper Boltzmann statistics assuming thermalization with the helium buffer gas at 7 K, this means a peak total molecule density of $\sim 4 \times 10^{8}$ cm^{-3} 133

5.36 Single-shot fluorescence signals from driving the RaCl $C^2\Sigma^+(1) \leftarrow X^2\Sigma^+(0)$ transition with pulsed dye (Credo) excitation at 15646.5 cm^{-1}, detecting the strong $C^2\Sigma^+(1) \rightarrow X^2\Sigma^+(1)$ fluorescence around 649 nm. Data collection stopped after 20 ms, but clearly the signals continued past this point. 135

5.37 Scan of the RaCl $C^2\Sigma^+(1) \leftarrow X^2\Sigma^+(0)$ transition with pulsed dye (Credo) excitation. The vertical line is the location of the predicted band head from [147]. The band head according to the 1972 data is not shown, as it is at 15639.4 cm^{-1}. This data was normalized against the co-recorded Ra $^1P_1$ absorption signal. 135

6.1 Top-down diagram of the dual-PMT setup. Red and orange wiggly lines represent fluorescence from different vibrational decay modes, originating from molecules probed inside our cryogenic buffer gas cell. Optical filtering is generally chosen to allow one decay into each PMT, but this does not need to be the case—only that the two PMTs have distinct wavelength-dependent light collection efficiencies. The plot inset is an example of a simultaneous PMT trace for a single shot in CaF, measuring the decays from $A(v' = 0)$ to $X(v'' = 0)$ and $X(v'' = 1)$ in orange and red, respectively. The raw PMT values cannot be compared directly as the gains and light collection efficiencies are different, as described in the text. 140

6.2 Photo of the dual-PMT implementation on the Minifridge table. In typical operation, light-blocking foil is placed all around the setup to prevent leakage from room lights and lasers. Note that the orientation of the PMT that detects the reflected fluorescence from the 50/50 beamsplitter is flipped relative to Fig. 6.1. 141

6.3 Calibrating the pickoff power for the diagonal decay light scatter measurement. The slope gives the factor that converts from measured pickoff power to true experimental laser power. DC backgrounds, such as electrical offsets or ambient light leakage, have been accounted for. 144

6.4 Example of the determination of the light collection efficiency for both PMTs at the on-diagonal frequency, according to Eq. 6.5. The slope gives the combined efficiency term $\varphi_i \varepsilon_i(752\text{ nm})\alpha$. Each color represents a different configuration of laser power attenuation achieved by swapping neutral density filters. The optical filters for PMT 2 should allow the on-diagonal light, while those for PMT 1 are intended to block it and only permit the light around 778 nm. Note that the laser power may vary by a significant amount within a set of data, emphasizing the need for coincident power monitoring. 145

6.5 Side-by-side comparison of the raw PMT signals for one single ablation shot of the RaF $A(v = 0) - X(v = 0, 1)$ b_{01}/b_{00} branching ratio measurement. Note the dramatic difference in vertical scale, to the point where we are almost at the electrical noise floor on the $v = 1$ channel. Still, there is a discernible signal. This data will be background-subtracted and integrated to obtain the two signals $\mathcal{S}_1$ and $\mathcal{S}_2$, whose ratio relates to the ratio of VBRs, determined in Eq. 6.7 for this experimental configuration. The spikes on the $v = 0$ channel are due to laser power jitter, which does not couple into the analysis. . 146

6.6 Plot of every simultaneous data point taken during the branching ratio measurement. The x-axis corresponds to PMT 1 looking at the $v = 1$ off-diagonal decay, and the y-axis is the $v = 0$ on-diagonal signal seen by PMT 2. This is before correcting for the on-diagonal leakage into the off-diagonal signal channel (see text for discussion). Each different color is a data set taken at a different probe laser power, showing how the behavior is linear with the same slope regardless of laser power. . 147

6.7 Measurement of the b_{01}/b_{00} ratio for the first excited state in RaF, yielding a value of 0.00044(16). Data was taken over the course of multiple days under different experimental conditions and remained consistent. The red horizontal line is the mean, with the shaded region indicating one standard deviation. The values shown include the correction for the leakage of the diagonal decay light into the off-diagonal channel, obtained from a linear fit as in the right side of 6.4; the uncertainty of this fit was treated as a possible systematic error and plotted here as the error bars, multiplied by 3 to give a 3σ range. The systematic uncertainty from the errors from the diagonal efficiency measurements is also included, but is smaller than the size of the points. This plot does not include every data point; see the section "cutoff analysis" for discussion on how this data was post-selected. 148

6.8 Histogram of all the data taken in the RaF X-A b_{01}/b_{00} branching ratio measurement, after applying the signal cutoff. Top: Each power plotted separately. If enough points for a power remained, the set was fit to a gaussian distribution, with resulting center and standard deviation shown. Bottom: All powers summed together in a single histogram, where the gaussian fit results are printed in the plot. From the standard deviation σ, the standard error $\hat{\sigma}$ is calculated. 149

6.9 Picking a cutoff for the full dataset shown in Fig. 6.6. The top plot shows the minimum of the standard error for the sample, achieved at a threshold value of 846 (vertical line). The piecewise-looking jumps at the right are caused by a lack of data points between these high cutoff values. Bottom shows the mean of the b_{01}/b_{00} ratio (green center line) as a function of the cutoff, with the standard error at each point given as the red error bars and the 1σ standard deviation by the light blue span. 150

6.10 Analogous plot to Figure 6.7 but for the YbOH $\tilde{A}(000)$ state decaying to $\tilde{X}(200)$ and $(12^{2,0}0)$. A slight trend seems visible in the data but appears to correlate with shot number more than laser power, as the measured values are relatively continuous at the switching points between data sets. We observed trends like this in a handful of measurements, but were unable to pin down an unambiguous cause as there was no way to force it to occur or not. Still, with enough data, the average seems to converge to a value that agrees with other measurements to within our experimental uncertainty. 152

6.11 Measured b_{01}/b_{00} ratio for the RaF $A - X$ band as a function of input laser power, demonstrating approximately no correlation between the extracted value with laser power. The purple horizontal span represents the standard error of the full sample, taken as $\hat{\sigma} = \frac{\sigma}{\sqrt{n}}$ for n data points. Both apparent outliers on the low side had ≤ 5 data points after the cutoff was applied. Error bars represent the standard error of each individual sample. Some of the samples had few data points, so an unbiased estimator of the standard deviation was used [154]. 153

6.12 Measurement of the b_{02}/b_{00} branching ratio for RaF. The results are consistent with zero, with larger error bars than previous measurements owing to the reduced measurement sensitivity at these wavelengths and the fewer data points taken. None of the single-shot data showed any signal in the $v = 2$ decay channel. 154

6.13 Similar branching ratio plots as above but for the measurement of b_{01}/b_{00} for the $C\,^2\Sigma^+_{1/2} \rightarrow X\,^2\Sigma^+_{1/2}$ band in RaF. Inset emphasizes the lack of dependence of the resulting value on the probe laser power, as expected. See Figures 6.8 and 6.11 for more details. 156

6.14 Level diagram summarizing our measurements of the vibrational branching ratios $b_{v'v''}$ in RaF. Also shown are the wavelengths for the laser cooling line at 752.7 nm and $v'' = 1$ vibrational repump line at 618.3 nm. 157

7.1 Before (left) and after (right) photos of epoxying on a chunk of pure barium metal (right above dark blue circular co-target). Even though the metal had a protective oxide layer, the presence of water vapor in the air resulted in the formation of $Ba(OH)_2$ powder, the majority of which was no longer rigidly attached to the target plate. 160

7.2 Reagent co-target testing to identify a suitable solid-state hydroxide source. Because the data was not taken in a rigorously systematic way, the bars show only the maximum signals achieved with each reagent; the telluric acid ($Te(OH)_6$) and aluminum hydroxide targets performed roughly equally. Aluminum hydroxide is significantly cheaper and possesses no safety hazards, making it the easy choice. . . 161

7.3 Testing various configurations for producing BaF. Data between the two plots are normalized to the "No enh." signal, referring to molecule production without enhancement light. The left data focused on co-ablation targets, where the line driven was at 13, 573.9648 cm^{-1} [159], where we detected the diagonal decays down to $X(0)$. Data for the right was obtained by driving the line at 12262.835 cm^{-1} [160] and detecting the off-diagonal decays to $X(1)$. Normally this detection scheme is weak, but BaF is suitable non-diagonal such that many of the decays are to this $X(1)$ state. 162

7.4 Left: chemical structures of the reagents tested for producing $CaNH_2$. Right: the target plate used for amine reagent testing, showing the four different pressed powders. Ethylenediamine is commonly abbreviated to en when represented as a ligand. The target at the very center is the CaF_2 sputtering target used as a source of calcium atoms. One point of note is the extra crystals on the edges of the urea target—these were not present when the powder was initially pressed, but did not seem to drastically alter the structure or quality of the target as a reagent. . 165

7.5 Single shot and scanning data for $CaNH_2$ while ablating the urea co-target, which seemed to yield the best signals. Left: Demodulated single-shot data showing the excess PMT signal when the CW light is on, corresponding to molecule fluorescence. Right: Scan around the resonant frequency reported in [164] for the $\tilde{B}\,^2B_1 \leftarrow \tilde{X}\,^2A_1$ transition in $CaNH_2$. 166

7.6 Averaged $CaNH_2$ fluorescence signals as a function of ablated reagent, at two different operating temperatures. In both cases, the urea co-target is the most successful. Error bars are the standard deviation of the sample values for each co-target. 167

7.7 Before-and-after overnight drying of the lanthanide trichloride co-targets on a radium-containing target plate. Note that the photos are inverted from left to right; the blue CuF_2 target is visible on both panels. a) $PrCl_3$ can be seen in bright green (bottom left) and $NdCl_3$ in pink (left). The stickiness is partially observable as a sheen on the targets. b) Next morning, the lanthanides had completely melted, leaving a liquid layer on the surface of the target plate. The drop cast radium was partially covered and the plate was deemed unsafe to install, rendering it radioactive waste. 169

7.8 Single-shot and scan data for pulsed dye excitation of calcium chloride, produced by co-ablating a calcium fluoride sputtering target with a pressed powder of silver chloride (AgCl). The single-shot data corresponds to the point on the scan with the largest integrated signal. Signal-to-noise ratio for this point is included inset in the scan trace. . 170

7.9 Single-shot and scan data for pulsed dye excitation of calcium iodide, produced by co-ablating a calcium fluoride sputtering target with a pressed powder of silver iodide (AgI). The single-shot data corresponds to the point on the scan with the largest integrated signal. Signal-to-noise ratio for this point is included inset in the scan trace. 171

7.10 Left: Fluorescence scans of some lines in uranium monoxide (see text for details), showing two lines recorded at high resolution. Right: Tests of various ablation co-targets in producing UO. The co-targets are: alumina ceramic, aluminum hydroxide pressed powder targets, thoria ceramic, and none. In the no co-target example, we believe the oxygens to be sourced from the extreme degree of oxidation of the pure uranium metal. 172

7.11 Scan of the hyperfine lines on the ^{237}Np ($I = 5/2$) $^{6}L_{11/2} \rightarrow {}^{8}L_{9/2}$ transition at 607.5 nm. Lines are labeled by the ground and excited hyperfine sublevels $F'' \rightarrow F'$. Only the $\Delta F = -1, 0$ transitions were observed, as the $\Delta F = +1$ transitions are expected to be a factor of 10 weaker. Inset shows typical line shapes for each of these transitions. . 173

8.1 Representation of the principle of magnetic shielding, using simulations from a three-layer nested square shield design. Region (A) is outside of the shields and (B) is inside (where the experiment would occur). The lines incident from the edges of the image represent the ambient magnetic field lines, defined in this simulation to be applied from left to right, which preferentially travel through the high permeability material rather than inside to the experimental region. A zoom-in on the thin shielding material in (C) shows a densely-packed collection of field lines, owing to the fact that they do not terminate, but rather travel through the shields and out to the other side. A few lines are visible representing field leakage through the outer layer of shields, but these are further redirected by the subsequent layer. . . . 179

8.2 Approximate maximum acceptable background magnetic field levels for an EDM-style measurement as a function of evolution time τ. The magnetic dipole moment of the molecular state undergoing the measurement was taken to be μ_B. The inset shows the limits for shorter times, of particular relevancy to molecular beam experiments. 180

8.3 Diagrammatic representation of the principle of magnetic circuits, showing the advantage of adding additional shielding layers in attenuating an external magnetic flux Φ_{ext}. (A) shows the analogous magnetic circuit for a single layer of magnetic shielding, while (B) shows the circuit for a two-layer magnetic shield separated by a gap. The pattern may be repeated for arbitrarily many shield layers. Subscript s denotes the shield, with a further subscript indicating which shield, following the notation that the numbering increases from the inner layer outwards. "gap" refers to the air gap between the shielding layers, and "int" to the interior region where the experiment takes place. 182

8.4 Photos of the shield assembly before and after installation of the three layers of mu-metal magnetic shields. Left shows the nested frame, while right shows the completed setup with degaussing coils. 185

8.5 Rendering of all of the shield plates, with an example plate expanded (left) to show detail. Central bores in each plate allow laser or vacuum access, while small holes lining the perimeter are used for mounting to the aluminum frame. Slits near the corners are where the degaussing coils are wound. The shields are slightly asymmetric, as seen by the depth of these slits—the top and left edges of the enlarged shield have slightly deeper slits, indicating that the plates are longer in these dimensions, allowing them to overhang on the neighboring plates to cover the corners better when fully assembled. The small pieces on the bottom plates and endcaps are used to connect between the split plates to ensure magnetic contact. 187

8.6 Diagrammatic representation of the degaussing coils for a single layer of the shielding, using a simplified cube as a stand-in for the rectangular prism of the shield. Each colored line is a coil wound 24 times around the plate at those locations. The resulting fields generated by sending AC current through these wires are shown as arrows on the right, where circulating paths around the shields in two directions allow for full saturation of all plates simultaneously. 188

8.7 Attempt at representing the connecting wires diagrammatically with dotted lines. The right figure shows just these connecting wires. Once the current reaches OUT, it returns via the same connectors back to the IN. Colors of the dotted lines attempt to show the color of the coil which the line is connecting to. 189

8.8 Comparing different simulation setups to test their consistency using a dummy 24" x 24" (x 48" for 3D) model shield. 2D and 3D refer to the dimensionality of the simulation, with 2D simulations being considerably simpler and faster to implement. BC refers to "boundary conditions," where the shields are modeled in COMSOL as infinitely thin sheets and the effects caused by their finite thickness are handled by the magnetic shielding module. FT means "finite thickness," where the shields were modeled as magnetic materials with an explicitly constructed thickness to benchmark the BC module within COMSOL. The comparisons were performed at a range of applied magnetic fields to test whether they would capture saturation behaviors—the 3D simulation would not converge at 100 G due to a lack of computer memory. 190

8.9 Comparison of shielding factors at the center of a 4-foot-long single-layer magnetic shield, with thickness 2 mm and no apertures, as a function of applied magnetic field in Oersteds, where in free space 1 Oe ≡ 1 G. The square prism shape has other side lengths of 2 feet each, while the cylinder was chosen such that the diameter fully enclosed the square, meaning $2R = 2\sqrt{2}$. As such, the cylinder shielding is slightly worse than the square prism, likely owing to its larger size. The calculated value comes from using Eq. 8.3 for this cylindrical geometry, using $\mu_r \approx 8 \times 10^4$. Discrepancies between this calculation and the simulation are likely due to slight variations in the permeabilities used in the simulations, which were taken from the $B - H$ curve provided from the mu-metal manufacturer. 191

8.10 Plot of the simulated shielding factor for a 2' x 2' 2D square shield with thickness 2 mm, given an applied external field of 100 mG (below the saturation value). The dotted lines show the asymptotic value with no gap. The shielding factor quickly drops to under 10% of its starting value with a gap on the order of just 0.1 mm. The photo on the right shows the simulated field lines near one of these corner gaps, where the leakage into the shielded region is represented by the lines in the bottom right quadrant. 192

8.11 Simulation of the effect of adding a metglas strip to cover an underlying gap in the corner assembly, for the same 2D test geometry as in the previous plots. Left is a photo of what this strip might look like in practice. The plot on the right shows the shielding factor when using a strip like this to cover a gap between the plates, showing that even when the gaps get quite large this covering returns much of the shielding ability. "no metglas" refers to the shielding factor of a 2 mm gap without metglas, to show that the shielding depends strongly on its addition. 192

A.1 Left: decay chain of Ra-226, taken from `https://www.nist.gov/image-23773`. Right: Activity of all daughter nuclides after starting from 10 μCi radium-226. Taken from `https://www.wise-uranium.org/rcc.html`. 216

A.2 Activity of 10 microCi Ra-226 (pure sample at t=0) versus time over one month, log scale. From `https://www.wise-uranium.org/rcc.html` 217

A.3 Images: Left: A target plate showing the central gold disk and a droplet of radium solution on top after it has fully dried (the current protocol). Right: An older target protocol, where the blue coloration in the middle is the result of radiolytic reactions between a radium chloride solution and the copper surface, likely forming copper (II) chloride dihydrate. 219

A.4 Images: the same target plate, before and after the addition of the ablation co-targets. Left: the xylitol-doped radium nitrate solution is fully evaporated in the center of the gold foil, even though it looks like a liquid droplet (the plate is being held vertically and the material does not move). Right: the ablation co-targets. Clockwise from top: Yb metal chunk, Yb powder-doped $Al(OH)_3$, $Al(OH)_3$, CuF_2, and $Al(OD)_3$. 219

A.5 Image: A barium test target featuring many different alumina porosities. The center is a typical drop cast target, and the white pieces are different types of alumina. Any dark coloration is the result of the ablation process. The metallic ring surrounding the targets is the indium seal, which is explained in the following section. 220

A.6 Image: two PTFE (Teflon) beakers of barium chloride solution during a test of the pre-evaporation protocol. Teflon is slippery and thus prevents any sticking of radium to the walls of the beakers, and because it is resistant to the hydrochloric acid in the solution. Based on our tests, the pre-evaporation process reduces the volume from 5 mL to 0.5 mL in around 3.5-4 hours, and will reduce the necessary handling time of the radioisotope by 90%. 221

A.7 Figure from `https://www.wise-uranium.org/rcc.html` 222

A.8 Images: 3D rendering of the cell before (left) and after (right) mounting of various attachments. The bores that create the internal cavity are visible as the three large through-holes on the left image. The target plate is the featureless plate visible on the right side of the right image. 223

A.9 Photo: Midway through the assembly process of an older cell version. Copper flanges are used to hold the windows in place. Indium wire can be seen on the left of the photo (above the screw on the table), as well as pressed between the left window and the cell. The uncovered hole visible on the right of the cell is where the target plate would mount. The helium cell outlet is extending to the right of the photo. 224

A.10 Photo: two cell bodies immediately after painting. They will dry in a fume hood for 24 hours before being handled. On both, the paint was airbrushed through the hole on the left of the top surface, creating a very dark interior region. 224

A.11 Photos: Right: A completed cryostat with all components in place, ready to take data. The 300 K stage is the blue layer, with part of the 30 K stage visible through the window on the bottom. Left: An early step in the construction where the 30 K and 4 K copper sections of the cold head are visible. The 30 K section is the portion slightly up from center, and the 4 K section is just below the joining segment of the two cube frames. 225
A.12 Right: The 4 K stage sitting within a partially-assembled 30 K stage. The cell is visible as the bottom copper part. The cell window on the left allows for laser access to the target, and the window on the right allows for laser access to the plume of atoms and molecules produced by laser ablation. Left: The completed 30 K stage as it surrounds the 4 K stage. Windows allow laser access through the 30 K stage to the cell. 226
A.13 The CRC Handbook lists the melting point of radon as 202 K, and the boiling point as 211 K. The `plot` at left shows the vapor pressure of Radon versus temperature (taken from `https://www.sciencedirect.com/science/article/pii/S0021961407000687`). 244
B.1 These marks (left and upper-right of the bore) are examples of dings that could impact the sealing ability of the cell, and would need to be sanded/filed away completely. 250
B.2 These sorts of scratches (between the two bores) are the result of the sanding process and are inevitable. They won't impact the sealing of the cell in almost all cases. 250
B.3 Diagram of the cell with each port explicitly numbered to match those listed in Table B.4 252
B.4 All of the parts used for assembling the cell laid out prior to assembly, except for two plates already attached. 254
B.5 Left: indium wire (mostly) pre-smoosh. Right: indium wire post-smoosh (some is missing due to coming off when I removed the plate). 254
B.6 How to cut indium wire to increase the contact surface area. This method increases the probability that the indium will seal properly when compressed 255
B.7 Photo of an indium gasket in accordance to the cutting scheme presented in Fig. B.6. Not the best example of a good cut, but still better than just being flat! 256
B.8 It is quite easy to tell when the window is cracked. 257

List of Tables

Number *Page*

3.1 Summary of some units and quantities used for describing radioactivity. Units listed lower are the SI-recommended variants. 39

4.1 Table of panels on the Minifridge 30 K intermediate stage and their current uses. 59

4.2 List of all species produced and studied in the Minifridge as well as the targets used to produce them. [a]Bolded recipes denote the most successful, in the cases where multiple were tested. A "&" indicates dual-ablated targets while "+" indicates combined pressed powders. . 70

5.1 Materials tested in the Rhodamine dye tracer test. [a] RS-99R from ZRCI refractory composites. [b] Product 8462K24 from McMaster-Carr. [c] Product 8484K84 from McMaster-Carr. 101

5.2 Testing various concentrations of sucrose and xylitol. Values of concentration are given as a range because the scale used has a limited resolution and because the behaviors were mostly the same within these limits. 106

5.3 List of high-resolution observed lines in RaOH. Double prime refers to ground state and single prime to excited state. The branch assignments are denoted by ${}^{\Delta N}\Delta J_{F_i' F_i''}$, where $F_i = F_{1,2}$ refers to the $J = N \pm 1/2$ spin-rotation components, and *not* the total angular momentum. For the comparison with predicted values, see [84]. 121

5.4 List of high-resolution observed lines in RaOD. Double prime refers to ground state and single prime to excited state. The line assignments are denoted by ${}^{\Delta N}\Delta J_{F_i' F_i''}$, where $F_i = F_{1,2}$ refers to the $J = N \pm 1/2$ spin-rotation components, *not* the total angular momentum. For the comparison with predicted values, see [84]. 128

6.1 Branching ratio benchmarking test results for CaF and YbOH. For both molecules, values recorded are for decays out of the ground vibrational level of the first excited $^2\Pi_{1/2}$ state. †The CaF DLIF values were taken by Phelan Yu on our supersonic beam source, and the values for YbOH are taken from [156]. As explained in the text, the supersonic DLIF values taken suffer from saturation on the b_{00} decay mode, resulting in an artificially larger value. The ratio of the two weaker decays b_{02}/b_{01} should not be affected in the same way, or at least not by as much. For the DLIF method, this last value was determined directly from signal ratios of the b_{01} and b_{02} decays, while for our PMT-based method it was inferred by taking the ratio of the first two lines. ‡Errors for the YbOH measurement were determined by propagating the published single-state 1σ errors in [156]. Only the values for the (02^00) and (12^00) were used, as the (02^20) and (12^20) were not measured using DLIF; their values will factor into our measurement, but are predicted to be inconsequentially small at our uncertainty levels. . . . 152

B.1 Sanding requirements for different aspects of the Minifridge cell. Note that not every surface needs to be sanded to vacuum-quality, which saves time in the process. 250

B.2 *brass has been the historical convention due to its thermal expansion matching copper better, but I have had bad luck torquing the 4-40 brass screws enough to get a good seal with the indium. Often the screwheads will break off which is annoying. On the other hand, using steel makes it possible to apply too much force for the windows and crack them... at the very least, always use stainless steel screws to secure the radium target plate to avoid screw breakage. 252

B.3 Table listing the parts attached to each cell port, accompanying the diagram B.3 253

"The universe is true for us all and dissimilar to each."

— Marcel Proust, *La Prisonnière*, from *In Search of Lost Time*

Chapter

I

Introduction

In 1903, Marie Skłodowska Curie defended her doctoral thesis *Recherches sur les substances radioactives*, which detailed her discovery of the element radium and its characteristic phenomenon of radioactivity; less than six months later she received the Nobel Prize in physics. It is under these auspices that our work here begins.

Immediately after its publication, radioactivity marked an intersection between the various scientific disciplines, as each took to describing how this novelty fit within their respective framework of the natural world. Radium (and its associates) presented new concepts in need of understanding, new laws in need of formulating, and new equations in need of deriving. It did not take long for the descriptions to catch up, making radioactivity more-or-less a "solved" problem, and radium just another element.

The science of today looks a little different than it did in 1903. Our physical models have proven themselves so accurate as to correctly predict the outcome of certain measurements to within 0.000000001% agreement [1]. At the same time, they fail under basic scrutiny when it comes to some fundamental questions, such as the origin of matter in the universe and the nature of the missing mass and energy which we deem "dark." This tension is unnerving—how can our description of the universe be so successful in parts, while clearly being incorrect or incomplete in others? With

no recent surprises to revolutionize our theories, we have taken to looking inward at what we already have.

Experiments allow us to stress test our models in an attempt to find faults in their predictive abilities. These faults manifest as a disagreement between theory and observation, where the nature of the disagreement either allows for modification of the theory or guidance towards the source of unexpected behaviors. To push our sensitivity to any faults, these tests must occur at the extremes of energy, precision, or both. Perhaps the most famous examples of extreme energies are those created in particle colliders, which have been instrumental in validating certain predictions (as with the Higgs) as well as prompting new ways of thinking (as with the development of quark theory).

Achieving high precision requires working with simple systems, free from the complicating effects of the environment or many-body interactions[1]. The most precise experiments utilize elementary particles—electrons and nucleons—and the atoms and small molecules they comprise. Lasers or other forms of electromagnetic radiation can probe these systems remotely and cleanly. With these types of measurements, fault-finding happens at the microscopic level, where theories are compared against measurements to fractions of a percent in the hopes of identifying where any deviations occur.

The goal then becomes designing an experiment that allows for precise measurements at extreme energies. In the lab, achieving these extremes requires careful engineering of macroscopic systems, where desired goals run up against practical materials considerations, sometimes in insurmountable ways[2]. Instead, let us reexamine what constitutes a "laboratory"; if we want to study behaviors inside intense electromagnetic fields, for example, why don't we look for where these environments already exist, rather than try to create our own?

Following this line of thinking brings us back to simple atomic and molecular systems. The region immediately surrounding an atomic nucleus can be considered one of the most energetic electromagnetic environments in the universe, with such little separation between the charged electrons and protons as to generate electric fields many orders of magnitude stronger than the largest ones possible in the lab. In these

[1] This is, of course, a simplification of the truth. Many-body systems can be studied extremely precisely as long as their respective interactions are understood well enough.

[2] For example, there are fundamental limits as to the strength of electric fields that can be applied in the lab, where exceeding these limits results in the breakdown of air or the materials generating the fields.

strong fields, the low-mass electrons obtain significant kinetic energies, where even in hydrogen one needs to consider the relativistic corrections to the electron's motion. In heavier nuclei the electric force only gets stronger, and related energy scales even greater, with inner-shell electrons achieving velocities over 50% the speed of light [2]. And we don't have to engineer an impossible apparatus or travel to the center of a neutron star to find these behaviors—they exist in the same atoms and molecules that we can already study so precisely. In these exotic, heavy nucleus systems, we have found our laboratory for pushing our theories to their limits. As it turns out, the heaviest, most extreme nuclei are all radioactive.

Through this circuitous route, we have re-motivated research on radioactive atoms and molecules, bringing us right back to the turn of the 20th century. However, in a subtle but important contrast, these unstable species now interest us not so much as a subject of study, but as tools with which we can probe the inaccessible parts of our theories.

Astronomy, nuclear science, fundamental physics, and chemistry have all seen recent interest in radioactive molecules for the above reasons [3], yet they all suffer from the same problem: working with radioactive molecules is hard. Many insidious features of these species conspire together to make their study significantly more challenging than stable molecules. However, as I just spent so long motivating, the scientific potential of radioactive molecules has started to outweigh the headache of dealing with them. Given that, for many disciplines, the use of radioactive molecules is still in its infancy, any experimental improvements facilitating their study have benefits that extend across scientific subfields. Much of the work I performed for this thesis has served to make these molecules more accessible in traditional laboratory settings.

This has been a (perhaps much too long) generic introduction to the modern interest in radioactive molecules. The following sections will introduce our specific motivation for using them to look for new physics, as well as provide some broader perspective as to how our technical developments might benefit other fields over the existing state-of-the-art.

1.1 Searching for signs of new physics

As alluded to in the general introduction, the Standard Model of particle physics works extremely well, having held up against every experimental check thrown at it in the last few decades [4]. Yet its framework fails to account for a process that could produce the observed matter-dominated universe [5]. Some physical process Beyond the Standard Model (BSM) therefore necessarily must exist, which will modify or

extend the existing theory.

In generating a matter-antimatter asymmetry, some phenomenon must exist which treats the two separately. Matter and antimatter are related to each other by the inversion of their combined charge (C) and parity (P). If a physical process behaves differently when both charge and parity are inverted, it is said to be CP-violating, and leads to different behaviors for matter and antimatter, potentially allowing for the generation of one over the other. As the laws of physics are generally believed to be invariant to the combined reflection of charge, parity, and time (CPT) [6], CP-violation is mathematically equivalent to T-violation. A general feature of BSM physics predictions, if they intend to explain the matter-antimatter asymmetry, is that they contain additional terms which violate CP symmetry. These terms typically include new (or modified) CP-violating particles or forces which by construction must interact with the known particles or forces. Searching for additional sources of CP-violation is thus equivalent to probing for new BSM physics.

Rather than observe them directly, experiments searching for new particles instead look for the consequences of the existence of these particles. In collider-based searches, this involves tracking the energies and trajectories of the detectable decay products to extrapolate their origin from some new particle, such as was done to identify the Higgs [7, 8]. A complementary route is to indirectly observe the signatures of these novelties through their interactions with electrons, nucleons, or nuclei, whose Standard Model behaviors can be calculated quite well. Focusing on the latter method for this work, we encounter the notion of "CP-violating observables," referring to the low-energy measurable consequences of the high-energy BSM physics[3]. Said another way, a new CP-violating particle or force would induce some CP-violating property in electrons and/or nucleons, which we should then be able to detect. This line of thinking is not unique to BSM physics searches; the anomalous magnetic moment of the electron, which is the precisely measured quantity I mentioned in the general introduction, is an example of a low-energy observable whose value receives contributions from interactions with every other higher-energy particle and force in the Standard Model [10].

[3] In addition to new high-energy particles, there is the possibility that new physics results from weakly coupled particles or forces, which may themselves not be too energetic, for example the hypothetical QCD axion [9]. Searches for these types of particles rely on different classes of experiments, some of which benefit from the advantages offered by molecules.

CP-violating observables

The observables in question are permanent electromagnetic moments of electrons, nucleons, or nuclei, whose existences would inherently violate CP symmetry. Each one is described briefly below.

A note on specificity: It might seem like I have cherry-picked three random electromagnetic moments out of the space of all possibilities. However, high-energy CP-violating physics will necessarily induce observable CP-violating effects everywhere that they can appear, the only difference being the magnitude at which these effects manifest. The moments listed just happen to be the lowest-order CP-violating electromagnetic moments, making them the easist to measure and relate to the underlying physics through theoretical calculations.

Electron electric dipole moment

Perhaps the most intuitive CP-violating moment is the electron's electric dipole moment (eEDM), written $\vec{d}_e$ or just the magnitude d_e. Classically, it can be thought of as resulting from an offset between the center of mass and center of charge of the electron[4]. As a vector quantity, an eEDM would necessarily point parallel or antiparallel to the spin ($\vec{S}$) of the electron, a consequence of the Wigner-Eckart theorem[5]. Because $\vec{d}_e$ is a polar vector and $\vec{S}$ is an angular momentum, an eEDM and spin behave in the following ways under certain symmetry reflections [12]:

$$\begin{aligned} T: &\quad \vec{d}_e \to \vec{d}_e \\ &\quad \vec{S} \to -\vec{S} \\ P: &\quad \vec{d}_e \to -\vec{d}_e \\ &\quad \vec{S} \to \vec{S}\,. \end{aligned}$$

In both cases, performing the listed symmetry inversions on an electron with an eEDM and spin that are originally aligned results in a qualitatively different electron, as the two are now anti-aligned. Thus, the existence of a permanent eEDM violates both T (equivalent to CP) and P symmetries separately. These are shown diagrammatically in Figure 1.1.

[4]The mathematical formulation is obviously more rigorous; see: [11].

[5]If the two pointed in any orthogonal directions, then the system would require a new quantum number to be described fully. This would have many obvious consequences, one of which being that atomic energy levels would admit twice as many electrons as they do now, since two electrons with the same spin could still satisfy the exclusion principle if their dipoles pointed in different directions.

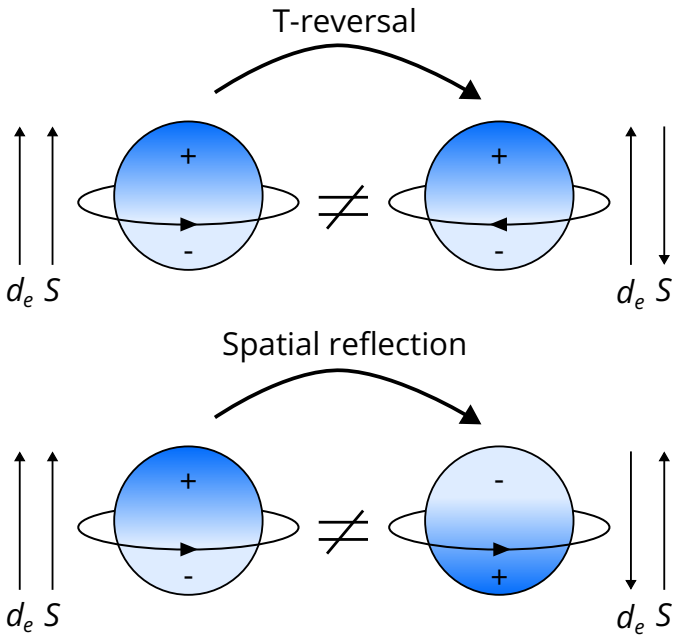


Figure 1.1: Diagrammatic illustration as to why a permanent EDM would violate T (equivalent to CP) and P symmetries. The color gradient represents the charge distribution of the system, and the circular arrow shows the classical interpretation of its intrinsic angular momentum (spin). Under a time reversal or spatial reflection, the resulting particle is qualitatively different from the one before the operation.

Much like classical electric dipoles, an eEDM interacts with an applied electric field $\vec{\mathcal{E}}$:

$$\hat{H}_{\text{eEDM}} = -\vec{d}_e \cdot \vec{\mathcal{E}} \propto -d_e \vec{S} \cdot \vec{\mathcal{E}} \, .$$

Experiments searching for an eEDM thus look for the energy shift associated with aligning the spin with an electric field, a term which should otherwise be zero[6].

Most CP-violating moment searches rely on a Ramsey-type measurement scheme. For an eEDM measurement, this means preparing a superposition of spins in an applied electric field and reading out the relative phase accumulation ϕ after some evolution time τ, which is proportional to d_e [13]:

$$\phi \approx \frac{d_e \mathcal{E} \tau}{\hbar} \, .$$

[6]On its own, an electron spin does not interact with an electric field, as spin is an intrinsic angular momentum (magnetic dipole) and thus only interacts with magnetic fields. Saying that this term should be zero is slightly misleading, as the Standard Model does predict an electron EDM background, but it is still orders-of-magnitude below the best experimental sensitivity.

These measurements are not performed on bare electrons in electric fields. For one, bare electrons are charged, meaning they accelerate in an electric field and would quickly fly away. A bigger reason, however, relates to the magnitude of the electric field $\mathcal{E}$. Previous measurements have concluded that d_e must be very small, otherwise it would have been observed already. Thus, in order to have a chance of detecting some accumulated phase ϕ, both a long evolution time τ and strong electric field $\mathcal{E}$ are desired. The strongest DC electric fields capable of existing in the lab are on the order of tens of kV/cm, after which arcing between the electrodes occurs. Contrast this with the (effective) electric fields $\mathcal{E}_{\text{eff}}$ present between the atoms in polar molecules, which for certain species has been calculated to be many tens of GV/cm—over 1000 times larger [14].

The ultimate quantum shot-noise sensitivity limit for an eEDM measurement in molecules is given by [15]:

$$\delta d_e = \frac{1}{2|P|\mathcal{E}_{\text{eff}}\tau\sqrt{N}}, \tag{1.1}$$

where the new terms P refer to the degree of polarization of the molecules with respect to the lab frame (more on this in Section 1.1 *Molecular sensitivity factors*) and N to the number of molecules measured per experimental shot. The most precise measurements of d_e thus want large molecule counts, strong effective electric fields, and long measurement times. It has been shown that the effective field in molecules comprised of a heavy atom bonded with an electronegative ligand scales as $\mathcal{E}_{\text{eff}} \propto Z^{2-3}$ for proton number Z of the heavy atom [16]. This molecular motif was not chosen arbitrarily, as will become clearer later. Important to note in the context of this thesis is that heavy atoms with $Z > 82$ are all radioactive, albeit to varying extents.

Two experiments have set the best measurement for d_e in the past decade. The most precise measurement as of today was performed using HfF^+ molecules and set an upper limit of $|d_e| < 4.1 \times 10^{-30}$ e cm [17], where e is the electron charge[7]. Before that, the limit was set using neutral ThO molecules, with a limit of $|d_e| < 1.1 \times 10^{-29}$ e cm [13]. Both of these measurements are orders-of-magnitude above the Standard Model prediction, which was recently re-calculated to be[8] $d_e = 1 \times 10^{-35}$ e cm [18].

[7] This limit, in SI units, is $|d_e| \lesssim 6.6 \times 10^{-51}$ C m (coulomb meters).

[8] A subtle point is that this calculation is not explicitly for the bare eEDM, but rather for a CP-violating semileptonic interaction between the electron and nucleons referred to as C_s. In a measurement, this C_s term is indistinguishable from d_e.

Details about specific eEDM search candidates as they pertain to this thesis will be described later in Section 1.1 *BSM physics sensitivity factors*, as much of the discussion applies to the other two CP-violating moments as well.

It is worth noting that neutrons and protons may also possess an electric dipole moment. These moments will contribute to the values of the Schiff and magnetic quadrupole moments discussed below. Direct measurements of the neutron electric dipole moment have set the most stringent limits on explicit sources of underlying hadronic CP-violation [19, 20], as they are the simplest and thus most tractable hadronic systems for calculations. Their measurements are quite distinct from those performed on heavy nuclei in molecules, and as such I will not discuss them here.

Schiff moments

Next we examine CP-violating electromagnetic moments of nuclei. Just like for the electron EDM, an intrinsic nuclear EDM would violate T symmetry and thus be CP-violating. However, as was pointed out by Schiff in 1963, an EDM of a nucleus would be completely screened by the orbiting electrons, preventing its detection [21]. Except that this is not entirely true; at the electric octupole (and higher) order of the electron-nucleus interaction, a nuclear EDM couples back in and interacts with the orbiting electrons in a non-dipolar (and therefore unscreened) way [22]. This results in a measurable atomic EDM that is related to the bare nucleus EDM[9] by a series of correction terms of progressively increasing order. The lowest-order term, which contributes the most significantly, is called the Schiff moment ($\vec{S}$, not to be confused with electron spin). The magnitude of $\vec{S}$ is quoted in units of e fm^3, or "electron charge femtometers cubed." The Schiff moment can be thought of as the residual nuclear EDM that is improperly screened by the electrons; this is not a rigorous mathematical description of the Schiff moment, but captures a lot of the correct behavior.

Like the eEDM, $\vec{S}$ is a polar vector that must point along the nuclear spin $\vec{I}$ as a consequence of the Wigner-Eckart theorem. This means the symmetry relations are the same as for $\vec{d}_e$:

[9] If higher-order CP-violating moments exist in the bare nucleus beyond a dipole moment, they also couple into the Schiff moment and contribute to the measurable atomic EDM.

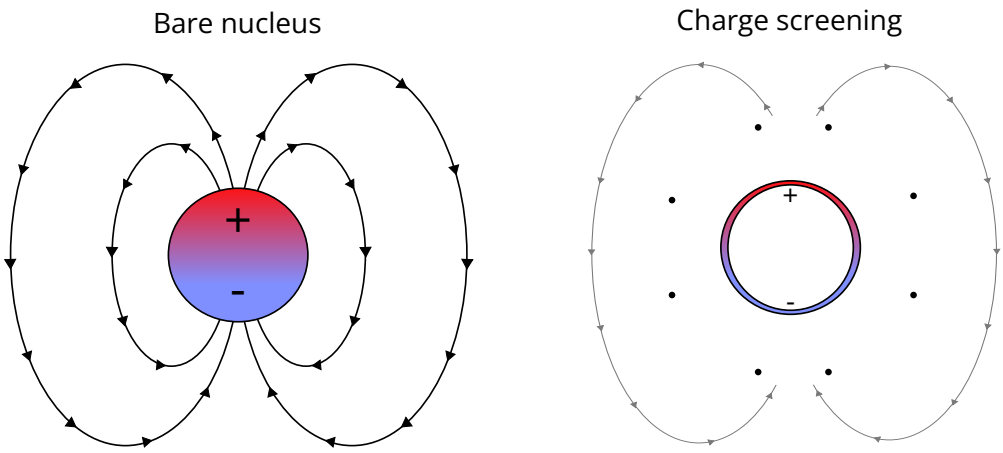


Figure 1.2: Attempt at interpreting the Schiff moment of an atomic system. Left: Intrinsic EDM of a nucleus with a CP-violating permanent dipole moment. The color represents a possible charge distribution, and the behaviors under T and P reflections are the same as in Figure 1.1. Right: Atomic EDM in this system with electrons (black dots), which rearrange to screen the majority of the bare nuclear charge. Now the dominant contribution to the measured, weaker EDM results from the Schiff moment, diagrammatically represented by the residual (unscreened) nuclear charge distribution. This Schiff moment is related to the underlying charge distribution of the bare nucleus; see [22] for a good discussion.

$$T: \begin{array}{l} \vec{S} \to \vec{S} \\ \vec{I} \to -\vec{I} \end{array}$$

$$P: \begin{array}{l} \vec{S} \to -\vec{S} \\ \vec{I} \to \vec{I}\,. \end{array}$$

Compared to electrons, which always possess spin $|\vec{S}| = 1/2$, nuclei may have spin 0. In these $\vec{I} = 0$ nuclei, the Schiff moment cannot exist as there is no axis onto which it can project.

$|\vec{S}|$ trends with atomic number Z, scaling as $|\vec{S}| \sim Z^3$, making high-Z radioactive atoms similarly attractive for these types of CP-violation measurements[10]. Other, more exotic properties of certain nuclei lead to further enhancement of the Schiff moment, which are described in Section 1.1 *Nuclear sensitivity factors*.

The current most precise atomic EDM measurement was performed in a vapor cell of mercury atoms, leveraging the high atomic densities achievable to yield $|d(^{199}\mathrm{Hg})| <$

[10] In reality, the scaling is more accurately described as $|\vec{S}| \propto Z \times A^{2/3}$ (see Eq. 1.3), but since the atomic mass goes as $A \sim Z$ this is a valid approximation.

3.1×10^{-29} e cm [23]. Calculations parameterize this measurement in terms of the underlying Schiff moment as[11]: $d(^{199}\text{Hg}) = -2.8 \times 10^{-17}(\frac{\mathcal{S}}{e\ \text{fm}^3})$ e cm [24]. This presents an important distinction between atomic EDM and electron EDM measurements: eEDM measurements all measure the same underlying quantity, while atomic EDMs/Schiff moments for every nucleus will be different as they arise from collective effects between all of the nucleons.

Nuclear magnetic quadrupole moments

The last electromagnetic moment of note, the nuclear magnetic quadrupole moment (MQM) also results from collective effects within the nucleus. Both being hadronic interactions, the MQM and Schiff moments originate from the same fundamental sources of CP-violation, just with these sources coupling to the low-energy particles in slightly different ways. Unlike the atomic EDM, the MQM is not screened [25]; its interpretation thus follows that of a classical magnetic quadrupole, analogous to the magnetic moment of a pair of anti-helmholtz coils. This moment may, as an example, be generated by a valence nucleon that possesses an EDM, whose nuclear orbit yields a nuclear MQM[12].

The MQM, with magnitude M, is a tensor moment, and thus is only supported by nuclei with $|\vec{I}| \geq 1$. The interaction of a MQM with the gradient of the magnetic field produced by an orbiting electron yields a measurable energy shift, which in a molecule is given by [26]:

$$\Delta E_M = W_M M \zeta |P| \, .$$

In the above, W_M is a calculated molecule-specific interaction strength between the MQM and the electron field, where $W_M \approx 1 \times 10^{33}$ Hz/e cm^2 for all molecules in consideration. ζ only depends on the values of nuclear and electron spin, and it generally follows that $\zeta \in (-1, 1)$ [26]. Last, $|P|$ is the same as above for the eEDM, parametrizing the degree of alignment of the molecule with the laboratory frame, where $|P| \in [0, 1]$. The molecules commonly considered for these types of CP-violation measurements, comprised of a heavy atom bonded to a lighter ligand, have an MQM energy shift which scales as $M \sim Z^2$ with the atomic number Z of the heavy

[11] The reason that the Schiff moment is interesting compared to just measuring the atomic EDM is that the underlying, fundamental physics connects more directly to $\mathcal{S}$ than it does to d_{atom}.

[12] Like with the other moments, a nuclear MQM may also be generated by CP-violating interactions between the nucleons, not just by inherent CP-violating moments of the nucleons.

nucleus [27]. Yet again, the case is made to use the heaviest nuclei possible, which are radioactive. Like with the Schiff moment, exotic properties of certain nuclei further enhance the MQM, as shown in the following sections.

No experiment has been conducted with the explicit goal of measuring a nuclear MQM, although there are several ones in development at the time of this writing. However, for atoms with nuclear spin $|\vec{I}| \geq 1$, measurements of the atomic EDM probe the underlying MQM. They are also sensitive to the Schiff moment[13], although in these systems the MQM contributes more strongly to the total atomic EDM as it is unscreened [25]. The most recent MQM-sensitive measurement was performed in 1989 in an eEDM search using atomic cesium, yielding $|d(^{133}\mathrm{Cs})| < 1.3 \times 10^{-23}\ e$ cm [28]. Cesium-133 has a large nuclear spin $I = 7/2$, supporting both a MQM and a Schiff moment—extracting the contribution to $|d(^{133}\mathrm{Cs})|$ from the MQM yields $M(^{133}\mathrm{Cs}) \approx 2 \times 10^{-33}\ e\ \mathrm{cm}^2$ [11].

BSM physics sensitivity factors

I have already mentioned how measurements of all of the listed moments scale with increasing Z, albeit to varying extents. If this were the whole story, the best possible molecule would contain an element somewhere from curium ($Z = 96$) to mendelevium ($Z = 101$), as these are the heaviest nuclides which could conceivably be acquired in sufficient quantities to perform a measurement with decent statistics. While this Z-scaling is broadly true, certain species have unique properties which dramatically amplify the energy shifts caused by CP-violating phenomena, making them especially sensitive probes of BSM physics. These specific properties manifest in either the nucleus of the high-Z atom or in the molecules formed from it, where the most sensitive BSM search candidates combine enhancements from both sectors.

Nuclear sensitivity factors

For the CP-violating moments originating from BSM physics in the hadronic sector—the Schiff moment and the MQM—certain high-Z isotopes possess anomalously large sensitivity enhancements originating from their nuclear structure. These nuclear enhancements fall into two partially related categories: deformations and energy structure.

[13] The many contributions to an atomic EDM for $|\vec{I}| \geq 1$ nuclei complicate the interpretation of the value extracted from a single measurement. As such, searches for BSM physics through nuclear CP-violation benefit greatly from multiple experiments in different systems.

While often thought of as perfect spheres, most nuclei deviate from this ideal description to varying degrees [29]. The extent and nature of this deviation is called the nuclear *deformation*. Mathematically, the position of the surface of the nucleus $R(\theta, \phi)$, and thus its shape, can be parameterized by the spherical harmonic functions $Y_{\lambda\mu}(\theta, \phi)$ as [30]:

$$R(\theta, \phi) = R_0 \left[1 + \sum_{\lambda\mu} \alpha_{\lambda\mu} Y_{\lambda\mu}(\theta, \phi) \right] , \tag{1.2}$$

where R_0 is the radius of a perfectly spherical nucleus. The summation leads to deviations from this spherical shape, with the coefficients $\alpha_{\lambda\mu}$ quantifying the magnitude of deviation described by a shape $Y_{\lambda\mu}(\theta, \phi)$.

The first order of deviation[14] occurs when $\lambda = 2$, corresponding to the $Y_{2\mu}(\theta, \phi)$ "quadrupole" term in the multipole expansion; the resulting shape change is called the *quadrupole deformation*, leading to a nucleus with a pancake or rugby ball shape. The coefficients for this deformation $\alpha_{2\mu} \propto \beta_2$, where $\beta_2 \in [0, 1]$ measures the extent of quadrupolar deviation from sphericity. Most nuclei possess some degree of quadrupole deformation [29], with the largest being around $|\beta_2| \approx 0.4$ [32].

A much rarer type of deformation occurs when $\alpha_{3\mu} \propto \beta_3 \neq 0$, leading to an *octupole deformation*. Only the $\mu = 0$ term, which results in a shape akin to a pear or avocado[15], is predicted to occur with any reasonable likelihood [33]. All of the calculated octupole-deformed nuclei with large Z occur near $Z = 88$ and neutron numbers $N \approx 134$ [34]. Precision experimental searches for this deformation have only been performed on the isotopes ^{220}Rn and ^{224}Ra [35], but they agree with older measurements on other isotopes (including ^{226}Ra) that heavily imply the existence of an octupole deformation in this region [36].

In spherical nuclei, only the valence nucleons contribute to the magnitude of the CP-violating electromagnetic moment, whether that be a MQM or Schiff moment. Nuclear deformations allow for the collective contribution from nucleons in inner shells too, greatly amplifying the desired quantity in some cases. The Schiff moment receives contributions from nuclear deformations as [38]:

$$S \propto \beta_2 \langle (\beta_3)^2 \rangle \, .$$

[14] The $\lambda = 1$ term would describe an offset in the nuclear center of mass, and is thus ignored [31].

[15] The $\mu = 1$ deformation results in a banana-shaped nucleus, while $\mu = 2, 3$ is peanut shaped.

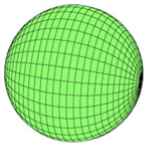
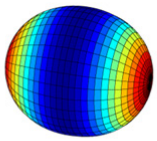
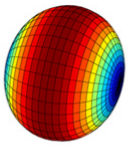
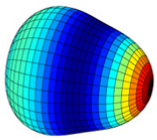
$\beta_\lambda = 0$	$\beta_2 > 0$	$\beta_2 < 0$	$\beta_3 \neq 0$
			

Figure 1.3: Illustration of the different types of nuclear deformations. $\beta_\lambda = 0$ for all λ yields a non-deformed, spherical nucleus. A quadrupole deformation $\beta_2 \neq 0$ leads to either prolate or oblate spheroids. $\beta_3 \neq 0$ results in an octupole-deformed pear- or avocado-shaped nucleus. Diagram modified from the one in [37].

The scaling for the MQM is a bit more complicated as the calculation involves summing over the individual interactions between all nucleons. In this calculation, the shape of the nucleon orbital impacts the degree to which it adds to the MQM; in distorted orbitals, such as from a β_2 or β_3 distortion, this contribution increases by a factor of a few. One can approximate the effects of quadrupole and octupole deformations as [27, 39]:

$$M \sim \beta_2$$
$$M \approx \langle (\beta_3)^2 \rangle \, .$$

The two terms are written separately as the nature of the contribution to the MQM originates from different effects: in a quadrupolar deformation it is of a "spin-hedgehog" nature [40], which does not have a clean scaling relation with β_2 but does increase in quadrupole-deformed nuclei; and for an octupole deformation it results from the current generated by an orbiting valence nucleon which may be directly related to β_3 [27].

The other nuclear enhancement is implied by, but not necessarily a requirement of, octupole deformations. In order to actually measure the energy shift associated with a CP-violating hadronic moment, the moment must have some defined orientation in the molecule frame. This is because the energy shift results from the interaction of electrons with the CP-violating moment, and changes sign depending on the relative orientation of the two. If the moment does not have a well-defined direction, the measurement would simply average over the energy shift of all orientations, which would be zero. Orienting this so-called "nuclear axis" onto the spin axis of the nucleus

requires mixing nuclear energy levels of opposite parity, which in perturbation theory has an inverse dependence on the energy splitting $\Delta E_\pm$ between the two levels. In systems with an octupole deformation, these states are generically closer than in most nuclei [27, 41], but this is not a rigorous requirement; certain nuclei may possess anomalously small splittings[16] due to coincidences in nuclear structure, not strictly caused by an octupole moment [42].

Incorporating all of the sensitivity enhancements to the Schiff moment and MQM, we arrive at [27, 38, 39]:

$$\mathcal{S} \propto \frac{\beta_2 \langle (\beta_3)^2 \rangle Z A^{2/3}}{\Delta E_\pm} \tag{1.3}$$

$$M \propto \frac{\langle (\beta_3)^2 \rangle}{\Delta E_\pm} \tag{1.4}$$

$$M \sim \beta_2 \tag{1.5}$$

$$M \sim Z^2 \,. \tag{1.6}$$

Molecular sensitivity factors

Equation 1.1, while formulated specifically for eEDM sensitivity, also applies to measurements of atomic EDMs. A generic EDM measurement, whether that be due to an eEDM, Schiff moment, or MQM, has a sensitivity:

$$\delta d \propto \frac{1}{|P| \tilde{V} \tau \sqrt{N}} \,, \tag{1.7}$$

Where I have introduced $\tilde{V}$ to represent vaguely the "strength of the interaction" between the CP-violating moment and some interacting field. This term depends on the nature of the molecule and can be calculated for different species. Minimizing the shot-noise uncertainty of a measurement thus requires maximizing the denominator of this term in Equation 1.7.

For measurements of any of these moments, the molecules need to be oriented in the lab frame[17], otherwise the BSM energy shift over all orientations averages to zero. Polarizing a polar molecule requires application of an external electric field, where the

[16] For example, the isotope ^{229}Pa is predicted to have nuclear parity doublets separated by just $\Delta E_\pm \ll 1$ keV [41, 42]

[17] An interesting proposal to overcome this requirement can be found in [43].

degree of this polarization is related to the energy splitting between opposite-parity molecular states[18]. This can be seen from perturbation theory: a state $|\psi\rangle$ is polarized in an $\mathcal{E}$-field if $\langle\psi|\vec{r}\cdot\vec{\mathcal{E}}|\psi\rangle \equiv \mathcal{E}\langle\psi|r|\psi\rangle \neq 0$, where we have defined $\vec{r}$ to point along the direction of the applied electric field for notational simplicity. However, field-free quantum states $|\psi\rangle$ have well-defined parities while r is parity-odd, meaning that $r|\psi\rangle$ has an opposite parity from $|\psi\rangle$, leading to $\mathcal{E}\langle\psi|r|\psi\rangle = 0$. Only by mixing multiple parity states into $|\psi\rangle$ will this expectation value be nonzero. According to first order perturbation theory, the (non-normalized) wavefunction will be:

$$|\psi'\rangle = |\psi\rangle + \mathcal{E}\sum_{i\neq j}\frac{\langle\psi_i|r|\psi_j\rangle}{\Delta E_{ij}}|\psi_i\rangle\ .$$

Maximal polarization $|P| \sim 1$ happens when $|\psi'\rangle$ is comprised of two opposite-parity states that are nearly fully mixed, requiring ΔE_{ij} between the states to be quite small[19]. This leads to the notion of *parity doublets*, or closely spaced molecular states of opposite parity. Certain diatomic molecules feature these parity doublets as a consequence of the interaction between orbital electronic motion and rotational motion of the molecule [13], but their existence follows from an electronic structure that makes them challenging to control optically. Generically, polyatomic molecules (three or more atoms) possess these parity doublets, where they occur in long-lived vibrational or even ground-state rotational levels [44].

Longer-lived states enable longer time evolutions τ during the measurement, providing another means by which to increase the experimental sensitivity. However, leveraging the full possible coherence time for a long-lived state requires slowing or trapping the molecules. Molecular laser cooling warrants a more detailed discussion (see Chapter 2.3 and Chapter 6), but here I will just mention that only very specific molecular structures are laser coolable, providing a tight constraint on the possible candidate molecules for BSM measurements.

Radium-containing molecules

In a fitting callback to the discovery of radioactivity, a class of candidate molecules that benefit from all of the above enhancement factors are those containing radium.

[18] This line of reasoning is the same as for the intrinsic CP-violating Schiff moment and MQM, whose projection onto the "nuclear axis" require the mixing of opposite-parity *nuclear* states. In that case, the operator that leads to this mixing is the CP-violating interaction of interest, rather than the $\mathcal{E}$-field in the current example.

[19] The mixing is also enhanced when the numerator is large, which occurs by applying a large polarizing $\mathcal{E}$ field. However, as has been pointed out, there are practical upper limits to this value.

Radium has $Z = 88$, larger than any other nuclide previously used in a BSM physics search except for thorium ($Z = 90$). On the nuclear side, radium is one of only two elements where its octupole moment has been characterized [35], and all isotopes near $A = 225$ have been shown to possess close nuclear levels of opposite parity [45]. Three isotopes exist with sensitivities to the three different CP-violating observables: ^{226}Ra ($I = 0$), ^{225}Ra ($I = 1/2$), and ^{223}Ra ($I = 3/2$). Even though all three are radioactive, none have such a short half-life as to render them impractical for these types of measurements.

While all of those nuclear enhancements are nice, none of them are inherently unique to radium; what really sets radium apart from the other high-Z, sensitive nuclei, are the molecules it forms. Radium is the heaviest alkaline earth element, bonding in similar ways as calcium, strontium, and barium do. As will be described more completely in Chapter 2, alkaline earth atoms bonded with fluorine (or fluorine-like) ligands produce molecules that are optically controllable and laser-coolable. Making the same types of molecules with radium allows us to leverage the advanced techniques already developed for laser control and cooling of the other alkaline earth elements, a feature which is incredibly rare in the space of all possible molecules.

Radium monofluoride (RaF) is the only radium-containing molecule to have been studied spectroscopically prior to this work [46–51]. These experiments sourced their radium atoms from the ISOLDE beamline at CERN, allowing them to study both the main isotopologue ^{226}RaF, as well as the shorter-lived ones ^{223}RaF, ^{224}RaF, ^{225}RaF, and ^{228}RaF, with an extremely efficient ion-based detection scheme. However, in the measurement process, their beams of RaF are accelerated to ≈ 40 keV, or roughly 1% the speed of light, a speed which presents a considerable challenge for engineering long coherence times τ for BSM physics experiments. In addition, their molecule flux is roughly 10^6 s^{-1}, many orders of magnitude below those achieved in buffer gas beam sources [52], described further in Chapter 4. While this existing work represents a truly remarkable feat, alternate methods of study that do not require collider facilities offer many advantages in terms of expanding the accessibility of these molecules to more groups around the world.

1.2 Interest from other fields

While our main motivation for studying radioactive molecules is for BSM physics searches, the techniques developed herein have the potential to benefit other types of measurements using these molecules. The following provides a brief overview of

other possible use cases for our techniques, partially inspired by [3].

Chemical studies often rely on macroscopic quantities of reagents to understand reaction behaviors and bulk materials characteristics. For radioactive species, macroscopic amounts often pose serious radiological safety hazards, adding an additional level of practical challenge to these experiments. Even more fundamentally, many radioisotopes simply cannot be gathered in sufficient quantities to perform bulk chemistry. Developing tools to work with these species at small quantities is thus instrumental to their study.

In lieu of classical, bulk chemical experiments, studies of individual molecules offers insight into the chemical properties of the constituents, as well as tests of theoretical quantum chemical models. Radioactive elements possess relativistic $5f$ orbitals which lead to nontrivial chemistry [53] that pushes the limits of what can be predicted computationally. Spectroscopic studies of these molecules contribute to understanding the nature of these bonds, where this understanding has the potential for significant, practical applications; as an example, further determination of the bonding nature of these radioactive elements allows for the development of separating agents, whether that be for better isolation of these trace materials for clean experiments or for mitigating environmental contamination [54].

The spectra of astronomical objects offer rich information about virtually every underlying physical and chemical process occurring within [55]. Stellar processes generate many different isotopes, where the isotopic composition may be measured and compared against theory on large spatio-temporal scales [56]. Radioisotopes with lifetimes shorter than the timescale of astronomical phenomena provide a window into the short-to-medium term dynamics of stellar evolution.

An example of an astrochemical radionuclide of interest is ^{26}Al, with a half life $t_{1/2} \approx 717,000$ years. Despite having a half-life significantly shorter than typical astronomical timelines, this isotope has been detected and is theorized to be produced in various stellar processes [57, 58]. Measurement of the isotopic ratio $^{26}\mathrm{Al}/^{27}\mathrm{Al}$ can detail the time-dependent behavior of the generation processes, which are currently debated. Molecules formed from ^{26}Al, including ^{26}AlF [59], have also been observed; these radiaoactive molecules offer advantages over bare atoms due to their many additional detection wavelengths, allowing for higher resolution mapping [3]. However, before these molecules may be detected via telescopes, their spectra need to be characterized to high precision here in a lab on Earth. The methods developed in our work on radium-containing molecules are directly applicable to spectroscopic investigations of

astronomically relevant radioactive molecules, including ^{26}Al(F, Cl, O, OH), which have all been observed in the interstellar medium for the stable isotope ^{27}Al.

Moving to the nuclear sector, properties of nuclei are often inferred spectroscopically due to the challenges of interacting directly with the nucleus. For example, one of the experiments performed on ^{225}RaF mentioned earlier measured the hyperfine structure of ^{225}Ra and demonstrated sensitivity to the distribution of magnetization within the nucleus [51], a property related to the nuclear form factors. Relating these two properties required advanced nuclear theory calculations [60], as the large nuclei feature complicated internal structure. Better measurements of this rich structure, requiring experiments on many heavy (radioactive) nuclei, thus lead to deeper understanding of the underlying interactions and provide model-dependent tests of nuclear theory.

These types of spectroscopic measurements often compare the results across a range of isotopes of the same element in order to extract the behavior originating from just the nucleus [61]. Even for low-Z elements, only a handful of isotopes will be stable, meaning that comparing across many isotopes will require developing tools to precisely study the ones that are radioactive.

Chapter

II

Atomic and molecular structure

Even with assumptions and approximations, no general description of every type of molecule exists. Rather, different species must be considered separately according to their bonding characteristics and constituent atoms. Thankfully, as far as molecules go, the types under investigation in this work lend themselves to a relatively straightforward "atom-like" description. This results from the nature of their bonds, where their singular valence electron dictates a large portion of their structure, as in the case of alkali atoms.

In fact, the electronic structure of our molecules of interest is remarkably similar to that of an alkali atom; as such, this section will begin with a brief overview of atomic structure, with a slight alkali-focused lilt, in order to showcase the parallels between the two and gently introduce molecular structure to those who are entirely unfamiliar. Like the other introductory sections, only the details necessary for understanding the work in this thesis will be included.

2.1 Atomic structure

The spinless, nonrelativistic electrostatic wavefunctions $|\psi\rangle$ and energy levels for an atom are derived by solving the Schrödinger equation:

$$\hat{H}_{\text{atom}}|\psi\rangle = E|\psi\rangle \ .$$

The electrostatic Hamiltonian $\hat{H}_{\text{atom}}$ for an atom with proton number Z and N_e electrons is given by:

$$\hat{H}_{\text{atom}} = \hat{T}_e + \hat{V}_{n,e} + \hat{V}_{e,e}$$
$$\hat{H}_{\text{atom}} = -\frac{\hbar^2}{2m_e}\sum_i^{N_e}\nabla_i^2 - \frac{Ze^2}{4\pi\epsilon_0}\sum_i^{N_e}\frac{1}{r_i} + \frac{e^2}{4\pi\epsilon_0}\sum_{i<j}^{N_e}\frac{1}{|r_i - r_j|},$$

where the first term $\hat{T}_e$ represents the electron kinetic energy, and the remaining terms describe the coulomb interactions between the electrons e with the nucleus $\hat{V}_{n,e}$ and with the other electrons $\hat{V}_{e,e}$.

Closed-form solutions to the above equation exist only for hydrogen, or hydrogen-like atoms, with $N_e = 1$. The electronic wavefunctions obtained via this solution are products of a radial term $R_{nl}(r)$ and an angular term $Y_{lm}(\theta, \phi)$, which introduce the quantum numbers n, l, m_l of the orbital. The final quantum number $m_s = \pm 1/2$ describes the orientation of the electron spin.

Even though these wavefunctions were obtained as solutions to a Hamiltonian with just one electron, they are used to describe the orbitals of more complicated atoms and molecules as they form a complete basis. In these multi-electron systems, the vast majority of the properties are dictated by the valence electrons; fully-filled inner shells, as they are spherically symmetric and closer to the nucleus than the valence orbitals, effectively only act to "screen" the charge of the nucleus by an amount equal to the total charge of the inner electrons. The effects of inner shell electrons can thus be treated as a perturbation on the wavefunctions and energies of the valence electrons.

Other interactions will also perturb the solutions obtained from $\hat{H}_{\text{atom}}$. These perturbations range in magnitude, with the largest leading to the so-called fine structure of the atom. Energy level shifts caused by relativistic momentum contribute at this order, as do interactions between the electron spin $\vec{s}$ and orbital angular momentum $\vec{l}$. The latter introduces the notion of angular momentum coupling, where a new coupled $\vec{j} = \vec{l} + \vec{s}$ forms which more accurately describes the total angular momentum of the system. In multivalent systems, a common coupling scheme is to first form total spin and orbital angular momentum vectors $\vec{S} = \sum \vec{s}$ and $\vec{L} = \sum \vec{l}$ which then couple together to form $\vec{J} = \vec{L} + \vec{S}$.

A concise way of representing the configuration of an atom is with a term symbol, defined as ${}^{2S+1}L_J$, where $S = \sum m_s$ and $L = \sum m_l$ quantify the total spin and orbital angular momentum of the valence electrons, respectively. J is the total angular

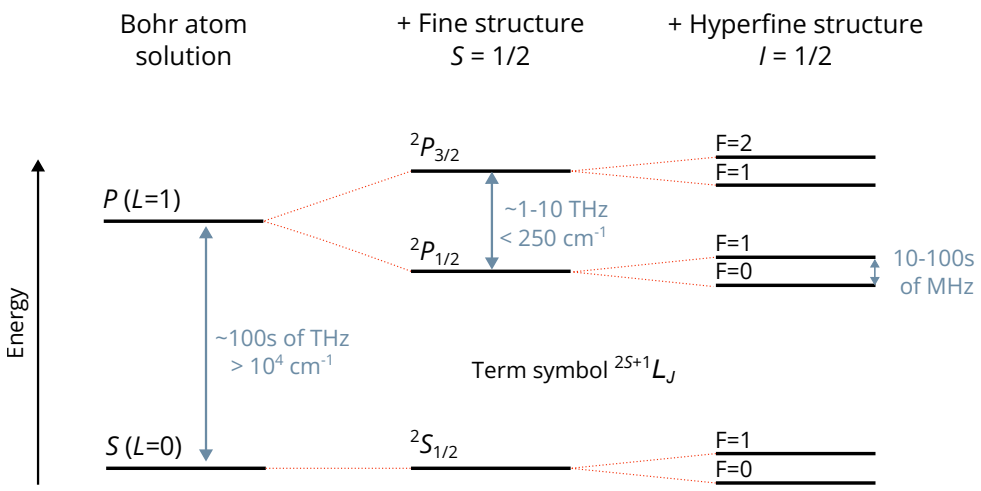


Figure 2.1: Diagrammatic representation of atomic energy levels under successive orders of perturbation, where the "Bohr atom solution" is the solution to the spinless, nonrelativistic electrostatic Hamiltonian. The atom represented is alkali-like, i.e. having one valence electron, as this is the structure closest to the molecules we study. For the hyperfine splitting, the nucleus was taken to have spin $I = 1/2$; this is absent for atoms with no nuclear spin. Magnitudes for the energy splittings at each order are shown, with values representative of the alkali atoms. $1\ \text{cm}^{-1} \approx \frac{29.98}{c}$ GHz.

momentum, taking a possible value $|L - S| \leq J \leq L + S$ depending on the relative orientations of $\vec{L}$ and $\vec{S}$. The value of J defines the *level* within the term. In the term symbol, L is represented in spectroscopic notation with a letter, where $L = 0, 1, 2, 3, 4, \ldots$ maps to $L = S, P, D, F, G, \ldots$(continuing alphabetically, skipping J, P, S). For example, the term symbol for ground state radium, which has two valence s-orbital electrons on top of fully filled radon-like inner core, is ${}^1S_0$, as it has total spin and orbital angular momentum 0. Ground state neptunium, with its four f, one d, and two s valence electrons, has a more exotic term symbol ${}^6L_{11/2}$, where L refers to an orbital angular momentum $L = \sum m_l = 8$, which just so happens to be represented by the spectroscopic letter L.

In atoms with nuclear spin $|\vec{I}| \geq 1/2$, interactions between this nuclear spin angular momentum and the electron spin and orbit contribute to the hyperfine structure, a (typically) weaker perturbation on top of the fine structure. The nuclear spin I couples with the spin-orbit coupled J to form a new total angular momentum $F = I + J$. This has the effect of splitting every atomic level into a number of hyperfine sublevels, where the total number of states is given by $2I + 1$ if $J > I$ or $2J + 1$ if $I > J$.

Electrons transition between energy levels in an atom via absorption or emission

of electromagnetic radiation. This radiation carries angular momentum of its own, meaning it couples to the atomic wavefunction in specific ways governed by *selection rules*, a set of conditions dictating which atomic states may be connected by some sort of interaction. For electric dipole transitions (the most common type of atomic transition), angular momentum algebra leads to the requirement that:

$$\Delta J = 0, \pm 1 \ (J = 0 \nleftrightarrow 0 \text{ transitions}) \tag{2.1}$$

$$\Delta M_J = 0, \pm 1 \ (\text{if } \Delta J = 0 \text{ then } M_J = 0 \nleftrightarrow 0)\,. \tag{2.2}$$

A final selection rule for electric dipole transitions comes from the nature of the electric dipole operator $\vec{r}$; as mentioned earlier in the context of EDMs, $\vec{r}$ is a parity-odd operator ($P\vec{r} = -\vec{r}$), meaning for transitions between an initial state ψ_i and final state ψ_f:

$$\langle \psi_f | \vec{r} | \psi_i \rangle = \int \psi_f^* \vec{r} \psi_i d^3 r \neq 0 \qquad \text{iff} \quad P\psi_i \neq P\psi_f \,,$$

meaning, verbally, the electric dipole operator will only connect two states of opposite parity. In atoms, this commonly looks like $\Delta L = 1$, e.g. $s - p$ transitions.

2.2 Molecular structure

The following section presents a brief and practical introduction to molecular structure; comprehensive descriptions of molecules require many pages of rigorous formalism, which the reader is encouraged to explore at their own pace in the many existing works which formed the basis of this chapter [62–67].

For a system comprised of multiple bound atoms, our spinless, nonrelativistic Coulomb Hamiltonian for N_e electrons and N_e nuclei looks like:

$$\begin{aligned}
\hat{H}_{\text{mol}} &= \hat{T}_e + \hat{T}_n + \hat{V}_{e,e} + \hat{V}_{n,n} + \hat{V}_{n,e} \\
\hat{H}_{\text{mol}} &= -\frac{\hbar^2}{2m_e} \sum_i^{N_e} \nabla_i^2 - \frac{\hbar^2}{2} \sum_i^{N_n} \frac{1}{M_n} \nabla_i^2 + \frac{e^2}{4\pi\epsilon_0} \sum_{i<j}^{N_e} \frac{1}{|r_i - r_j|} \\
&\quad + \frac{e^2}{4\pi\epsilon_0} \sum_{i<j}^{N_n} \frac{Z_i Z_j}{|R_i - R_j|} - \frac{e^2}{4\pi\epsilon_0} \sum_{i,j}^{N_e,N_n} \frac{Z_j}{|r_i - R_j|} \,,
\end{aligned}$$

where R and r refer to the nuclear and electronic coordinates, respectively.

Unsurprisingly, no analytic solution exists for the above Hamiltonian[1]; as with atoms, a number of assumptions and approximations are made in order to model molecular

[1] The single-electron hydrogen molecular ion, $H_2{}^+$, can in a sense be "solved" with assumptions and approximations, although the degree to which this solution can be described as analytic or exact is debatable [68]

structure. The most impactful of these approximations follows from the large mass mismatch between nuclei and electrons, where we assume that any electron dynamics occur on a much shorter timescale than the nuclear motion and thus the nuclei appear quasi-static in the frame of the electrons. This so-called Born-Oppenheimer approximation allows for the treatment of the electronic and nuclear wavefunctions independently,

$$\hat{H}_{\text{mol}} \approx \hat{H}_e \otimes \hat{H}_n \, .$$

The interpretation of this will be explored in the following sections.

A word of note: Generally, the mathematical treatment of molecules depends strongly on the composition of the molecule and its symmetry. As the work in this thesis only concerns linear diatomic or polyatomic molecules (except for briefly in Section 7.2), the following discussion will contain details specific to these species.

Electronic energy

The electronic part of the Hamiltonian describes the electron orbits and Coulombic energies, analogous to Section 2.1. A key difference between the electronic structure of molecules and atoms stems from their respective symmetries, where the spherical symmetry of atoms gives way to a reduced or sometimes nonexistent symmetry in the molecule.

The molecules we employ are comprised of a heavy, electropositive alkaline earth(-like) metal bonded to a light, electronegative fluorine(-like) ligand[2]. A simple, physicist's view of the way this molecule forms is by the donation of one of the electrons from the metal to the ligand, allowing the fluorine(-like) species to achieve a complete valence shell while the metal retains a singular electron. In a way, the resulting molecule looks somewhat like an alkali atom: one valence electron mostly orbiting a screened atomic core[3]. This interpretation, however simplistic, is supported by detailed ab initio quantum chemical studies [69, 70].

Given the reduced symmetry of the system, we cannot consider the spherical harmonics of the bare alkaline earth atom to be the electronic angular momentum eigenstates; instead, the strong electrostatic forces between the nuclei set a quantization axis within the molecule, onto which all of the electronic angular momenta are projected. Despite

[2] By alkaline earth(-like) I simply mean an atom with a $^1S_0$ ground state configuration, and by fluorine(-like) I mean any functional group which is one electron short of a full valence shell, like the halogens, but also multi-atom hydroxyl, thiol, monoamine (etc.) groups.

[3] In reality it is more accurately likened to an alkaline earth cation, as it has given up one of its electrons.

this difference, the way we treat these molecular states is quite similar to the atomic ones. Instead of a an electronic orbital angular momentum L, we consider its projection on the internuclear axis Λ, where Greek letters are generally used to indicate molecular values. If we define the internuclear axis to be $\hat{n}$, then Λ is obtained by summing the individual $\hat{n}$-projections of the electronic angular momentum $\hat{L}_{\hat{n}}$ eigenstates m_l. Because the $+\hat{n}$ and $-\hat{n}$ projections are degenerate (up to perturbations), this can be written $\Lambda = |M_l| = |\sum m_l|$, where $\hat{L}_{\hat{n}}|\psi\rangle = \hbar m_l|\psi\rangle$.

Spin-orbit coupling occurs in molecules just as in atoms, where the resulting combined angular momentum Ω is given by the eigenstates of $\hat{J}_{\hat{n}}$, the projection of $\hat{J}$ along the internuclear axis. This is formed by the addition $\vec{\Omega} = \vec{\Lambda} + \vec{\Sigma}$, where $\vec{\Sigma}$ is the vector corresponding to the projection of the sum of the electron spin S on the internuclear axis.

With all of this, we can construct the molecular term symbol:

$$^{2S+1}\Lambda_{\Omega}^{(+/-)}, \tag{2.3}$$

where all terms were defined above except for the $(+/-)$, which signifies whether a $\Lambda = 0$ wavefunction is symmetric/antisymmetric with respect to reflection about a plane containing the internuclear axis. Like with the atomic term symbol, Λ is represented by a letter, where $\Lambda = 0, 1, 2, 3, 4, \ldots \rightarrow \Sigma, \Pi, \Delta, \Phi, \Gamma, \ldots$[4]. In $\Lambda = 0$ states, it is necessarily true that $\Omega = S$, and as such sometimes Ω is omitted from the term symbol because it can be inferred from the $2S + 1$ superscript.

Molecular term symbols often include a leading character to signify (approximately[5]) the ordering of the state in energy relative to the ground state. In this prescription, the ground state is labeled X by convention, and successive electronic excitations are labeled with $A, B, C, D, \ldots$ with spin-orbit split states being labeled with the same letter. Lowercase versions of these letters indicate the state possesses a different spin

[4] If, like me, you are curious as to how the ordering of the Greek letters works, you will find that it is disappointingly less systematic than for atoms. The first terms $\Sigma, \Pi, \Delta, \Phi$ were chosen due to their phonetic resemblance to S, P, D, F. In the atomic case, after F the trend continues alphabetically, which for the Greek alphabet would mean that X (capital χ) follows Φ, but instead it seems that Γ was chosen to parallel the Latin alphabet trend of G. Then in an even more surprising twist H is the next letter used for both atoms and molecules, likely because it follows G in the Latin alphabet, and is the same symbol for capital η. However, alphabetically and etymologically it does not fit here, breaking any sort of pattern besides visual resemblance. Higher-order terms are exceedingly rare for molecules, and there does not appear to be any consensus as to which letters should come next.

[5] This is approximate because, in some cases, the states are designated with an ordinal letter before all states have been discovered; upon the observation of a new, intermediate energy level, the old orderings are not redone in order to avoid confusion. As such, this label more accurately represents the ordering of the state relative to the ground state at the time of its discovery.

symmetry from the ground state, which we rarely encounter in our single-valence molecules. As an example of these term symbols, the ground state of RaF ($\Lambda = 0$, $S = 1/2$) is $X\,^2\Sigma^+_{1/2}$, while the first excited states are $A\,^2\Pi_{1/2}$ and $A\,^2\Pi_{3/2}$. Replacement of $\Sigma \rightarrow S$ and $\Pi \rightarrow P$ demonstrates the correspondence with alkali atoms (see Figure 2.1). In polyatomic molecules, a tilde is often added to this label[6]; the ground state of RaOH is thus represented by $\tilde{X}\,^2\Sigma^+_{1/2}$.

Energy of nuclear motion

The multiple nuclei in molecules may move relative to some center of mass via a linear displacement (vibration) or angular displacement (rotation). While not immediately apparent, the kinetic energy term $\hat{T}_n$ in $\hat{H}_{\text{mol}}$ describes both of these motions, although a proof of this statement lies beyond the scope of this thesis [67].

As a further simplification, let us consider the vibrations and rotations separately. There are actually rigorous grounds to do so, owing to the ability to convert between rotational frames using Euler angles[7]. As such, this separation of vibrational and rotational structure is *not* an approximation, but rather a mathematical nicety.

With this separation, we now have:

$$\hat{H}_{\text{mol}} \approx \hat{H}_e \otimes \hat{H}_v \otimes \hat{H}_{\text{rot}}$$
$$E_{\text{tot}} \approx E_e + E_v + E_{\text{rot}}\,.$$

This treatment neglects smaller effects originating from the interactions of these terms with themselves or with other quantities such as nuclear or electron spin. As in the atomic case, these effects act as perturbations on the states obtained by solving the above. The electron spin interacts with its orbital angular momentum and the nuclear spin(s) in a manner qualitatively identical to the atomic case, and as such these perturbations will not be explicitly mentioned in the context of molecules, although they are still present.

Vibrations

In a naïve model, atoms in molecules may be treated as simple harmonic oscillators. Within each electronic state, this leads to a series of vibrational levels with energies

[6] This tilde helps prevent confusion in other types of polyatomic molecules, such as asymmetric top molecules, where the molecular term symbol switches back to using Latin alphabet letterings to designate the symmetry group rather than the angular momentum.

[7] This thesis will not prove this statement. For a lengthier discussion, see [62] and the citations therein.

$E_v \approx (v + 1/2)hc\omega_e$ for vibrational quanta v and vibrational constant ω_e. Even at $v = 0$, i.e. no quanta of vibration, this still contributes a zero-point energy (ZPE) to the molecular state. More sophisticated vibrational modeling schemes exist, including the addition of anharmonic terms $E_v = hc\left\{\omega_e(v + 1/2) - \omega_e x_e(v + 1/2)^2 + O(v^3)\right\}$, where $\omega_e x_e$ is treated as its own constant, rather than the product of two values. Higher-order harmonic terms $O(v^3)$ have dimishing coefficients and are ignored in most treatments.

Diatomic molecules only possess one vibrational mode, referring to the relative stretching and compression between the two atoms. In this thesis, this quanta will typically be represented parenthetically, often following the term symbol such as $X\,^2\Sigma^+(v = 0)$ to refer to the vibronic ground state of RaF. Linear polyatomic molecules with N atoms possess $3N-5$ vibrational degrees of freedom, with nonlinear molecules having $3N - 6$. For a linear triatomic molecule such as RaOH, this corresponds to three modes of vibration: Ra–O stretch (v_1), out-of-plane Ra–O–H bend (v_2), and O–H stretch (v_3). The out-of-plane bend contains two degenerate, perpendicular degrees of freedom, so the true bending eigenstates are linear combinations of these two. This combination contains angular momentum (see Figure 2.2), leading to an additional quantum number associated with the projection of this angular momentum l on the internuclear axis. This projection can take a value from $v_2, v_2 - 2, \ldots, 0$, meaning it is often omitted for $v_2 = 0$ and $v_2 = 1$ states as the only allowed projection is $l = v_2$. Importantly, the states $\pm l$ possess opposite parity and are *nearly* degenerate[8] ($\Delta E \sim 10$ MHz), providing the so-called parity doublet that allows for easy polarization in an applied electric field, satisfying the condition in 1.1 (*Molecular sensitivity factors*).

The representation of the vibrational quanta for a linear triatomic molecule in this work is $(v_1 v_2^l v_3)$; the vibronic ground state of RaOH is thus denoted $\tilde{X}\,^2\Sigma^+(000)$.

A note on notation: When considering transitions between two levels, parameters referring to the excited state are generally given a prime, e.g. $v' = 1$ denoting one quanta of vibration in the excited state. The ground (or lower) state parameters, rather than being unprimed, instead have two primes, e.g. $v'' = 1$. This thesis will follow this (rather cumbersome) notation.

---

[8] The degeneracy in this case is lifted via the interaction of the orbital angular momentum of the bending mode with the rotation of the molecule.

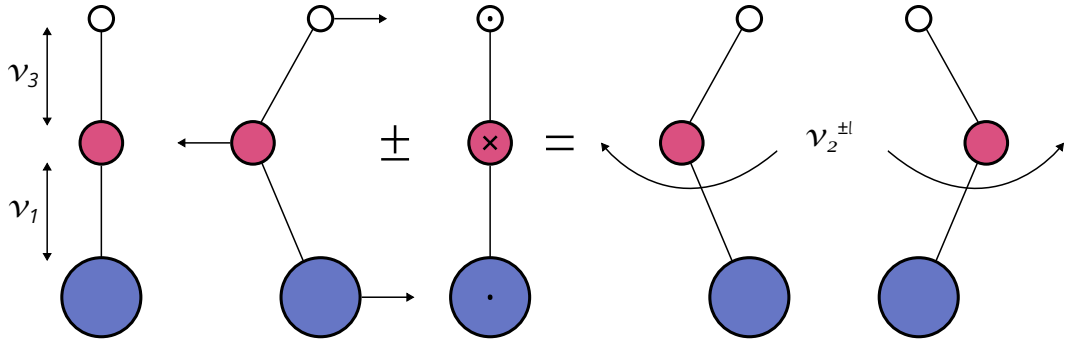


Figure 2.2: Vibrational modes of a linear triatomic molecule, such as RaOH. v_1 and v_3 correspond to stretching between the outer atoms relative to the inner one. Because the bending motion is doubly-degenerate, the true bending mode vibration is a linear combination of the two, which possess an angular momentum. The projection of this angular momentum is given by l, where the states corresponding to $\pm l$ are almost, but importantly not, degenerate. In molecules like RaOH, where the blue atom in the example above is quite heavy and the white is extremely light, the bending motion is more like a gyrating of the light atom about the internuclear axis.

The vibrational constant ω_e sets the spacing between successive vibrational levels, generally on the order of 100's of cm^{-1}, where $1\ \text{cm}^{-1} \approx \frac{29.98}{c}$ GHz.

Rotations

To first order, a rotating molecule may be treated as a rigid rotor, meaning we may neglect the effects of the molecule "flopping" or vibrating as it rotates. In three dimensions, a generic molecule possesses three moments of inertia I (not to be confused with nuclear spin) about which these rotations may occur. For diatomics and linear polyatomics, this reduces to two as rotations about the internuclear axis have no moment of inertia. The remaining two axes are degenerate owing to the cylindrical symmetry of the molecule, meaning the only allowable rotation is "end-over-end."

The Schrödinger equation for a quantum rigid rotor with moment of inertia I is given by:

$$\hat{H}_{\text{rot}}\psi_{\text{rot}} = \frac{\hbar^2}{2I}\hat{\vec{R}}^2\psi_{\text{rot}} \equiv B\hat{\vec{R}}^2\psi_{\text{rot}}\ ,$$

where we have introduced the rotational constant $B = \frac{\hbar^2}{2I}$, and $\hat{\vec{R}}$ is the typical angular momentum operator, referring to the angular momentum of the rotation now (R is used instead of J to avoid confusion with other angular momenta of the system). Eigenfunctions which satisfy this equation are just the spherical harmonics, with

rotational energies given by:

$$E_{\text{rot}} = BR(R+1)\ .$$

Thus, the spacing between successive rotational states is given by:

$$\Delta E_{\text{rot}} = E_{R+1} - E_R = 2B(R+1)\ ,$$

which grows with increasing R. B sets the scale of the spacing, which, for the molecules considered herein, is generally around $B \sim 0.1\ \text{cm}^{-1}$, on the order of GHz. Keep in mind that the above two expressions describe a rigid rotor with no other interactions; in molecules, we will see that the other angular momenta present require a more nuanced treatment.

Hund's cases and spin-rotation

The above discussion glanced over a subtle point, which is that R is often *not* a good quantum number of the system, thus $E_{\text{rot}} = BR(R+1)$ is undefined and molecular levels must be labeled by some quantity other than R. While the expression $\hat{H}_{\text{rot}}\psi_{\text{rot}} = B\hat{\vec{R}}^2\psi_{\text{rot}}$ remains valid, proper treatment involves expressing $\hat{\vec{R}}$ in terms of the well-defined operators of the system. Doing so introduces the notion of Hund's cases, referring to the various coupling schemes for molecules classified by the interaction strengths between their angular momenta. A full treatment of Hund's cases is not necessary in understanding this work; for more details, see: [62, 63].

Molecular states without electronic orbital angular momentum[9], such as the $^2\Sigma^+$ ground states of RaF and RaOH, are generally best described in Hund's case (b). The proper treatment involves first forming $\vec{N} = \vec{\Lambda} + \vec{R}$, which in our case of $\Lambda = 0$ means $\vec{N} = \vec{R}$. Despite this equivalence, rotational levels in Hund's case (b) are always labeled by N, as it is technically more precise terminology. This means that rotational energies scale as $E_{\text{rot}} = BN(N+1)$ and successive levels are separated by $\Delta E_{\text{rot}} = 2B(N+1)$. In polyatomic molecules, an additional term can contribute to $\vec{N}$ originating from the angular momentum arising from nuclear motion, denoted $\vec{G}_l$. This extra term is nonzero in bending vibrational modes, such as the $v_2 \neq 0$ levels in Fig. 2.2, leading to $\vec{N} = \vec{\Lambda} + \vec{R} + \vec{G}_l$.

In Hund's case (b), the electron spin is not pinned to any molecule quantization axis, leaving it free to interact with the rotation of the molecule. This can be thought

[9] Or in states with weak spin-orbit coupling.

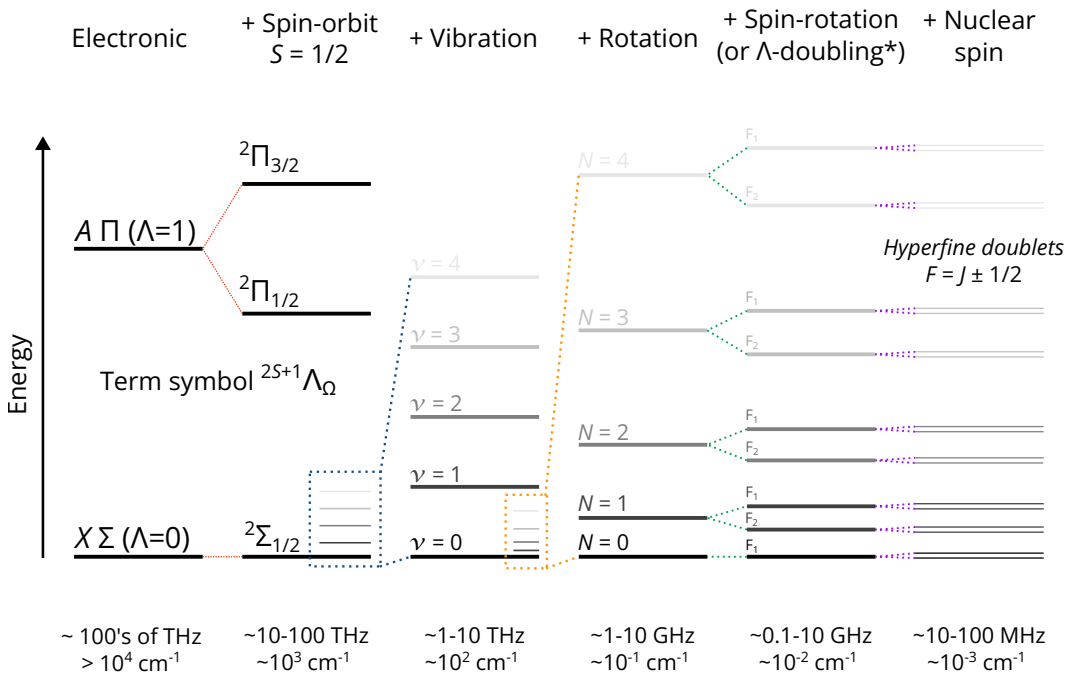


Figure 2.3: Attempt at visualizing the hierarchies of energies in a molecule, using a system like ^{226}RaF ($I_{\mathrm{Ra}} = 0, I_{\mathrm{F}} = 1/2$) as reference. After the spin-orbit splitting, the excited $A\,^2\Pi$ levels are no longer shown to provide room for expanding the ground state levels, although they each contain a ladder of successive states just as for the ground $X\,^2\Sigma^+_{1/2}$. The spin-rotation constant γ is assumed to be greater than 0, otherwise the F_1/F_2 ordering flips. Λ-doubling is not present in the above X state, as it has $\Lambda = 0$, but in other states with $\Lambda > 0$ (such as the excited $A^2\Pi$) it leads to a qualitatively similar level structure to the spin-rotation splitting shown. Hyperfine doublets are caused by interactions with the ^{19}F nuclear spin, further splitting the levels into two; if a spinful isotope of radium was chosen, such as ^{225}Ra ($I = 1/2$), even more hyperfine states would be present. Numbers at the bottom give characteristic values for the energy separation of the levels introduced at each level. Nothing is to scale.

of as the electron spin interacting with the magnetic field generated by the rotating charges of the nuclei and electrons. This interaction forms a total angular momentum $\vec{J} = \vec{N} + \vec{S}$, which introduces a corresponding interaction term in the Hamiltonian:

$$\hat{H}_{\mathrm{sr}} = \gamma \vec{N} \cdot \vec{S}\,.$$

The spin-rotation constant γ parameterizes the strength of this interaction. Energies associated with spin-rotation states are thus given by:

$$E_{\mathrm{sr}} = \frac{\gamma}{2}\left(J(J+1) - N(N+1) - S(S+1)\right)\,.$$

In systems with a single valence electron, like most of the molecules we study, $S = 1/2$ and thus $J = N \pm 1/2$. Except for the $N = 0$ state, which only has $J = N + 1/2 = 1/2$

as J cannot be negative, it follows from this that every rotational level N splits into two spin-rotation components separated by:

$$\Delta E_{\mathrm{sr}} = \gamma(N + 1/2) \, .$$

An additional notation distinguishes these two split levels: $F_1(J)$ refers to the $J = N + 1/2$ component, while $F_2(J)$ refers to $J = N - 1/2$. Note that $F_{1,2}$ is simply a shorthand to indicate the spin-rotation sublevel, and *not* to be confused with the total angular momentum including nuclear spin, which is typically also written F.

In the molecules we study (as determined during the work in this thesis), γ for the ground state is generally ~ 100 MHz, while for excited $C\,^2\Sigma^+$ states it can be significantly larger, around ~ -10 GHz (where the negative sign is not a typo). The good quantum numbers for this coupling case are Λ, N, S, J.

In states with both orbital angular momentum and spin, such as the first excited $A/\tilde{A}$ states of RaF/RaOH ($^2\Pi_{1/2}$, $\Lambda = 1$), Hund's case (a) is most frequently used. Here, rather than forming $\vec{N}$, instead the spin and angular momenta first couple to form $\vec{\Omega} = \vec{\Lambda} + \vec{\Sigma}$ (as described in Section 2.2), which then couple to $\vec{R}$ to form $\vec{J} = \vec{\Omega} + \vec{R}$. In Hund's case (a), rotational levels have (relative[10]) energies given by $E_{\mathrm{rot}} = BJ(J + 1)$, and with successive levels separated by $\Delta E_{\mathrm{rot}} = 2B(J + 1)$. Levels in this coupling scheme are labeled by the good quantum numbers $\Lambda, S, \Sigma, J, \Omega$.

Because the electron spin strongly couples to the orbital angular momentum, it only weakly interacts with the molecular rotation, leading to a negligible spin-rotation splitting generally on the order of MHz or smaller. Instead, case (a) molecules experience Λ-doubling; without molecular rotation the states $\pm\Lambda$ are degenerate, but the Coriolis-type interaction of the orbital angular momentum with rotation results in mixing between the $\pm\Lambda$ states, leading to a small splitting on the order of $\sim$ kHz – MHz. The split states also possess opposite parities, denoted[11] e/f, meaning Λ-doubling leads to parity doublets that may be used for polarizing the molecule.

Transitions between molecular states separated by ΔJ are often described with a shorthand spectroscopic notation given by:

$$^{\Delta N}\Delta J_{F_i' F_i''}(J'') \, ,$$

[10] The "true" rotational energy includes a factor of $-B\Omega^2$, although this is often ignored as it applies to every level equally.

[11] e/f do not refer to specific positive or negative parities, but rather depend on J as $P_e = (-1)^{J-S}$, $P_f = (-1)^{J-S+1}$

where as before, primed indices refer to the excited state and double prime to the ground state. F_i and ΔN are only used for case Hund's case (b) states, where the former indicates the spin-rotation components F_1 or F_2 of the ground and/or excited states (not the total angular momentum including nuclear spin F). Similarly to the term symbols, ΔN and ΔJ are written with a letter by convention[12], where $\Delta N, \Delta J = -1, 0, 1 \rightarrow P, Q, R$. Examples of these for lines we measured are shown in Table 5.3 in Chapter 5.4.

2.3 Selection rules and laser cooling

As with atoms, the angular momenta of molecules lead to selection rules governing the allowable electromagnetic transitions between levels. The nature of these selection rules depend on the Hund's case, or angular momentum coupling scheme, that describes the level.

In both case (a) and case (b), we have [71]:

$$\begin{aligned}
\Delta J &= 0, \pm 1 \quad (J = 0 \nleftrightarrow 0) \\
\Delta M &= 0, \pm 1 \quad (M = 0 \nleftrightarrow 0 \text{ if } \Delta J = 0) \\
\Delta \Lambda &= 0, \pm 1 \\
\Delta S &= 0 \qquad \text{(weakly broken in case (b))} \\
P\psi_i &= -P\psi_f \quad \text{(parity requirement for E1 transitions)} .
\end{aligned}$$

Specifically for transitions between two case (a) states, we additionally have:

$$\Delta \Omega = 0, \pm 1 \quad (\Omega = 0 \nleftrightarrow 0) ,$$

and for case (b):

$$\Delta N = 0, \pm 1 \quad (N = 0 \nleftrightarrow 0) .$$

A more complicated situation arises when transitioning between two Hund's coupling cases, as is the case for transitions such as ${}^2\Pi_{1/2} \leftarrow {}^2\Sigma^+$ like the first electronic excitation in RaF/RaOH[13]. In these transitions, the first set of selection rules still determines the allowable transitions. When attempting to calculate transition amplitudes, however, it becomes necessary to represent one of the states in the other basis, e.g. by writing a case (b) state in terms of a linear combination of case (a) states.

[12] ΔJ components greater than ± 1 are labeled in alphabetical order, with $\Delta J = \pm 2$ corresponding to O and S, respectively.

[13] Note that it is spectroscopic convention to list the excited state first, with an arrow denoting the direction of the transition as in absorption or emission, or just a dash if this direction is unimportant to the discussion.

With these selection rules dictating the possible destinations of a transition, it becomes possible to link together initial and final quantum states such that transitions between them keep the molecule restricted to a small subset of the total levels. This forms the basis of photon cycling, and further leads to laser cooling; as photons carry momentum, repeated absorption and emission can reduce the total entropy of the system, cooling the molecules either translationally (slowing) or internally (cooling).

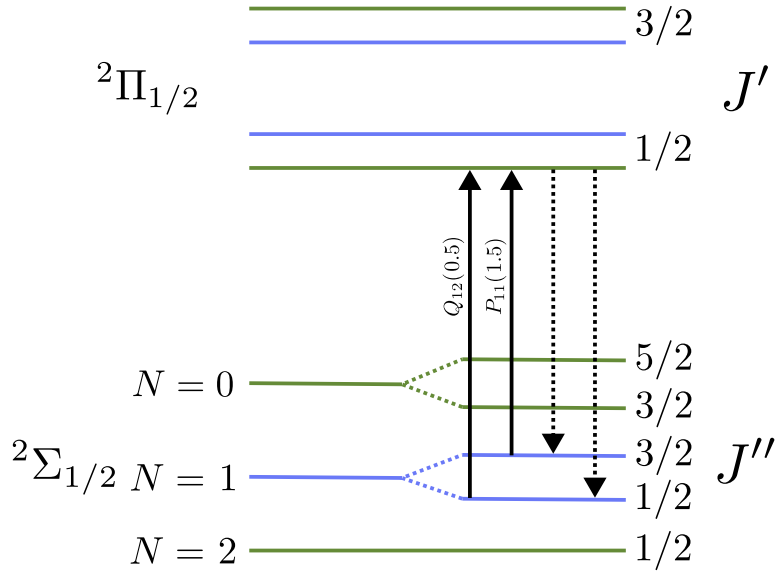


Figure 2.4: Level diagram depicting photon cycling closure on a $^2\Pi_{1/2} - {}^2\Sigma^+_{1/2}$ transition, such as the $A - X$ band of RaF/RaOH. If two lasers (solid lines) drive the $P_{11}(J'' = 1.5)$ and $Q_{12}(J'' = 0.5)$ transitions from both $N = 1$ spin-rotation levels to the parity-allowed Λ-doubling component of the excited $J' = 1/2$ state, then the only allowable decays (dotted lines) are to the same initial states, allowing for repeated excitation. Colors indicate parity. Adapted from [72], which has many similar diagrams for other types of transitions.

In general, the narrow linewidths offered by modern lasers allow us to precisely control which two states we couple via an electronic excitation. However, because spontaneous emission of this excited state is an incoherent process, we must rely on the selection rules governing the decay process to put the molecule back in a desired final state. As this process requires the cycling of many thousands of photons, specific states need to be chosen such that the likelihood of decaying to some unwanted destination outside of the cycling loop becomes vanishingly small. The rotational selection rules permit these so-called "closed" cycling transitions, which have been worked out for the relevant Hund's cases and collected nicely in [72].

Importantly, vibrational structure has not yet come up in this discussion. This high-

lights an extremely consequential point: vibrational stretches do not possess selection rules[14]. Instead, any electronic excitation or decay may change the vibrational level by any amount. The probability of moving between vibrational levels scales closely with the degree of vibrational wavefunction overlap between the two states, a point elaborated on further in Chapter 6. While we have control over the vibrational change in the excitation by tuning the laser frequency, the spontaneous emission occurs purely probabilistically according to the likelihood of these vibration-state-changing decays. In molecular laser cooling, this fact sets the ultimate limit on how many photons a molecule may cycle. The only proven workaround is to select molecules which, by the nature of their bonds, are anomalously unlikely to change their vibrational quanta in a decay—this is one of the main reasons for us choosing to study molecules with a structure like RaF and RaOH.

[14]While a bending vibration does carry angular momentum, and thus is subject to selection rules, this detail does not come up in this work. See [62] for a discussion. Even so, the other vibrational quanta referring to the stretches may change, and so the listed problems persist.

Chapter

III

Radioactivity

The study of stable atoms and molecules has a long and extensive history, one that we will not endeavor to summarize here. By contrast, aside from a few notable counterexamples—such as those involved in nuclear medicine or energy—radioactive atoms and molecules have remained severely underutilized compared to their stable counterparts.

Restricting our focus to experimental AMO, we see that this trend persists: stable atoms are understood well enough to be employed in advanced quantum simulators [73], and these techniques are rapidly being ported over to complex polyatomic systems [74]. Radioactive molecules, on the other hand, are still in their infancy. Aside from RaF, comprehensive molecular spectroscopy exists only for the species containing isotopes with such long half-lives that they are experimentally "not radioactive," such as uranium and thorium[1]. Even just considering atoms, the most fundamental units of structure in our universe, we see that many short-lived isotopes lack basic spectroscopy.

It seems, however, that the tides are changing. As mentioned in the introduction, radioisotopes provide a pathway to higher sensitivity BSM searches, among many

[1]While not definitionally true, this classification of molecules as "radioactive" or not by length of their half-lives follows the accepted usage in the radioactive molecule community [3]. Of course, in this distinction, I am only comparing against the dominant isotopes of uranium and thorium, such as ^{235,238}U and ^{232}Th. ^{229}Th, with its half-life of ~7916 years, suffers from many of the same challenges described in this chapter.

other advantages [3]. Because radioactivity in AMO is still a relatively unexplored area, and since few groups within this community have performed open-source radioisotope handling, this chapter is intended to serve as a practical introduction to radioactivity, specifically as it pertains to AMO experiments. This is not intended to be an extensive treatment of radioactivity—much of this information is taken from personal experience working with these materials as well as the Caltech Radiation Safety Training and Reference Manual [75].

3.1 Basics and terminology

A radioactive atom, or radionuclide[2], is an atom whose nucleus is energetically unstable and will decay by some method into a different "daughter" nucleus or nuclear isomer, radiating energy in the process. The main three modes of radioactive decay are characterized by emission of a certain type of particle: alpha decay results in the emission of a ^{4}He nucleus (α particle), beta decay in the emission of an electron or positron (β^- or β^+ particle, or commonly written just β), and gamma decay in the emission of a photon (γ particle). Other types of decays exist, but they are either so rare that their occurrence does not warrant any additional considerations—as with spontaneous fission[3] or cluster decay—or, in the case of neutron emission, so different in behavior as to possess entirely distinct safety hazards that are outside the scope of this discussion. A radionuclide might have multiple possible decay modes, each with their own probability of occurrence.

The different types of decays are distinguished by their kinetic energies and penetrating powers. Alpha particles are emitted with the highest average energies, between 4 – 10 MeV. However, their large mass means they start with a relatively low velocity, while their 2+ charge allows them to easily transfer energy to their environment via electromagnetic interactions. As such, even the highest energy alpha particles can only travel around 10 cm in air before being stopped; any practical thickness of solid material will fully block alpha particles, including a sheet of paper or the protective outer layer of the epidermis. Beta particles are generally emitted with energies of 0 – 2 MeV, with only a handful[4] of isotopes exceeding energies of 4 MeV. Despite this

[2] The term radioisotope is often used interchangeably.

[3] A notable counterexample is ^{252}Cf ($t_{1/2} \sim 2.6$ y) with a spontaneous fission branching of ~3% [76]. This isotope has a long enough half-life to conceivably be used in a lab-scale AMO experiment. It is also routinely produced for industry use, and therefore can be acquired in significant quantities. Experiments working with this isotope would need to account for the neutrons emitted in the spontaneous fission process.

[4] The isotope ^{16}N is an outlier, capable of emitting an electron at ~10 MeV [77], around twice as much energy as the next most energetic beta emitter.

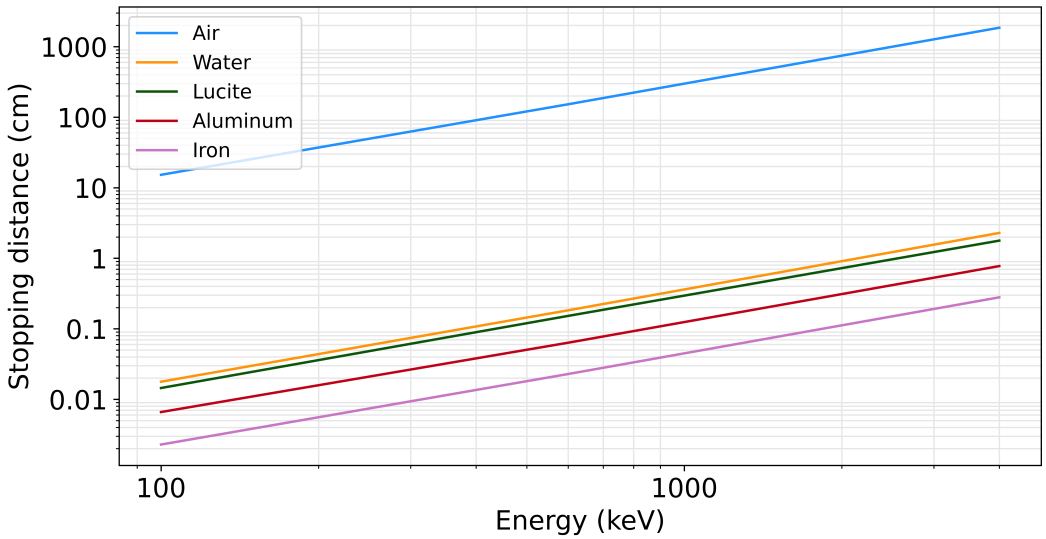


Figure 3.1: Maximum ranges of beta particles in selected materials. Plot adapted from material in [75].

wide range, the vast majority of beta particles are $\lesssim$ 500 keV. A plot of beta energy versus stopping distance for a small selection of materials is shown in Fig. 3.1. Gamma decays carry energy between 0.05 – 5 MeV and are attenuated by dense material such as lead, requiring many cm of material to achieve any appreciable reduction for high energy emissions. For example, to reduce the gamma radiation intensity by 90% for the Ra-226 chain, around 5.5 cm of lead shielding is needed [78].

A radionuclide is described by its half-life $t_{1/2}$, the time it takes for half of a sample of this material to decay. The half-life is unique for every radioisotope and does not depend on the material quantity. *Activity* is defined as the number of disintegrations per second and is a measure of "how radioactive" a sample is. One decay per second is one becquerel (Bq), the SI unit for radioactivity. Historically, activity was measured in curies (Ci), where 1 Ci = 3.7×10^{10} Bq = 37 GBq. Curies are a convenient unit for us to work with, as the curie was originally defined as the activity of one gram of Ra-226; as such, a sample of Ra-226 has an activity in curies equal to its mass in grams, allowing the two quantities to be used interchangably[5]. It is worth stressing that this is *only* true for Ra-226, and in general the instantaneous activity for a sample of N atoms is given by:

[5]This is not exactly true—updated measurements put the specific activity of Ra-226 closer to 36.5 GBq or 986 mCi per gram [79]. However, absolute measurements of sample activity or radionuclide amount are challenging, so treating 1 Ci $\approx$ 1 g for Ra-226 is fine at our level of precision.

$$A = \frac{\ln(2)N}{t_{1/2}} \,. \tag{3.1}$$

Activity does not consider the type nor energy of the decays—this information is contained in the *dose*, the measure of radiation energy absorbed in a material. More detailed discussion of dosage, including biological dosage, is provided in Sec. 3.2.

The decay product of a heavy radionuclide is often also radioactive. This introduces the concept of a decay chain, the series of decays of a specific radioisotope as it progresses towards stability. Consequently, a sample of pure material will build up population of its daughter nuclides over time, whose hazards also need to be considered in the experimental design. As an example, the first daughter of radium-226 is radon-222, which is a radioactive gas that has the potential to diffuse into the surrounding area if not contained. The full decay chain for ^{226}Ra is shown in Figure 3.2. This also means that a sample of material can get *more* radioactive over certain timescales, as the accumulation of daughter nuclides will add to the total activity (see Figure 3.3 for an example of this in Ra-226).

Because a radioactive decay process transfers a radionuclide between two states of discrete energy, the decay products also carry some discrete energy. For alpha and gamma emissions, this means that the energies for any decay are deterministic. In general, alpha decays from a specific nuclide to another always carry the same energy, and gammas have a few possible values depending on the nuclear state in which the daughter ends up. A radioisotope will thus have a characteristic alpha and gamma emission spectrum, where measurement of this spectrum for some sample allows for determination of its radiological makeup. This does not apply to beta decay, as emission of an electron (or positron) is accompanied by simultaneous emission of an electron antineutrino (or neutrino) in order to preserve lepton number. The two decay particles thus split the total energy, where each individual product can have any value up to the total.

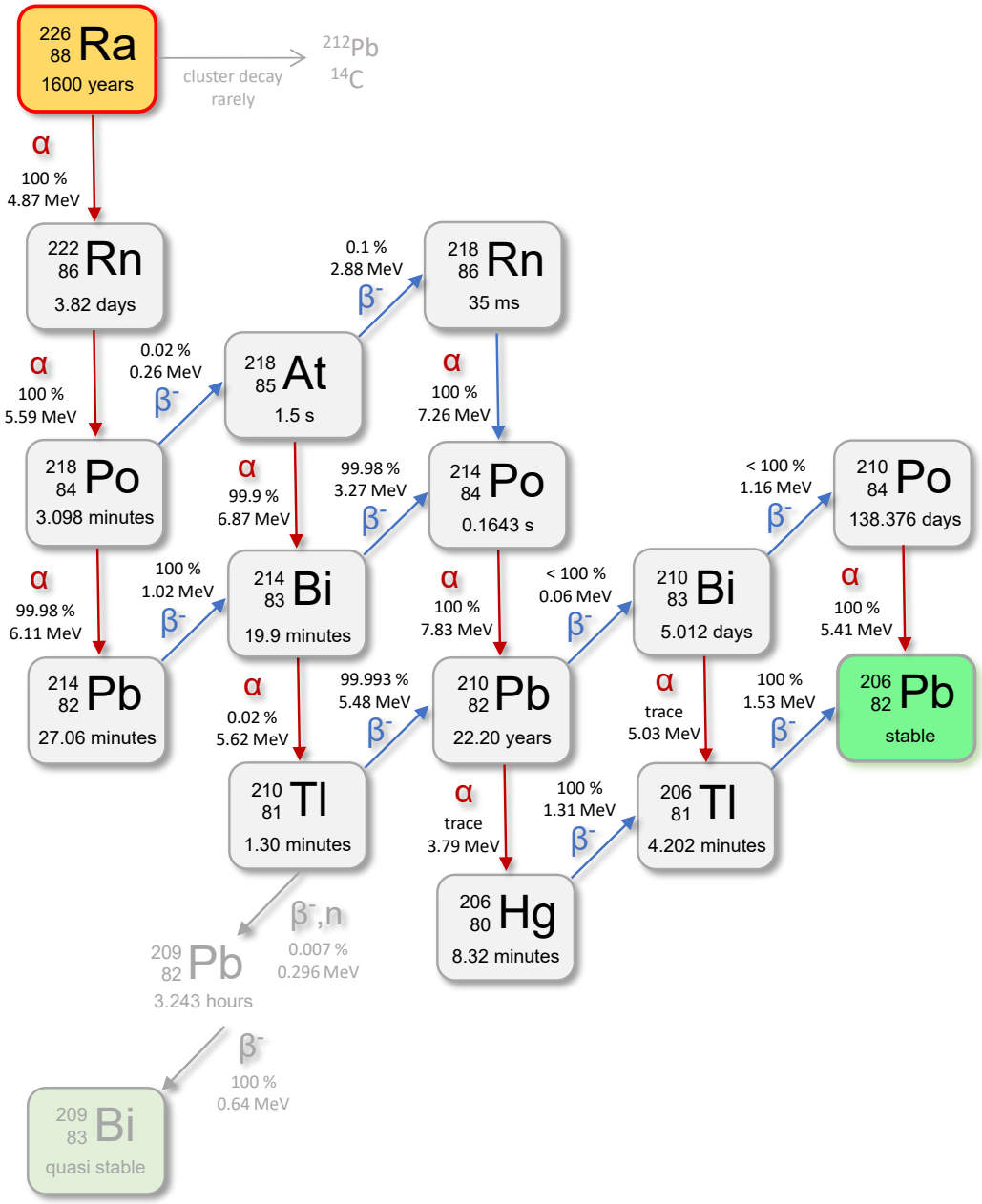


Figure 3.2: Decay chain for ^{226}Ra. Gamma emissions are not shown, but occur most strongly in the beta decays of Pb-214 and Bi-214 and weakly along during the alpha decay of Ra-226 to Rn-222. Decays with vanishingly rare probabilities are not shown. Plot taken from [80].

Quantity	Units	Unit relation	Usage	Typical values
Activity	Ci Bq	1 Ci = 3.7×10^{10} Bq	Describing how "hot" a sample is; how many decays per second	1 μg of Ra-226 has activity 1 μCi; 1 μg of Ra-225 is 40 mCi
Absorbed dose	rad Gy	1 Gy = 100 rad	Total absorbed energy; mostly used for large, instantaneous doses	Dental x-ray: ~0.07 rad; LD50 for humans: ~450 rad (whole body exposure)
Equivalent dose	rem Sv	1 Sv = 100 rem	Rough quantification of health risk from chronic, long-term exposure	NRC yearly exposure limit is 5 rem; average yearly background in the US is ~310 mrem

Table 3.1: Summary of some units and quantities used for describing radioactivity. Units listed lower are the SI-recommended variants.

3.2 Dosage

After a decay product is emitted, it is either neutralized by the air or absorbed into a material. While travel through the air will lead to ionized air particles, which could conceivably be a complication in certain experiments, the vast majority of attention spent on the hazards of radiation concern its uptake in materials, most notably the human body. The language surrounding dosage is often obtuse, so this section is an attempt to demystify it.

An unfortunate reality: just like how activity may be represented by two possible units (Bq or Ci), all concepts pertaining to dosage have a "historical" representation and a corresponding SI unit. Based on experience, the historical units are still more common in documentation here in the United States, including the Nuclear Regulatory Commision's most up-to-date Code of Federal Regulations (10 CFR). As such, we will primarily write in terms of these units. Table 3.1 summarizes all (relevant) quantities.

The unit of *absorbed radiation dose* is the rad, with a corresponding SI unit called the gray (Gy). One rad is equivalent to an absorption of 0.01 joules of radiation energy per kilogram of matter, or $\sim 6.24 \times 10^7$ MeV absorbed in one gram of matter (recall that individual radioactive decays tend to carry energies $\sim$ 1 MeV). Typically, absorbed radiation dose is quoted when describing large, instantaneous radiation events, such as during medical scans or nuclear disasters. Examples of typical doses in rads are given in table 3.1.

Absorbed radiation dose only considers the amount of energy absorbed; in biological

systems, the form of this energy also impacts its ability to cause adverse health effects. Multiplying absorbed dose in rads (grays) by a weighting factor specific to the type of radiation gives the *equivalent dose* in rem[6] (sieverts). Both beta and gamma radiation have a weight of 1, while alpha (and larger) particles have a weight of 20. The weighting factor for neutrons depends on their incident energy, but always falls somewhere within this range [81]. Equivalent dose is an attempt to correlate the amount of absorbed radiation with long-term health effects and is used to quantify chronic, cumulative radiation exposure[7]. A commonly reported statistic is that radiation-induced cancer incidence increases at a rate of 0.055% per rem [81], although this value is highly model-dependent and should be treated as a rough guideline. Occupational exposure limits are quoted in rem, which for radiation workers in the US are generally no more than 5 rem/year.

Because radioactive emission is isotropic, the dose rate drops with the square of the distance from the emitting source. This leads to one of the main methods of radiation mitigation, referred to as *distance shielding*. Maintaining physical distance from the source is one of the most straightforward ways to reduce one's radiation exposure without requiring careful experimental engineering. The other simple form of shielding is *time shielding*, whereby a material is handled for as little time as necessary. Because dose is a cumulative metric, an optimization of handling time and distance should be found so as to reduce the total absorbed biological dose. This introduces the concept of ALARA, or "As Low As Reasonably Achievable," describing the principle of minimizing the radiation dose as much as possible by combining all available methods of shielding.

Reducing exposure to all types of radiation requires careful experimental design tailored to the type and source. This design should always be discussed and coordinated with the relevant administrative departments. As a reference, the safety protocol that we developed for our handling of radium-226 is provided in Appendix A. I will stress that I am not trained to give any instruction in the realm of medical physics, and that any notes or pieces of wisdom contained in this thesis are the result of my own learned experiences which do not apply to every situation.

This has been an extremely brief discussion of dosage, intended to include only

[6] rem is an acronym of "roentgen equivalent man," which is misleading as its modern definition bears no connection to the roentgen, the unit for radiation exposure in air. The word rem, rather than the full term it stands for, is used when referring to the quantity.

[7] There is another way of describing equivalent dose that includes an additional weighting factor for the type of tissue absorbing the radiation. Given that, in this work, the radiation was not highly targeted to any specific part of my body besides the hands, this additional treatment was not necessary.

the information relevant to this type of work. Further details describing our safety protocols and radiation mitigation are mentioned later in section 5.1, and a description of radiation monitoring is provided in Appendix A.

3.3 Radium-226

As most of the work contained in this thesis concerns the study of radium and radium-containing molecules, we will present some information specific to these species.

Radium is an alkaline earth metal with no stable isotopes. The overwhelming majority of radium present on Earth exists as the isotope ^{226}Ra, which originates in the decay series of uranium-238 via the process:

$$^{238}\mathrm{U} \overset{\alpha}{\rightsquigarrow} {}^{234}\mathrm{Th} \overset{\beta^-}{\rightsquigarrow} {}^{234m}\mathrm{Pa} \overset{\beta^-}{\rightsquigarrow} {}^{234}\mathrm{U} \overset{\alpha}{\rightsquigarrow} {}^{230}\mathrm{Th} \overset{\alpha}{\rightsquigarrow} {}^{226}\mathrm{Ra}\ .$$

From this point, the radium decay series proceeds as in Figure 3.2.

Other isotopes exist as byproducts of rarer decay chains, such as ^{225}Ra and ^{223}Ra (from ^{233}U and ^{235}U, respectively), or are produced in nuclear reactors. Radium-226 has the longest half-life of all of the radium isotopes by a wide margin, with $t_{1/2} \approx 1600$ y. This half-life presents a major experimental annoyance; it is short enough such that even small masses of radium-226 are considerably radioactive, but long enough such that any spills or contamination cannot be "cleaned up" by waiting out a number of half-lives until they decay away. To elaborate on this latter point: say an experiment works with either radium-226 or radium-225 ($t_{1/2} \approx 15$ d) in some apparatus. On human timescales, the amount of radium-226 will remain essentially unchanged and the apparatus will only become more radioactive (Figure 3.3). For the case of radium-225, after ~ 100 days, only around 1% of the starting material remains, and by one year no radiation will be detectable (Figure 3.4), meaning the experiment has essentially decontaminated itself. The design and disposal considerations for the two situations will be different as a result.

In addition to its half-life that is simultaneously too long and too short, another challenge unique to radium-226 is its first decay product: radon-222. Radon is a noble gas, whose lack of reactivity makes chemical sequestration difficult. ^{222}Rn, specifically, is the radon isotope with the longest half-life ($t_{1/2} \approx 3.8$ d), sufficiently long to migrate appreciable distances. Measures must be taken to avoid nonlocal contamination or ingestion by inhalation.

The worldwide distribution of uranium-238 in soil and seawater produces varying amounts of radon near ground level. Because it is infeasible to eliminate it entirely,

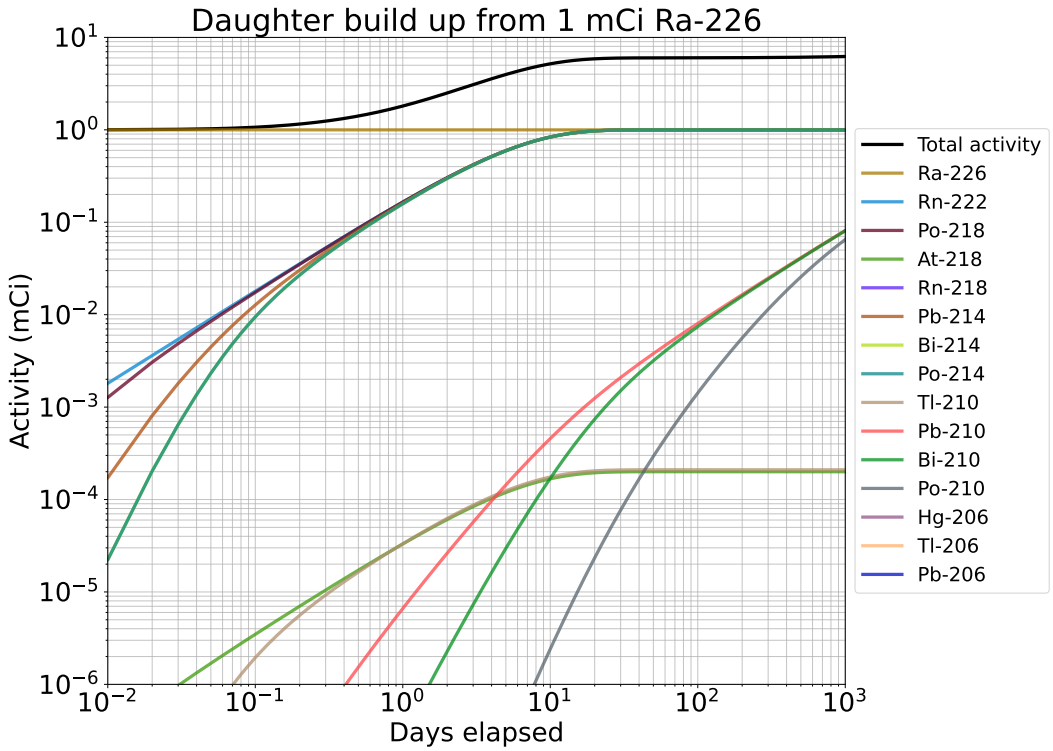


Figure 3.3: Log-scale buildup of radium-226 daughters as a function of elapsed time, starting with a pure 1 mCi (1 mg) sample of radium. At one day, the total activity of the sample is already twice that of the initial sample, and plateaus to around 6 times higher after 10 days. Note that the y-axis is activity and not quantity—to convert to quantity, use Equation 3.1.

the US Environmental Protection Agency recommends limiting radon levels to 4 picocuries per liter of air, with the average level across US homes being 1.3 pCi/L [82]. For radon-222, this corresponds to a recommended maximum of $\approx$ 70000 atoms, or 1.17×10^{-19} mol, per liter. Background radon levels can be mitigated by either physical restriction of the radon or by maintaining sufficient air turnover in the region of generation.

Roughly five alpha particles, four beta particles, and numerous gamma rays are emitted as ^{226}Ra progresses towards ^{206}Pb, presenting challenges from all main types of radiation[8]. Of these beta emissions, most of them are quite energetic, in the $\sim 1 - 5$ MeV range. Following Figure 3.1, betas with this energy can travel an appreciable distance in air, meaning some form of physical shielding is advisable during the handling process.

[8] It is true that neutrons emission and cluster decay are possible branches in the radium-226 decay chain, but they are so vanishingly rare as to not require consideration at any experimentally-relevant quantities. If one is working with enough radium such that the neutron emission from thallium-210 becomes relevant, it is doubtful they will be reading this thesis for any inspiration.

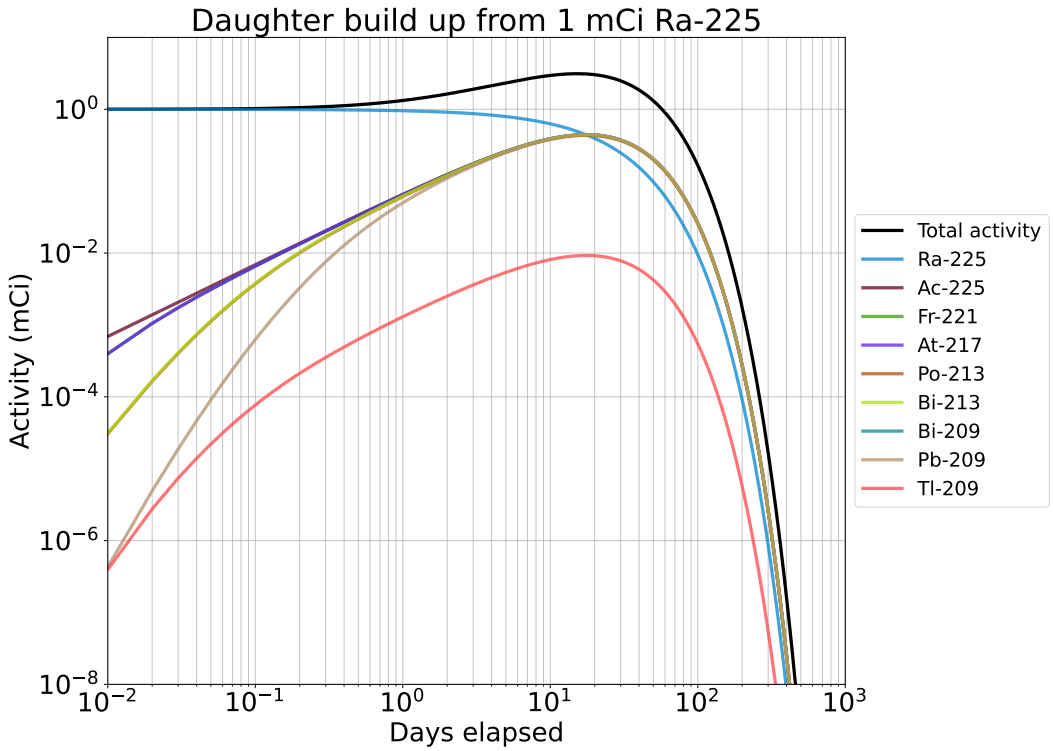


Figure 3.4: Log-scale buildup of radium-225 daughters as a function of elapsed time, starting with a pure 1 mCi (1 mg) sample of radium-225. Compared to radium-226, the shorter half-life of this isotope means that 99% of the initial material has decayed away by 100 days.

Gammas are emitted primarily during the decays of ^{214}Pb and ^{214}Bi and are also on the energetic side. Under normal handling conditions, these gammas contribute to the majority of the biological exposure. Without gamma attenuation, a 1 mCi (1 mg) sample of radium will lead to a biological dose rate of ~ 1 mrem/h at a distance of 1 meter away. Dose rates at other distances will follow from the inverse square law.

All isotopes of radium exhibit the same chemical toxicity, originating from its alkaline earth chemistry. This causes the body to treat radium as it would calcium, leading it to accumulate in bones[9]. In fact, radium is considered "the most toxic radioactive element" [83]. Safe handling of radium requires considerable measures to prevent ingestion, not just for the radiological risks, but the chemical ones as well.

[9]This preferential uptake in the bones is the reason that $^{223}RaCl_2$ sees use as a metastatic bone cancer treatment.

Chapter

IV

Tabletop cryogenic apparatus - the Minifridge

Before a molecule may be studied spectroscopically, or used in a precision measurement experiment, it must be made; only an infinitesimal fraction of the total possible molecules are readily available in nature. Even more complicating is that the optical addressability and relatively simple electronic structure that we desire are consequences of a highly reactive electron configuration. Thus, study and use of these molecules requires producing them in an environment that isolates them from anything they may react with, including themselves.

Furthermore, for a molecule to be useful for most modern precision studies it must also be low-energy (cold), both internally and translationally. As described in Chapter 2, molecules have a mess of internal quantum states, a consequence of their vibrational and rotational structure. To illustrate the consequences of this, consider the distribution of molecules across rotational states J at a temperature T given by the Boltzmann distribution[1]:

$$P(J) = \frac{(2J+1)e^{-BJ(J+1)/k_BT}}{\sum_{J=0}^{\infty}(2J+1)e^{-BJ(J+1)/k_BT}}, \tag{4.1}$$

[1] This assumes a rigid rotor model of rotational states.

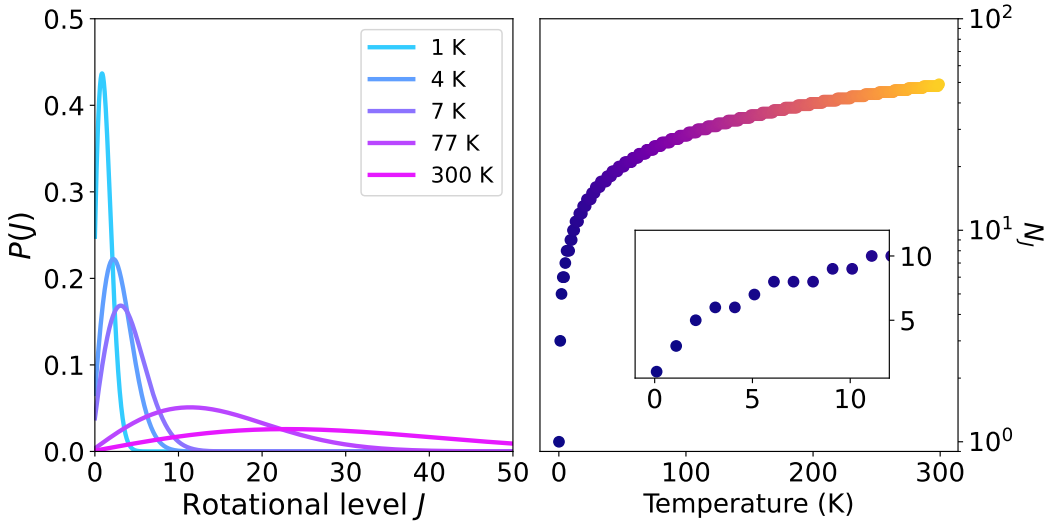


Figure 4.1: Visualization of the rotational state distribution as a function of temperature for a molecule with a similar rotational constant to RaF [84]. Left: Rotational state occupation fraction $P(J)$ as a function of temperature for a few selected values. Right: Number of rotational levels N_J that make up 90% of the total occupied states, quantifying the spread of the molecular population.

with the resulting rotational distributions $P(J)$ shown in Figure 4.1. Since optical control involves the resonant excitation of molecules from specific ground states to specific excited states, being able to condense the molecules into a small number of ground states has the same effect as increasing the total number of usable molecules in the experiment. If these molecules are to be used in a measurement that involves any sort of coherent time evolution—which includes every variation of modern molecular EDM searches—then they also need to be traveling slowly or captured in a trap.

Many methods have been implemented to circumvent some or all of these challenges. One way of directly making cold, trapped molecules involves starting with already laser-cooled and trapped atoms, leveraging the advanced and comparatively simple experimental techniques to bring these species to ultracold temperatures. In the formation of neutral molecules, these trapped atoms are brought together and bonded together through coherent optical transfer to a molecular ground state through a weakly-bound excited vibrational state [85]. In fact, this technique was recently applied to form a Bose-Einstein condensate of polar molecules, the hallmark of quantum degeneracy, for the first time [86]. However, formation of ultracold assembled molecules requires starting with atoms that are themselves laser coolable, severely restricting the space of possible products.

Foregoing laser forces entirely[2], ion trapping is a means of confining atoms and molecules simply through the application of DC and RF electric fields [87]. As a relatively species-agnostic method, they can possess trap depths as deep as 10's of eV [88] ($\sim 10^5$ K)—a trapping potential around a billion times deeper than conventional neutral atom tweezer potentials [89]. These potentials have no trouble capturing simple molecules as long as they are not originating from accelerated beam sources. While this seems like a massive experimental simplification, only charged particles will experience an appreciable force in these electric fields, restricting the application to atomic and molecular ions. Because of Coulomb repulsion of the trapped ions, the density of molecules in ion traps is many orders of magnitude less than can be achieved in optical traps of neutral molecules, with a practical upper limit for ion traps of around 10^9 cm^{-3} [90].

For the vast majority of neutral species which lack the necessary criteria for ultracold assembly, molecule production occurs via laser ablation, where target materials for the desired molecules are vaporized by high energy laser pulses, typically 0.1 – 100 mJ delivered in 10 ns. In the resulting ablation plasma, the reagents present in the target react to form energetic molecules with temperatures of thousands of kelvin [91, 92]—much too hot to be of any use in a precision experiment, necessitating removal of entropy in some way or another.

A general-purpose way of producing cold and slow molecules, and that which is the basis of this work, is cryogenic buffer gas cooling [52]. In this method, the laser ablation occurs in a cryogenic cell, a metallic enclosure fixed at some low temperature, often on the order of 1 – 10s of kelvin. This cell is filled with an inert noble gas which is itself at cryogenic temperatures due to collisions with the cold cell wall. Energy is removed from the hot molecules via elastic and inelastic collisions with the cold buffer gas (Fig. 4.2). Through this process, molecules are cooled electronically, vibrationally[3], rotationally, and translationally, without any experimental techniques that are specific to the molecule of interest besides the choice of ablation target. From this already internally cold starting point, molecules may then be studied directly in the cell or extracted into a beam, with characteristic buffer gas beam velocities on the order of 50 – 200 m/s [52]; these velocities are sufficiently slow to allow for direct laser cooling into optical traps [94].

[2]Foregoing laser forces for the *trapping* force; lasers are still typically used to achieve cooling to the trap motional ground state.

[3]Collisional cooling of vibrational energy is much less efficient than that for electronic and rotational energy, owing to the significantly lower cross section for vibrational-state-changing collisions—see for example the review in [52] and in-depth treatment in [93].

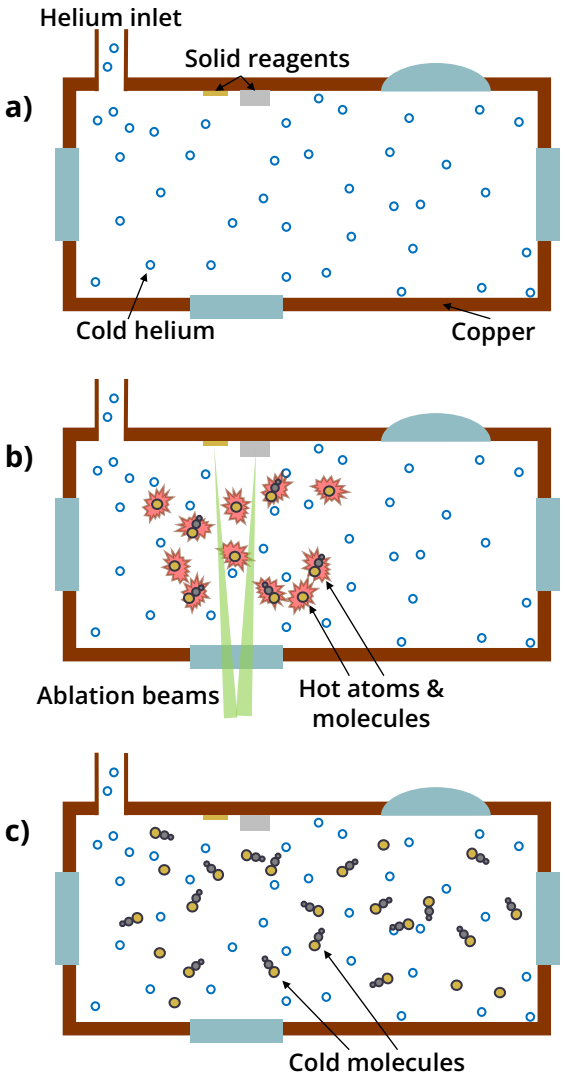


Figure 4.2: Diagrammatic representation of buffer gas cooling of laser-ablated molecules. **a)** The cryogenic cell made of copper is filled with helium gas, which thermalizes with the cell at 4 K. **b)** Pulsed ablation lasers vaporize material off of solid reagent targets which react to form various energetic atoms and molecules. **c)** Elastic and inelastic collisions with the buffer gas cool the ablated species.

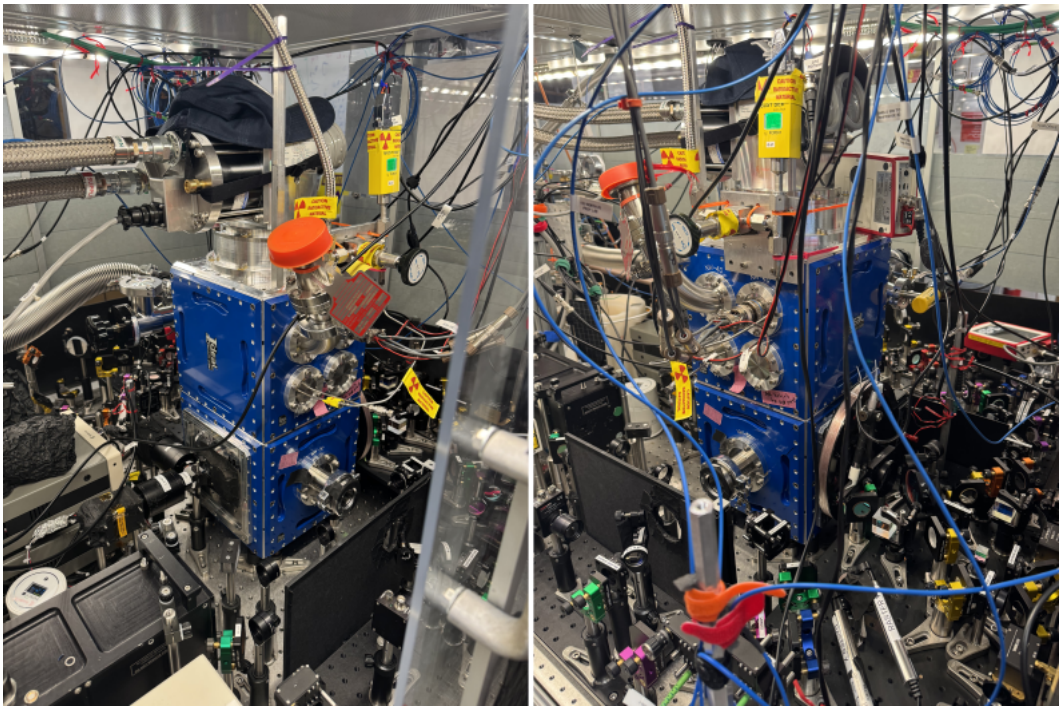


Figure 4.3: Photos of the Minifridge on the optics table from two different angles. Features are easier to see on the rendering, Figures 4.5 and 4.6. Note that the cold head orientation is flipped 180 degrees between this photo and the renderings, but all other components match.

This chapter is intended to serve as a general introduction to our cryogenic buffer gas apparatus, detailing the design and principles of operation; specifics of working with radioactive species will be described in the subsequent chapter. However, it is worth a brief mention of the advantages of cryogenic buffer gas cooling as they pertain specifically to radioactive molecule production. As described in the introduction, gas-phase molecules containing radioisotopes are typically produced in the beamline of a collider facility, which produces them at speeds reaching an appreciable fraction of the speed of light. Slowing these molecules to the point where they could be used in a Ramsey-type measurement or captured in a trap will be a formidable task requiring facility-level infrastructure. Apart from those with the shortest half lives ($t_{1/2} \lesssim 1$ day), there is no reason why a generic radioisotope would not be compatible with the buffer gas cooling methods described in this chapter; this claim is validated in Chapter 5.

4.1 Cryostat design

The tabletop cryostat constructed for this work—which I nicknamed the "Minifridge" since it makes things cold and is smaller than our other cryostats—was designed to minimize the cooldown cycle time while also simplifying the construction over

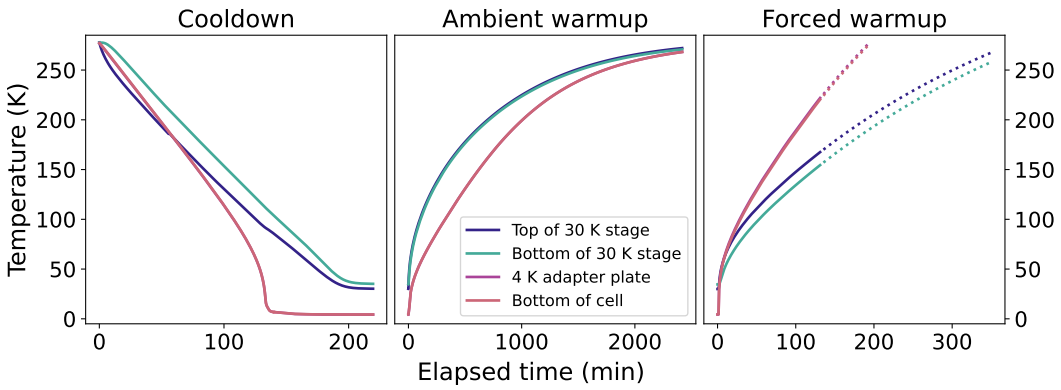


Figure 4.4: Temperatures of cryostat stages across different thermal cycles. Room temperature corresponds to a reading of 280 K as these diodes are not calibrated for accuracy at high temperatures. For all three plots the 4 K adapter and cell temperatures are within a fraction of a degree and thus the traces are overlapped. Left: Cooldown to 4.2 K from room temperature. The cell reaches its base temperature at just over two hours from the start of cooldown. Center: Warming up to room temperature without heating. After around a day and a half the cryostat is above the dew point, meaning it can be opened without introducing moisture into the system due to condensation. Right: An example of a forced warmup, achieved by driving the 30 K top and 4 K adapter cartridge heaters with 0.5 A. Solid lines are data and dotted lines are fits using a simple model based on Newton's Law of Heating. Data after two hours was modeled rather than taken experimentally as we run the heaters on a timer to mitigate the potential to overheat and damage the system. Because of the lower thermal mass and better conductance, the 4 K stage warms up more quickly. If desired, up to four times more current may be run through the heaters to further expedite the warmup.

previous cryogenic buffer gas sources (see [95]). A main reason that both of these are possible simultaneously is the usage of a sealed cryogenic cell versus an open beam source; in a sealed source, the total thermal mass can be significantly smaller and allow for a less powerful cryocooler, whereas for a beam source with continual buffer gas flow a larger volume is often desired to reduce the background pressure caused by the buffer gas, necessitating more cooling power. Initially, the Minifridge was intended to be an assistant to the existing beam sources in the lab, where we would test ideas that were interesting but would divert the attention of the more sophisticated apparatuses away from their main goals. However, as we will see later on in Chapter 5, the specific design features of the Minifridge made it uniquely suited for work with radioactive species. A selection of custom or modified part files for the cryostat and cell can be found in [96].

Cooling to 4 K is achieved via a Gifford-McMahon (GM) style cryocooler[4]. Com-

[4]Sumitomo RDK-205D with F-40L compressor

pared with pulse tubes[5], GM coolers are around half the size, have around half the cooling power at 4 K, and—at the time of this writing—cost around half as much. One notable difference between the two that could limit the use of a GM cooler is vibrations; because the regenerator in the cold head physically moves during the cooling cycle, the cryocooler produces vibrations that are strong enough to be felt by hand on the table and surrounding components. Thankfully, our optical setup and measurement protocol is insensitive to small movements, so we do not need to worry about mitigating this vibration. Experiments with stringent alignment requirements however, such as tweezer arrays or quantum gas microscopes, would need to further decouple the vibration from the optics table.

The moving regenerator of a GM cooler has another consequence: every so often, the cold head needs to be replaced. For our model, we were quoted a lifetime of 10, 000 hours, equal to just over one year of continual operation. Unless the experiment is designed to allow for easy removal of the cold head, this creates quite the headache. We extend this replacement period by only running the cold head as necessary; when we leave for the day, we turn off the cryostat. Overnight, the system ambiently warms up a little (see Fig. 4.4). In the morning, an automated script turns everything on to start cooling down, so that when we arrive the cell is at 4 K. This allows us to run the cold head only as needed, and if we assume it is only on for eight hours a day (and not weekends), this extends the lifetime to around five years—much more in line with a typical PhD timescale.

Vacuum chamber

Because our lower cooling requirements allow for a more compact cryocooler compared to the pulse tubes used in typical beam experiments, the overall vacuum region can be much smaller. The vacuum chamber we chose is made from components sourced by IdealVacuum and is largely comprised of stock parts with minimal custom machining required.

Another reason we chose this type of design was its modularity; given that this was initially a prototyping and testing apparatus, we wanted the ability to easily reconfigure the setup without the need for expensive and time-consuming custom parts. There was also the possible idea to convert the Minifridge to a mini-beam at some point in the future, which could be achieved by simply adding on more cube frames. After we

[5]The reference for comparison is a Cryomech PT415 pulse tube, as it is common within the community

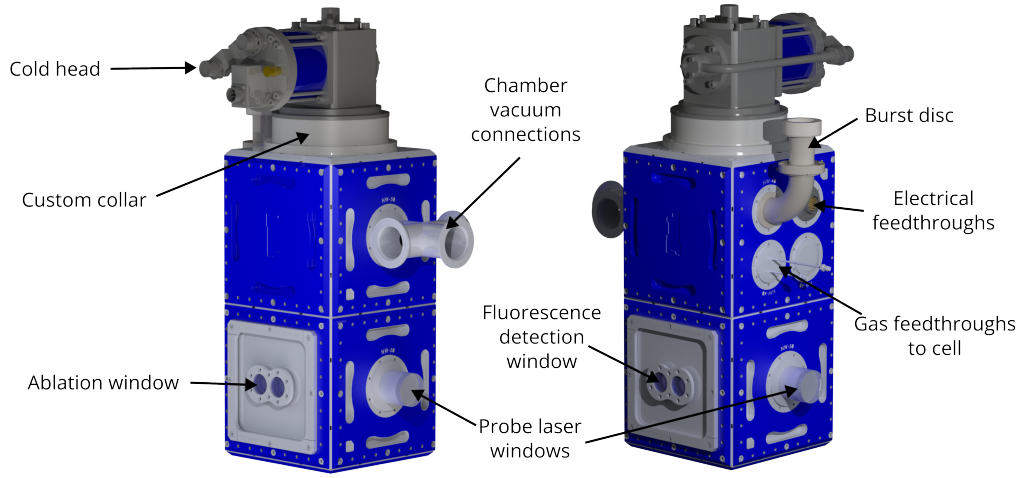


Figure 4.5: Rendering of the full cryostat exterior. Unless significant modifications are being made only three plates need to be removed to perform any task inside the chamber. These plates are visible on the second rendering above: the blank plate, fluorescence window plate, and probe laser window plate. Depending on the access required, removal of only one of these might be possible. In the photos of Figure 4.3, the cold head extends towards the fluorescence detection side, not the ablation side.

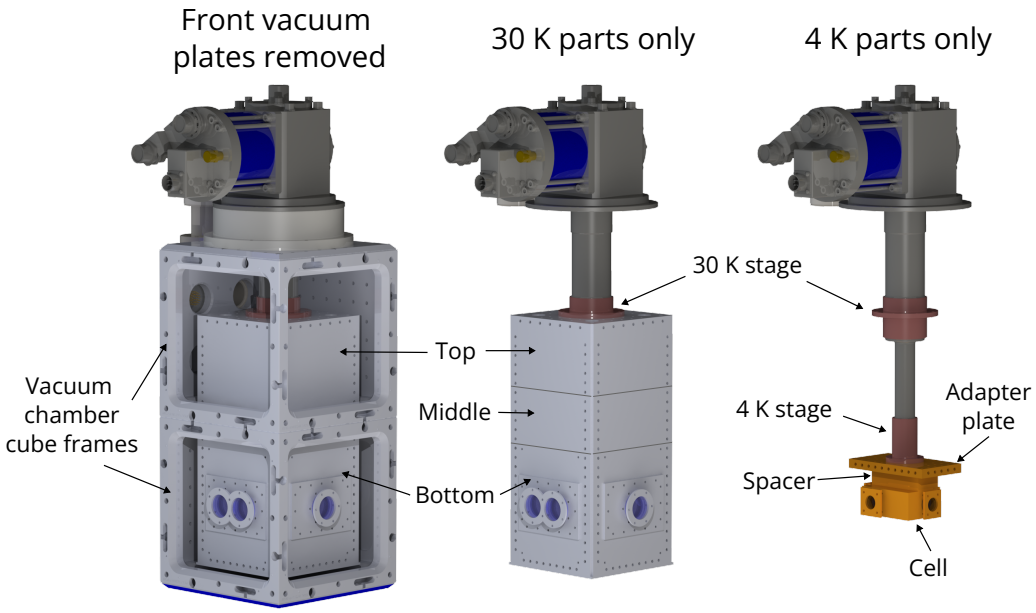


Figure 4.6: Renderings of various stages of disassembly of the Minifridge. Orientation is the same as the left render in 4.5. The leftmost image makes it clear why the 30 K stage was designed in three sections, as the middle plates are completely blocked by the vacuum cube frames and cannot be removed easily.

ended up modifying the apparatus to work with radioactive materials, the beam idea was tabled, and the initial configuration of the Minifridge vacuum chamber is quite similar to the current design described here.

The cold head is mounted to a custom collar on the top of two vertically stacked 9" x 9" x 9" cube frames (Figure 4.5). The collar allows proper positioning of the cold finger relative to the bottom cube so that the cell can be centered with respect to the external vacuum chamber windows.

The side plates on the upper cube frame are used for feedthroughs and vacuum connections. Because the repeated reconnection of electrical and gas line feedthroughs can be time-consuming and prone to errors, a single plate was chosen to contain both types of feedthroughs, with the idea that this plate would never need to be removed during normal operation. The buffer gas is fed through one line of a dual 1/8" tube fluid feedthrough connector[6]. The other tube could introduce other gas-phase reagents, but is unused in our setup. Electrical connections to the cryogenic temperature sensors and heaters are made through a hermetically sealed 32-pin connector[7]. Individual pins on this connector can pass up to 3 A, which allows us to drive our cartridge heaters with an appreciable current. For safety reasons, we included a burst disc[8] to relieve pressure in the event that the system over-pressurizes due to rapidly sublimating gas. One other plate on the top cube connects to the vacuum system to pump out the chamber volume (detailed in 4.1), while the last two plates are blanks.

All optical access to the cell occurs on the bottom cube (see section 4.1 for specifics). Two opposite sides shown in Figure 4.5 have a single, centered window nipple for probe laser access down the long dimension of the cell. These windows have broad visible+NIR coating to study species with wide-ranging transition frequencies, and were made in-house by epoxying Thorlabs WG11508-AB to LDS NW40-150-HN, using EPOTEK 302-3m to seal the window to the half nipple and TorrSeal to strengthen the outside of the seal.

The remaining two sides are used for laser ablation and fluorescence collection. Both of these sides use IdealVac plate P109976, but have been modified with smaller windows to reduce background light levels and blackbody heat load. A custom aluminum window adapter was fitted in place of the large glass pane, which supports two 1.5" circular windows. A 3D-printed frame secures the windows against o-rings. The

[6] 113032 from Accu-Glass
[7] Lesker IFTRG327018B
[8] MDC 420036

ablation window is uncoated to prevent damage of any anti-reflection coating, while the fluorescence collection window has the same broadband visible+NIR coating as the windows on the perpendicular side. Unused windows are taped over with black tape to prevent additional light from entering the chamber, but are left in place in case the probe laser axis is ever switched.

Vibration-damping standoffs[9] screw into the chamber from the bottom. The height of the chamber is set by optics pedestals, which thread into the standoffs and are clamped down to an optics table. Because the regenerator inside the GM cooler moves during the cooling cycle, the cryostat vibrates at around 1 Hz. This vibration does not cause any problems for our measurements, but we still mitigate it to preserve the stability of lasers and cavities that are on the same optics table.

Gas handling

The sealed cell design of the Minifridge requires a gas handling manifold that is capable of pumping the cell and chamber independently. This manifold is shown diagrammatically in Fig. 4.9. Because there is no continual gas flow to form a beam, the vacuum pumping speed requirements are quite low, and the entire system is pumped by a modest turbo + diaphragm pump station[10]. Connections between the vacuum and chamber are all KF, either KF 40 or 25. Between the cell and the buffer gas lecture bottle are VCR gas lines. We use helium as our buffer gas, as all other noble gases freeze at our desired operating temperatures of $4 - 7$ K.

The gas manifold also needs to allow for the introduction of a calibrated amount of helium buffer gas into the cell. A conflat tee with a pressure gauge[11] on it sits between the helium lecture bottle and the cell to act as a load lock. To load helium into the cell, this tee is first filled to a desired pressure, then closed off from the helium bottle and opened into the cell. The internal volumes of all components of this part of the gas line are known, so measuring the pressure allows for determination of the exact amount of buffer gas added via the ideal gas law. Alternatively, the pressure inside may be inferred from the reading on the gauge closest to the cell. By accounting for the thermomolecular pressure drop from the room-temperature gauge to the cryogenic cell [97], we estimate[12] the pressure ratio from the cell p_c to the room measured "warm" pressure p_w to be $p_c/p_w \approx 0.15$.

[9] 9213K17 or equivalent from McMaster-Carr
[10] HiCube 80 Eco Pumping Station from Pfeiffer.
[11] Instrutech Busy Bee
[12] Note that, if using this reference, we are in the regime where $Rp_w \approx 0.5$

In practice, gauge inaccuracies for measuring helium make this calculation somewhat troublesome, and the information is not even that useful as the helium will adsorb[13] onto components in the cell at 4 K, meaning the cell pressure is nontrivial to determine. So, we simply find what value of helium in the load lock maximizes our signals and add that much[14]. An example of one of these helium optimization scans is shown in Figure 4.7.

Gas lines inside the chamber are all 1/8" copper tubing with VCR connections. Mounted to the 30 K stage and to the 4 K stage are two heat exchangers—copper cylinders around which the gas line is wound and brazed (shown in Fig. 4.8). These cylinders are thermally anchored to their respective stages to pre-cool the helium before it reaches the cell, preventing the addition of room-temperature gas to the 4 K cell. The 30 K heat exchanger also helps to reduce the heat load on the cell from the gas line itself, cutting down on the temperature gradient experienced across the gas line near the cell. For a sealed source, these heat exchangers are almost certainly unnecessary.

30 K intermediate stage

Between the room-temperature vacuum chamber and the 4 K cell is an additional enclosure, which we call the "30 K stage" referring to its typical baseline temperature. The purpose of this stage is to prevent 300 K room-temperature black body photons from reaching the cell; this is because the heat transfer between two black bodies has a fourth-power dependence, $\dot{Q} \propto T_h^4 - T_c^4$, where subscripts h and c denote the "hotter" and "colder" black bodies, respectively. By inserting an intermediate stage at 30 K between the 300 K and 4 K regions, the black body heat load on the cell is cut by a factor of $\frac{(300\ \mathrm{K})^4-(4\ \mathrm{K})^4}{(30\ \mathrm{K})^4-(4\ \mathrm{K})^4} \approx 10000$.

All components of the intermediate stage are custom parts made of aluminum 6061, as it is cheap and easy to machine. Copper C10100 could be used in this stage for superior thermalization with the cold head, but aluminum is more than sufficient given our heat loads and cooling power at 30 K. One point to mention is that this stage does not need to be vacuum-tight like the outer chamber; the main focus is on maintaining thermal connection between the components. All 1/8" thick parts were cut on the water jet, and everything else was fabricated elsewhere. All parts are

[13] See Sec. 4.1 "Helium sorbs"

[14] This amount does depend on the types of targets used, as different components in the cell will adsorb different amounts of helium. When drastically changing the ablation targets, reoptimization of the introduced helium is advised.

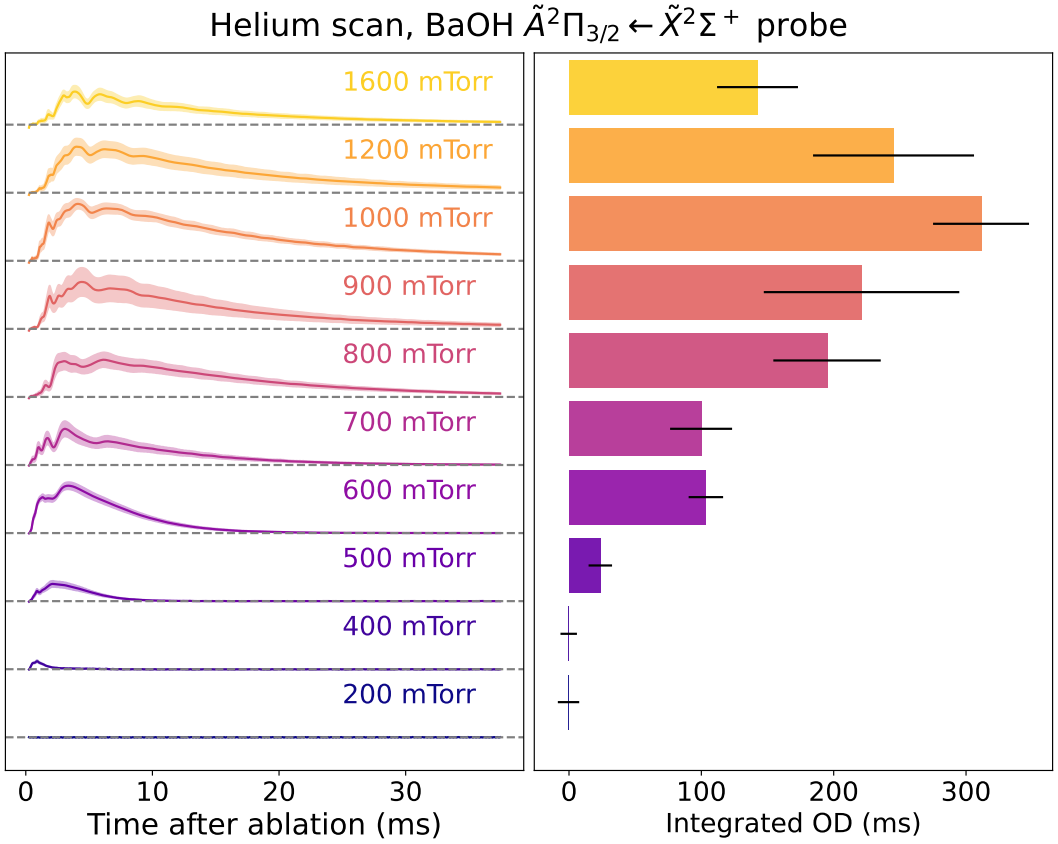


Figure 4.7: Finding the optimal helium value via an absorption measurement of the overlapped $Q_{21}(1.5)$ and $R_{22}(0.5)$ lines on the $\tilde{A}\,^2\Pi_{3/2}(000) \leftarrow \tilde{X}\,^2\Sigma^+(000)$ transition in BaOH [98], produced by co-ablating barium metal with aluminum hydroxide powder. Each color above represents a different cumulative amount of helium added. Left: fractional laser absorption versus time after ablation, offset for visibility. The dotted lines represent the zero and one values for each respective trace, corresponding to 0% and 100% laser attenuation due to absorption by the molecules. For example, the 1000 mTorr trace peaks at around 90% absorption. The time traces show that complicated pressure dynamics occur within the cell, perhaps occurring due to acoustic waves or vortices [99]. Right: integrated optical depth of each absorption trace. Pressure values listed are *not* the pressure readings inside the cell, but rather the cumulative readings of the pressures on the gauge attached to the load lock region before adding the helium. For example, the first set of data was taken after filling the load lock with helium until the gauge read 200 mTorr, after which the helium was allowed to flow into the cell. This process was repeated with another 200 mTorr, bringing the total amount of helium added to 400 mTorr, and so forth. This process should be repeated whenever a new type of target is loaded to better understand the helium adsorbing properties and optimal helium levels. Generally, helium densities that yield successful molecule production are on the order of 10^{15} cm^{-3}.

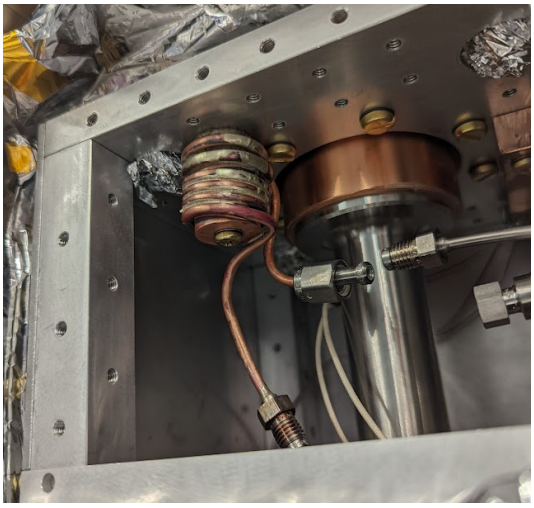


Figure 4.8: Photo of the heat exchanger thermally anchored to the 30 K adapter plate on the top. VCR connectors are placed on either end of the heat exchanger to facilitate its relocation or removal without the need to drastically alter the rest of the gas lines.

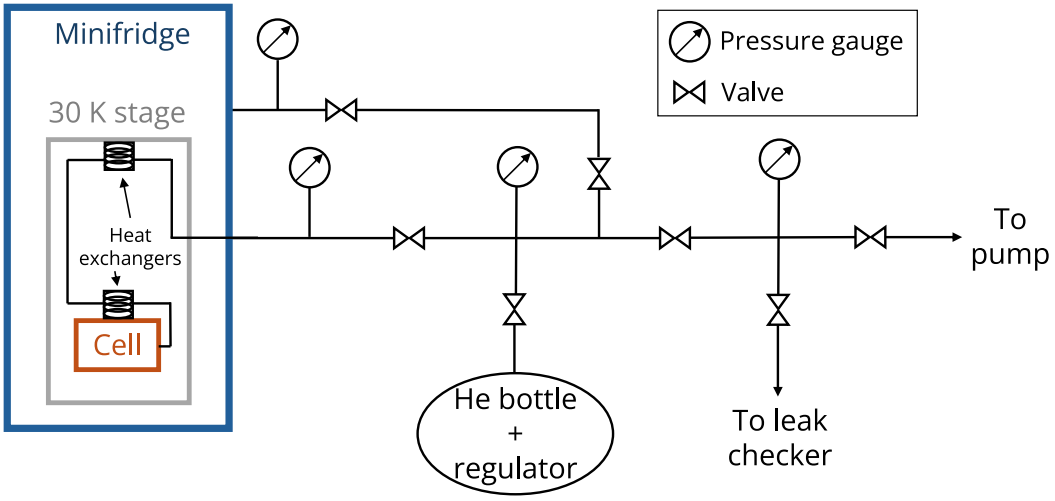


Figure 4.9: Diagrammatic representation of the Minifridge gas handling manifold before upgrading to work with radioactive samples. This is a simplification of the current gas manifold, which is shown in 5.3.

connected with brass screws and belleville washers[15], to ensure that the connections do not become loose as parts cool and contract.

A 1/4" thick adapter plate mounts to the 30 K stage of the cryocooler (Figure 4.10), with both threaded and through holes for mounting different components. We call it an adapter plate as it "adapts" the M5 screw hole pattern on the cold head to a more usable and customizable pattern. Vertical bars with thickness 3/4" are suspended from the four corners of this plate. These bars are thicker than structurally necessary, but the extra thickness ensures adequate heat transfer between the far regions of the intermediate stage and the cold head. To demonstrate this, we can solve the heat

[15]Also called Belleville "disc springs."

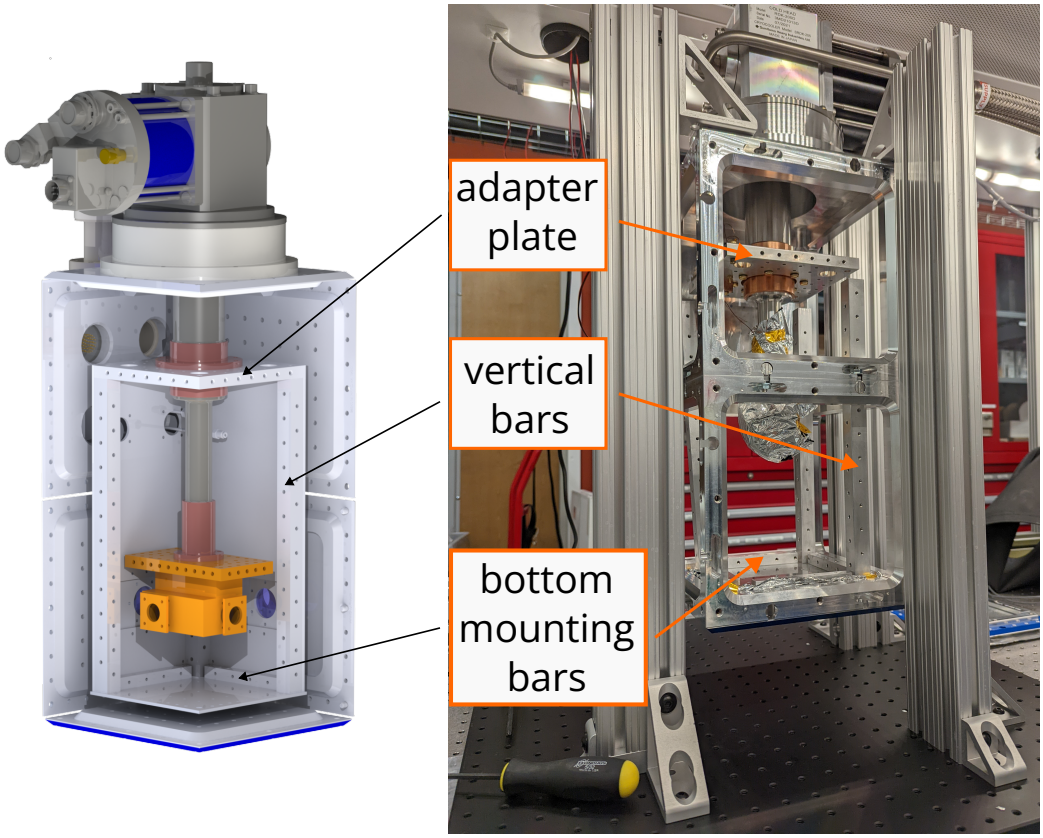


Figure 4.10: A cutaway rendering and assembly photo of the 30 K stage, explicitly pointing out some of the components described in the text. 80-20 struts were used to raise the Minifridge during assembly so that the bottom plate could be attached.

equation:

$$\frac{dQ}{dt} = -kA\nabla T \,,$$

where Q is the local heat, k is the thermal conductivity, and A is the cross-sectional area of the material. If we assume a linear conductivity and in 1-D:

$$\frac{dQ}{dt} = -kA\frac{\Delta T}{\Delta x} \,.$$

Using the Stefan-Boltzmann law, an estimate of the black-body heat load from the 300 K stage is $\sim$ 1 W, or $\frac{dQ}{dt} = 1$ W at the bottom of the 30 K stage. For aluminum 6061 at $\sim$ 30 K, $k \approx 45$ W/(m·K) [100]. Thus we have:

$$1\ \mathrm{W} = -45\frac{\mathrm{W}}{\mathrm{m}\cdot\mathrm{K}} \times A \times \frac{T_{top} - T_{bot}}{l} \,,$$

where l is the length of the shielding surface. Our 30 K stage is 0.34 meters long. If we assume the top is held steady at 30 K from the cold head and that the heat is carried

evenly by the 4 vertical support rods, we see a cross-section-dependent temperature as follows[16]:

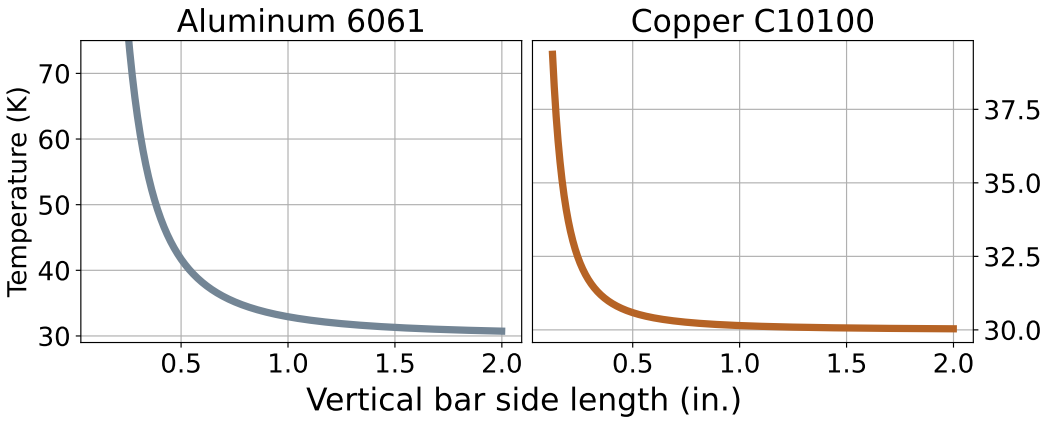


Figure 4.11: Temperature of the bottom of the 30 K stage as a function of support bar material and thickness, assuming a 1 W heat load on the bottom. Copper was included as an example high-conductivity material, with a thermal conductivity coefficient of $k \sim 900$.

These plots imply that, in order to maintain a temperature within 10 K at the bottom of this stage, vertical square bars with a side length of at least 0.5 inches are required.

A 1/8" thick plate mounts to these vertical support bars to close off the bottom. On top of this bottom plate are four 1/2" thick bars running along the edges to provide additional mounting holes. The reason for this bottom plate design with added bars rather than a unibody part is twofold: we wanted the bottom plate to be very thin to provide some clearance from the outer vacuum plate, meaning it would be too thin to have its own hole pattern on the side. On the other hand, if the part were machined from a single piece of aluminum it would be unreasonably expensive, so we cut the thin part on the water jet and added the cheap custom bars after the fact.

Various types of 1/8" thick panels close off the 30 K stage from the sides. These side plates are split into three independent regions: the top, middle, and bottom. The top and bottom regions can be accessed by removing the respective outer vacuum chamber plates. The middle region is blocked by the joint between the upper and lower cube frames, and cannot be removed under normal operation (see Fig. 4.6). As such, the region inside the intermediate stage was designed so that these plates would

[16]This crude approximation does not include the temperature dependence of the thermal conductivity, which would make the conductivity slightly better as the aluminum heats up. A more careful treatment would yield similar results at the temperatures of interest, however.

	North	East	South	West
Top	Blank	Blank	Gas & electrical feedthroughs	Blank
Middle	Blank	Blank	Blank	Blank
Bottom	Centered 1.5" window for probe laser access	Dual 1.5" windows, only one used for ablation	Centered 1.5" window for probe laser access	Dual 1.5" windows, only one used for fluorescence collection

Table 4.1: Table of panels on the Minifridge 30 K intermediate stage and their current uses.

not need to be removed in order to have full access. A full description of the plates is given in Table 4.1.

Like with the vacuum chamber, the side panels on the intermediate stage have different features depending on their position relative to the cell. Plates on the top section are either blank or have bores to pass feedthrough connections into the 4 K region. The middle plates are all blank. All four bottom plates have windows that match the window patterns of the vacuum stage, and custom frames were cut on the water jet to mount the windows. As mentioned previously, because the 30 K stage is not vacuum-tight, the windows only need to be secured against the aluminum plates such that there is sufficient thermal connection. We apply a small amount of Apiezon N vacuum grease at the overlap regions between parts to improve the thermal contact. Kapton tape is adhered at any aluminum-glass interface to prevent the metal from scratching the windows, and also because tightening the windows on metal burrs applies a highly localized force that might cause cracks.

In order to lower the black body heat load from the room-temperature vacuum chamber, blankets of multi-layer insulation (also called superinsulation) cover the entirety of the 30 K stage. These blankets are made from four layers of aluminized biaxially oriented polyethylene terephthalate (aluminized BoPET), trade name Mylar, which possesses both high infrared reflectivity and emissivity [101]. To make these blankets, we cut four sheets of Mylar that are slightly bigger than the side plates and secure them together using small strips of kapton tape[17]. The blankets are screwed into the side plates; to make the through holes for screws, we found it best to apply a piece of kapton tape to the screw location on the blanket and punch a hole using a small hollow hole punch. This method creates a kapton grommet through all four layers, allowing for easier insertion of the screws.

[17] The sheets are connected at a small number of points to increase the vacuum conductance between the sheets.

The temperature of this stage is monitored by two silicon diodes[18], one near the cold head connection at the top and the other at the bottom. During typical operation, the baseline temperatures for the top and bottom are 30.25 K and 35 K, respectively, in somewhat remarkable agreement with the crude predictions from 4.11. Also on the top is a cylindrical cartridge heater[19] which we use to greatly speed up the warming of the chamber as shown in Fig. 4.4. To thermally connect this cartridge heater with the 30 K stage, we take a rectangular piece of copper C10100 and drill a hole to fully insert the cartridge with minimal clearance. The heater is fixed in this piece of copper using a thermally conductive epoxy[20] and the copper is mounted near the cold head connection on the top of the 30 K stage. As with the aluminum plates, a thin layer of vacuum grease is applied to increase the heat dissipation from the cartridge heater assembly into the aluminum stage.

All electrical components inside the vacuum chamber are connected via Manganin wire. Manganin is an alloy that is desirable for cryogenic systems as its heat conductance is very low, less than 1% that of pure copper. Its electrical resistance is also uniform across a wide temperature range, helping to ensure accurate readings from the silicon diodes.

4 K stage

Components attached to the 4 K portion of the cold head are made from copper C10100. A custom adapter plate mounts to the cold head to provide additional threaded holes in convenient locations. Because copper is soft, all of these threaded holes, as well as any in other copper parts, have stainless steel HeliCoil threaded inserts to strengthen the threads and reduce the likelihood of stripping the copper. Between the adapter plate and the cell is a solid block spacer which vertically positions the cell for optical access and maintains thermal contact between the cell and the cold head[21]. A small amount of Apiezon N vacuum grease is used between all connections from the cold head to the cell. Typical baseline temperature for our operation is around 4.2 K, measured on the adapter plate and the bottom of the cell with two additional silicon diodes. Unlike with the 30 K stage, these two diodes read almost the exact

[18] DT-670A1-CU from Lakeshore Cryotronics

[19] Omega CSH-101120-120V

[20] Henkel Loctite STYCAST 2850FT with catalyst 24LV

[21] Making the spacer out of a solid block of copper was definitely overkill. In hindsight, I should have ran the heat transfer calculations and designed a solution that is more efficient with the material and cost. For example, using a small number of copper spacing bars rather than one large solid block would be cheaper while still achieving the necessary thermal conductance between the cell and the 4 K cooling stage of the cold head.

same temperature due to the better thermal conductance of this stage. When there is a discrepancy between their readings it is indicative of poor thermal connection, often due to a lack of tightening of the cell mounting screws.

On the top of the adapter plate we mount another cylindrical cartridge heater. Running this heater in a low-current (5 – 50 mA) configuration will warm the cell to temperatures ranging from 4 K to 40 K, which is useful for altering the rotational state population of our molecular species and for desorbing helium. In higher-current operation, the cartridge heater speeds up the warm-up process in tandem with the one for the 30 K stage.

In cryogenic systems with higher heat load, such as in a beam apparatus, a copper enclosure can be built to surround the cell like in the 30 K stage. For our purposes this was not necessary.

Helium sorbs

Another feature on the top of the adapter plate is a helium "sorb." Because helium does not freeze at 4 K, it can build up if not pumped out by the vacuum system fast enough and lead to an elevated background pressure that is difficult to diagnose and remedy.

Even though helium does not freeze at 4 K, it can adsorb into different materials, with an efficiency that depends on temperature. An effective sorb material in the 4 K to 10 K range is activated charcoal—due to its extremely high porosity, it can trap on the order of 100x its volume in helium gas [102]. We use activated carbon 12 x 30 mesh from Calgon Carbon.

While experimental evidence suggests that silver-soldering the charcoal to the copper results in the best helium pumping, it has been shown that the simpler method of epoxying the charcoal to the copper using Stycast is sufficient [102]. To make the sorb, a thin layer of epoxy is applied to a copper plate, resting the plate so that it is level and facing upward. Charcoal flakes are then dropped onto the epoxied surface to coat as much as possible. Once the epoxy has cured in this position, the plate can be lifted and any unsecured charcoal gently shaken off. Part of the sorb is left unpainted by epoxy, with a hole drilled in this section to fasten the sorb to the adapter plate for thermal contact.

In ambient environments, charcoal will absorb water vapor. This trapped water will reduce the sorb effectiveness at low temperatures, so it needs to be pumped out before

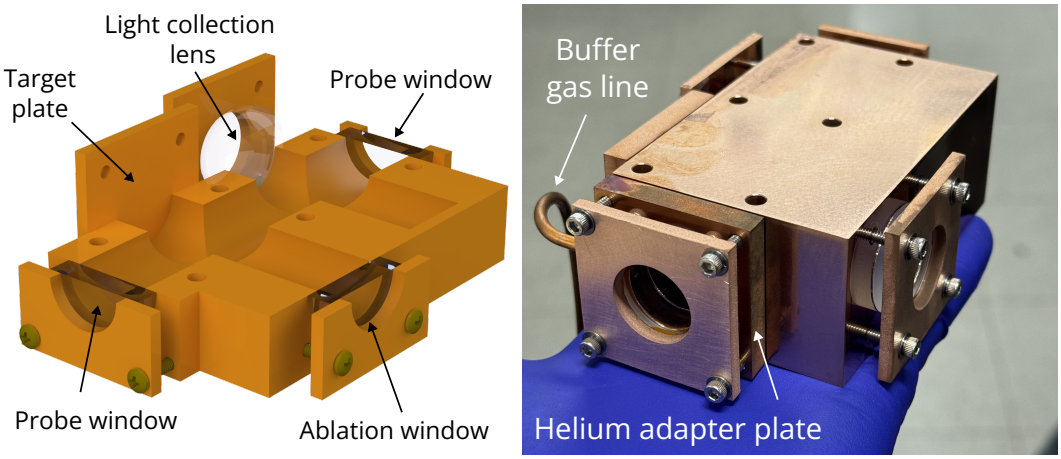


Figure 4.12: Cutaway rendering and photo of the cell in the same orientation. Features mentioned in the text are identified.

cooling to below the water freezing point. Heating the sorbs while under vacuum will dramatically speed up the water release rate, so in an apparatus with a large volume of charcoal it may be advisable to add heaters to the sorbs.

All this being said, because we are using a sealed cell the need for sorbs is low. This is partly why only one small sorb is used in the Minifridge, compared with the extensive sorb "fins" used in the beam apparatuses in the lab [95].

Cell

Molecules are produced and studied in the cell. Three 0.75" diameter bores in a block of copper C10100 create a hollow region with a volume of ≈ 48 cm^3, where the ports allow for various configurations of laser access and fluorescence collection. Optics and other mounting plates are attached to the sides of the cell at these bores using threaded hole patterns in the cell body. In each of these holes, we install stainless steel HeliCoil threaded inserts to strengthen the threads.

Because this is a sealed cell, connections to the cell body need to be leak-tight to prevent depletion of buffer gas and potential leakage of harmful gases. We use indium as a cryogenic vacuum gasket [103]. A ring of indium wire rests between the two vacuum sealing surfaces; when these surfaces come together they depress and deform the indium wire, which sticks to both sides and prevents gas flow at the joining region just like a standard o-ring. The cell body and any plates attached to it are sanded down to Ra 0.1 μm, where Ra is the arithmetic average roughness (not the element radium), to ensure that the indium wire is capable of sealing to an acceptably low leak

rate—this is achieved by sanding to 1000 – 2000 grit sandpaper[22]. Typical leak rates for the cell are below 10^{-9} mbar·l/s, measured using a helium leak checker[23]. There are technical tricks for working with indium, which are described in the cell assembly guide in Appendix B.

Helium buffer gas is introduced via a custom plate mounted to the long bore of the cell. We silver braze a 1/8" copper tube in the side of this plate to connect with the rest of the gas handling manifold via a VCR fitting. The plate is mounted directly onto the cell body and features a separate hole pattern with threaded inserts for securing a window onto the other end. This procedure was chosen over brazing directly onto the cell body as the smaller mass of the custom plate makes it easier to heat up for the brazing process, and it is also more easily replaceable if any braze clogs form that render the part unusuable.

All cell optics aside from the ablation window are coated with a broadband visible + NIR antireflective coating, allowing for operation in many wavelength regimes without changing out the cell. For the ablation window, no coating is used, as the high-intensity pulsed laser light is capable of burning spots in antireflective coatings. This ablation window is also made out of UV fused silica rather than the cheaper N-BK7 glass for its superior damage threshold to laser pulses, and has a slightly angled (wedged) face to prevent the focused beam from back-reflecting in the laser path and potentially damaging upstream optics. Cell optics part numbers can be found in Appendix B. 1/8" thick copper plates press the optics onto the indium wire, compressing the wire and forming a vacuum seal.

The light collection bore does not puncture all the way through the cell body (see Fig. 4.12). To reduce the light scatter from ablation and laser probes, we coat this section of the cell with an ultra low reflectance black paint[24] which we airbrush directly onto the cell interior. Since outgassing is not an issue as the cell will be at cryogenic temperatures, we do not bake out the cell after painting.

The last feature of the cell is the target plate, which contains the chemical precursors for our molecules of interest. Specifics of the targetry are described later in this section.

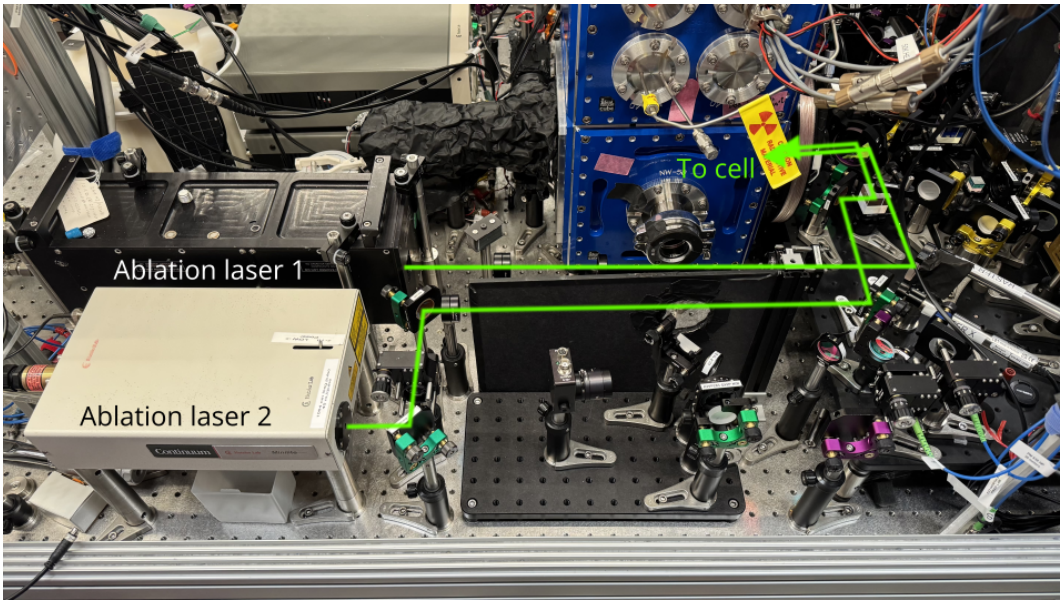


Figure 4.13: Photo of the dual-ablation setup employed on the Minifridge. The beam paths are merged using a 1" PBS cube before entering the cell. Each laser path features multiple mirrors to allow for individual steering on the target plate.

4.2 Atom and molecule production

Production of gas-phase atoms and molecules occurs via laser ablation. In this process, beams from pulsed Nd:YAG lasers[25] at 532 nm are tightly focused onto the target plate, ablating the reagents they hit. The pulses from these lasers have a duration of $\approx$ 10 ns and are expanded to $\approx$ 1 cm before being focused by a 200 mm focal length lens external to the cryostat. Expanding the beams before focusing allows for a tighter focal point at the target plate which increases the intensity of the ablation. It also means that the beams are larger as they pass through the windows, lowering the risk of laser-induced damage. Ablation energies vary depending on the target and are empirically determined to maximize the signal—generally, for ablation of pure metals such as Yb or Ba, energies around 2 to 5 mJ produce the best signals, whereas pressed powder targets require energies from 5 to 40 mJ.

We attempted at one point to perform ablation at 1064 nm by removing the doubling crystal and Q-switch from ablation laser 2. Running this way, the pulse length ends

[22] 1000 grit is more than sufficient for our purposes, but the extra polish achieved by going to 2000 makes for a visually appealing cell.

[23] Pfeiffer ASM 340

[24] MH2200 manufactured by Huntington Ingalls Industries, previously Alion Science and Technology

[25] Both ablation lasers are q-switched pulsed Nd:YAG lasers frequency doubled to 532 nm. Ablation laser 1 is from Quantel/Big Sky and 2 is a Continuum (now Amplitude) Minilite II model.

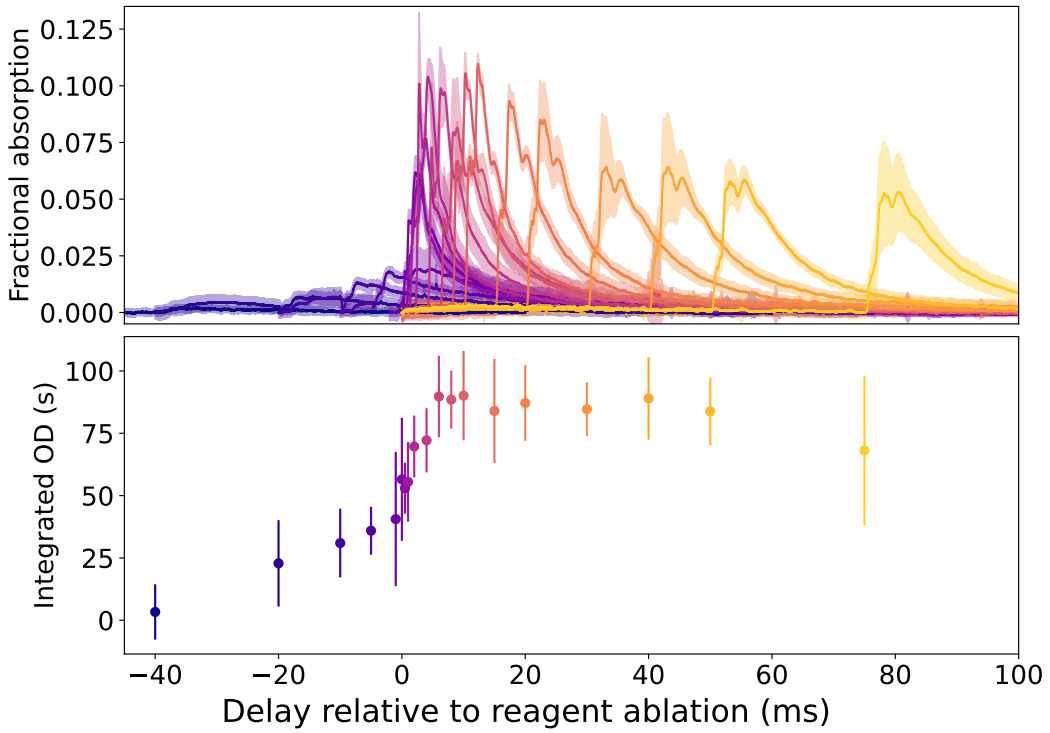


Figure 4.14: Testing the importance of ablation delay for dual-ablation production of YbOH. Yb metal was ablated with a variable delay relative to ablation of $Al(OH)_3$ pressed powder. Top: Absorption fraction of a probe laser driving the ${}^{Q}Q_{11}(1.5)$ line of the $\tilde{A}\,{}^2\Pi_{1/2}(000) \leftarrow \tilde{X}\,{}^2\Sigma^+(000)$ band in YbOH, which is at 17323.6728 cm^{-1} [104]. The OH reagent target was always ablated at $t = 0$. Each color represents a data set taken with a different delay timing. The bottom plot shows the respective integrated absorption signals for each of these delays, with error bars indicating one standard deviation of the integrated values within a data set. Negative delay corresponds to ablation of metal before OH.

up being closer to 100 μs. This resulted in decreased signals across all operating configurations, where we only were able to observe any molecule production on the ablation shots right after steering the laser to a new spot on the target. Our best guess for what is happening is that the lengthened pulse no longer has sufficient instantaneous energy to ablate, but enough to desorb some of the material that has been distributed onto the surface of the target from previous ablation shots.

Following ablation, vaporized atoms and molecules react to form various products which then thermalize via collisions with the cryogenic buffer gas. Species-selective atom and molecule production is achieved by steering the ablation lasers onto the different targets present in the cell. For atoms and some molecules, only a single target may contain all necessary reagents, in which case only one ablation laser is needed.

Otherwise, two separate ablation lasers are used to hit two different targets. When two pulses are employed, the relative time delay between the two may be adjusted, allowing for another opportunity to optimize molecule production. For example, we observe an increased production of MX molecules, where M is an alkaline earth(-like) metal and X is a fluorine(-like) ligand, when we ablate the metal anywhere from 10 to 50 ms after the ligand target, shown in Figure 4.14.

Molecule production may be further improved via light-assisted chemical enhancement [105]. Often, the reaction pathways which yield the desired molecules are endothermic, meaning that reaction barriers may only be overcome in the energetic early-time ablation plasma. Laser excitation of reagent atoms to energetic metastable states can provide enough energy to make these reactions exothermic, increasing molecule yield by more than an order-of-magnitude in many cases. Because this is a resonant effect, it unambiguously demonstrates that the excited atom participates in molecule formation, which is useful when association of the observed signal with a specific molecule is nontrivial. Furthermore, in congested spectra with overlapped isotopologues, this process enhances only the isotopologue of interest, allowing for an easier assignment of spectral features [106]. An example of chemical enhancement to produce RaF molecules is shown in Figure 4.15.

Chemical enhancement may also improve reaction yields in reactions that are already exothermic. As two species come together to form a molecule, their incoming kinetic energy needs to be dissipated in order for them to remain bound, otherwise they will simply fly apart with the same energy as they approached. An excited-state atom can emit a photon to act as the third body in this reaction process, removing energy from the system and allowing the resulting molecule to stay bound. In this realization of enhancement, it is actually desirable that the excited state is not *too* long-lived, otherwise it is unlikely for an emission process to occur while the reacting atoms are in a bound attractive potential.

With macroscopic reagents and chemical enhancement, we produce around 10^{11} – 10^{12} molecules per ablation shot. We have also demonstrated production of molecules starting from trace reagents, with a detection floor around 10^{8} molecules, assuming we are probing on a strong transition (see Supplemental Material in [84]).

Ablation targets

Opposite the ablation window is the "target plate," a square piece of copper C10100 with side length 1.5" and thickness 0.25". This target plate contains the solid-state

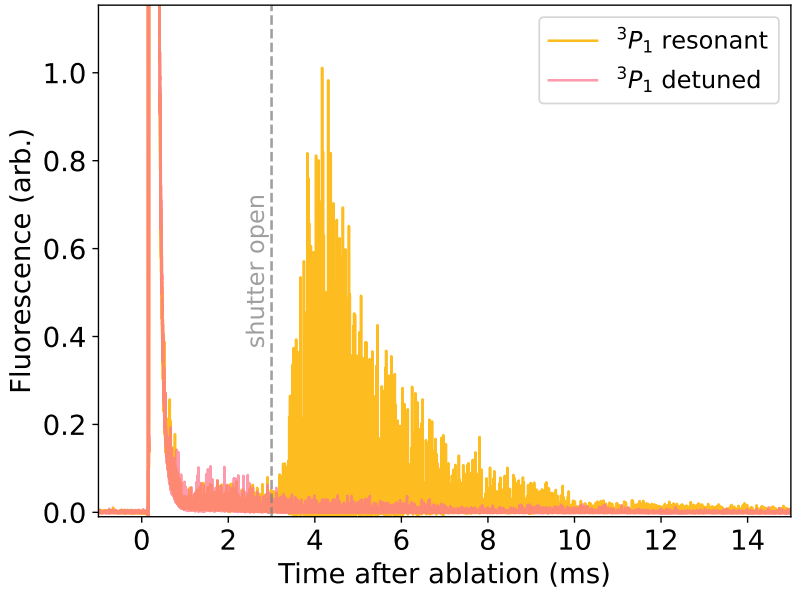


Figure 4.15: Demonstration of chemical enhancement on fluorescence signals for radium monofluoride (RaF). For both traces, we are driving the $C\,^2\Sigma^+(0) \leftarrow X\,^2\Sigma^+(1)$ transition at 618 nm with a 50 kHz pulsed dye laser and detecting the strong fluorescence at 602 nm. At 3 ms after ablation, a shutter opens allowing roughly 1 W of enhancement light to enter the cell. When the enhancement light is resonant with the radium $^1S_0 \rightarrow {}^3P_1$ transition at 13999.357 cm^{-1}, we see an increase in molecular fluorescence, indicating more molecules were formed.

atomic and molecular precursors for producing molecules via laser ablation. These precursors may range in size from ~ 1 millimeter up to the area of the 0.75" diameter bore, and this full area may be occupied by as many distinct targets as can fit. The only requirement for a target is that it can be attached to this target plate and maintain its attachment at cryogenic temperatures.

In the Minifridge, we frequently work with a few different types of target materials. The simplest are pure metals such as ytterbium or barium, which we epoxy on as chunks a few millimeters in size. These chunks may be taken from a larger piece of metal, as both Yb and Ba metals are soft enough to be cut by wire cutters, or acquired as small pieces to begin with. Despite often being the smallest target on a given target plate, pure metals can sustain many tens of thousands of ablation shots without being depleted, while simultaneously yielding extremely strong and consistent atomic signals. Barium metal, in the presence of moist air, will decompose to barium hydroxide ($Ba(OH)_2$), a white powdery substance (see photos in Chapter 7.1). This decomposition has occurred while waiting for the epoxy to cure, rendering the barium metal target useless. To prevent this, we apply a thin layer of Apiezon N vacuum

grease to the barium metal target to shield it from the air.

To form molecules, one method is to ablate a single target that contains all molecular constituents. This works when the reagents are safe to handle and mix into a custom target or when there already exists some sort of simple material that contains all desired atoms. An example of the latter would be a calcium fluoride (CaF_2) sputtering target, a high-purity ceramic comprised of only calcium fluoride, which we ablate to produce calcium monofluoride (CaF). As for the custom targets, we produce these by mixing some combination of powder compounds and pressing them in an 8 mm diameter hydraulic die press for 10 – 30 minutes at 1 GPa. Before pressing, these powders are ground with a mortar and pestle or ball mill to below 200 mesh size (roughly 75 microns) in order to produce uniform pressed pellets[26]. Sometimes we include polyethylene glycol (PEG) powder at a concentration of around 5% by mass to act as a binder and prevent the pellet from disintegrating upon removal from the die. Because the PEG binder contains hydroxyl groups, we typically omit it when making targets for non-hydroxide molecules. We rarely want to use the entirety of this target in a single cell, so we instead break off chunks to epoxy onto the target plate and save the remainder for a future cell by storing in an airtight dry box. A single spot on these pressed powders can sustain a few hundred ablation shots before the molecule signal degrades, making them a little worse than pure metals. Moving the ablation spot on the target will recover the initial behavior, assuming the new spot has not been previously ablated.

It is not always the case that a single target can be used to produce a desired molecule of interest, nor is it always the case that we want just a single target. An advantage of the dual-ablation setup is that we can modify the molecule being produced simply by steering one (or both) of the ablation lasers onto different targets. This is especially important when making molecules out of trace species, as we would not want to commit to putting the limited reagent into a combined target if we know we want to use it to produce multiple types of molecules. Generally, this situation manifests as having one target supply the metal and one target supply the ligand. To introduce nonmetal reagent groups such as -F, -OH, or $-NH_2$, we typically use hydraulic-pressed chemical powders, examples for each being copper (II) fluoride (CuF_2), aluminum hydroxide ($Al(OH)_3$), or urea ($CO(NH_2)_2$). These co-targets are made in the same way as a combined target, just without containing the metal of interest. We can also

[26] Some targets have been made from powders with large grain size, and we observe that the ablation varies much more from shot-to-shot than when these targets are made from more uniform powders.

source certain ligands from other types of materials, such as fluorines from a calcium fluoride sputtering target.

When working with trace materials or highly radioactive substances such as radium, we employ a method called "drop casting," where a liquid solution is evaporated on a substrate to deposit the species of interest in a thin, even layer [84]. This method is described in much more detail in Chapter 5.2.

There is no way to know *a priori* which reagent forms the desired molecule most efficiently. When identifying candidate reagents, we try to follow the heuristic of keeping them as chemically simple as possible. From here we sort by the ones that have the highest stoichiometric fraction of the species of interest and which seem most thermodynamically ready to part with this ligand[27]. However, the ultimate determination happens inside the cryostat. Examples of testing processes to identify suitable co-targets, including for -OH and -NH_2 molecules, are sprinkled throughout Chapter 7.

A summary of all of the atoms and molecules produced in the Minifridge over the course of this thesis is given in Table 4.2, along with the reagents used for producing them.

We have found that the helium adsorption properties of the targets affects the molecule production in sometimes strange ways. As explained previously, different targets inside the cell will adsorb helium to different extents. Most of the time, we find that targets perform better at 7 K than at 4 K. Our best explanation for this is that the gentle heating will pre-desorb some helium off of the targets, which then aids in molecule thermalization. Other experiments that produce molecules in similar ways have noted that pre-firing or pre-heating the cell to desorb some helium has yielded increased molecule counts as well [107]. At 4 K, we believe that a significant fraction of the helium adsorbs onto the targets, meaning that the only buffer gas available for cooling and thermalization is that which is desorbed during the ablation process. However, not all targets benefit from this heating; see Figure 7.6 for an example.

4.3 Optical spectroscopy

The large optical access to the cell enables the simultaneous use of multiple spectroscopic methods. Modifying the cell layout can also allow for sending in lasers at other

[27] Other considerations, such as chemical compatibility and safety, should also be taken into account. For example, some candidate reagents we identified are so toxic as to preclude their usage, despite potentially sourcing the desired ligand in an efficient way.

Produced species	Target composition[a]	Notes
Ba	**Barium metal** $BaCl_2$ drop cast	>300 ms fully bottomed-out absorption lifetimes
BaF	**Barium metal & CuF_2 powder** $BaCl_2$ drop cast & CuF_2 powder Barium metal & AlF_3 sputtering target	See Chapter 7.1 for description of the identification of copper fluoride
BaOH	**Barium metal & $Al(OH)_3$ powder** **Barium metal & $Te(OH)_6$ powder** Barium metal & $Fe(OH)_3$ powder Barium metal & $Cu(OH)_2$ powder $BaCl_2$ drop cast & $Al(OH)_3$ powder	See Chapter 7.1 for description of the identification of aluminum hydroxide
BaO	Barium metal & $Cu(OH)_2$ powder	Only a handful of successful shots ever observed
Yb	**Ytterbium metal** Yb + $Yb(OH)_3$ combined powder	
YbOH	Yb metal & $Al(OH)_3$ powder Yb + $Yb(OH)_3$ combined powder	Both methods produce roughly the same molecule signals
CaF	CaF_2 sputtering target	
CaCl	CaF_2 sputtering & AgCl powder	Chapter 7.2
CaI	CaF_2 sputtering & AgI powder	Chapter 7.2
$CaNH_2$	**CaF_2 sputtering & urea powder** CaF_2 & ammonium phosphate powder CaF_2 & melamine powder CaF_2 & ethylenediamene HCl powder	Chapter 7.2
Ra	**Radium nitrate drop cast with xylitol** Radium chloride drop cast Radium-painted watch hands	Chapter 3.3
RaF	Ra drop cast & CuF_2 powder	Chapter 5.6
RaCl	Ra drop cast & AgCl powder	Chapter 5.7
RaOH	Ra drop cast & $Al(OH)_3$ powder	Chapter 5.4
RaOD	Ra drop cast & $Al(OD)_3$ powder	Chapter 5.5 describes aluminum deuteroxide synthesis
WC	Tungsten carbide sputtering target	
U	Uranium metal	
UO	**U metal & $Al(OH)_3$ powder** U metal (oxidized) U metal & ThO_2 ceramic	Chapter 7.3
UO_2	U metal & $Al(OH)_3$ powder	
Np	NpO_2 in KCl pressed powder	Chapter 7.4
Th	Th metal ThO_2 ceramic	Both methods produce roughly the same signals
ThO	Th metal & $Al(OH)_3$ powder ThO_2 ceramic	Both methods produce roughly the same signals
K	KCl pressed powder	Used as absolute frequency reference for RaF (Chapter 5.6)
He*	Yb + $Yb(OH)_3$ combined powder	Metastable helium observed by driving the $2^3S_1 \rightarrow 2^3P_{0,1,2}$ lines

Table 4.2: List of all species produced and studied in the Minifridge as well as the targets used to produce them. [a]Bolded recipes denote the most successful, in the cases where multiple were tested. A "&" indicates dual-ablated targets while "+" indicates combined pressed powders.



Figure 4.16: Example target plates. Target materials shown include: hydraulic-pressed powders, pure metals, pieces of sputtering targets, dried radioisotope solutions on gold foil, and radium-painted watch hands, all of which are described throughout this thesis. Details about the radioactive targetry are given in 4.3.

angles and directions, limited only by the optical access into the cryostat.

In the current configuration, which has remained relatively unchanged for the last three years, probe lasers travel through the 3.5 inch long "axial" bore, perpendicular to the direction of ablation. This includes atomic or molecular absorption probe lasers, whose transmissions are measured on an amplified photodiode outside the cryostat to determine the optical depth and subsequently the atom or molecule number in the cell. We chose this longer axial bore as the probe direction as optical depth scales with the length of the atomic or molecular cloud, although in previous iterations of the cell we sent the absorption probes down the path parallel to the ablation beams (which we now use for fluorescence). Optical absorption of weaker features can be enhanced by

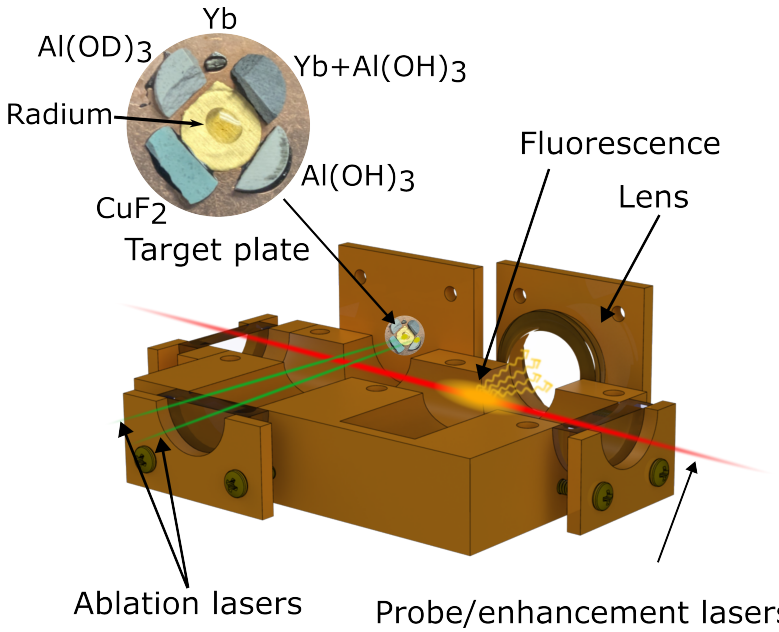


Figure 4.17: Cut-away diagram showing the methods of optical spectroscopy performed inside a Minifridge cell. Probe lasers may be used for absorption or fluorescence measurements. Reproduced from [84].

multi-passing these beams through the cell, or by employing frequency-modulation absorption spectroscopy [108].

When working with trace isotopes, an atomic or molecular absorption probe parked on a known line provides a useful normalization tool to account for the shot-to-shot production fluctuations. We also send the chemical enhancement laser through this bore, where it is expanded to fill as much of the diameter as possible without adding to the light scatter or heating the cell. A mirror on the other side of the cryostat retroreflects this beam to increase the total intensity of enhancement light, maximizing the population in the metastable excited state. This enhancement light excites the same ground state atoms that we address with our atomic absorption probe, so we offset the atomic probe as much as possible in the cell to mitigate optical pumping effects on our absorption signal.

Also through this axial bore, we send our tunable pulsed or continuous-wave (CW) molecule probe lasers to generate laser-induced fluorescence. Detection of the fluorescence occurs through the light collection pathway, which is parallel to the ablation bore but offset by ≈ 4 cm. A 25.4 mm focal length lens mounted to the cell roughly collimates the molecular fluorescence as it exits the cell and then the cryostat. This fluorescence is optically filtered to cut out the light from nonresonant ablation glow (or

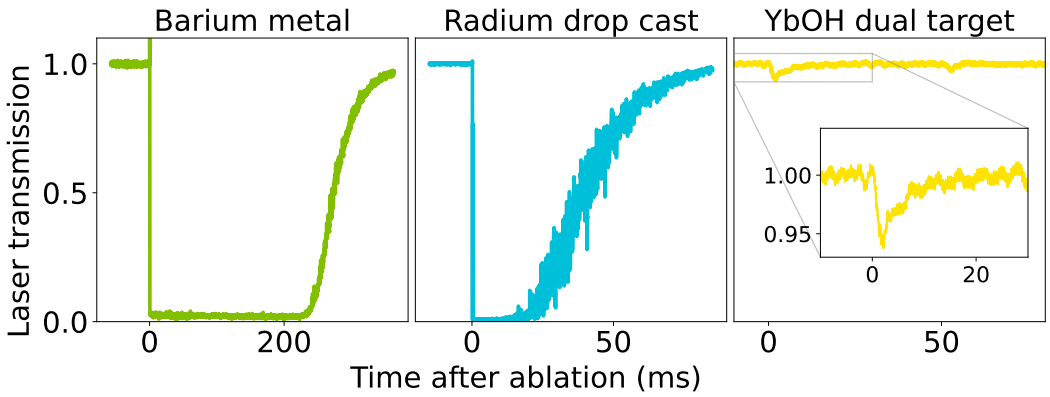


Figure 4.18: Representative direct DC absorption plots labeled by the type of ablation target. For the atomic signals, the $^1S_0 \rightarrow {}^1P_1$ transition was driven, at 553 nm for barium and 483 nm for radium. YbOH absorption was performed on the main $\tilde{A}\,^2\Pi_{1/2} - \tilde{X}\,^2\Sigma^+$ line at 577 nm. Each plot color is roughly the color of the probe laser, as seen by eye. Note the differences in time scales—we achieved full attenuation of a barium $^1P_1$ probe laser for nearly one third of a second, visible clearly by eye as an extinction of the beam.

unwanted spontaneous decays) and re-focused onto a photomultiplier tube (PMT) or imaged on a camera.

For most of this work we opted to record fluorescence signals on PMTs because of the advantages offered by their fast time resolution. Since we are collecting fluorescence that is close to the source of the laser ablation—both in space and time—there is a significant amount of background light. As mentioned before, we partially mitigate this by painting the opposite side of the light collection bore with an antireflective coating. When possible, we also try to observe atomic or molecule fluorescence that is at a different wavelength than the transition we are driving, allowing us to optically filter out the light from the probe lasers as well as the broadband light produced in the ablation plasma. This filtering is not perfect, and there is still a significant amount of light leakage that makes it to the PMT. The timing resolution of the PMT allows us to introduce "dead time" in the probe laser sequence, where we are able to interpolate the signal contamination due to ablation glow and subtract it away on a shot-by-shot basis. This methodology was crucial to observing trace molecule signals, and is described in detail in Chapter 5.3. Using a PMT also allows us to temporally interleave multiple probe beams, using one as a normalization signal when our molecule production is too weak to normalize on an absorption probe.

We have tested fluorescence detection with other methods, albeit to a much lesser extent. While it foregoes the timing resolution offered by a PMT, a camera allows for

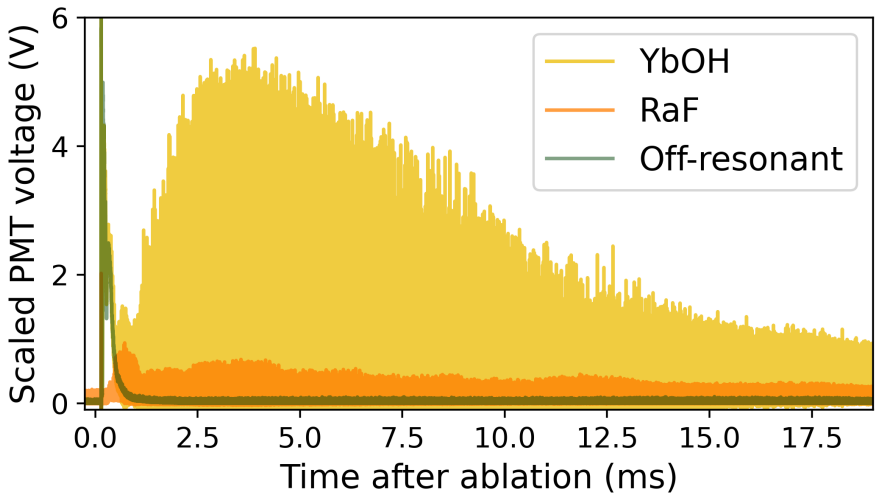


Figure 4.19: Representative fluorescence traces labeled by the molecule being studied. Heights are scaled to account for the different PMT gains used for different wavelengths. For all traces, we were exciting the molecules with our high-repetition rate pulsed dye laser at 50 kHz. To make YbOH, we ablated both ytterbium metal and $Al(OH)_3$ pressed powder, and did not use any chemical enhancement light. We excited the main line at 577 nm and detected the off-diagonal decay to the Yb − O stretch at 595 nm. For RaF, we produced molecules by co-ablation of the radium drop cast target with a CuF_2 pressed powder target in the presence of 1 W of chemical enhancement. For this fluorescence data, we drove the $C\,^2\Sigma^+(0) \leftarrow X\,^2\Sigma^+(0)$ transition at 602 nm and detected the decays down to $X\,^2\Sigma^+(1)$ at 618 nm. The final (green) trace shows the signal when our laser is off resonance of the YbOH transition, where the early time signal is still visible due to ablation glow. Note that the pre-ablation background is greater for the RaF trace than for the YbOH and off-resonant trace; this is due to the increased light leakage of the pulsed dye laser through the PMT filters at the RaF wavelengths.

spatial discrimination of the fluorescence, as we know the desired signal should overlap with the location of the probe laser beam. Using a sCMOS camera[28] we observed resonant fluorescence signals of BaOH that correlated with chemical enhancement (Figure 4.20). We attempted this with an EMCCD[29] as well, to somewhat less success. Ultimately, for trace molecules, we were unable to get camera detection to work as we had no means of preventing the background light from complicating the signals. The camera data is also not robust against short-lived fluorescence originating from laser scatter off of macroscopic chunks of ablation detritus, an example of which is shown in Figure 4.21. On a PMT, these bright excursions typically last only a handful of microseconds, allowing for their rejection as outliers.

[28] Thorlabs CS2100M-USB

[29] Hamamatsu C9100-13

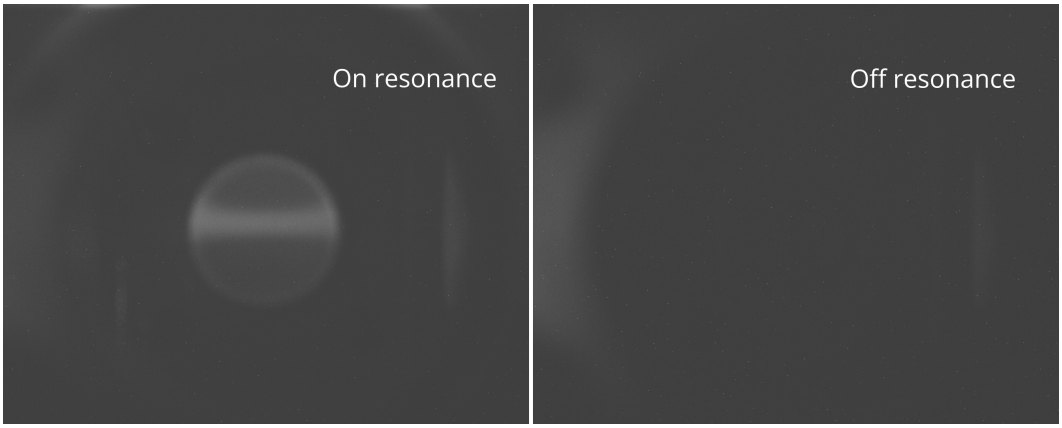


Figure 4.20: Laser-induced fluorescence of BaOH observed by a sCMOS camera pointed at the light collection window. Gain has been increased in software to make the fluorescence visible. We probed the $\tilde{A}^2\Pi_{3/2} \leftarrow \tilde{X}\,^2\Sigma^+$ main line at 12043.493 cm^{-1} (830 nm) and observed the decay between these same two states. Optical filtering cut out most of the ablation fluorescence, as demonstrated in the off resonant image.

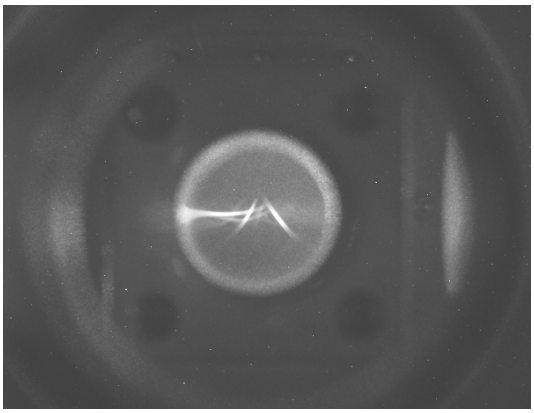


Figure 4.21: Camera image for a single data shot showing bright streaks of laser scatter off of macroscopic ablation dust. The molecule fluorescence band is visible like in Figure 4.20, but is overwhelmed by the nonresonant laser scatter. Off-diagonal detection with appropriate optical filtering would fix this issue.

In an attempt to better understand the ablation glow, and to configure the Minifridge to perform dispersed laser-induced fluorescence, we also imaged the fluorescence plume on a fiber-coupled spectrometer[30]. To get the fluorescence into the fiber, we set up a lens with a focal length matched to the mode field diameter of the fiber and placed this setup right up against the window of the Minifridge. In this (admittely quite unsophisticated) configuration, we were able to observe off-diagonal $\tilde{A}^2\Pi_{1/2}(000) \rightarrow \tilde{X}\,^2\Sigma^+(100)$ decays in YbOH at 595 nm by probing the main line with a broadband linear cavity dye laser[31]. Observing this decay required running with the largest slit available on the spectrometer to admit the most light possible, which reduced the wavelength resolution. However, the peak was still visible (Figure 4.22), meaning this test did succeed as a proof-of-principle, albeit requiring many improvements to make

[30] StellarNet SILVER-Nova X-Slit zAP-1 TEC Spectrometer
[31] Coherent 599

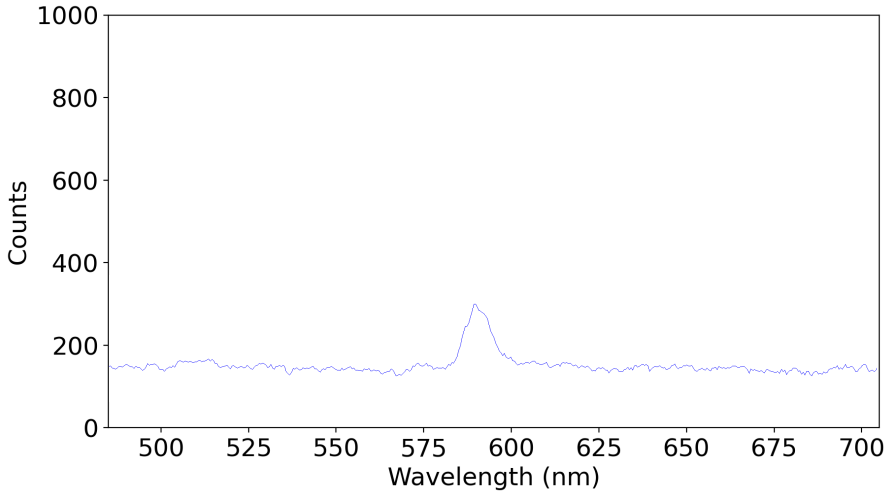


Figure 4.22: Off-diagonal decay in YbOH observed by imaging on a fiber-coupled spectrometer. The strong 577 nm probe light was optically filtered out, allowing for detection of photons from the decay to the ground state Yb – O stretch vibration at 595 nm.

it useful for precise measurements. With these improvements, this could be a simple method for measuring vibrational branching ratios, of particular relevance for laser cooling experiments (see Chapter 6).

Without driving any transitions, we also looked at the light produced in the ablation process to see if we could gain any insights as to what comprises this glow. Data was taken by ablating the targets at 5.31 Hz while integrating the fluorescence signals for 2 s and averaging. Unsurprisingly, there were a lot of peaks corresponding to strong atomic transitions, but also some for molecules (see Figure 4.23). For YbOH, we observed the main line decay fluorescence at 577 nm which correlated with blocking/unblocking the OH and Yb ablation pathways, although this data is not shown.

As to what causes this ablation fluorescence, we have a few theories. We know that the hot plasma produces highly excited atoms [110], and reactions between these atoms will produce excited state molecules which decay via chemiluminescence. However, as we see in our PMT data, this glow lasts for a significantly longer time than the lifetime of the strong molecular and atomic excited states. We believe that there is some mechanism which leads to a delayed excitation of the ablation products, perhaps due to collisional excitation from long-lived excited state atoms. For example, laser absorption measurements in Minifridge have observed helium buffer gas in its metastable $^3S_1$ state after ablation [111], which has a radiative decay lifetime of 7800 s [112]. This metastable state is also extremely energetic at nearly 20 eV above

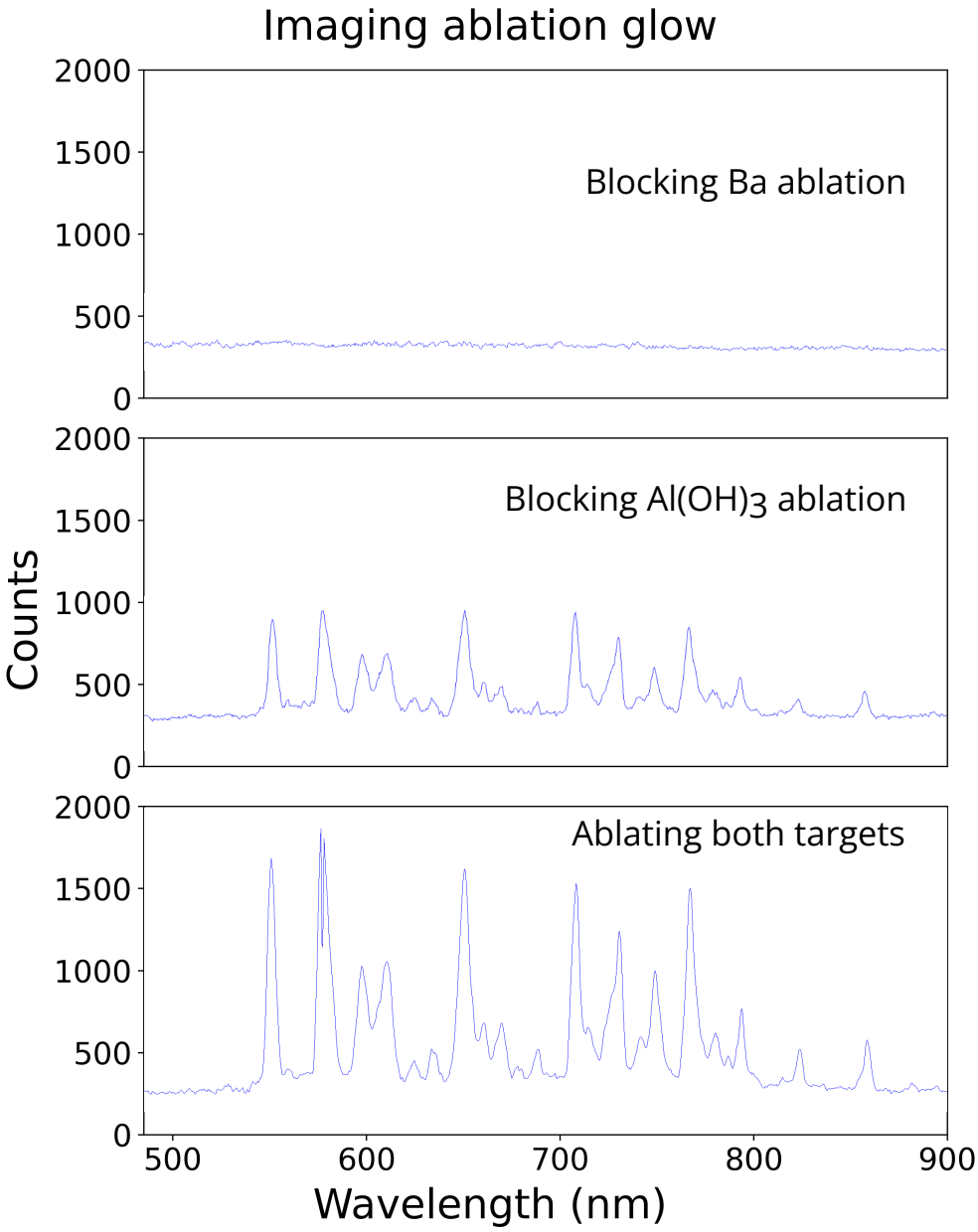


Figure 4.23: Dispersing the fluorescence from ablation on a fiber-coupled spectrometer. Data was taken in a few configurations of BaOH ablation. Top: Ablating the $Al(OH)_3$ pressed powder co-target but not the barium metal. Middle: Ablating the barium metal but not the co-target. Bottom: Ablating both targets. Broad peaks are found at a significant portion of the visibile spectrum, hinting at the origin of the nonresonant "glow" that we observe. A 532 nm longpass filter was used in front of the fiber coupling side of the spectrometer to filter out the intense ablation laser light. The observed lines correlate quite well with the strong transitions in neutral barium—see [109]. Many of these lines originate from transitions between two excited states, rather than through the ground state.

the ground state, corresponding to a photon wavelength of 62.6 nm. Work by others in the group have shown some correlation between the ablation glow lifetime and metastable helium decay rate [113], although not rigorously[32]. As for the various peaks in this dispersed ablation fluorescence measurement, we did not attempt a systematic deconvolution, opening up the potential for this as future work.

[32] By decay rate, I mean the decay rate of the helium absorption signal, not the radiative decay rate due to spontaneous emission.

Chapter

V

Production and spectroscopy of radium-containing molecules

Even though heavy, radioactive nuclei have previously been identified as extremely promising candidates for certain BSM physics searches [3], no experiment has been constructed to benefit from their enhanced sensitivity. This is understandable when considering the additional complications that come with these species; many radionuclides of interest can only be acquired or handled in miniscule quantities relative to what we use for stable molecules. As a reference, radium-226 is distributed in units of $\sim$ 1 mg, and our permitting allows us to load $\approx$ 50 μg into our apparatus at any given time[1]. Contrast this with the values for YbOH, where our targets may have hundreds of milligrams of Yb starting material and yet we still struggle to resolve certain signals (see Figure 5.1 for a visual comparison). Additionally, in a beam, extracting the molecules from the cell contaminates the entire system, rendering it unsafe to open without sophisticated safety protocols. One could conceive of an experiment that loads a lot of material at once with the goal of never opening again—this would only be plausible if it is certain that the setup will never need to change (wishful thinking), the molecule has already been fully characterized (none of them have), and the

[1]It is true that this permitted quantity is a somewhat artificial limitation that could be overcome with additional regulatory approval. However, for an experiment such as ours, this value tends to be similar across similar institutions.

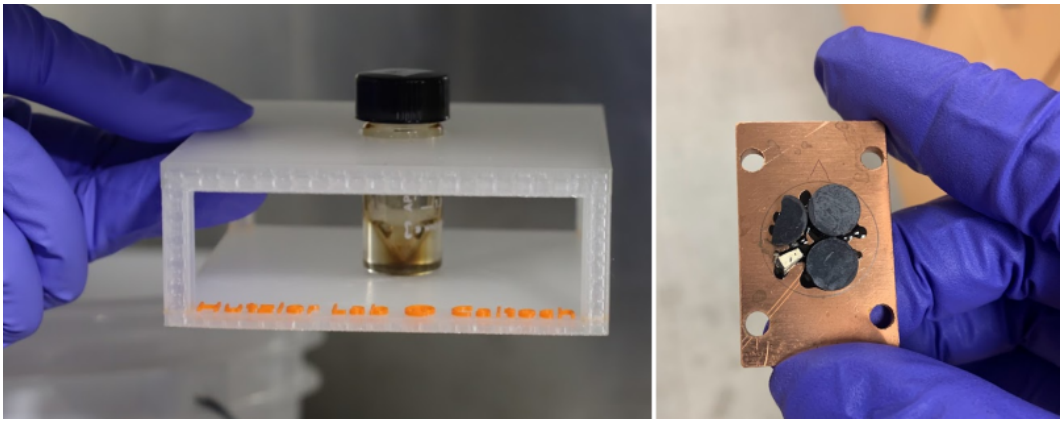


Figure 5.1: Visual comparison of the quantities of material we have available to us. Left: photo of the vial containing 1 mg of radium-226 in the form of $^{226}Ra(NO_3)_2$ salt, about 20 – 100 times more material than we use in a single cell. The white speck is smaller than a grain of fine sand and is resting in the tip of the v-vial. Radiation damage has turned the glass brown, obscuring the material. Right: target plate for one of our other sources showing three black Yb + $Yb(OH)_3$ pressed powder targets and a chunk of pure ytterbium metal. Total mass of ytterbium on this singular target plate is just under 1 g—over 1000 times more than the amount of radium we distributed across 30 cells. Photos taken by Phelan Yu and Arian Jadbabaie.

materials can even be acquired in that quantity (unsafe, expensive, and impractical).

Rather than overcome these challenges, recent efforts in the EDM search space have opted to push the sensitivity limits using stable species. Laser slowing of a highly EDM-sensitive molecule was recently shown [114], with optical trapping surely soon to follow. Moderately heavy polyatomic molecules have been loaded into a magneto-optical trap [115], where the extra coherence time offered by the trap may make these systems competitive in certain BSM physics searches even though they lack the extreme intrinsic sensitivity offered by ultraheavy molecules. A pathfinder experiment performed an EDM measurement protocol on polyatomic molecules loaded into an optical dipole trap [74], showing how a real measurement might look once the proper EDM-sensitive species can be trapped. And clever tricks have been shown that leverage the complex molecular structure to engineer transitions that are insensitive to external electromagnetic fields while still maintaining their sensitivity to new physics [116].

One common thread linking all of these recent developments is that they can also be implemented on radioactive molecules. So, once we solve the practical challenges of working with these trace isotopes, all of the breakthroughs made to push the sensitivity with stable species will be directly applicable to the more intrinsically sensitive radioactive ones.

Around a year into the life of the Minifridge we came to the realization that the closed cell design was uniquely suited to handle radioactive materials. In the radiation community, there is a significant distinction between working with radioactive sources that are open versus sealed; i.e., sources where a user could come in contact with the radionuclides during normal use and ones where part of the apparatus would need to be destroyed in order to access the radioactive material. In the sealed case the risk of contamination to users and to the environment is significantly reduced[2], relaxing the most stringent safety and regulatory challenges. As such, sealed sources can generally contain much higher activities and be handled in environments that are not necessarily dedicated to radiation work, making the regulatory approval and licensing process much simpler. While it is certainly not impossible to work with an open radioactive source, they generally require much more advanced safety measures that complicate the experimental protocol.

For virtually all of its runtime our cell is technically a sealed source, meaning the barriers to overcome in order to study radioactive molecules were significantly less overwhelming. It was beginning to seem possible that incorporating these understudied radioisotopes in our experimental protocol was not just possible, but was within reach. Through discussions with Caltech's radiation safety officers we concluded that as long as we could install the radioactive material in the cell safely—and guarantee that it stays there—then it should be relatively straightforward to study these materials similarly to the stable molecules we had already produced. Of course, we would still have to contend with the unique challenges that came with the limited material availability, but this is part of what made the project interesting.

Immediately the focus turned to radium. As an alkaline earth element, it bonds to form the same types of molecules that our group and close collaborators have already spent many years studying, which are of particular interest in the fields of BSM searches and laser cooling [117]. Furthermore, while sourcing radium-226 is nontrivial, it is still significantly easier than some more exotic radioisotopes of interest to the community, such as radium-225 [118], francium-223 [119], or protactinium-229 [120]. As it is found naturally as the main product of uranium-238 decay, and because it has a relatively long half-life of 1600 years, radium-226 can be acquired in usable quantities without having to rely on dedicated production at collider facilities or in-situ extraction from parent nuclides. Radium-226 monohydroxide (^{226}RaOH)

[2]Of course, this is assuming the source has been designed to properly contain the radioactive material, otherwise it would not be considered "sealed." This distinction is especially important for radium-226, which decays into radon-222, a radioactive noble gas

in particular combines the heavy (but obtainable) nucleus with a molecular structure that enables parity doublets and laser cooling simultaneously [44].

With ^{226}RaOH identified as the target species, the first goal was simply to prove that we could make these molecules inside our cryogenic buffer gas cell. Traditionally, demonstrating the production of a specific molecule would occur via some kind of mass-spectrometric measurement. These techniques are unavailable to us; they either rely on motional measurements of ions in a trap or by sending our molecules to a mass spectrometer, which would require a separate, dedicated apparatus. Instead, we need to verify that we have indeed made the molecules we claim to have made through spectroscopic means, while simultaneously contending with low quantities of starting material and lack of any pre-existing spectroscopy. This chapter details the technical changes that enabled this and the results that followed.

All of the radium molecular data was taken alongside Phelan Yu, as the experiment required more than two hands (and one brain) to operate. We both contributed to the developments that enabled this project to work; the plots herein are my own unless otherwise noted, but the underlying data is very much shared between us.

5.1 Radioactive remodel

Before starting work with radium, we developed a Standard Operating Procedure (SOP) to submit to Caltech's radiation safety committee for approval. This SOP details our experimental protocol and justifies many of the design features. An example version of this type of document modeled after our own is provided in Appendix A for reference.

The main procedural modifications were to the installation and removal of ablation targets. Previously, the cell would remain in place while we unmounted a spent target plate and attached a fresh one. As a consequence of the ablation process, dust from the various reagent targets collects at the bottom of the cell and would often spill a little into the bottom of the chamber during this removal process, or blow around slightly due to room air currents. While previous dusts could simply be cleaned up afterwards, it should go without saying why this is unacceptable when working with radium. Dusts are among the most dangerous forms of radioactive material as they are incredibly difficult to localize and can travel significant distances through the air or by contact spreading[3]. Unfortunately, without developing a way of recycling the

[3] Even if this dust were not an issue, say because it was guaranteed to be stuck within the cell, repeated installation of fresh targets would cause a buildup of spent radioactive material inside the cell that would quickly cause us to exceed our gamma emission limits.

ablated target material within a closed cell, spent targets still need to be removed and new ones need to be added.

Our solution was simple: rather than replace the target plate on the cell, just replace the entire cell. With the target plate still mounted, any radioactive dust remains fully contained and the whole cell can be disposed of as radioactive waste. While somewhat wasteful from a materials standpoint, as the cell is made of a significant amount of optics[4] and custom-machined copper, this was by far the simplest way to avoid contaminating anywhere outside of the cell.

With this new disposal method in place, there are now only three times in the experimental protocol where the apparatus may be considered an "open source": the installation and removal of the cell inside the Minifridge, when the gas lines between the cell and the gas manifold are connected and disconnected; and the mounting of the radioactive target plate onto the cell, which will be discussed in the following section on ablation targets. Regarding the former, this would not normally be a problem as the risk of dust traveling upwards through a long, thin, bending gas line is practically zero. Unfortunately, working with radium brings along an entirely new consideration in the form of radon. The first decay product of radium-226, radon-222 is a radioactive noble gas with a half life of 3.8 days. It is crucial to prevent the spread of radon into the lab, and desirable to restrict it to certain parts of the experiment to avoid contaminating the gas lines.

We prevent the unwanted release of radon when opening the gas lines by using a cold trap. The helium fill line connected to the cell features a dip that extends a few centimeters downward right next to the cell. Before we need to disconnect the gas lines and expose them to room air, we submerge this segment in liquid nitrogen. As the copper tubing thermalizes with the 77 K liquid, any radon gas freezes to the inner walls, as the freezing point of radon is roughly 200 K. This process traps the radon (as well as most atmospheric gases) in the cold trap region of the gas lines. After waiting for a few minutes to allow the radon sufficient time to come into contact with cold tubing and freeze out, we disconnect the gas lines and perform any necessary operations. Before warming up, we always ensure that the lines have been re-sealed, either with a VCR plug or by connecting to the rest of the gas manifold.

It is worth contextualizing to what level the spread of radon is a concern in this experiment. As mentioned in Chapter 3.3, radon is present virtually everywhere as

[4] Even in normal operation, the various optics on the cell would need to be replaced periodically as they become caked with ablation dust.

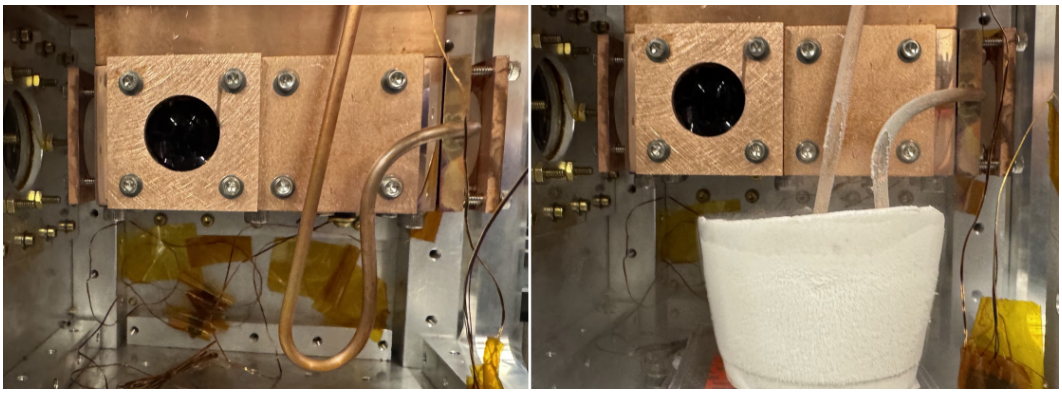


Figure 5.2: Photos of the cold trap region of the cell gas lines. A styrofoam cup contains the liquid nitrogen.

a background gas, with the average level inside US homes being 1.3 pCi/L and the outdoor level being 0.4 pCi/L [82]. Common monitoring equipment struggles to read values below 0.1 pCi/L—if we are releasing significantly below this limit, it would contribute negligibly to the background radon level. We are *not* advocating for the release of radioactive materials into the environment, but rather examining whether our release amounts would even be detectable above this already existing background level.

The following briefly summarizes a discussion from Appendix A. Starting from a 50 μCi sample of radium-226, after some time the steady-state radon-222 activity will also peak at 50 μCi, as it cannot deplete more quickly than it is supplied. If we assume a complete, instantaneous release of this radon into our ~5 m^3 volume optics table enclosure, this results in a concentration of 10 nCi/L, which would be reduced to below the background level in ~30 minutes of airflow. If, instead, the radon releases uniformly into the entire room rather than just the optics table, the concentration would reach 400 pCi/L. Both of these values, while high, are not catastrophic, especially since they refer to instantaneous concentrations. With typical HVAC conditions in the lab, even a fully open 50 μCi source of radium-226 would only result in a radon concentration of 1 pCi/L—a value indistinguishable from background[5]. Still, to keep radiation levels as low as reasonably achievable, we engineered our protocols to prevent any release of radon from occurring.

The room-temperature side of the gas handling manifold also required an overhaul in order to safely accommodate radon. The first line of defense was to trap the

[5]It is worth noting that in the event of an HVAC failure, the loss of air flow could result in local concetrations of radon which are greater than these values.

radon wherever possible, so we included activated charcoal filters in line with the gas manifold[6]. These filters are capable of catching up to 90% of radon at room temperature and 99% at 0°C [121] if we decide to cool the filters at any point in the future[7]. To mitigate the negligible amount of radon that manages to make it to the vacuum pump, we connected the exhaust port of the vacuum system to a building exhaust rather than venting into the lab. In the event of a power outage we included a normally-closed valve[8] that automatically shuts when its power is cut, as the loss of vacuum and cryopumping could otherwise cause unwanted gas flows in the system, spreading radium and possibly dust. Much like for the cell, the room-temperature side also has a cold trap region, where we can submerge the gas lines in liquid nitrogen while pumping out or filling helium to prevent the flow of radon in either direction.

One thing to note is that we do not employ any additional radiation shielding on the apparatus other than what is achieved by the cryostat itself. The copper cell blocks all alpha particles and virtually all beta particles, while the remaining betas are blocked completely by the vacuum chamber. Gamma radiation, being much tougher to attenuate, is able to make it out of the cryostat. When loading 50 μCi of radium-226 (and letting the daughters build up over the course of a week) we measure 0.1 – 0.2 mrem/hour when holding the Geiger-Müller probe right up against the chamber. While this is a non-negligible dose rate, we very rarely work with our hands this close to the apparatus. Thanks to the inverse square law, the measured dose just one meter away—which is still closer than we typically work—is indistinguishable above background levels. Thus, we decided to avoid engineering any cumbersome lead shielding.

Radiation monitoring and personal dose

To confirm that the system is not releasing unexpected radon into the environment, we have two radon monitoring devices constantly running[9]. One of these sits right next to the cryostat on the optics table and is WiFi enabled to allow remote monitoring. The other is in the corner of the room near the experimental control workstation as a "just in case" detector. Generally, these systems measure a value that fluctuates with the background level between 0 and 1 pCi/L and do not read higher when we

[6] Ancorp VSRC-250-QF25-O for the KF gas lines and NuPure 00040-A-VR4-He-Xl for the VCR gas lines

[7] There was the thought to have an actual mini fridge on the table to cool the charcoal filters, where on the sides of this fridge we could drill small holes to allow the gas lines to pass in and out.

[8] Part CV25-K2K2-ECLVV-24DC from MKS

[9] RadonEye Pro and RadonEye RD200.

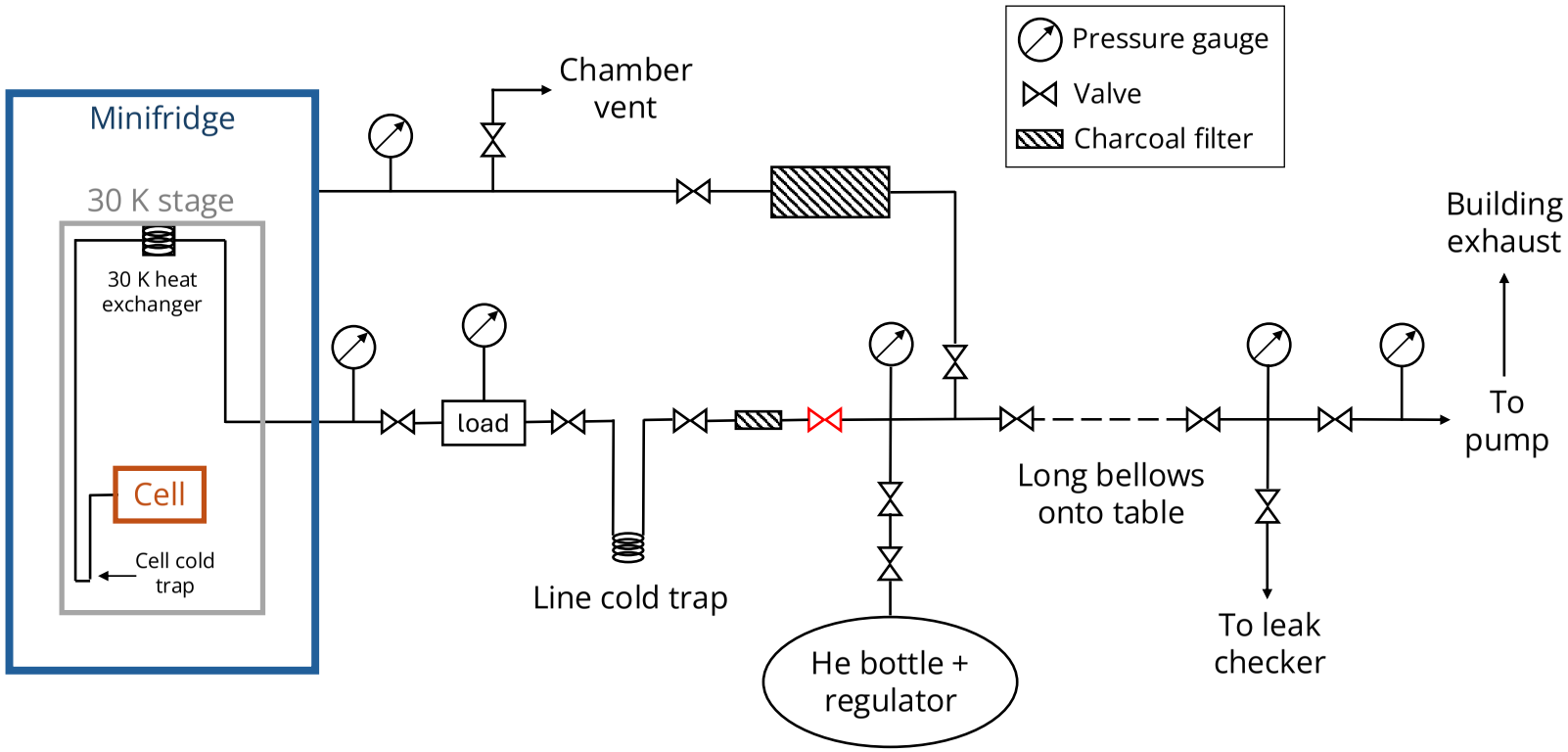


Figure 5.3: Updated gas handling manifold for accommodating radioactive material. The red highlighted valve is the normally closed valve. "load" is the load lock volume. Figure inspired by the one made by Nick Hutzler for the radium SOP.

have radium properly loaded in the cryostat. We know they work, however; during an instance where an ablation laser was incorrectly focused onto a cell window, causing it to crack, the table reading rose to around 3 pCi/L after the chamber was opened. This value lowered quickly as the lab air turned over, and the "just in case" room monitor never registered a value above background.

Dosimeters are worn by all personnel when handling radium or a cell containing radium. This includes one ring dosimeter worn on the dominant hand and one full body dosimeter clipped somewhere near the chest area. As we have moved to handling larger quantities, the person performing the target preparation has been wearing an additional ring dosimeter on their non-dominant hand as well. Each calendar quarter these dosimeters are sent for analysis and exchanged for new ones. To put into perspective the types of doses we have experienced, at our highest use rate of radium we were fabricating around 10 cells per quarter with an average quantity of 30 μCi per cell[10]. We also received a shipment of 1 mCi which we aliquoted into a number of smaller samples[11]. I performed the vast majority of the handling during this time, and my annual full body dose was measured to be 11 mrem, with my hand dose measured at 83 mrem. These are well within the annual dose limits for radiation workers, with the full body dose likely being a measurement of the background level rather than any additional dose received from the radium.

5.2 Radium ablation targets

At the onset of this project, we were confident we knew how to solve every challenge that came with these novel substances except for one: the ablation targets. Our initial permit allowed us to install 10 μCi of radium-226 at a time, or around 10,000 times less material than we would use if this were a stable element such as ytterbium. On top of this, we restricted ourselves to only manipulating the radium in a liquid solution, to avoid the dust problem mentioned above and because a 10 μg sample of solid radium is so physically small as to be impractical to handle precisely. This required developing a target fabrication protocol that yielded efficient molecule production while still adhering to our safety and permitting limitations regarding handling.

Another restriction we faced was our inability to chemically convert the sample to different forms; as non-experts, we did not feel comfortable performing radiochemistry on these dangerous and limited materials. Any manipulation of the radium solution

[10] Five cells of 20 μCi, two with 25 μCi, and three with 50 μCi

[11] This work was performed with the help and guidance of Prof. Alyssa Gaiser from MSU/FRIB, who also directed the aliquoting protocols.

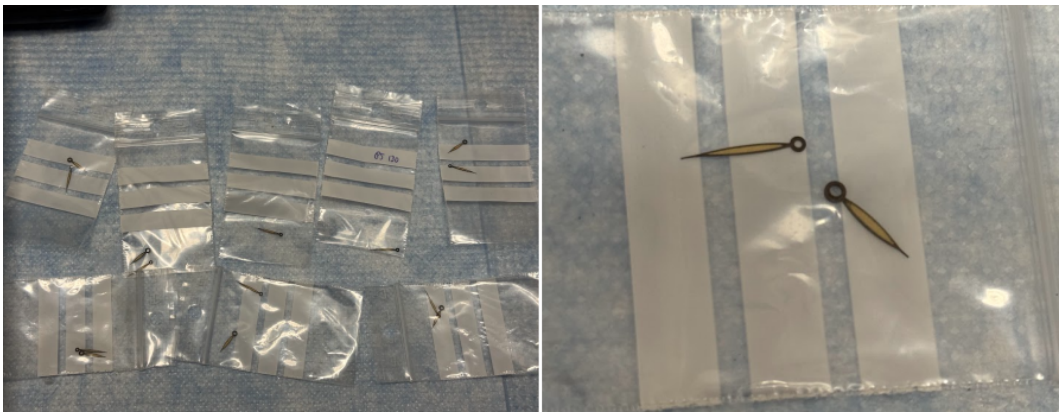


Figure 5.4: Photos of some of the radium-painted watch hands. Note that they are no longer glowing not because the radium has decayed, but rather because the crystal structure of the zinc sulfide phosphor has degraded after being bombarded by radiation for so many years.

thus needed to be a physical process, such as evaporation. We were not going in blind, thankfully, as we had inspiration from the work in Andrew Jayich's lab at UCSB, where they evaporated a solution of $RaCl_2$ to produce radium ions via laser ablation [122]. However, ion experiments only need to successfully produce a handful of their species of interest during ablation, whereas if we wanted any chance of seeing our molecules spectroscopically we would need at least many millions.

The following sections detail the different ways we have successfully made radium ablation targets as well as the lessons learned in the development process.

Watch hands

A few weeks prior to our first delivery of technical-grade radium, we ordered around 50 antique watch hands from a watch repair vendor online. These watch hands were painted with a radioluminescent paint based on the decays of radium-226, popular for creating glow-in-the-dark watches and military dials up until the 1960's[12]. The paint was applied to a paper-like material, held in place by a metal frame. A Geiger counter confirmed that they were indeed radioactive, with the activity of each watch hand around 10 nCi[13].

We had already performed a dry run of the cell installation and removal procedure, but before we cracked open our first glass ampule of expensive radium solution we

[12] This is the same paint notorious for causing the disease and deaths of the "radium girls" who worked in the factories that painted the dials.

[13] The hour hands, which are thicker, are about twice as active as the minute hands.

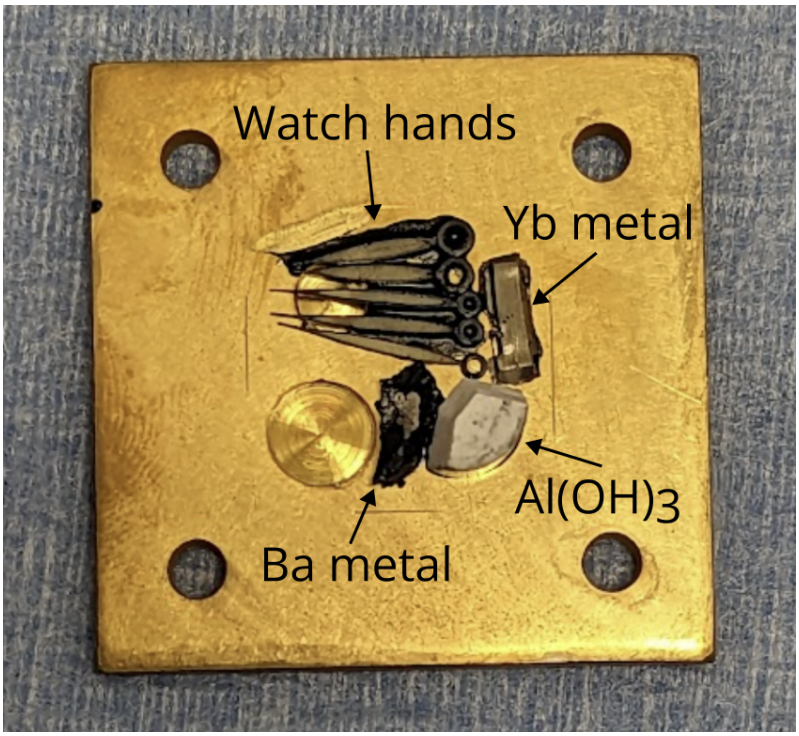


Figure 5.5: The first ever radium target plate, showing the five radium-painted watch hands epoxied to the plate with Stycast. Before attaching the targets, we electroplated the copper target plate with pure gold (see Section 5.2 for discussion). We also pocketed out two wells, seen on the bottom left and underneath the watch hands. These wells were unused.

wanted to test on some lower-stakes material. These watch hands were perfect for this, as they were cheap, the radium was already firmly embedded in the luminous paint, and their individual activies were low enough that the likelihood of a catastrophic contamination event was minimal. Still, they produced a detectable amount of radon, making them useful for diagnostic purposes, and hopefully had enough radium to observe atomic absorption signals. Our first radium target is shown in Figure 5.5.

At the time we had no means of producing 483 nm light to drive the strong ${}^1S_0 \rightarrow {}^1P_1$ transition. Instead, we used a Ti:Sapphire laser[14] at 714 nm to probe the weaker ${}^1S_0 \rightarrow {}^3P_1$ line, benefitting from the fact that the large spin-orbit coupling in radium makes this transition much stronger than the analogous one in the lighter alkaline earth elements.

We observed around 50 instances of weak absorption signal over the course of 2000 ablation shots. The largest absorption dips we measured on our photodiode were

[14]Coherent MBR-110

around 0.0015 V on a background level of 0.3 V, corresponding to an absorption fraction of 0.5%. Given a Doppler-limited lineshape, we can convert this absorption fraction to a peak atom density [123]:

$$\begin{aligned} n_{peak} &= \frac{1}{\sigma l} \ln\left(\frac{P_0}{P_{peak}}\right) \\ &= \frac{\Gamma_D}{\sigma_0 \gamma}\sqrt{\frac{8}{\pi}}\frac{1}{l}\ln\left(\frac{P_0}{P_{peak}}\right) \\ &\approx 3 \times 10^8 \text{ cm}^{-3}\,, \end{aligned} \tag{5.1}$$

where the radiative width for the $^3P_1$ transition is $\gamma = 1/(2\pi \times 422 \text{ ns})$ [124], the resonant cross section is $\sigma_0 = \lambda^2/2\pi = (714 \text{ nm})^2/2\pi$, the background laser power was $P_0 \approx 0.3$ mW, the power at peak atom density was $P_{peak} \approx 0.2985$ mW, the cell length is $l = 3.5$ in, and we assumed[15] a Doppler width $\Gamma_D \approx 100$ MHz. If we assume a uniform distribution of radium atoms throughout the cell volume, this corresponds to roughly 1.25×10^{10} atoms produced on a good ablation shot. Given an approximate activity inside the cell of 50 nCi $\approx 10^{14}$ atoms, these yields are believable but relatively inefficient compared to other target materials.

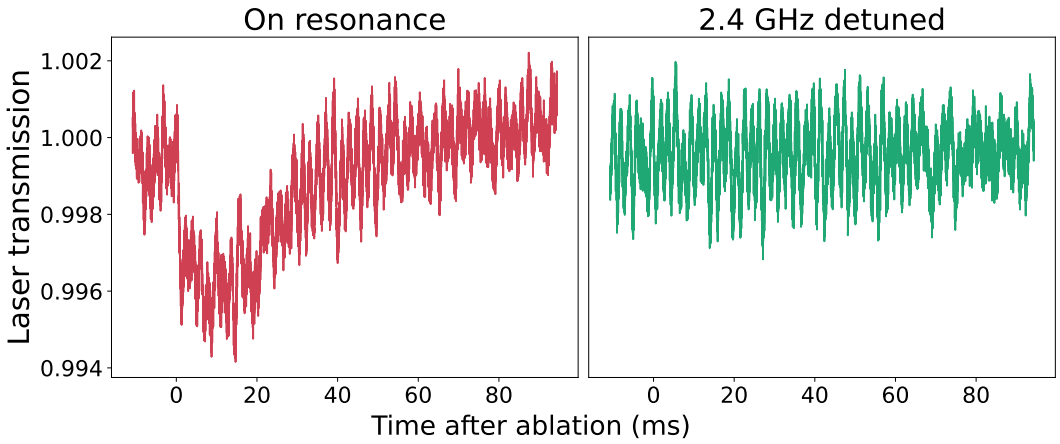


Figure 5.6: Early traces showing resonant absorption of the $^1S_0 \rightarrow {}^3P_1$ transition in ^{226}Ra while ablating radium-painted watch hands. At most, we were able to observe around 0.5% absorption of the 13999.357 cm^{-1} laser light.

For this data, the ablation energy was quite high at around 40 mJ/pulse; we believe this elevated pulse energy was needed to properly vaporize the paint off of the paper. At lower energies it seemed like the ablation was just poking holes in the paper, potentially blowing it out of the frame but not vaporizing it (see Figure 5.7).

[15] This Doppler width is pretty characteristic for these buffer gas cells, although was not explicitly measured at the time. Recent measurements indicate that our Doppler widths are somewhere around 70 MHz, although this is with an updated cell geometry.

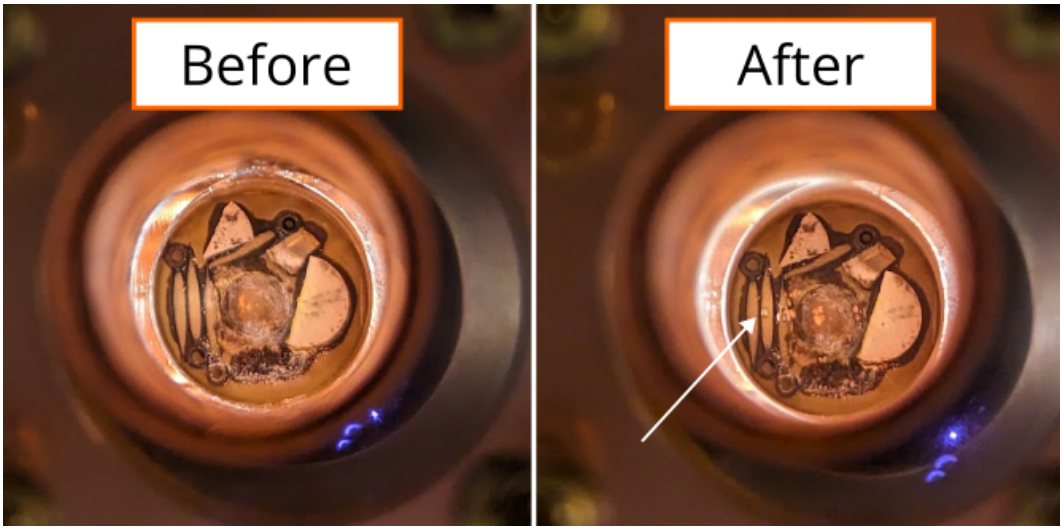


Figure 5.7: Before and after photos showing the ablation of the radium-painted watch hands. Note that the layout is different as this is from the second radium target. The arrow points out a part of the watch hand that appears to have been completely blown out of the frame, potentially contributing to the inconsistent atom signal.

Drop casting

We deposit the radium atoms from our liquid solutions onto our target plate via a method called drop casting—for our purposes, this is just a technical way of saying "evaporation." Using a pipette, we place individual droplets of our radium solution onto a heated target plate and allow them to dry, leaving behind the radium atoms while the volatile solvent evaporates away. The target plate is generally heated to 5 – 10 °C below the boiling point of the solution to encourage rapid evaporation while preventing bubbling, which may splatter radioactive material. In order to constrain the solute to a small area, we use drops between 2 – 5 µl. With larger volumes there is a chance for the droplet surface tension to break, spilling the material in unpredictable ways and depositing material in undesirable locations, in extreme cases even potentially rendering the target plate unusable. It takes on average 10 – 30 seconds for a droplet to evaporate, trending longer as the target builds up on the surface and stops conducting heat as effectively as the bare copper.

For our first few targets, we drop casted solutions of radium chloride ($RaCl_2$) that we acquired from the radioisotope supplier Eckert & Ziegler[16]. These arrived as pre-portioned glass ampules of 10 µCi each, initially in a volume of 5 ml that we later negotiated down to 0.5 ml. This volume reduction was critical for quality-of-life—depositing that first sample of 5 ml in drops of 2 ul took me around 12 hours

[16]Catalog number 8226.

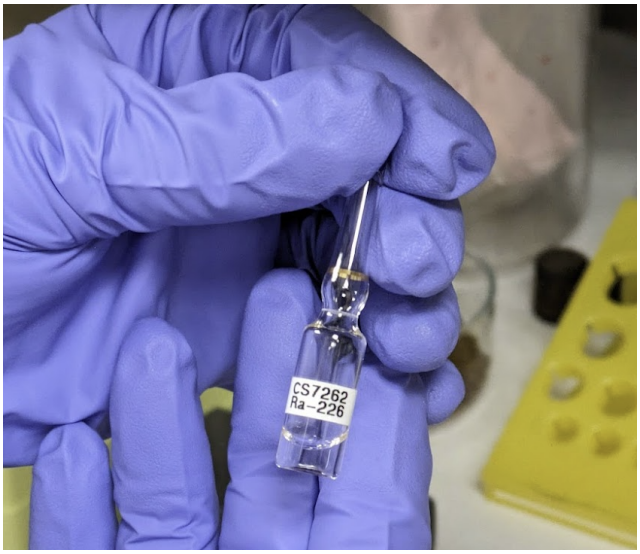


Figure 5.8: Photo of the glass ampoule containing our 10 μCi sample of radium-226 chloride in 500 μL of solution. The meniscus is visible below the printed label.

of constant, repetitive dropping. A procedure that takes this long was unsafe and impractical for a long-term protocol. For our subsequent 5 ml samples, we took to pre-evaporating the solution in custom-made PTFE[17] beakers under a heat lamp. These radium chloride solution come dissolved in 0.1 M HCl, where the weak acid helps prevent the radium ions in solution from sticking to the glass walls.

Once we had developed a functional procedure and felt comfortable with it, we began working with larger amounts of radium per cell. The chloride solutions were only available in quantities of 10 μCi each and were quite expensive, so we instead purchased 1 mCi of radium nitrate ($Ra(NO_3)_2$) from the U.S. Department of Energy's National Isotope Development Center, which was a factor of 100 less expensive per mass of radium. This nitrate sample arrived as a dried salt, which we then dissolved in 0.1 M nitric acid and aliquoted into smaller concentrations. By performing the aliquoting ourselves we could control the total liquid volumes of each sample. We chose to prepare twenty vials of 10 μCi in 100 μl each for our upcoming cells, and four vials of 200 μCi in 200 μl to act as "medium-term" storage, which we would further distribute at a later date when we had a better idea of the quantities we wanted to use per cell. Given the large radium activity of this 1 mCi sample, this dissolution and aliquoting procedure was guided by professor Alyssa Gaiser from Michigan State University and FRIB.

Finding out that the radioactive solution would contain acid was slightly alarming;

[17] PTFE, or Teflon, is not the best material for this purpose, as under exposure to ionizing radiation it will degrade and release fluorine into the solution [125] Generally, HDPE or PEEK plastics should be used instead as they are similarly machinable but more radiation-resistant. PTFE is generally the easiest to acquire, which is why we went for it as this was not a long-term solution.

while pure copper is inert to hydrochloric acid, copper passivates in air to form an outer layer of copper oxide which the hydrochloric acid will attack[18]. Given that chemistry of our radioactive materials was something we wished to avoid, we had the idea to gold plate the copper target plates, which we performed in-house by electroplating with potassium aurocyanide. In these earlier target plates we also milled wells to contain the drop casting liquid, as the concern was that the solution would spread out and spread the limited material over a large surface area, leading to smaller yields per ablation shot. After a few test cells we realized that these square wells[19] had the unwanted effect of trapping the material in the corners during the drop casting process; if the liquid droplet touched the walls, it would wick to the edges of the well and remain there until fully evaporated, meaning all of the material would concentrate in the corners and on the walls of the well and drastically reduce the total number of successful ablation shots. The ablation lasers also had a hard time accessing any material on the walls as these surfaces were perpendicular to the direction of laser propagation. We attempted to remedy this by instead milling spherical pockets using ball nose end mills. Unfortunately, both the updated well geometry and the electroplating were detriments to the performance of our targets, as we would come to find out.

Before working with radium we loaded a few cells using a $BaCl_2$ solution as a proxy. Being the next lightest alkaline earth element, barium should behave chemically quite similar to radium, allowing us to prototype molecule production techniques without expending any of our trace material. Starting with a 10% w/v solution of barium chloride[20], we prepared various samples ranging from the stock concentration down to a 10 μCi-equivalent of 44 nmol $BaCl_2$. While these barium tests helped us to iterate and optimize on our fluorescence detection side, they were only minimally useful in guiding our target production protocol. At high solute concentrations the targets do not deposit at all like how they do at low concentrations, forming a thick, crystalline substance rather than depositing in a thin layer.

Radiolysis

A much more sinister effect we encountered, and one that merits its own discussion, is the additional chemistry that occurs due to ionizing radiation. Without this so-called radiolysis, radium and barium should behave nearly identically from a chemical

[18]This passivation and attack is accelerated under heat and high airflow, both of which factor into our drop casting protocol.

[19]By "square well" I mean that the walls and the base form a right angle, not that the well itself is square-shaped. All wells we attempted were circular.

[20]Catalog number 035584.AP from Thermo Scientific Chemicals

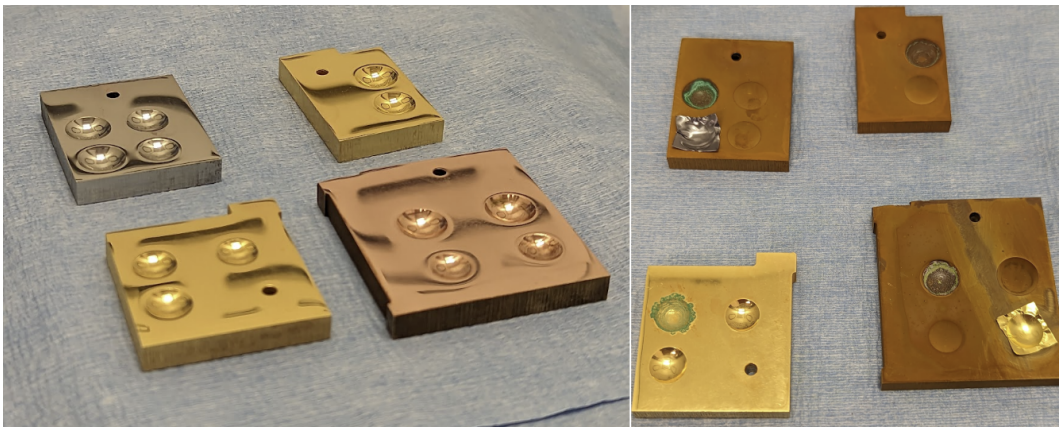


Figure 5.9: Tests of electroplating copper with various metals. Left photo shows the base layer, where we electroplated either 24 K gold, nickel, or 24 K gold onto nickel. All of these were then electroplated with pure gold (which appears as a dull brownish color rather than shiny) and tested with a barium solution. The photos on the right show the degradation of the wells where the solution was added, including a reaction leading to some green crystallization. These tests also show the strong coffee ring formed by these spherical wells. Two of the wells have foils pressed in them which we were also testing at the time.

perspective. Unfortunately, this is an unavoidable consideration we must contend with.

The mechanisms underlying radiolysis are complex, depending strongly on the composition of the solution and the nature of the ionizing radiation. Predicting the consequences of ionizing radiation in a solution requires an understanding of the physics and chemistry of the individual components as well as their interactions and bulk properties. As an illustrative example we will consider the radiolysis of liquid water, which is the system in which radiolysis has been characterized most comprehensively [126].

The effects of radiation on water, as for other solutions, may be divided into three time scales in which different physical descriptions are appropriate. The earliest regime, generally considered to be $\lesssim 10^{-15}$ s (1 fs), is below the time scale of molecular bond formation and breaking. Here we see the rise of three main products:

$$\rightsquigarrow H_2O \rightarrow H_2O^{\bullet+},\ H_2O^*,\ e^-\ , \tag{5.2}$$

where $H_2O^{\bullet+}$ and H_2O^* denote singly-ionized and excited-state water molecules, respectively, and the wiggly arrow denotes ionizing radiation. Note that in the singly-ionized case the unpaired electron is explicitly represented, as these radical molecules

are highly reactive. e^- is the electron emitted from the ionization of water—to put some numbers out there, around 10^4 electrons are emitted per MeV of absorbed radiation [126], and the first alpha decay of radium-226 to radon-222 carries 4.87 MeV.

Now we can consider the downstream effects caused by the creation of these three species. This brings us to the intermediate "physico-chemical" time scale, where chemical reactions begin to occur in the region immediately around the radiation event. From here, the ionized water can either absorb another ejected electron or transfer a proton to another water molecule:

$$\begin{aligned} H_2O^{\bullet+} + e^- &\rightarrow H_2O^* \\ H_2O^{\bullet+} + H_2O &\rightarrow H_3O^+ + {}^{\bullet}OH\,. \end{aligned}$$

The ejected electron, in addition to the reaction above, may also be absorbed by a regular water molecule:

$$\begin{aligned} e^- + H_2O \longrightarrow (H_2O^{\bullet-})^* &\longrightarrow H^- + {}^{\bullet}OH \\ e^- + H_2O &\longrightarrow H^{\bullet} + OH^-\,, \end{aligned}$$

where the second reaction may only proceed with higher energy electrons.

Last, the excited water molecule may decompose in a number of ways:

$$\begin{aligned} H_2O^* &\longrightarrow H^{\bullet} + {}^{\bullet}OH \\ H_2O^* &\longrightarrow H_2 + O(^1D) \\ H_2O^* &\longrightarrow 2\,H^{\bullet} + {}^{\bullet}O^{\bullet}(^3P) \\ H_2O^* &\longrightarrow H_2O + \gamma\,, \end{aligned}$$

where the oxygen may end up in its excited ^1D state or its ground ^3P state. From here, the various byproducts engage in a series of chemical reactions as they progress towards more stable species.

This is just a sampling of the best-understood molecular phenomena present during the radiolysis of water. For completeness, here is a summary of all (currently known) possible products [126, 127]:

$$\rightsquigarrow H_2O \longrightarrow e^-, H^\bullet, H^+, H^-, O(^1D), {}^\bullet O^\bullet(^3P), O^{\bullet -}, \\ O_2{}^{\bullet -}, OH^-, {}^\bullet OH, OH^+, H_2, HO_2{}^{\bullet -}, H_2O^{\bullet +}, H_2O^{++}, H_3O^+, H_2O_2 \quad (5.3)$$

This excessive level of detail is intended to emphasize how the chemistry of radioactive solutions is entirely unlike that for stable species. When ionizing radiation impacts a homogeneous sample of pure, unaerated water, it can yield upwards of 17 different products, virtually all of which are highly reactive. The addition of even one extra species will complicate this landscape even further.

We witnessed the effects of radiolysis directly in our radium chloride drop casting runs. Many of the above radiolytic products are electroactive, meaning they can undergo charge transfer reactions at the contact point between the solution and a metal substrate [127]. Pure copper should be inert to the weak hydrochloric acid concentration present in our early radium solutions, but we further proceeded with gold electroplating the copper in the hopes of making it even more chemically resistant. Unfortunately, as we later learned, the electroplating process does not deposit just the gold, but other molecules present in the solution as well. We witnessed reactions between the gold layer and the deposited liquid, which hinted at radiolysis, but we were able to later replicate these without a non-radioactive solution by simply increasing the hydrochloric acid concentration, implying that this was not solely a radiolytic effect.

In any case, we ceased using the gold electroplated copper and switched to using bare copper metal. In our test runs using barium chloride, no level of acid concentration was able to yield a reaction with this copper. When we switched to radium chloride, the effects were dramatically different. Our first run produced a deep blue-green surface layer almost immediately, which our best guess was due to the formation of hydrated copper (II) chloride or hydroxide. Repeated drops caused this layer to develop three-dimensional features somewhat akin to solid bubbles. In an even more unsettling turn, the second run on bare copper yielded a target that looked entirely different, with a much lighter hue and more even deposition. Because this liquid solution was pre-evaporated in a PTFE beaker, we believe that this behavior and coloration was caused by copper (II) fluoride. The third test produced a target that was visually similar to the first, but with a much larger spatial extent and a distinctly non-circular shape.

Around this time we realized that if we wanted to produce good, consistent RaOH signals, then we needed more a more repeatable target production protocol. While

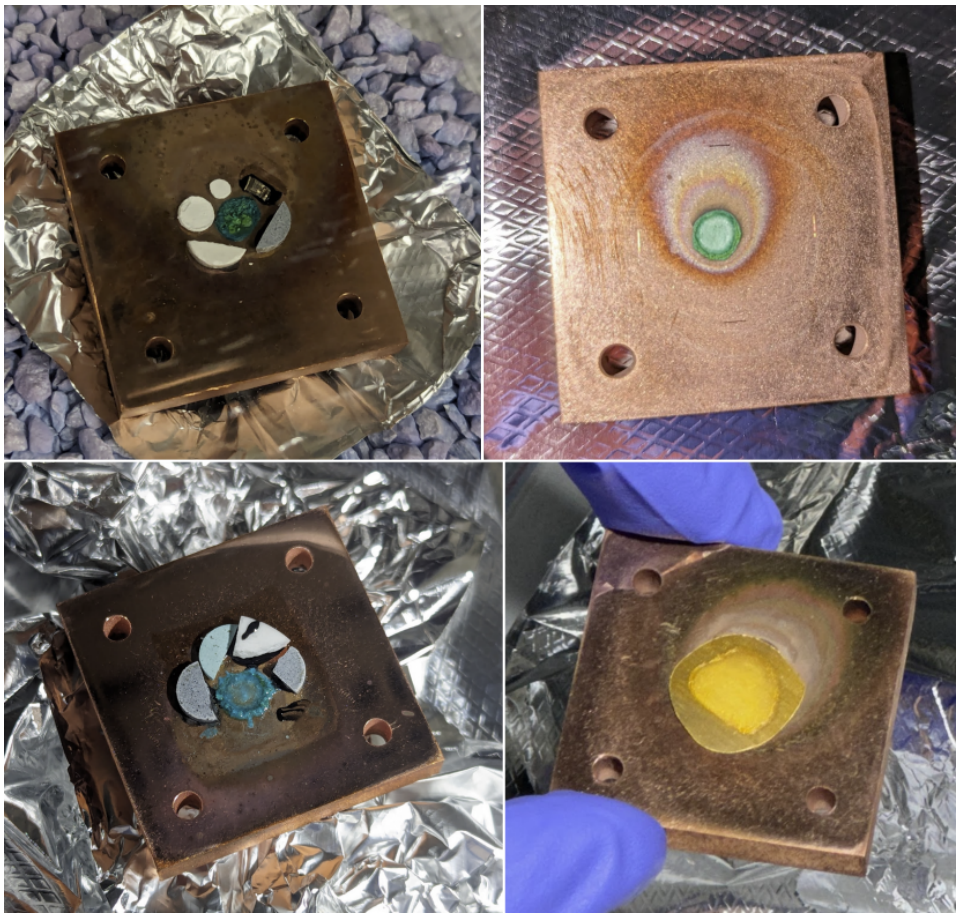


Figure 5.10: Photos demonstrating four qualitatively different radiolysis effects on our early targets. On plates with co-targets attached, the radium drop cast target is always in the center. Top left: formation of a crusty blue-green surface layer via the reaction of the radium chloride solution with pure copper. The color indicates the formation of either copper chloride or copper hydroxide. Top right: likely the formation of copper fluoride, owing to our use of a teflon beaker for pre-evaporation of the radium chloride solution, which almost certainly leeched fluoride ions. We believe copper fluoride to be the resultant material because of the lighter green coloration and the fact that this was not observed in tests without the pre-evaporation. Bottom left: similar to the top left, but with a much more crystalline structure, possibly copper hydroxide or chloride again. Bottom right: radiolysis of pure gold foil, likely forming gold chloride (lighter yellow region inside the larger gold circle).

the gold electroplating did not work, pure gold foil should not possess the same impurities that presumably caused the electroplated targets to fail. However, even the most inert metal[21] was not immune to radiolysis. In our trial of drop casting radium chloride onto 0.005" thick pure gold foil, we actually converted the surface of the gold into what we believe was gold (III) chloride, an assumption we made based on the orange-red coloration.

Thankfully, not all hope was lost, as this is when we received the radium nitrate. In our first drop casting of the nitrate solution onto gold foil, we observed what seemed to be crystallization and deposition of the material *on* the surface, with no perceptable changes to the nature of the gold foil itself. From this point on, all drop casting runs were performed with radium nitrate, and no unwanted radiolysis has been documented. As to the reason for this different behavior between the nitrate and the chloride, perhaps it is because chloride ions and radicals are exceptionally reactive and corrosive, moreso than the equivalent for nitrate. In addition, gold (III) chloride is a stable compound[22], whereas pure gold nitrate has never been synthesized[23], meaning that a straightforward reaction pathway exists for one of the possible reagents but not the other.

Coffee rings and crystallization

The dynamics of water droplet evaporation are surprisingly complex. As a droplet dries, competing forces lead to internal flows, carrying along with them the solute particles which then deposit nonuniformly. Given that we desire a uniform target, understanding and overcoming this phenomenon is a priority.

One well-studied consequence is the "coffee ring effect[24]," where suspended particles in a liquid tend to deposit in a ring shape during droplet evaporation, with a significant lack of material inside this ring. Many techniques have been developed to counteract this effect, some of which we explored and implemented in our setup, but most of which are incompatible with our protocol.

There are several published methods of overcoming the coffee ring effect [128] that we

[21]Technically, by most metrics, iridium is actually more inert than gold, is substantially more costly and made unnecessary by the fact that the gold foil ended up suiting our needs.

[22]As is gold (I) chloride, although it is not the primary oxidation state

[23]Nitratoauric acid, on the other hand, has been produced and is used commercially to extract gold, and is closely related to the simple nitrate.

[24]The coffee ring effect has a lot of industry interest not because of its effect on coffee, but rather because of inkjet printing, where a nonuniform drying of suspended inks will lead to lower-quality prints.

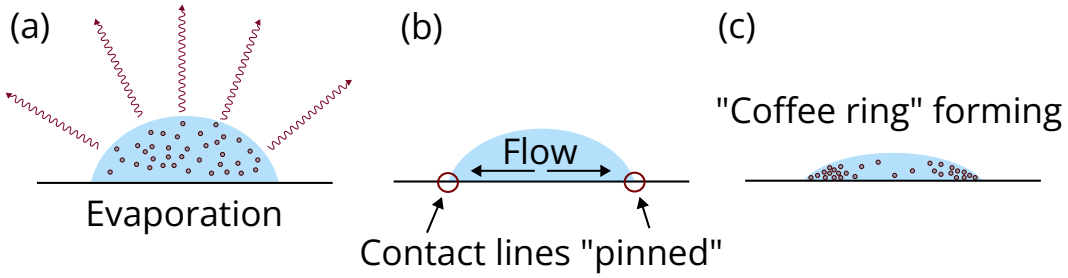


Figure 5.11: Illustration of the formation of coffee rings in drying droplets. Contact line pinning, a phenomenon which locks the edge of the droplet in place through the evaporation process, leads to a net outward flow within the droplet as the liquid that evaporates near the contact line needs to be continually replaced. This flow results in accumulation of dissolved particles at the edges, leaving behind a ring of material when the droplet fully evaporates.

never attempted, either because they were much too complicated or would simply never work with our safety protocols. One method is to destabilize the contact line pinning, allowing the edge of the droplet to creep inward during the evaporation process. This is done either by creating a superhydrophobic substrate with chemical treatment or by micropatterning. While we could have conceivably performed the necessary chemical treatment, the nature of our drop casting protocol means that this would be futile; we do not add one droplet to the target plate, but rather tens to hundreds in the same spot. After the first droplet dries, the deposited material will disrupt the superhydrophobicity of the substrate and defeat the purpose of the treatment. Many of the chemical treatments also rely on the addition of contaminant atoms, such as the chlorine atoms in the coating octadecyltrichlorosilane.

Instead of altering the substrate, applied electric potentials, surface acoustic waves, or localized heating can disrupt the internal flows directly. The first requires inserting electrodes into the liquid, which is impractical with our radioactive solution. The latter two could theoretically be possible in our setup with sufficient development; however, the time required to model and engineer a surface-wave protocol or directed laser heating seemed like too involved of an endeavor. In addition, concerns about microsplattering of the liquid due to the mechanical disruption of the flows precluded further investigation.

A geometric way of disrupting the coffee ring effect is to deposit the droplet on a convex surface. This would lead to impractical ablation target geometries, with additional concerns about the droplet liquid spilling down the sides of the convex substrate. A consequence of this is that the concave spherical wells we had attempted previously

were actually maximally bad from a geometric standpoint.

The following sections describe methods we tested that actually worked, to varying degrees. Specifically, the section on matrices (Section 5.2) contains the target protocol developments that enabled most of the data in this section. Important to note is that our radium is actually in solution, not a suspension, so it is unclear whether solving the coffee ring effect is actually what we want to do. Instead, we wish to disrupt the crystallization of the radium salts, as crystal growth concentrates the material at the nucleation sites. Relative to the coffee ring effect, the disruption of crystallization is considerably understudied, yet some of the fixes that address the coffee ring effect might also apply to crystallization.

Porous substrates

Rather than deposit our radium *on* some surface, what if instead we distributed it *in* some medium? An inert material with some perfectly calibrated porosity would theoretically lock the dissolved radium in a uniform, three-dimensional network, producing stable ablation signals over the range of the target.

The ideal material probably does not exist, or is highly custom, so we tested a few candidate materials and porosities. Alumina (Al_2O_3) ceramics were immediately identified as they are readily available over a range of different porosities. First, we wanted to test the material dispersion properties of the various porosities. We dissolved ~50 mg of Rhodamine 590 chloride laser dye in 10 ml of 0.1 M hydrochloric acid to act as a dye tracer, allowing visible inspection of the distribution of solute particles. The acid mimicked the acid concentration of our radium chloride targets to test the chemical compatibility of the alumina. Also in this test we included two forms of silica aerogel, one hydrophilic and one hydrophobic. The materials tested are summarized in Table 5.1 below.

To test the material distribution, we dropped 20 5 µl drops of the dye solution onto the different porosities of materials, and one drop each onto the aerogels. The hydrophilic aerogel decomposed immediately, while the hydrophobic one maintained a nice droplet that slowly dried over the course of 45 minutes. While potentially useful for creating a uniform spatial distribution of material, it is highly unlikely that the hydrophobic aerogel would be compatible with our handling and cryogenics, and so we stopped investigating it further.

Photos of the dye tracer tests are provided in Figure 5.12. To summarize, the 48%

Material	Thickness	Notes
48% porosity alumina[a]	1/16"-1/8"	Cut horizontally from stock 1/8" thick piece, rough surface as a result
48% porosity alumina[a]	1/32"	Cut horizontally from stock 1/8" thick piece, rough surface as a result
48% porosity alumina[a]	1/32"	Stock thickness from manufacturer; smooth surface
Nonporous alumina[b]	0.015"	Stock thickness from manufacturer; smooth surface
Alumina-bisque ceramic[c]	1/4"	Cut at a 45 degree angle to make thinner, was hard to cut
Aerogel (hydrophilic)	-	Extremely fragile, nearly impossible to handle/cut
Aerogel (hydrophobic)	1/2"	Extremely fragile, nearly impossible to handle/cut

Table 5.1: Materials tested in the Rhodamine dye tracer test. [a] RS-99R from ZRCI refractory composites. [b] Product 8462K24 from McMaster-Carr. [c] Product 8484K84 from McMaster-Carr.

porosity alumina distributed the material the best in the bulk, while not allowing full penetration to the bottom where it would be less accessible. The nonporous alumina allowed very little material penetration, while the ceramic permitted the liquid to seep all the way through and attack the copper.

We also tested the barium chloride solution on other substrates, none of which showed much promise over the above listed ones. We tested on the alloys Inconel 625, Hastelloy, silicon carbide[25], and a quartz frit[26]. All of these substrates deposited the material in a larger area and with a worse coffee ring than plain copper, and so were abandoned.

In addition to the above materials we also tested drop casting a barium chloride solution directly onto our ablation co-targets, with the logic that co-localizing the reagents would lead to more efficient molecule production. We only tested this on the aluminum hydroxide ($Al(OH)_3$) pellets, as optimization of RaOH production was still the goal at this time[27]. In the drop casting process, we noticed that the surface of the pressed powders began appearing glassy and reflective, indicating some sort of

[25] We used a relatively porous version of silicon carbide, which just allowed the drop casting liquid to mostly slip through.

[26] Similarly porous to the silicon carbide, most of the material did not stay in the medium.

[27] Also because the addition of water to copper fluoride can lead to the formation of HF, which was highly undesirable.



Figure 5.12: Photos showing the rhodamine dye tracer test on the various alumina substrates. Starting from the top left, the materials follow the order of Table 5.1 row-wise starting from the top left, except for the very last aerogel which is the hydrophobic variant. Note the visible "coffee ring" made from dye on the nonporous alumina.

physical or chemical change occurring. When we tried ablating these targets we not only observed no molecule yield, but no atomic yield either. Regarding the lack of molecules, we believe that either the acid or the heating + acid in the drop casting process liberated the hydrogens from the aluminum hydroxide powders, preventing the formation of BaOH molecules. As for the lack of barium atomic signal, this is still perplexing—our best guess is that the helium adsorption properties of the targets changed dramatically, which affects all aspects of the ablation and thermalization.

Matrices

In searching for a solution to our target uniformity issues, we found inspiration from MALDI (matrix-assisted laser desorption/ionization), a technique used in mass spectrometry [129]. In MALDI, a small quantity of some molecule of interest (the "analyte") is dissolved in solution with a crystallizing molecule (the matrix), and allowed to evaporate, leaving a crystallized matrix containing dispersed analyte molecules. This

matrix is hit with a laser beam to desorb the analyte particles, a process reminiscent of our laser ablation.

While definitely a good source of ideas, directly porting over methods from MALDI for our purposes would not be advisable. The primary reason for this stems from the choice of matrix molecule; MALDI matrices are chosen such that they resonantly absorb the incoming laser light, so that in the desorption process their analytes become ionized. We wish to produce neutral molecules, not ions. As such, we need to search for an entirely new class of matrices.

In the process of finding a suitable matrix molecule, we realized that our choice had the potential to solve additional problems with our drop casting protocol that has not yet been mentioned. When evaporating our radium solution onto the gold foil (and in the absence of radiolysis), it was unclear how well the crystallized radium salt was sticking to the gold, and whether some of it flaked off during ablation rather than vaporizing. Tests with barium nitrate demonstrated that the dried solution could be scraped off relatively easily with a toothpick, giving us some worry as to the behavior of our radium inside the cell at cryogenic temperatures. By adding a matrix, we had the ability to choose some species that would adhere much better to the gold foil on the ablation target. We also had reason to believe at the time that co-localization of hydroxyl groups with the radium led to increased RaOH production[28].

To summarize, our requirements for a candidate matrix species were for it to be: soluble, crystallizing, sticky, non-absorptive to 532 nm light[29], and preferably hydroxide-containing. As it turns out, sugars (and the related sugar alcohols) are among the simplest non-volatile hydroxide-containing solids, crystallize, and are notoriously sticky[30]. Sugar also caramelizes or forms various different candy stages depending on its water concentration and temperature, and we theorized that perhaps we could leverage the caramelization of sugar to create some sort of hard and strong matrix network. Since there is no *a priori* way to determine whether a candidate molecule would make a good matrix, we performed qualitative testing on various sugars, sugar

[28]This claim was never proven or disproven, as we only ever tested one matrix for molecule production, and it contains hydroxide groups. However, this line of thinking fortuitously led to the matrix that ultimately enabled this project to be successful

[29]It is not obvious that this requirement is necessary. However, because the absorptivity of the matrices used in MALDI enhances their production of ions, and because we wished to produce neutral molecules rather than ions, we believed that we should avoid any absorptive matrices

[30]I vividly recall laying out all of these conditions one day in the lab to Phelan, in a time when we were especially downtrodden after failing to reproduce RaOH signals, after which I jokingly suggested that we use sugar as a matrix, before we both realized its potential for success. This represents a key integration of humor with the scientific method.

alcohols, and other soluble hydroxide-containing matrix candidates to assess their uniformity and target plate adhesion. A discussion of the testing is provided below.

A brief note on a relevant distinction between sugars and sugar alcohols: Sugars contain at least one ketone (R-O-R) or aldehyde (R=O) group, whereas sugar alcohols replace this with a hydroxyl (R-OH) group. Structurally, a sugar alcohol is essentially a carbon chain where each carbon has one hydroxyl group bound to it. This structural distinction means that sugars will polymerize when heated to a certain temperature, forming units of two or more simple sugars. This process leads to caramelization, which drastically alters the bulk physical properties. Further heating will irreversibly burn the sugar, breaking it down into constituent carbon compounds and water vapor. Sugar alcohols do not undergo the caramelization process, and instead will melt at temperatures around the caramelization point of sugar. They are also considerably more stable, requiring a much higher temperature to decompose.

We drop casted 28 solutions onto three test target plates. For all of the following, the listed chemicals were dissolved in solution at a concentration much below their solubility limit. Ten tests contained aluminum hydroxide ($Al(OH)_3$) or boric acid ($B(OH)_3$) at both low and high concentrations, both with and without 0.1 M nitric acid. In all of these cases, the solutions dried to form a somewhat uniform crystalline network on the copper, but flaked off extremely easily. Handling these materials would be impractical as they would likely dislodge from the target plate during typical operating conditions. As such, they were disregarded as potential matrices for containing radium.

The remaining 18 tests all contained either sucrose or xylitol. Sucrose ($C_{12}H_{22}O_{11}$), also known as table sugar, is a true sugar comprised of one glucose and one fructose subunit. Xylitol ($C_5H_{12}O_5$) is the second simplest sugar alcohol that is solid at STP. We initially chose xylitol over erythritol, the simplest sugar alcohol, because of its lower melting point at $\sim 95\ ^\circ C$, quite close to the temperature of our drop casting protocol. The thinking was that melting the xylitol could help to uniformize the material if it happened to crystallize in unexpected ways, offering us a way of manipulating the target structure after we had performed the handling.

The first tests on these species explored the effects of temperature on the target structure. As mentioned above, we were interested in exploring the possibility of creating caramelized or candied targets out of sucrose, which requires heating to various sugar candying temperatures [130, 131]. We also wanted to observe whether the melting of

xylitol would lead to more uniform target distribution. To our dismay, heating the sucrose targets to temperatures that encouraged polymerization led to the formation of air bubbles underneath the surface of the droplets. These bubbles would either take a very long time to relax, or the surface of the bubbles would crystallize and trap the air pocket underneath a hard shell. In either case, it was apparent that the caramelization process, although interesting, was a detriment to the formation of uniform targets[31]. The xylitol targets that were present on the target plate during these elevated temperatures darkened quite significantly, but appeared visually uniform. Occasionally they would form sticky bubbles, but these would pop with additional heating time. Because the material became incredibly viscous as the solvent evaporated away, this popping occurred relatively slowly, meaning there was no dramatic ejection of material.

We performed additional tests varying the concentration of sucrose and xylitol. Those results are summarized in Table 5.2 below.

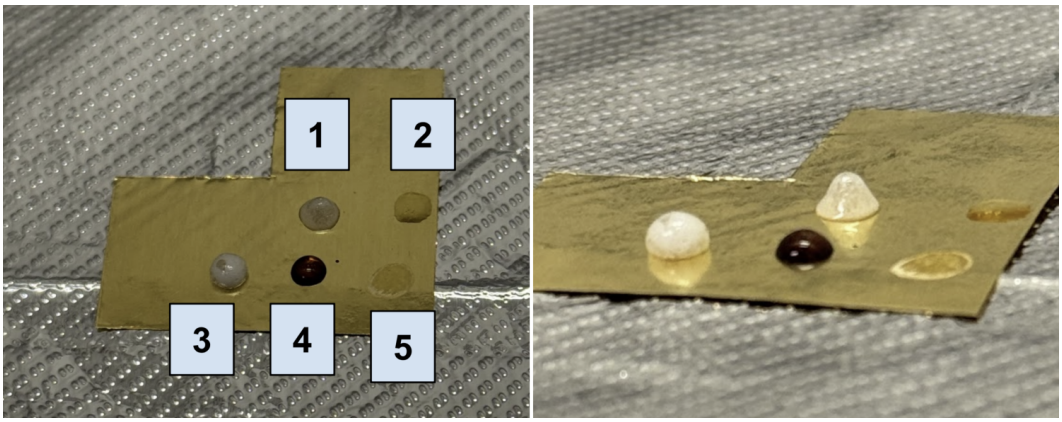


Figure 5.13: Accompanying photos for Table 5.2, showing some of the different concentrations of sucrose and xylitol tested as matrices. Note that, despite their reflective sheen, all of these targets have been drying for a long time and are quite immobile at this point.

Through these tests, we identified xylitol as the clear winner. The presence of a very small amount of xylitol, around 4 average-sized crystals each with an approximate mass[32] of ~250 μg, when dissolved in a 100 μl solution led to repeatable, uniform-

[31] Unfortunately, in learning this we sadly shot down our hopes of winning the ig nobel for creating radioactive candy.

[32] We did not have a scale that was capable of measuring this low, so my means of obtaining this value was to measure out a detectable value on our scale and count the number of crystals that contributed to this mass. In the measurement, 0.05 g of xylitol contained 183 crystals, leading to a per-crystal average mass of 273 μg. Of course, the precision of the scale means that this number should be treated as an order-of-magnitude approximation.

	Sucrose	Xylitol
0.1-1 mM	Noticeable coffee ring. Not tested in the apparatus.	Noticeable coffee ring, some material present on the inside. When tested in the experiment, results in a nonuniform distribution of material. (spot 5 in Figure 5.13)
1-100 mM	Formed a short, bubbly crystal	Flat, uniform-looking and clear-colored. This is the concentration we have been running with lately. (spot 2 in Figure 5.13)
100-1000 mM	Formed a tall, bubbly crystal (spot 1 in Figure 5.13)	Flat, uniform-looking and color ranging from clear-yellow to dark brown. We have used this concentration in the past but the difficulty in producing consistent targets from run to run means we now use less.
1-10 M	Formed a tall, bubbly crystal. Evaporation took upwards of 10 minutes per drop. (spot 3 in Figure 5.13)	Flat and uniformly dark. However, requires a very long evaporation time due to high surface tension preventing water escape.
10-50 M	Formed a tall, caramel-colored droplet that never appeared to fully evaporate. (spot 4 in Figure 5.13)	Tall and bubbly droplet.

Table 5.2: Testing various concentrations of sucrose and xylitol. Values of concentration are given as a range because the scale used has a limited resolution and because the behaviors were mostly the same within these limits.

looking targets. Interestingly, the targets do not visually appear to fully evaporate into a crystal, instead forming an extremely thick gel. The viscosity of this gel is high enough such that there is no migration of the material on the target plate after completion of the drop casting—we have suspended the plate vertically for many weeks and the gel did not move under the effects of gravity.

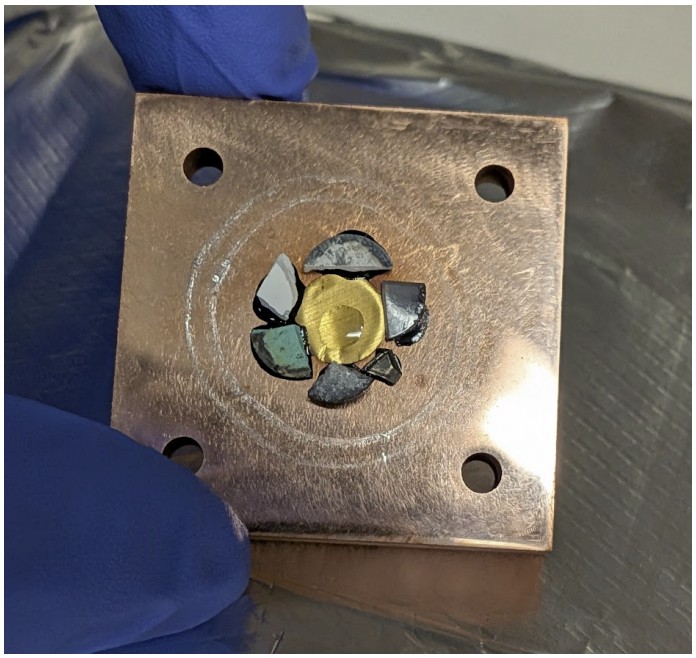


Figure 5.14: Photo of a representative radium target with xylitol. The thick gel (center) is extremely viscous and does not move under the effects of gravity, allowing us to handle it and install it into the cell, where it may remain suspended for weeks without movement. It appears to be wet because of the glare, but has been drying for at least a day. For reference, the diameter of the gold foil is 5/16", made by a hole punch.

Xylitol might also have specific benefits pertaining to radium. Given its use as an artificial sweetener, studies have examined its interactions with dissolved oral calcium, showing that xylitol actually forms complexes with calcium ions [132], outcompeting water in the process. In our implementation, given the chemical similarity of radium to calcium, these complexes might form with our dissolved radium and help disrupt the crystallization process.

One last aside about the safety of our drop casting mixtures: Sugars and sugar alcohols, when combined with strong oxidizers such as nitric acid, can form chemical propellants commonly referred to as "rocket candy." As it turns out, sucrose and xylitol are actually two of the most commonly used starting materials for these explosives. For xylitol specifically, measures must be taken to avoid the formation of xylitol pentanitrate (XPN)—our chemical mixture of weak nitric acid is incapable of nitrating the xylitol directly, but certain additives (e.g. acetic acid) will form xylitol pentaacetate, which is readily nitrated to XPN.



Figure 5.15: Photo of a Yb + $Yb(OH)_3$ pressed powder target that has been removed from one of our other sources. Initially, these targets look like flat pucks (see Figure 5.1). When the ablation laser is steered by hand, as was the case here, the resulting inconsistencies in the ablation locations are immediately visible. Photo from Arian Jadbabaie.

5.3 Spectroscopic improvements

Various improvements to our production and detection scheme enabled the observation of these trace molecules. The main problem we needed to solve was the limited, inconsistent ablation target, coupled with a large initial search range to locate the first RaOH transition (elaborated in Section 5.4). The following sections detail the changes implemented to do just that.

Ablation rastering

A non-radioactive, macroscopic ablation target might sustain tens of thousands of ablation shots on one spot before needing to move to a fresh target location. Our drop cast targets, which generally form a thin, viscous film, do not have this luxury; their densest target spots might yield a few hundred successful ablation shots, while the average is $1 - 10$ before needing to move.

Because of the infrequent need to change target spots, other setups in the lab rely on manually steering the ablation laser mirrors until the signal recovers. This process leaves many un-ablated spots on the target, as shown in Figure 5.15. In order to

efficiently utilize our trace material, we need a systematic way of ensuring we ablate the entire target with no missed regions.

To accomplish this, we installed a motorized mirror mount in the optical path for the radium ablation laser. Before ever ablating the target, we steer these motorized mirrors to the bounds of the radium target while firing the ablation laser with very little energy so as not to actually ablate any material. A camera looks into the target so that we can establish the motor positions for the edges, which feed into a program that calculates the ablation positions for the entire target. An example of the camera image we see showing the two ablation beams on separate targets is shown in Figure 5.16

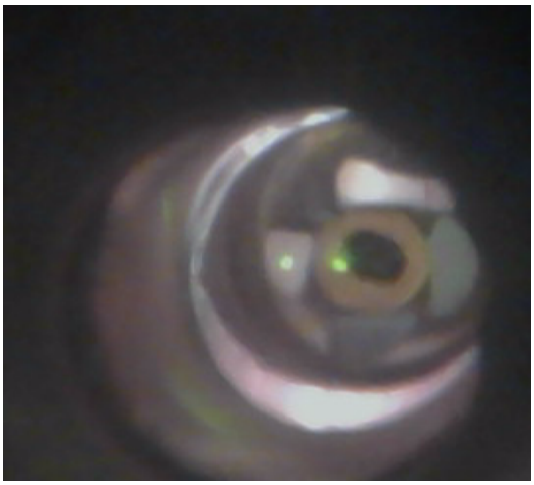


Figure 5.16: Still from the camera feed we use to align the ablation lasers. The reagent co-targets are clearly discernible, especially with a reference photo of the target. The two ablation laser beams, firing at very low energy so as not to actually ablate any material, are visible. The laser to the right is steered across the edges of the drop cast radium target (center-right, dark oval) to establish the bounds for our automated rastering program.

This rastering scheme was implemented by Phelan Yu; further details can be found in our publication [84].

Probe laser chopping

The closed-cell design of the Minifridge means that any nonresonant glow from the ablation plasma can enter into our molecule fluorescence detection [133, 134]. We generally observe this nonresonant fluorescence lasting a few milliseconds after ablation, which we attribute to metastable species collisionally exciting the various atoms and molecules in the cell, which then fluoresce at many different wavelengths. For macroscopic species, this does not present an issue, as the desired signals tend to overwhelm any glow. In the trace reagent regime, we are contending with small signals and an inconsistent ablation glow as the target changes drastically from shot-to-shot; combined with our limited quantities, averaging many ablation shots is not an option.

To remedy this, we implemented in-shot background subtraction via rapid probe laser modulation. By strobing our probe laser on/off much quicker than the time

scale of the glow, we can model the glow signal for each shot and subtract it from our measured fluorescence. Laser modulation is achieved with an acousto-optic modulator combined with an RF switch. The first-order diffraction beam out of the AOM is turned on and off via a 50 kHz square wave signal sent to the RF switch, allowing fast laser switching. An example of the raw and demodulated signal is shown in Figure 5.17

This required upgrading the timing resolution of our DAQ to be able to sample enough points in each probe laser on/off window. We implemented a high-resolution PXI oscilloscope capable of 5 Megasamples per second[33], which corresponds to 50 samples per each on/off window at a 50 kHz chopping rate, sufficiently many to not worry about undersampling. With this card, the upper limit for chopping rate would be around 500 kHz. However, there is no additional benefit from chopping this fast or faster in terms of glow rejection, as the features within the glow are on a much slower time scale. In fact the chopping starts to become detrimental as the finite molecular excited state lifetimes become comparable to the switching time scale, as molecules may remain excited across the switch and emit their photons during the "off" section, complicating the signals.

Tunable broadband lasers

In our attempts to first locate transitions corresponding to RaOH, we needed the ability to scan over a wide frequency range in as few shots as possible. Modern laser systems prioritize narrow linewidths in the sub-MHz range and generally lack tunability over more than a nanometer or two—we were going to have to scan upwards of 10 nm. There are modern systems with this degree of tunability, but they still suffer from the narrow linewidth "issues" that would make a scan of this size take upwards of 100,000 ablation shots. With our limited material, this many dead shots was simply not an option.

Thankfully, lasers were not always this good. Our workhorse for the initial identification of RaOH was a linear-cavity dye laser manufactured nearly 50 years ago[34]. The selection of laser dye achieved the broad tunability, and the removal of intra-cavity etalon assembly broadened the linewidth to $\Delta\nu \sim 1\ \mathrm{cm}^{-1} \approx 30$ GHz while still maintaining continuous-wave operation.

[33] NI PXI-5922
[34] Coherent 599

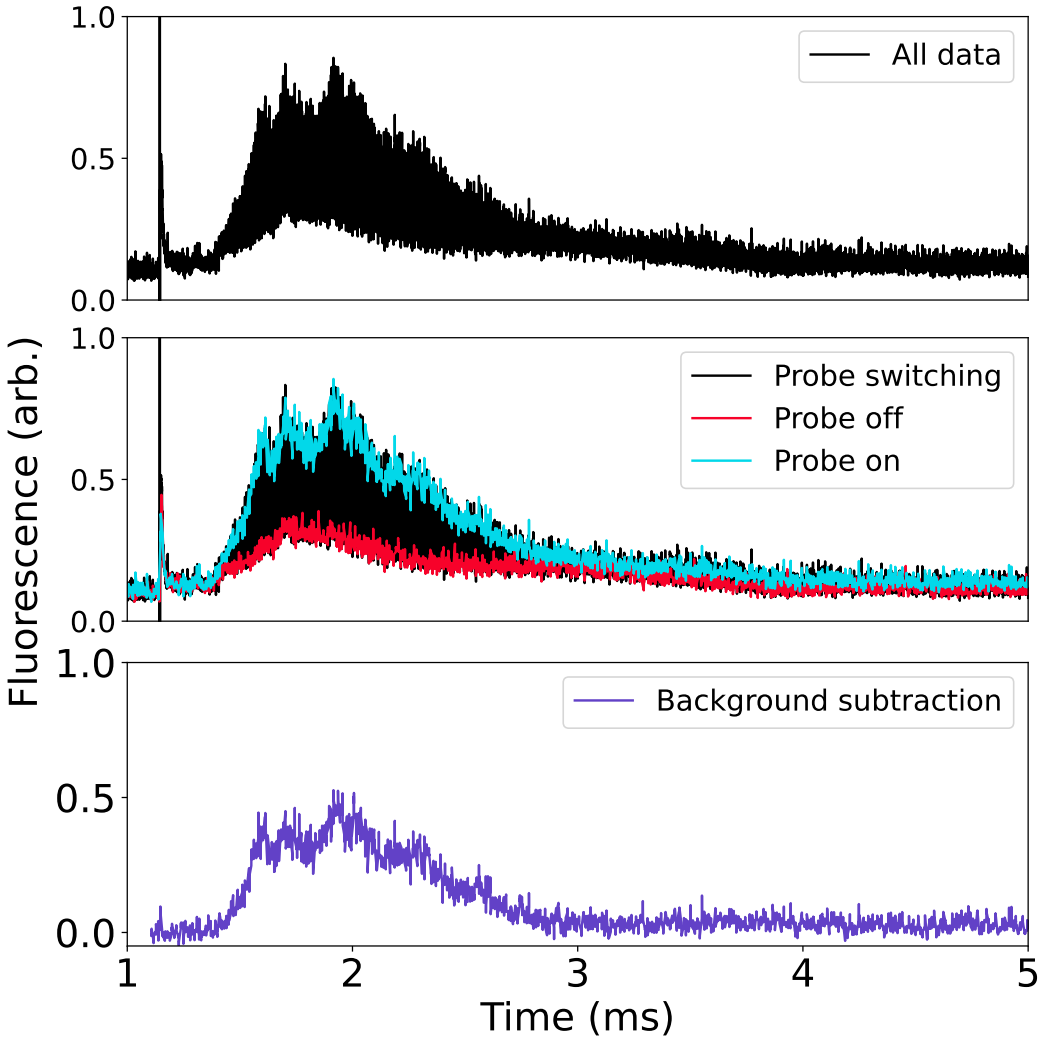


Figure 5.17: Traces showing the fast chopping demodulation process on a representative fluorescence signal for RaOH. Top: All PMT data shown. The bump in the lower edge of the data around 1.5 – 2 ms corresponds to ablation glow, which varies significantly from shot-to-shot; if we just integrated this data, the glow would lead to a false signal. Middle: Splitting the raw data into three regimes corresponding to when the probe is on or off, or when the AOM is switching between the two. This switching data is thrown out for the analysis, as the magnitudes in this switching region depend on how the AOM switching is aliased into our data collection, and thus varies shot-to-shot. Bottom: Signal obtained by subtracting the "signal on" trace from an interpolated version of the "signal off" trace. We integrate this subtracted trace to obtain our fluorescence signal for this shot.

We also acquired a high-repetition rate pulsed dye laser[35]. Pulsed lasers achieve high instantaneous laser intensity, allowing easy saturation of molecular transitions. With

[35]Sirah Credo modified to be pumped by a Spectra-Physics Talon 532-40 at 50 kHz. Thanks to Ana Duarte for helping us acquire the laser.

a linewidth of $\Delta\nu \sim 0.07$ cm$^{-1} \approx 2.1$ GHz, this laser allows us to bridge the range between low and high resolution.

One caveat of both of these lasers is that, because they produce a lot of laser light across a broad wavelength range, and have pretty significant power fluctuations, any molecule fluorescence signals on top of the laser scatter background are pretty much unresolvable. The most convenient mode of operation thus is to filter out the probe laser light, requiring detection of molecule (or atomic) fluorescence on a decay channel different from the one being probed. Molecules generically have other vibrational decay modes which satisfy this requirement, but they may be extremely weak, as in the case of RaF (see Chapter 6). The high intensity of the pulsed dye laser can easily drive vibration-changing transitions, allowing us to detect on the strong on-diagonal decays.

Signal normalization

With the in-shot background subtracted detailed above, we are able to account for the fluctuations in undesirable fluorescence that result from changing ablation spots on our target. But changes to the ablation spot affect our molecule fluorescence, too. While not a problem for qualitative determination of whether or not we have signals, these fluctuations will complicate lineshapes and make accurate spectral feature assignments impossible.

To solve this, we use one of a number of methods of signal normalization. Before we had any confirmed molecule lines, we normalized our signals to absorption on the radium atoms produced during ablation. As part of virtually all data sets, we send in a 483 nm ECDL[36] probe resonant with the strong radium-226 $^1P_1$ transition at 20715.6028 cm^{-1} and record the outgoing power on a photodiode (see the following section for an interesting discussion about this frequency). Because this method normalizes the molecular signal on a species separate from the molecules, it assumes that the number of atoms relative to the number of molecules remains consistent, which should be approximately true as long as we do not change any parameters relating to production.

A much more accurate normalization scheme uses a transition in the molecule of interest when one is known. We perform this molecule normalization in a number of ways depending on the type of measurement. One method involves interspersing

[36] Laser made by MOGLabs based on a 488 nm diode from Nichia

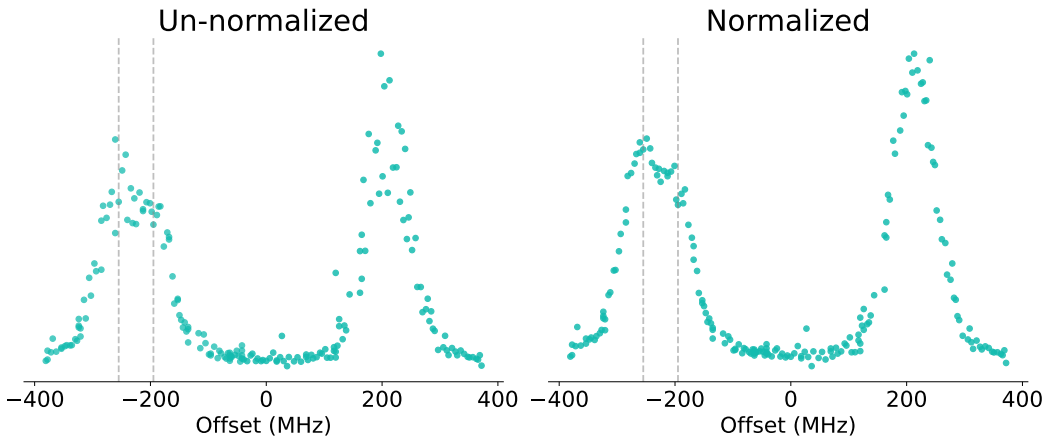


Figure 5.18: Effect of normalization on a set of lines in RaF. The lines shown are the ${}^{P}P_{11}(J'' = 2.5)$ and ${}^{P}Q_{12}(J'' = 1.5)$ transitions in the $C^2\Sigma^+(0) \leftarrow X^2\Sigma^+(0)$ band, where 0 offset in the plots corresponds to 16609.4065 cm^{-1}. Without normalization, the hyperfine doublet (indicated by dotted lines) on the P-branch is not cleanly resolved. The lineshapes are also better defined in the normalized case, leading to more precise fits. For this data, normalization was performed by driving the ${}^{P}Q_{12}(0.5)$ line of the $X - A$ band at roughly 13284.6370 cm^{-1} and collecting the diagonal fluorescence on a second PMT.

the pulsed dye with a chopped CW probe, where the short pulses from the pulsed dye occur in the dead time of the chopping sequence. Either laser may be used as the scanning or normalization laser, depending on what level of resolution we desire for the measurement. The two lasers may even address different wavelength ranges, as long as the light from both decays can be detected. For example, in RaOH, the pulsed dye could drive the vibration-changing transition $\tilde{A}(100) \leftarrow \tilde{X}(000)$ while the CW probe drives the vibration-preserving $\tilde{A}(000) \leftarrow \tilde{X}(000)$. The dominant decay from each state will be vibration-preserving and within the same wavelength range[37] to be detected on the same PMT, allowing normalization on the same molecule but on an entirely different transition from the one being scanned.

The other molecule normalization schemes utilize two chopped CW probes. With only one detection PMT, these two CW probes can be interleaved with some dead time between them just like the method described above with the pulsed dye probe. The background measurement part of the duty cycle, where neither laser is sent into the cell, needs to occur frequently enough to capture the time-dependent glow behavior. If two PMTs are used for detection, with each one observing a different wavelength range, the two CW probes may be used on different transitions; we employ

[37] This is because the $\Delta v = 0$ decay $\tilde{A}(100) \rightarrow \tilde{X}(100)$ is very close to the origin, as the vibrational constants for the ground and excited states are similar.

this method for high-resolution scans of RaF $C - X$ while normalizing on $A - X$. Diagrams depicting the duty cycles for the different forms of normalization are given in Figure 5.19.

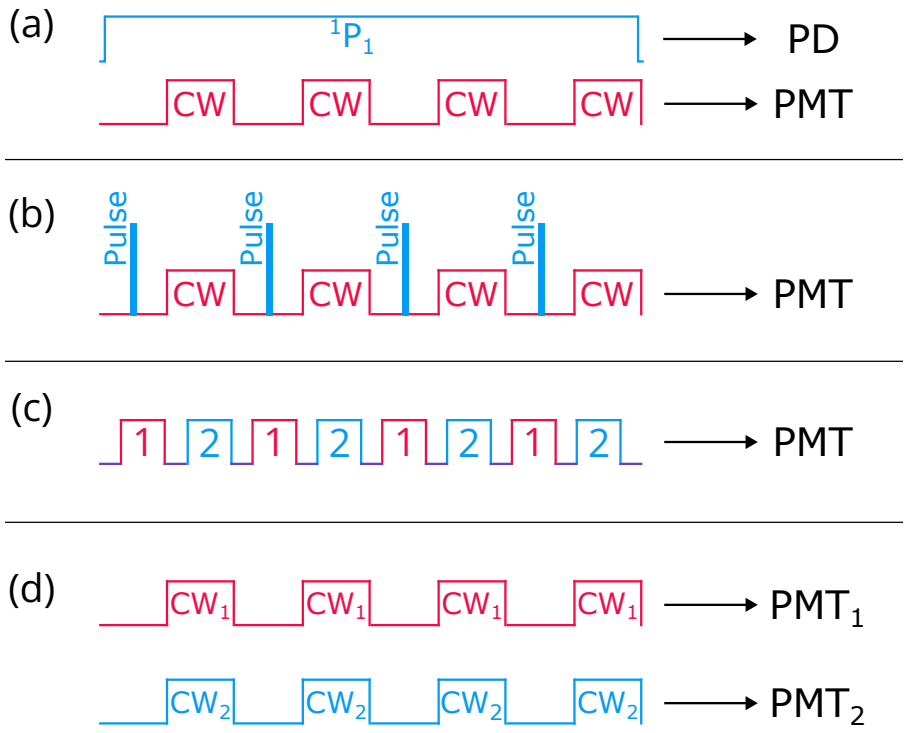


Figure 5.19: Diagrammatic representation of the methods of normalization employed in our work. (a) Atomic normalization on the Ra $^1P_1$ transition. Laser absorption of the 483 nm light is detected on a photodiode, while molecule fluorescence from the chopped CW probe is detected on a PMT. (b) Interspersed pulsed dye and chopped CW normalization. Either laser may be used as the probe or normalization signal depending on the desired resolution of the measurement. (c) CW normalization with only one PMT, achieved by temporally interleaving the two chopped CW beams. (d) CW normalization with two PMTs, where the optical filtering for each PMT only admits the decays from one of the probe transitions.

Radium $^1P_1$ measurement

Through our use of the radium $^1P_1$ transition as a diagnostic tool, we noticed that the NIST ASD recommended frequency ([135, 136]) differed slightly from where we observed the resonance, a discrepancy that was also remarked upon in a publication from the Jayich lab [137]. Given that no reported measurement agreed with what we anecdotally observed, we performed our own calibrated measurement of this transition energy.

The target used for this data was made by drop casting 10 μCi of radium chloride in 0.5 ml of 0.1 M HCl onto bare copper. While ablating, we scanned our 483 nm ECDL from 20715.58 to 20715.63 cm^{-1} and recorded the transmission on a photodiode. Since this was early on in our target development, our atom production was both inconsistent and weak. To account for the inconsistencies, we sent in our $^3P_1$ enhancement laser, heavily attenuated, to use as both fluorescence and absorption normalization. The weak signals actually benefitted us as they meant our absorption never fully bottomed out, which would have made determination of the center frequency more challenging.

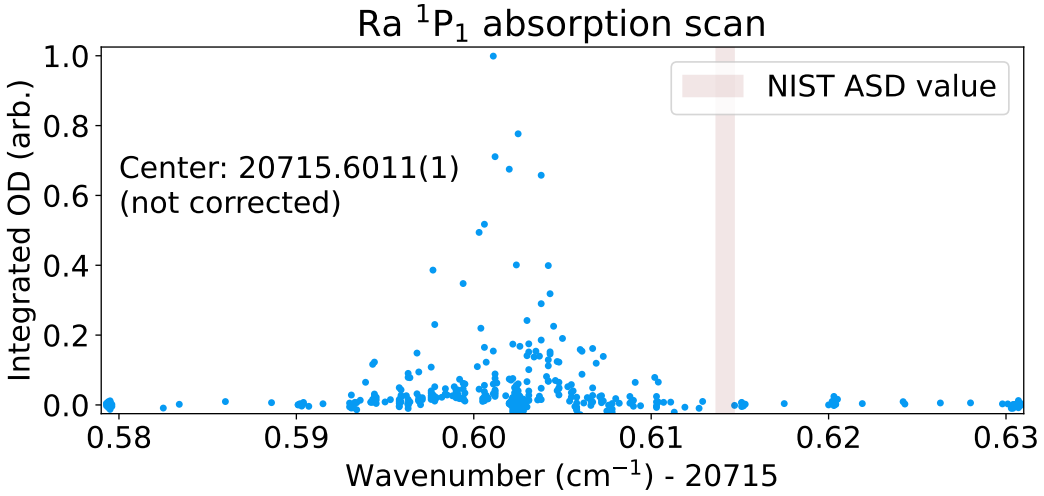


Figure 5.20: Uncorrected scan of the ^{226}Ra $^1S_0 \rightarrow ^1 P_1$ transition at 483 nm. Fitting this data to a Voigt profile gives a measured line center of 20715.6011(1) cm^{-1}, where values in parenthesis correspond to 1σ fit errors. By accounting for our absolute wavemeter offset we report an updated transition frequency of 20715.6028(1) cm^{-1}.

Typically, an absolute frequency calibration would involve scanning our $^1P_1$ laser while recording three values: absorption of our $^1P_1$ on a a species with known, well-documented lines; absorption of our $^1P_1$ on the radium sample; and the measurement of our $^1P_1$ frequency on a wavemeter or other device capable of measuring relative frequencies with high precision. The known lines serve as the absolute frequency reference. However, it is unlikely that the radium transition is exactly overlapped with a known, absolute reference line. The wavemeter thus provides an accurate relative measurement, allowing us to extrapolate the absolute frequency of our desired transition by taking the laser frequency difference from a nearby known reference line. For the radium $^1P_1$ transition at 483 nm, the calibrating species with nearby transitions is generally diatomic tellurium (Te_2).

The measurement procedure would be as follows: first, we would scan across some Te_2 lines close to where we think the radium $^1P_1$ line is while co-recording the laser frequency on a wavemeter. By matching up the known lines with where we observed the lines, we can correct for any absolute frequency offset of our wavemeter, which will generally be stable over the course of this measurement. Then, while still co-recording the laser on our wavemeter, we would perform a scan of the radium $^1P_1$ transition. We can then take the center frequency of this scan and correct for the wavemeter offset from our earlier Te_2 measurement to obtain an absolute frequency measurement of the transition.

Now, after describing all of that, we unfortunately were not able to get a functioning measurement working with a Te_2 oven. Instead, we performed the absolute reference on a molecular iodine I_2 cell. The literature reference for iodine lines does not extend blue enough to use with our Ra $^1P_1$ laser, so we used a separate laser to perform the absolute referencing to iodine lines near 553 nm[38]. The idea was that the absolute offset of the wavemeter should not change too much over the range from 553 nm to 483 nm, and that an absolute calibration to known lines at one wavelength should apply to the majority of the wavemeter range.

To calibrate our wavemeter to iodine, we measured some lines in a room temperature I_2 vapor cell while monitoring the laser frequency on our wavemeter. Precise line center determination was achieved with a saturated absorption setup [138], eliminating the broadening effects due to Doppler shifts. These measurements are compared with the known lines in Figure 5.21.

We find the wavemeter offset by fitting our data to find the peak centers and comparing our measured centers against a database of known I_2 lines. We measured an isolated line at 18060.42939(2) cm^{-1} and identified this with a known line at 18060.43107 cm^{-1}. Taking the difference gives an absolute wavemeter offset of 0.00168(2) cm^{-1}, or 50.4 MHz.

Adding this offset value to our measured line center (and propagating the fit errors) gives an updated $^{226}Ra\ ^1S_0 \rightarrow {}^1P_1$ transition energy of 20715.6028(1) cm^{-1}.

5.4 RaOH

With these experimental upgrades in tow, we finally began our search for RaOH. Theoretical predictions put the transitions from the ground $\tilde{X}^2\Sigma^+(000)$ state to

[38] This wavelength was chosen because we already had a stable laser operating at this wavelength, and the iodine lines are well known in this region

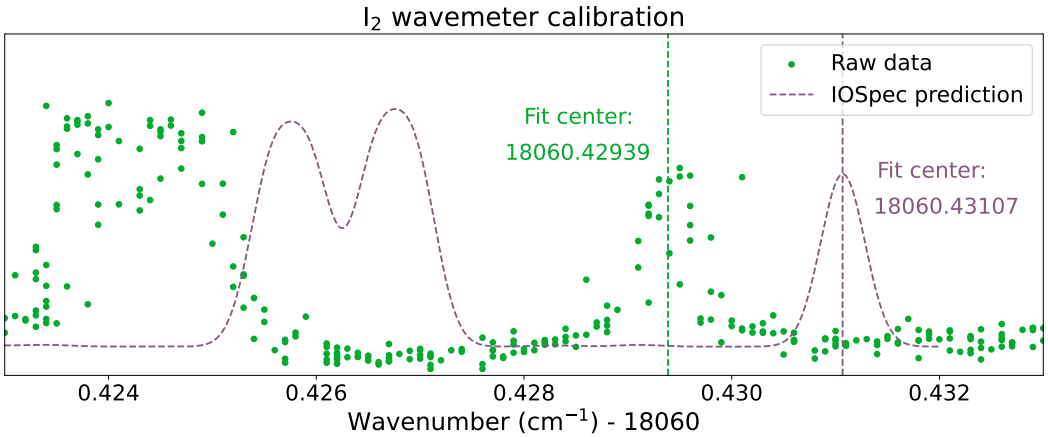


Figure 5.21: Saturated absorption (Doppler-free) scan of a few lines in molecular iodine. Green points are data, and dotted lines are the predicted I_2 spectrum from IOSpec5, a program based on measurements in [139]. This frequency range was chosen because our laser was already tuned to the $^1S_0 \rightarrow ^1P_1$ transition in barium at 553 nm. The dotted peaks correspond to the same transition, and the offset between the two is used to calibrate the wavemeter.

the $(v_1' v_2' v_3') = (000)$ levels of $\tilde{A}^2\Pi_{1/2}$ and $\tilde{C}^2\Sigma^+$ at $12798 \pm 160\ \mathrm{cm}^{-1}$ and $15749 \pm 160\ \mathrm{cm}^{-1}$, respectively [70]. Represented as wavelengths, these predictions correspond to search ranges from 771.1 nm to 791.3 nm for the $\tilde{A}-\tilde{X}$ band and 628.6 nm to 641.5 nm for $\tilde{C}-\tilde{X}$.

Initial detection of RaOH relied on our broadband linear cavity dye laser, with a linewidth $\Delta\nu \sim 1\ \mathrm{cm}^{-1} \sim 30$ GHz. The question about which transition to look for was answered by this laser, as our 5 W 532 nm pump[39] can only efficiently pump dyes in the visible range, producing light from roughly 550 to 650 nm. No suitable infrared laser dyes exist for driving the $\tilde{A}-\tilde{X}$ band unless we had a red-line pump, such a krypton laser, which we did not. As such, our first spectroscopy focused on the $\tilde{C}-\tilde{X}$ transition. All data for our radium-containing molecules, unless otherwise noted, also utilized roughly 1 W of chemical enhancement laser light on the ^{226}Ra $^3P_1$ line generated from a Ti:Sapphire laser at 714 nm.

Using our laser configured with DCM Special[40] dye, we searched for the $\tilde{C}\,^2\Sigma^+(000) \leftarrow \tilde{X}\,^2\Sigma^+(000)$ transition. To reject the intense, unstable broadband light, we optically filtered the excitation wavelength and detected the weaker decays to $\tilde{X}\,^2\Sigma^+(v_1 v_2 v_3)$, where $(v_1 v_2 v_3) = (100),\ (02^00),\ (02^20)$ are the possible decays within our filtering

[39] Coherent Verdi V-5
[40] DCM laser dye doped with some Kiton Red 620

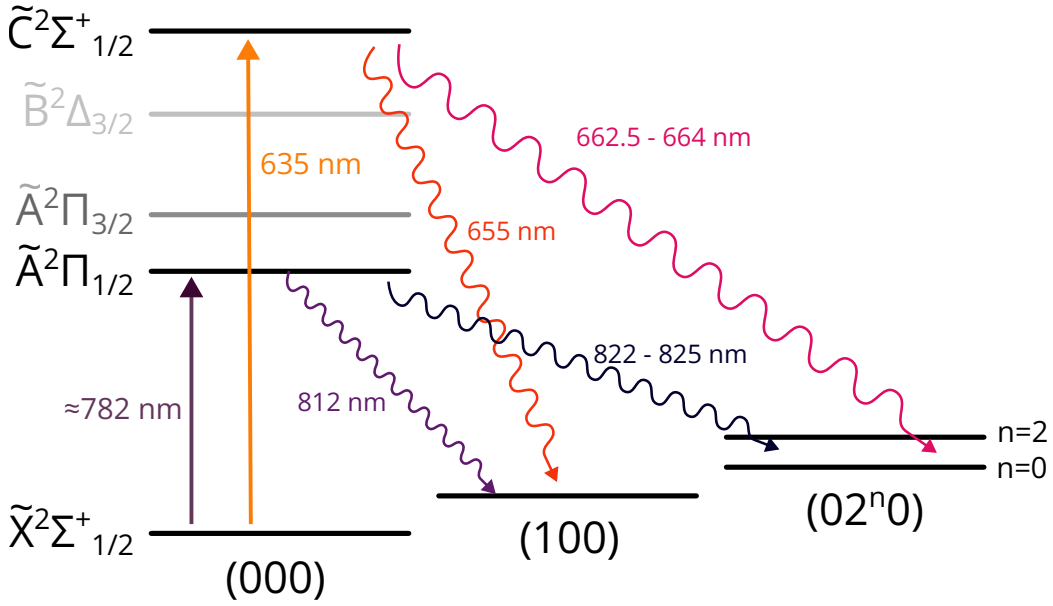


Figure 5.22: Level diagram for RaOH, showing wavelengths of relevancy to this data. Values for the $\tilde{A}$ state are approximate as the main line has not been rigorously identified yet. Numbers separated by – indicate the wavelengths of decays to both (02^{n}0) states.

range[41]. The results of this broadband scan are summarized in Figure 5.23.

Once we identified a region of interest in the broadband scan, we switched to using our fast pulsed dye laser with linewidth $\Delta\nu \sim 0.07$ cm^{-1} ~ 2.5 GHz in order to resolve the crude molecular structure. As we had yet to explicitly identify a transition in the molecule, this data was taken without normalization. At this medium resolution, we resolved clear rotational branch progressions which we were able to fit to an effective Hamiltonian model of a $\Sigma^+ - \Sigma^+$ transition with a large negative spin-rotation constant, commensurate with observations in the similar molecules YbOH [140] and BaOH [141] (see our Supplemental Text in [84] for discussion).

These medium resolution results encouraged us to push to even higher resolution. By using a single-longitudinal-mode ring cavity CW dye laser[42] with linewidth $\Delta\nu \sim$ 500 kHz, we mapped out 29 individual lines at Doppler-limited resolution of $\approx$ 100 MHz FWHM. A plot of all of these lines, with insets showing our strong SNR, is shown in Figure 5.24. We were able to fit each of these lines to a Voigt profile and extract line centers to $\sim$ MHz uncertainty. All identified lines are collected in Table 5.3.

[41]The filter stack used was: 2x FBH660-10 → BLP01-532R-25 → FESH0700 → FSR OG590 colored glass filter → FELH0650 → BLP01-532R-25 (again)

[42]Coherent 699

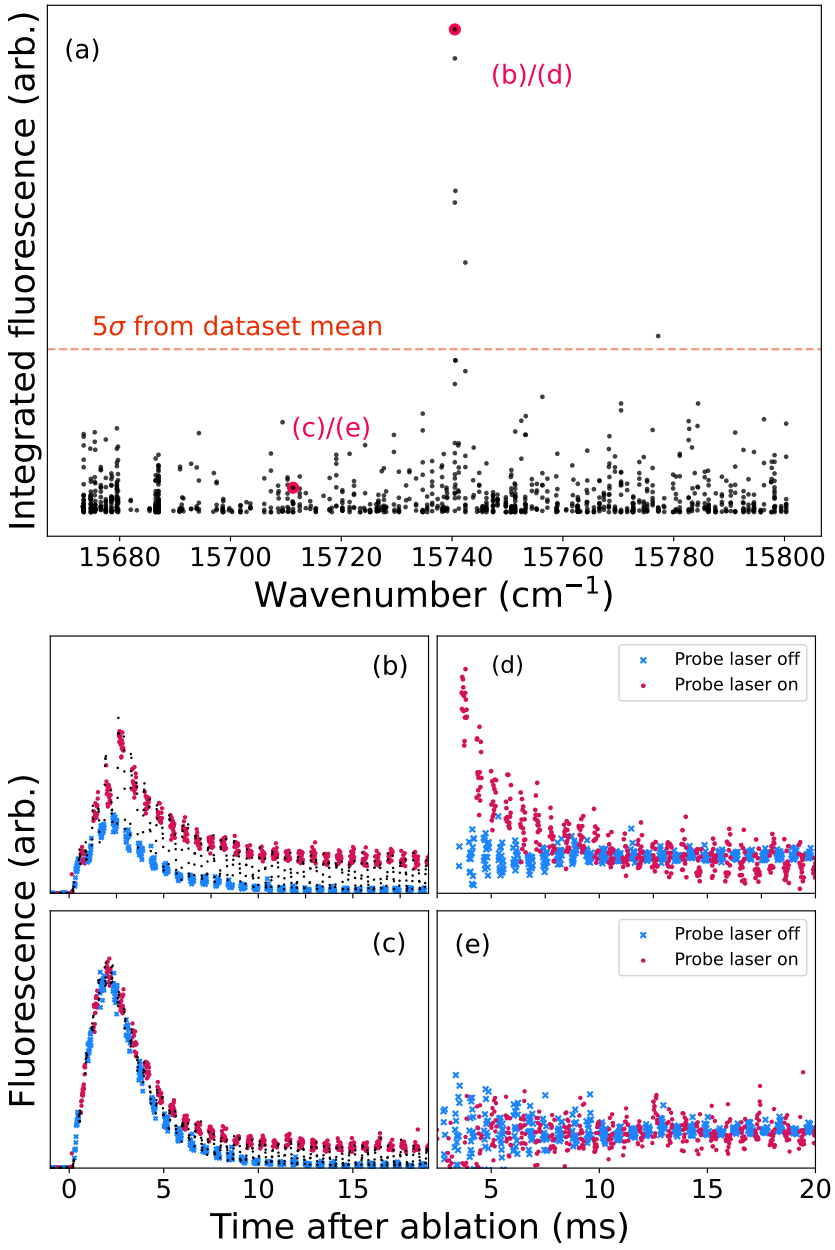


Figure 5.23: Low-resolution survey scan data showing the initial identification of RaOH band. The entire scan, which took one afternoon to perform, is shown in (a), highlighting the region of high fluorescence intensity near 15740 cm^{-1}. Raw data for highlighted points at 15740.5 and 15711.3 cm^{-1} are shown in (b) and (c), respectively, showing the early-time fluorescence due to nonresonant glow. Magenta (blue) points are when the laser is unblocked (blocked) through the cell, and black is the switching region between the two. The modulation frequency is only 1.5 kHz as this data was taken using a mechanical chopper wheel instead of an acousto-optic modulator as in later data. Traces (d)/(e) show the background-subtracted signal of (b)/(c), emphasizing the excess fluorescence present at early time when the laser is resonant and passing through the cell in (b).

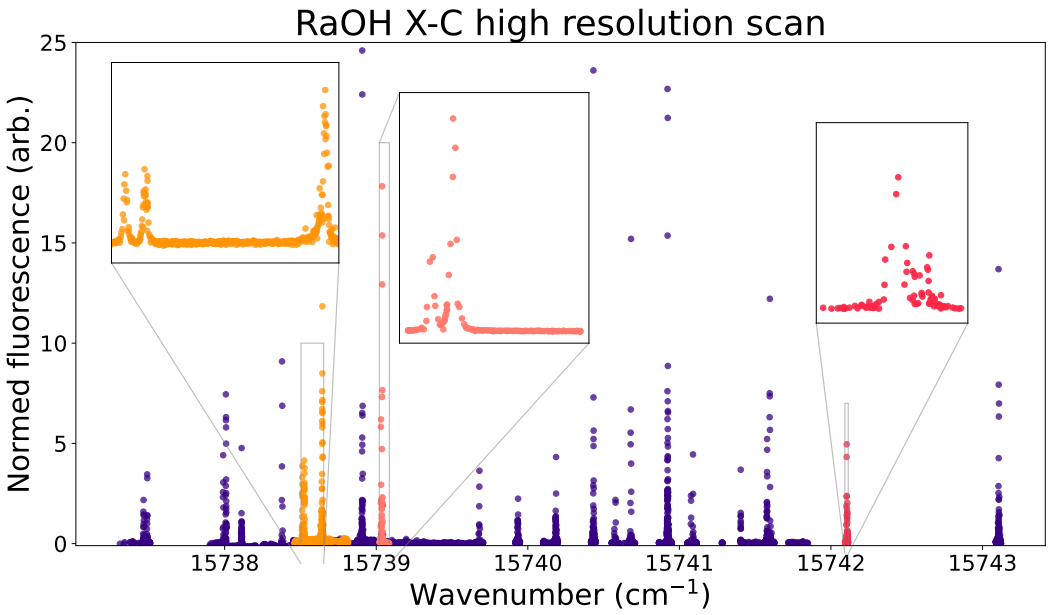


Figure 5.24: High-resolution scan of RaOH $\tilde{C}\,^2\Sigma^+(000) \leftarrow \tilde{X}\,^2\Sigma^+(000)$. Data was normalized using our pulsed dye laser signal to account for production fluctuations. Colored insets show zoom-ins on specific data ranges, emphasizing the good lineshapes with strong SNR. Not all of the range was scanned; once we had located enough lines to accurately predict the progressions, we stopped measuring in regions where no lines were expected so as not to waste our limited material. To see a version of this plot where the rotational branches are explicitly shown, see our publication [84].

From these line positions, we were able to fit an effective molecular Hamiltonian:

$$\hat{H} = B_0''\hat{N}_g^2 + \gamma''\hat{N}_g \cdot \hat{S}_g + T_0 + B_0'\hat{N}_e + \gamma'\hat{N}_e \cdot \hat{S}_e\,, \tag{5.4}$$

where the g, e subscripts (in addition to the double and single primes) refer to the ground and excited states, respectively. This fit allowed extraction of the rotational constant B_0, spin-rotation constant γ, and excited state origin energy T_0. These values, as well as their predictions against theory, described in detail in our publication [84].

Even though we had a good sense that these lines corresponded to RaOH, we still performed a number of sanity checks. We confirmed that the signal required ablating both the radium drop cast target and the $Al(OH)_3$ reagent co-target by removing one at a time. We also confirmed that the signal correlated with sending in resonant $^3P_1$ enhancement light (see Figure 5.29 for a plot of this in RaOD, or [84] for a plot showing the resonant behavior in RaOH). All of these checks provided further evidence that our molecule was RaOH.

Branch	N''	J'	Observed (cm^{-1})	Branch	N''	J'	Observed (cm^{-1})
${}^{P}P_{11}$				${}^{P}P_{22}$			
	1	1/2	15739.03143(4)		2	1/2	15738.9078(2)
	2	3/2	15738.51250(8)		3	3/2	15738.64436(3)
	3	5/2	15737.9902(2)		4	5/2	15738.37921(1)
	4	7/2	15737.4653(1)		5	7/2	15738.1116(1)
${}^{P}Q_{12}$				${}^{R}Q_{21}$			
	1	1/2	15739.03924(2)		0	1/2	15740.06471(5)
	2	3/2	15738.52575(9)		1	3/2	15740.57113(5)
	3	5/2	15738.0086(2)		2	5/2	15741.07680(3)
	4	7/2	15737.48898(9)		3	7/2	15741.5787(1)
${}^{R}R_{11}$				${}^{R}R_{22}$			
	0	3/2	15739.6815(2)		1	3/2	15740.57882(3)
	1	5/2	15739.9346(2)		2	5/2	15741.08966(2)
	2	7/2	15740.1851(1)		3	7/2	15741.59675(10)
	3	9/2	15740.4329(1)		4	9/2	15742.1041(2)
	4	11/2	15740.68031(6)		5	11/2	-
	5	13/2	15740.92336(9)		6	13/2	15743.10720(2)

Table 5.3: List of high-resolution observed lines in RaOH. Double prime refers to ground state and single prime to excited state. The branch assignments are denoted by ${}^{\Delta N}\Delta J_{F_i' F_i''}$, where $F_i = F_{1,2}$ refers to the $J = N \pm 1/2$ spin-rotation components, and *not* the total angular momentum. For the comparison with predicted values, see [84].

Attempts at $\tilde{A} - \tilde{X}$

After first identifying the $\tilde{C} \leftarrow \tilde{X}$ transition in RaOH, we wished to do the same for the $\tilde{A} \leftarrow \tilde{X}$ band, as this is the main line which would be used in any laser cooling or molecular EDM experiment.

As mentioned at the beginning of the RaOH section, finding a suitable broadband laser system in the infrared range presented the largest challenge, as no laser dyes absorb 532 nm and emit near 780 nm efficiently. Recall the linewidth of our linear cavity dye laser is $\Delta\nu \sim 1$ cm^{-1}, so a decent amount of output power is required to achieve high power spectral density; even when we park the laser on the band head, only $\lesssim 1\%$ of the broadband laser light will be resonant with any molecular transition. Without output power in the $\gtrsim$ 100's of mW, finding any molecule fluorescence requires as much luck as it does patience.

Another feature that makes the $\tilde{A} - \tilde{X}$ band great for the molecule but challenging for our detection scheme is its predicted laser-coolability. Laser cooling transitions in molecules have a high probability of maintaining their vibrational level through

the excitation-deexcitation process—this enables the repeated cycling of entropy-removing photons (see the next Chapter 6 for more context). Our measurement scheme, in order to filter out the strong broadband light from our survey laser, requires detecting these vibration-changing decays. Predicted branching out of the $\tilde{A}(000)$ to both $\tilde{X}(100)$ and $\tilde{X}(02^00)$ is roughly 1% [69], around $1/3 - 1/4$ of that for the $\tilde{C} - \tilde{X}$ transition[43]. As we later observed with RaF (see Chapter 6), these molecules might have significantly better branching ratios than were calculated, making our detection scheme even more challenging.

For our survey scan of the $\tilde{A} - \tilde{X}$ band, we tested two methods of generating the desired broadband IR light. The first was simply to use the best dye available at these emission wavelengths, LD700, with our linear cavity dye laser. Unfortunately, repeated scans across the full uncertainty range did not yield any detectable molecule fluorescence. The dye had a tendency to degrade quickly, dropping in power significantly over the course of one day of data.

The other method, and one which we are still improving, involves broadening a narrow-linewidth laser using electro-optic modulators (EOMs). EOMs can be used to add sidebands to a carrier laser frequency, spaced from the carrier by some applied RF drive on the EOM. If we take a 50 MHz resonant EOM and drive it with extremely high RF power, we can apply many orders of sidebands to our carrier laser frequency, creating a forest of narrow lines spaced by 50 MHz. Given that any molecular transitions in our cell are broadened due to the finite Doppler temperature, this essentially turns our single-frequency laser into a broadened-linewidth laser. This method has the advantage of allowing us to use a Ti:Sapphire laser as the initial light source, of which we have many stable and high power options available to us. We achieve roughly $10 - 20$ orders of sidebands from our 50 MHz EOM circuit[44], bringing our initial $\sim$ 500 kHz laser to around a $1 - 2$ GHz linewidth. Still, at this level, we are not doing any better than we would if we simply used our pulsed dye laser, which has the advantage of significantly higher instantaneous intensity during its pulses. We instead further broaden the CW laser by sending this resulting light into a resonant 2 GHz EOM[45], which allows us to reach a final linewidth of nearly 20 GHz. Throughout all of this, the degree of broadening depends on the RF power we send to the EOMs, meaning that we could theoretically use this procedure to achieve all levels of spectro-

[43] This value of $1/3 - 1/4$ comes from communications with our collaborator Lan Cheng at Johns Hopkins, who performed the calculations for the $\tilde{A} - \tilde{X}$ band as well.

[44] PM8-NIR_50, with associated RF driver, from Qubig

[45] PM9-NIR_2.0, with associated RF driver, from Qubig

scopic resolution without changing the laser system. This mode of laser broadening was initially implemented by Yuxi Yang and Phelan Yu, and has been picked up by Xukun Lin for further development.

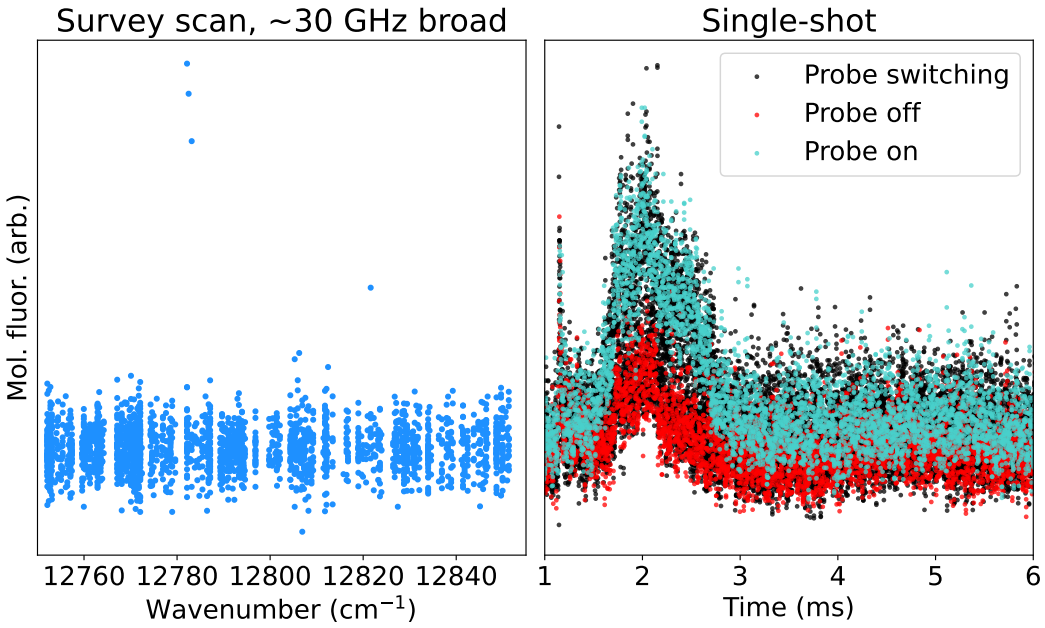


Figure 5.25: Initial survey scan of the RaOH $\tilde{A} - \tilde{X}$ band near 782 nm. To achieve $\sim$ 30 GHz linewidth in the infrared range, we broadened a Coherent 899 Ti:Sapphire laser according to the methods described in the text. Regions of excess fluorescence were identified around 12782 cm^{-1}, only 16 cm^{-1} away from the predicted value [70]. The plot on the right shows the highest-SNR single shot from the scan.

Figure 5.25 shows the result of a full survey scan with the maximum achievable broadening. A couple regions of note, notably around 12782 cm^{-1}, yielded a few shots with what appeared to be excess fluorescence, just as we had seen with the $\tilde{C} - \tilde{X}$ band. We then narrowed our search space by cutting power to the 2 GHz EOM. With a new linewidth of around 3 GHz, we scanned the regions of excess fluorescence identified in Figure 5.25. Confusingly, we were unable to find any signals near 12782 cm^{-1} in this configuration. We repeated this measurement a number of times and could not replicate this fluorescence.

During the initial survey, we also identified the region around 12806 cm^{-1} as potentially yielding some signals. When we re-scanned this range with our laser configured to medium-resolution, we saw some unambiguous fluorescence traces, shown in Figure 5.26.

All of this above $\tilde{A} - \tilde{X}$ data was taken before we had improved our targetry through

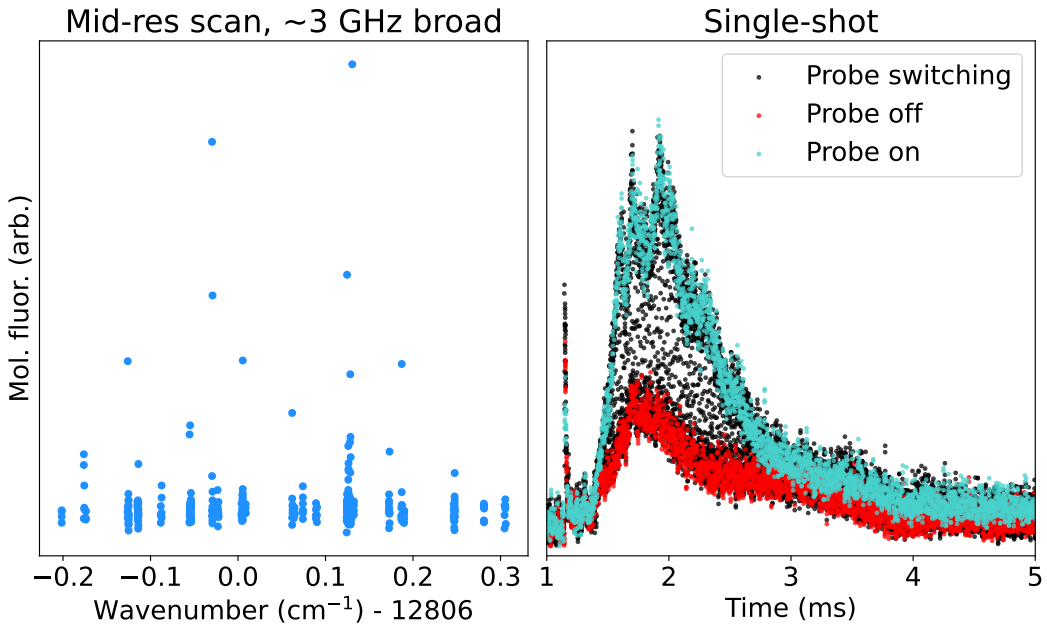


Figure 5.26: Medium resolution scan of RaOH $\tilde{A} - \tilde{X}$ near 781 nm. As mentioned in the text, our repeated measurements could not corroborate the excess fluorescence indicated by the low resolution scan, but a number of shots showed signal near 12806 cm^{-1}. The plot on the right shows the highest-SNR single shot from the scan.

the addition of xylitol or the implementation of two PMTs simultaneously. As such, shot-to-shot fluctuations were considerable and we had no means of performing normalization.

After implementing the xylitol protocol we made a few more attempts at repeating this measurement, both with the same laser systems as well as with the pulsed dye laser. We tried driving the main line as well as the vibration-exciting line $\tilde{A}(100) \leftarrow \tilde{X}(000)$, with the hopes that the stronger decays from this transition would be easier to observe. Unfortunately, in none of these configurations did we find anything significant, and with the progress we were making on the $\tilde{C} - \tilde{X}$ high resolution spectroscopy, this work was tabled. Given our developments and strong SNR on the $\tilde{C} - \tilde{X}$ transition, we were definitely surprised to have so much trouble finding this first excited state.

5.5 RaOD

Another way of verifying production of RaOH is to measure an isotope shift. Exchange of the protium and deuterium isotopes ^{1}H $\rightarrow$ ^{2}H (henceforth written as H $\rightarrow$ D) modifies the zero-point vibrational energies, shifting the band head by a few wavenumbers [142]. This shift is relative, meaning it does not involve a separate computation of the electronic energies for the molecule, which is where most of the

transition uncertainty originates. Thus, we should be able to easily observe RaOD once we find the RaOH band head—if not, this means we likely do not have the right molecule. The extra mass of D compared to H will also modify the molecular moment of inertia I, which factors into the measurable rotational constant B via $B = \frac{\hbar}{4\pi c I}$. Thus, measurement of the rotational progression will confirm whether this scaling behaves as expected for RaOH → RaOD, providing yet another piece of evidence for the observation of RaOH.

To produce RaOD, we co-ablated our radium drop cast target and a reagent co-target of pressed aluminum deuteroxide ($Al(O^2H)_3 \equiv Al(OD)_3$). We synthesized this molecule ourselves as it is not commercially available; details of the synthesis procedure are given later in this section.

Survey spectroscopy on the RaOD $\tilde{C}^2\Sigma^+ \leftarrow \tilde{X}^2\Sigma^+$ origin band utilized only the $\Delta\nu \sim 2.5$ GHz linewidth pulsed dye laser, as the isotope-shifted band head could be predicted much more precisely given our prior observation of the same transition in RaOH. This shift was calculated to be roughly 9 cm^{-1} red of RaOH [70]. Initial scans covering 15719 cm^{-1} to 15741 cm^{-1} identified a strong fluorescence signal at $\sim$ 15729 cm^{-1}, redshifted from RaOH by $\sim$ 9 cm^{-1}. A subsequent finer-grained scan around this region is shown in Figure 5.27.

Following this, just as with RaOH, we scanned a narrow-linewidth laser to resolve the low-N lines in high-resolution, identifying a total of 32 spectral features. The scans corresponding to these features, as well as their spectroscopic assignments, are shown in Figure 5.28. The centers of these lines were determined via Voigt profile fits and collected in Table 5.4. We performed a similar fit to an effective molecular Hamiltonian to extract molecular constants B_0 and γ for both the ground and excited states, detailed in our publication [84].

To further identify this molecule as RaOD, we took data while ablating the different co-targets to demonstrate correlation of RaOD fluorescence with ablation of our $Al(OD)_3$ co-target. We also performed the chemical enhancement checks, as we did with RaOH. Data for both of these are shown in Figure 5.29.

Synthesizing aluminum deuteroxide

In order to produce radium deuteroxide (RaOD), we needed an ablation source of deuteroxyl (-OD) groups. The most logical choice would be the deuterated version of our hydroxide source, $Al(OD)_3$. Unfortunately, while certain deuterated compounds can be easily purchased, aluminum deuteroxide is not one of them; if we wanted the

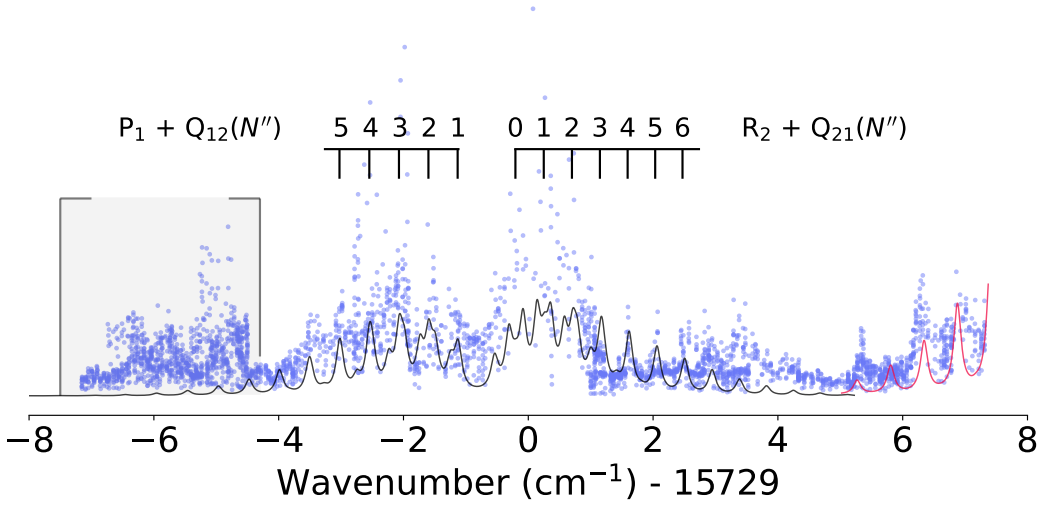


Figure 5.27: Medium-resolution (~ 0.07 cm^{-1}) pulsed dye spectrum identifying the band head and coarse features in RaOD. Black overlaid lines are the predicted spectrum at the recorded linewidth and temperature of 7 K. Red lines are the prediction for RaOH, which we observe because of hydroxide residue in our target materials. The grayed region to the left is believed to be the $\tilde{C}(100) - \tilde{X}(100)$ vibrational overtone in RaOD, which is expected to be redshifted from the main line by ~ 4 cm^{-1}

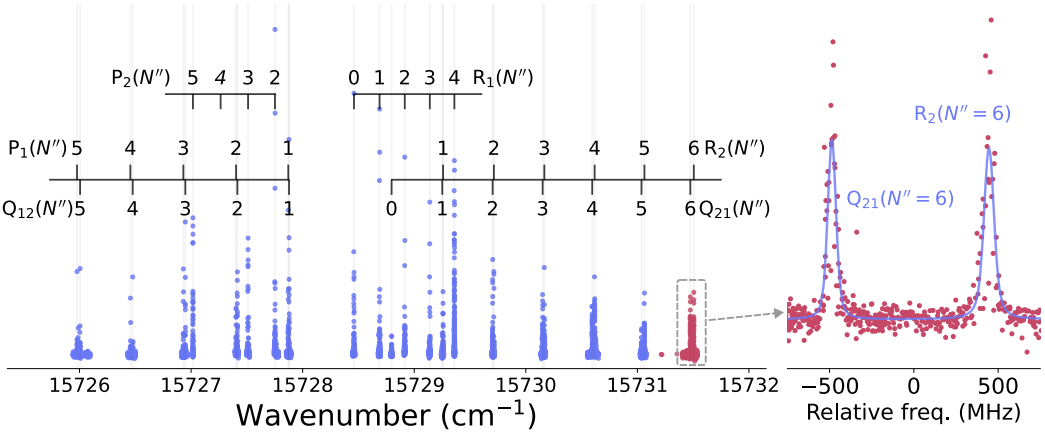


Figure 5.28: High-resolution spectrum of the low-N region in RaOD, identifying the 31 lines used in the Hamiltonian fit. The $P_2(N'' = 4)$ line was not scanned. The R-branch $N'' = 6$ doublet from this spectrum is enlarged on the right, overlaid by the Voigt profile fits that were used to extract line centers.

deuteroxide co-target that is most similar to ours for hydroxide, we would need to synthesize it ourselves.

We were unable to find a guide to synthesizing $Al(OD)_3$. However, there are published instances of producing $Al(OH)_3$ from a number of different reaction pathways. Since deuterium, or ^{2}H, is just an isotope of hydrogen, our logic was to find which of these

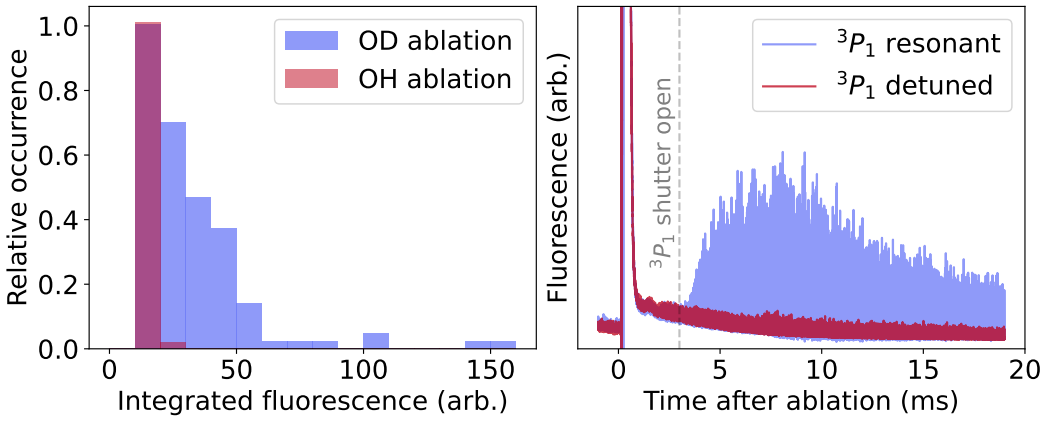


Figure 5.29: Plots showing effects identifying this molecule with RaOD. Left: Histogram of RaOD fluorescence signals while ablating hydroxide and deuteroxide co-targets. A strong line in the RaOD spectrum was probed as the reagent ablation laser was switched between the $Al(OD)_3$ and $Al(OH)_3$ pellets, resulting in a fluorescence signal only when vaporizing the deuterated target. Right: Time trace for representative fluorescence signals when our enhancement laser was on and off resonance with the $^3P_1$ transition at 13999.357 cm^{-1}. In both cases, a mechanical shutter opens at 3 ms to allow the light to enter the cell, showing the signal enhancement achieved when this laser is resonant with the transition in ^{226}Ra.

reactions sourced the hydrogen from a reagent which could be easily replaced with a commercially available deuterated version. From a literature search, we identified the reactions that have been performed (or claimed to have been performed) that also satisfy the reagent substitution condition as follows[46]:

$$\begin{aligned} Al_4C_3 + H_2O &\rightarrow Al(OH)_3 + CH_4 \\ NaAlO_2 + H_2O \rightarrow NaAl(OH)_4 + H_2O &\rightarrow Al(OH)_3 + NaOH \\ AlCl_3 + (Na,K)OH &\rightarrow Al(OH)_3 + (Na,K)Cl\,(aq.) \\ AlN + H_2O &\rightarrow Al(OH)_3 + NH_3\,. \end{aligned}$$

Heavy water (D_2O), and simple deuterated acids and bases (NaOD, KOD, DCl) are commercially available, as are the starting sources of aluminum listed above. Despite attempting all of the above reactions besides the second one, and the fact that they are simple one-step procedures, the bottom reaction was the only one we were able to reproduce.

[46]Note that none of these reactions are stoichiometrically balanced.

Branch	N''	J'	Observed (cm^{-1})	Branch	N''	J'	Observed (cm^{-1})
${}^{P}P_{11}$				${}^{P}P_{22}$			
	1	1/2	15727.871(1)		2	1/2	15727.752(2)
	2	3/2	15727.403(2)		3	3/2	15727.511(8)
	3	5/2	15726.931(3)		5	9/2	15727.016(4)
	4	7/2	15726.456(4)		9	17/2	15725.988(2)
	5	9/2	15725.978(1)				
${}^{P}Q_{12}$				${}^{R}Q_{21}$			
	1	1/2	15727.8780(9)		0	1/2	15728.797(1)
	2	3/2	15727.415(2)		1	3/2	15729.251(5)
	3	5/2	15726.948(3)		2	5/2	15729.703(1)
	4	7/2	15726.478(2)		3	7/2	15730.151(9)
	5	9/2	15726.004(2)		4	9/2	15730.595(6)
					5	11/2	15731.037(2)
					6	13/2	15731.475(3)
${}^{R}R_{11}$				${}^{R}R_{22}$			
	0	3/2	15728.460(2)		1	3/2	15729.259(1)
	1	5/2	15728.689(3)		2	5/2	15729.714(2)
	2	7/2	15728.915(2)		3	7/2	15730.166(1)
	3	9/2	15729.140(2)		4	9/2	15730.617(5)
	4	11/2	15729.360(1)		5	11/2	15731.063(6)
					6	13/2	15731.506(5)

Table 5.4: List of high-resolution observed lines in RaOD. Double prime refers to ground state and single prime to excited state. The line assignments are denoted by ${}^{\Delta N}\Delta J_{F_i' F_i''}$, where $F_i = F_{1,2}$ refers to the $J = N \pm 1/2$ spin-rotation components, *not* the total angular momentum. For the comparison with predicted values, see [84].

The reaction $AlN + 3H_2O \rightarrow Al(OH)_3 + NH_3$ was reported in [143]. When we set out to test this synthesis we were running low on heavy water, so we first tried the actual reaction listed rather than the deuterated version.

We placed a beaker of 100 ml DI water on a hot plate, heated to 40°C and gently stirring. Using a pH strip we verified that the pH of the water was $4 - 5$ as expected[47]. We then added AlN such that it was 3% w/v (3 g/100 ml) and stirred the solution for ~24 hours, measuring the pH along the way to verify it reaches $\sim 9 - 10$, indicating the formation of NH_3. This pH change happened between 45 and 90 minutes. Accompanying this pH change was the formation of a precipitate.

Since this appeared to work, we proceeded with heavy water instead of water by adding 3.675 g of AlN into 100 ml of D_2O, heating and stirring as previously. The

[47] Pure DI water will absorb CO_2 from the air to form carbonic acid, turning it slightly acidic.



Figure 5.30: $Al(OH)_3$ precipitate.

solution did become basic, but took significantly longer (> 2 hours), which could be because we were not pre-warming the heavy water but also because the reaction kinetics are slower. In order to ensure the reaction proceeded fully, we let the sample stir on the hot plate for two days. The beaker was covered with plastic wrap to prevent evaporation of the D_2O and ND_3.

After both solutions were left to react, we extracted the supernatant and poured the powder slurry onto weighing boats. Both were placed into a vacuum oven where the $Al(OH)_3$ was dried for 6 hours at 60°C and the $Al(OD)_3$ for 24 hours at 50°C. This was not enough time to fully dry the hydroxide unfortunately, as evidenced by the clumpiness of the resulting power. The deuteroxide dried fully, and we used a mortar and pestle to turn it into a fine powder with a final mass of 6.13 g. Assuming a full conversion to $Al(OD)_3$, this corresponds to an experimental yield of 85%.

Verification of $Al(OD)_3$ **synthesis**

To prove that what was synthesized was truly $Al(OD)_3$, we tested a sample of the powder at the Caltech solid state NMR facility, the results of which are summarized in Figure 5.32. ^{2}H NMR was performed to verify the presence of deuterium as indicated by a characteristic Pake doublet. ^{1}H and ^{27}Al NMR were performed on both the homemade $Al(OD)_3$ powder as well as a commercially available $Al(OH)_3$ sample to verify that the two materials were structurally similar despite ours containing a significantly reduced amount of ^{1}H.



Figure 5.31: Aluminum deuteroxide powder after drying in the vacuum oven and crushing with mortar and pestle.

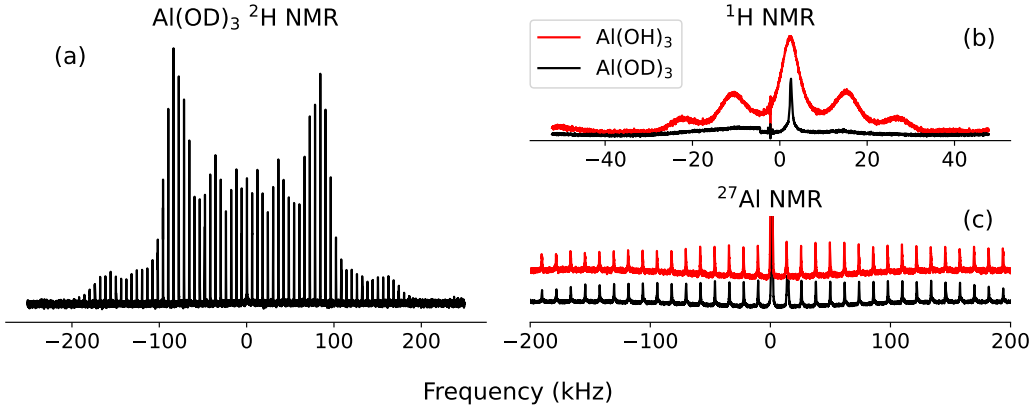


Figure 5.32: ^{2}H magic-angle spinning NMR spectrum confirming synthesis of aluminum deuteroxide powder. The two peaks near ±84 kHz form a Pake doublet corresponding to the $I = -1 \rightarrow 0$ and $I = 0 \rightarrow 1$ transitions in deuterium, which are split into narrow sidebands separated by the magic-angle spinning frequency of 6 kHz. (b) ^{1}H NMR of synthesized $Al(OD)_3$ against commercial $Al(OH)_3$. The integrated signals indicate that the synthesized sample is roughly 5% H instead of D, likely owing to uncontrolled ambient humidity during synthesis. (c) ^{27}Al magic-angle spinning NMR of both samples (offset for visibility), demonstrating structural agreement between the two. This data was taken by Sonjong Hwang, who also greatly assisted with the interpretation.

5.6 RaF

Significant spectroscopy has been performed on the various isotopologues of RaF at CERN's ISOLDE facility. Work on our end largely focused on performing high-resolution line center determinations of the low-J laser cooling and repump lines, a challenging measurement to perform in their accelerated molecular beams owing to their broader lineshapes.

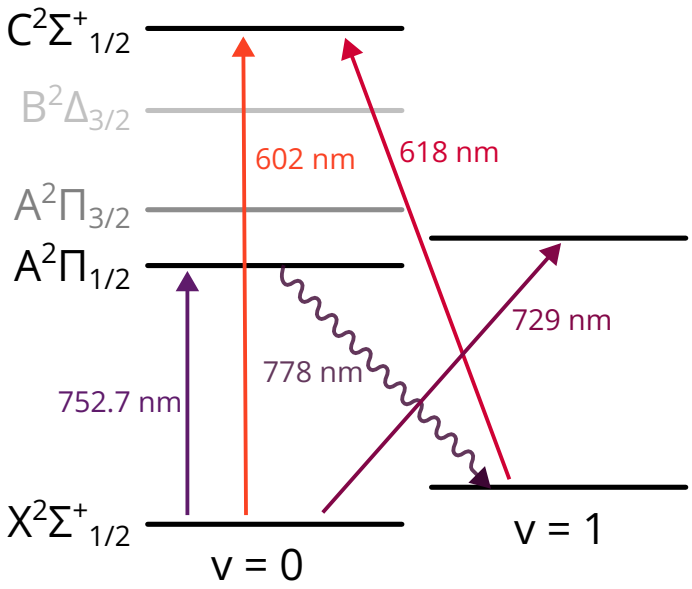


Figure 5.33: Level diagram showing the relevant states and transitions in RaF. Arrows indicate driven transitions, which might have also been used for fluorescence detection, and wiggly lines indicate lines only used for fluorescence detection.

As further elaborated in Chapter 6, RaF is predicted to have extremely favorable vibrational branching ratios, making it a great laser cooling candidate. Rotational closure for this type of molecule is achieved by driving the $P_1(1.5)$ and $Q_{12}(0.5)$ lines on the $A\,^2\Pi_{1/2} - X\,^2\Sigma^+$ band (see Fig. 2.4). The band head, shown in Fig. 5.34, is quite congested, making clean determination of the $Q_{12}(0.5)$ line impossible without employing a doppler-free spectroscopic technique, as it is obscured by the (stronger) overlapping $P_1(2.5)$ line. The $P_1(1.5)$ line, on the other hand, is isolated enough to be fit on its own. To obtain an absolute frequency measurement, we took this spectrum and then scanned across the D2 line in atomic potassium, which is known absolutely to very high precision [144], allowing us to correct for our wavemeter offset.

The potassium data contains 18 overlapping hyperfine transitions from the isotopes ^{39,40,41}K. Because ^{39}K makes up $\sim 93\%$ of the natural abundance, only the six transitions from this isotope were considered in the modeling. Relative intensities $S_{FF'}$ of the transitions from ground hyperfine state F to excited state F' were obtained from the equation[48] [145]:

$$S_{FF'} = (2F+1)(2F'+1)\begin{Bmatrix} F & F' & 1 \\ J' & J & 1 \end{Bmatrix}^2 . \tag{5.5}$$

[48]Note that the book equation includes a term $S_{JJ'}$ in order to report the absolute intensity. Because the J, J' values are the same within the D2 lines, this is just a global intensity shift, which is a value we floated in our fits anyways.

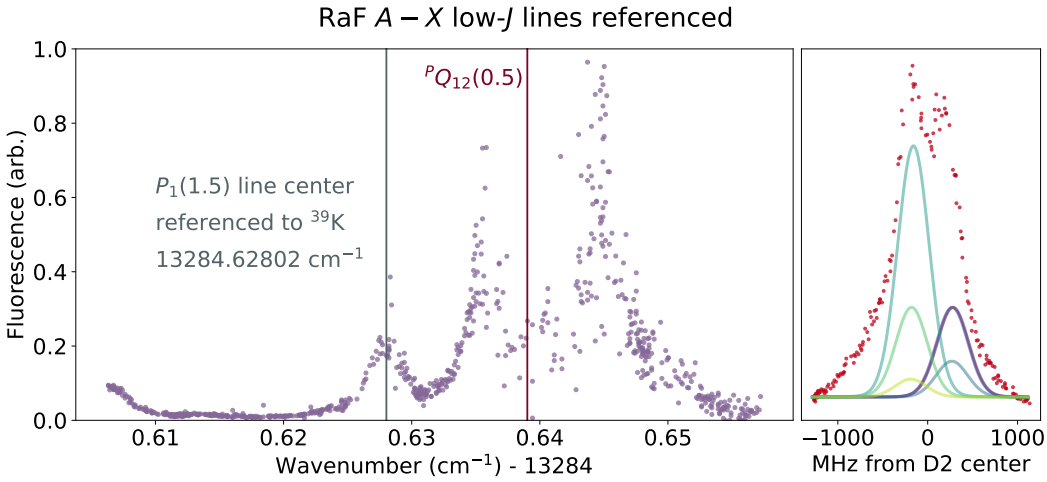


Figure 5.34: Measurement of the low-J lines on the RaF $A-X$ transition. The $P_1(1.5)$ cycling line is isolated enough to establish a clean line center, which we referenced to the potassium D2 transition [144]. The other cycling line $^{P}Q_{12}(0.5)$ unfortunately overlaps with the (stronger) $P_1(2.5)$ line, which is the peak around 13284.635 cm^{-1}, as well as a cluster of P_1 lines at around 13284.645 cm^{-1}. The right panel data points show our scan over the potassium D2 line, with the curves below representing the six hyperfine transitions and their relative intensities. The sum of these were used to fit the measured D2 line shape to determine the center frequency and extract a wavemeter offset, which is applied to the RaF data on the left.

From here, we were able to fit the measured D2 spectrum to a sum of Voigt profiles with these relative intensities to extract our wavemeter offset, which we then applied to the RaF low-J spectrum.

In previous work on RaOH, we were never able to detect the molecules via absorption measurements. Given that we generally produce diatomic molecules around 10 times more efficiently than polyatomics, we attempted this detection scheme again with RaF this time, looking for absorption of our laser around the strong $P_1(2.5)$ line near 13284.6361 cm^{-1}. Figure 5.35 shows these results. We observed a peak molecule density of roughly $\approx 6 \times 10^7$ cm^{-3} in the $N'' = 2$ rotational state, the first direct determination of radium-containing molecule density inside the Minifridge. From the Boltzmann population at 7 K (recall Equation 4), and with the value for the rotational constant B which we determined in [84], this represents around 15% of the total molecule population, meaning we can estimate a peak density inside the cell of around 4×10^8 cm^{-3}; assuming a uniform distribution of molecules throughout the entire cell volume yields a total molecule number of roughly 2×10^{10}.

Recently, we mapped out the $^{P}P_{11}(1.5)$ and $^{P}Q_{12}(0.5)$ repumping transitions on

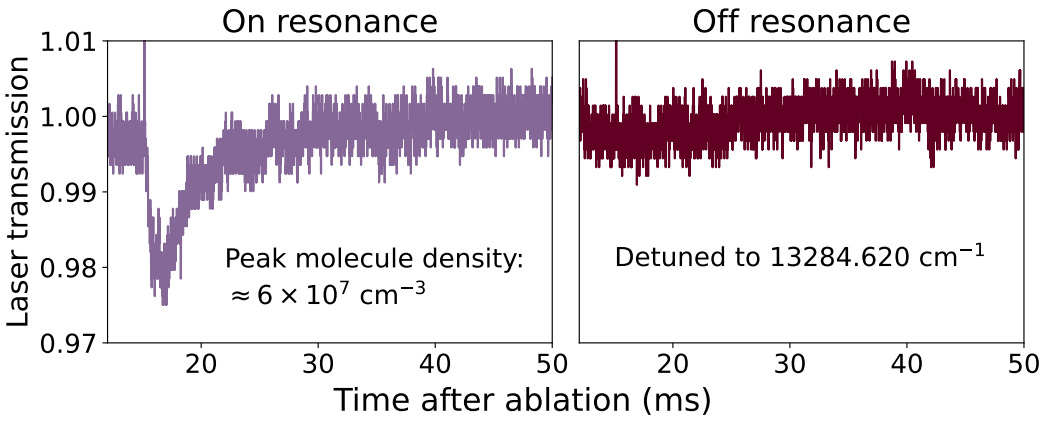


Figure 5.35: Resonant absorption signals for RaF around the $P_1(2.5)$ and ${}^{P}Q_{12}(0.5)$ lines. Using Eq. 5.1, we convert this laser transmission dip into an approximate molecule density, where this number refers to just the density of molecules that are in this exact $N'' = 2$ rotational state. Using the proper Boltzmann statistics assuming thermalization with the helium buffer gas at 7 K, this means a peak total molecule density of $\sim 4 \times 10^8$ cm^{-3}

the $C\,^2\Sigma^+(0) \leftarrow X\,^2\Sigma^+(1)$ band to high resolution as well, representing the last lines needed to begin laser cooling. We also performed a scan of the $C(0) - X(0)$ band, where we observed a parity-dependent hyperfine splitting originating from the fluorine nuclear spin; Figure 5.18 from earlier shows an example of one of these hyperfine doublets, whose origin we are actively working to understand. A full analysis and description of all of these recent results is ongoing.

5.7 RaCl

Technically speaking, RaF is not actually the first nor the only radium-containing molecule to be studied spectroscopically. In fact, its identification comes nearly 70 years *after* the detection of two bands assigned to radium chloride (RaCl) [146]. This data, taken by diffracting a hollow cathode discharge of $RaCl_2$, was recently re-analyzed [147] to give band head positions with a quoted precision of $\approx$ 30 GHz. These bands tentatively correspond to transitions out of the ground $X\,^2\Sigma^+$ state to the excited states $A\,^2\Pi_{3/2}$ and $C\,^2\Sigma^+$ at 14786.57 cm^{-1} and 15390.75 cm^{-1} (676.3 nm and 649.7 nm), respectively.

Given the prior existence of this data, and the relative ease with which we have been able to produce and detect RaF after our many experimental improvements, it should be straightforward to observe RaCl. While an in-depth investigation of the molecule is not presently of interest, there are a few justifications for its study: first, RaCl

is predicted to be laser-coolable, albeit to a lesser extent than RaF [147, 148]. The dichloride $RaCl_2$ is also one of the few radium-containing compounds to see industrial use, used as a nuclear medicine [149] and in the separation of radium from uraninite. Finally, extending past RaCl to RaBr and RaI (and even RaH, RaD, and RaT) would enable a systematic study of the radium + halide(-like) diatomics, of possible utility for benchmarking and improving quantum-chemical calculations.

Production of RaCl followed from co-ablation of the xylitol-based radium drop cast target with a pressed powder of silver chloride (AgCl). To make this target, 0.2 g of silver chloride powder was pressed in an 8 mm die press for 30 minutes at 1 GPa; no binding agents or other additives were used. For details about the selection of this co-target, as well as tests performed on CaCl and CaI, see Section 7.2. Like with RaF, production of RaCl benefitted from chemical enhancement using 850 mW of Ra $^3P_1$ light at 13999.357 cm^{-1}.

Rather than probing the $C^2\Sigma^+(0) \leftarrow X^2\Sigma^+(0)$ main line at 649 nm and detecting the weak fluorescence to the $X^2\Sigma^+(1)$ state, we opted to instead drive the vibration-exciting transition $C^2\Sigma^+(1) \leftarrow X^2\Sigma^+(0)$ at 639 nm and detect the strong diagonal fluorescence down to $X^2\Sigma^+(1)$. This is the same scheme we used for our initial published medium-resolution spectrum of RaF [84]. Thanks to the large instantaneous intensities of our high-repetition rate pulsed dye laser, driving this weak transition is straightforward. We were easily able to identify what appeared to be the band head with strong SNR, with single-shot data shown in Figure 5.36. After a few hundred ablation shots, we obtained a medium-resolution spectrum (Figure 5.37), showing a deviation of the band head from the predicted value by a few wavenumbers.

While not technically the first spectroscopy of RaCl, this represents its first *laser* spectroscopy. We demonstrated relatively straightforward production, which was refreshing for a new radium-containing molecule, and indicates that similarly easy production should be possible for the other halides RaBr and RaI as analogous co-targets exist. Unfortunately, this is where the work on RaCl stopped; there is still a significant amount of low-hanging spectroscopic fruit left with this molecule that could provide insight into the nature of the chemical bonding characteristics of radium.

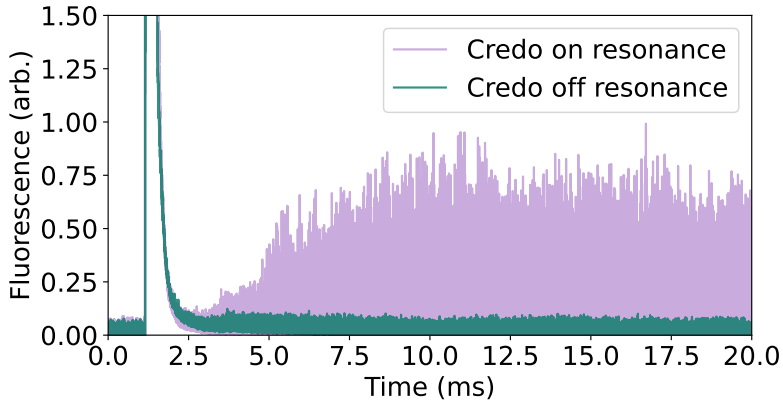


Figure 5.36: Single-shot fluorescence signals from driving the RaCl $C^2\Sigma^+(1) \leftarrow X^2\Sigma^+(0)$ transition with pulsed dye (Credo) excitation at 15646.5 cm^{-1}, detecting the strong $C^2\Sigma^+(1) \rightarrow X^2\Sigma^+(1)$ fluorescence around 649 nm. Data collection stopped after 20 ms, but clearly the signals continued past this point.

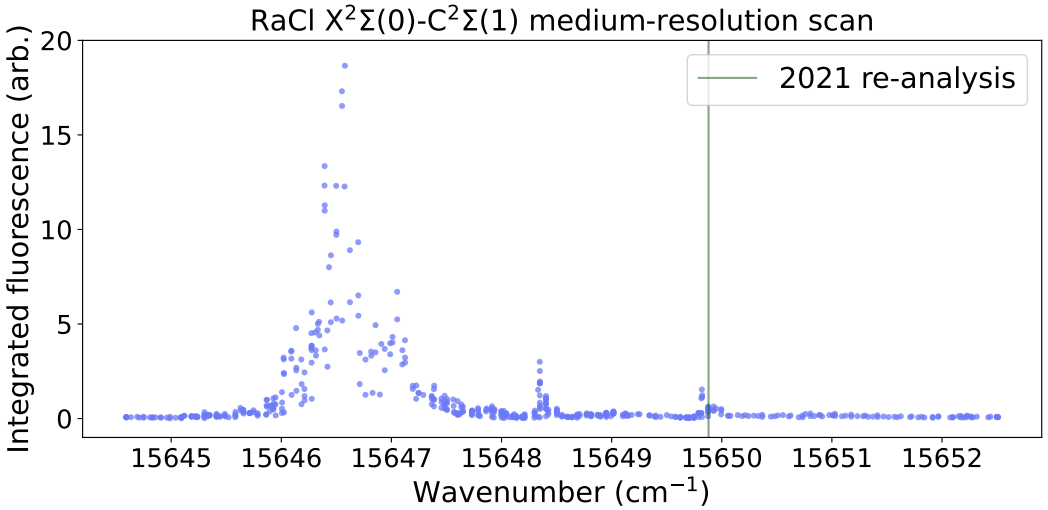


Figure 5.37: Scan of the RaCl $C^2\Sigma^+(1) \leftarrow X^2\Sigma^+(0)$ transition with pulsed dye (Credo) excitation. The vertical line is the location of the predicted band head from [147]. The band head according to the 1972 data is not shown, as it is at 15639.4 cm^{-1}. This data was normalized against the co-recorded Ra $^1P_1$ absorption signal.

Chapter

VI

Vibrational branching ratios of radium monofluoride

For a molecule to be directly laser-coolable using an experimentally tractable number of lasers, it must possess what are called highly diagonal Franck-Condon Factors (FCFs). As explained in 2.3, each time a molecule undergoes spontaneous emission, there is a chance that it changes its vibrational state. The FCFs $f_{v'v''}$ are the squared overlap integrals of the vibrational wavefunctions ψ_v in the ground and excited states, $f_{v'v''} = |\langle\psi_{v'}|\psi_{v''}\rangle|^2$, whose values relate to the relative likelihood of the various vibrational decay pathways [150]. Diagonal elements give the overlap of the states with the same vibrational number $v' = v''$, while off-diagonal elements give the overlap of states with $v' \neq v''$. This integral will range from 0 to 1; if the diagonal elements are close to 1, the molecular state is said to be "highly diagonal," and thus will often decay without changing its vibrational state.

The experimentally measured likelihood of decaying to any possible vibrational state is encapsulated in the Vibrational Branching Ratios (VBRs). These values $b_{v'v''}$ will track with the FCFs, but will differ slightly as a function of the frequency difference between the states $\omega_{v'v''}$ as [151]:

$$b_{v'v''} = \frac{f_{v'v''} \times \omega^3_{v'v''}}{\sum_{v=0}^{\infty} f_{v'v} \times \omega^3_{v'v}} \,.$$

This relationship assumes the validity of the Born-Oppenheimer approximation for the system; non-adiabatic effects from changes in the nuclear separation during decay can modify the $b_{v'v''}$ values in nontrivial ways [152]. If a certain excited state has a diagonal VBR of $b_{v'v'} = 0.98$, that means that 98% of the time the v' level in some excited state decays without changing the vibrational level, only the electronic and possibly rotational levels.

A note about terminology and jargon: because their concepts are so closely related, the language surrounding FCFs and VBRs is often jumbled. While "diagonal" has a technical meaning in terms of the FCF matrix, it is often employed as a catch-all way to say "vibrational-quanta-preserving." For example, it is common to encounter the phrase "off-diagonal decay" referring to vibration-changing decays and "diagonal VBR" meaning the vibrational branching ratio corresponding to the $v' = v''$ decay. The notion of FCFs and VBRs is also used interchangably throughout the literature; here we will try to adhere to the language of VBRs, as they describe the actual probability of decaying to the various possible vibrational states and as such their value is of greatest experimental relevance.

Since angular momentum selection rules allow electronic and rotational transitions to be closed (see Section 2.3), the number of photons that may be scattered by a molecule before being lost to some unaddressed state is limited by the VBRs. Once the molecule enters a different vibrational manifold, an additional laser may be used to repump it back into the desired vibrational level, returning it to the cycling configuration. As such, the true limitation on the number of photon scatters is the *sum* of the VBRs for all decays which are addressed by lasers. Assuming an excited state $v' = 0$ (for notational simplicity), the expected number of photon scatters $\bar{N}$ before a vibrational loss is thus given by:

$$\bar{N} = 1 / \left(1 - \sum_{v''} b_{0v''}\right) \,, \tag{6.1}$$

where the sum is over the vibrational states v'' that are repumped.

Depending on the frequency of the cycling transition and initial momentum of the molecule, around $10^3 - 10^4$ photons scatters are needed for laser slowing and an additional order of magnitude for laser cooling/trapping. We can take RaF as an example:

the laser cooling transition is at 752 nm, so each photon will impart a momentum kick $\hbar k = \frac{h}{752\text{ nm}} \approx 0.5\,\text{amu}\times\text{m/s}$. To slow a molecule with initial velocity ~ 100 m/s, this corresponds to roughly $\bar{N} \approx 40,000$ photon scatters, requiring repumping enough vibrational decay channels such that $\sum_{v''} b_{0v''} \approx 0.9999$. For reference, strontium monofluoride (SrF), the first molecule to be cooled and loaded into a magneto-optical trap, has a branching fraction of 0.98 for the $A(v' = 0) \rightarrow X(v'' = 0)$ decay and 0.9964 when summing the branching fractions of the lowest three vibrational levels [94]. In theory, one could keep adding arbitrary numbers of lasers to repump all possible loss channels, but this becomes impractical rather quickly; the first experiment to load a tweezer array of polyatomic molecules required 12 repump frequencies [153].

Molecules are identified as good candidates for laser cooling through calculations of their VBRs. Preliminary calculations for RaF put the diagonal VBR b_{00} in the range of 0.996 [49] to 0.999999 [148]; somewhere between very laser coolable and *astonishingly* laser coolable. If true, laser cooling of RaF should be achievable with three (or even fewer) lasers. However, accurate predictions for heavy elements are challenging, and at a certain value of precision the Born-Oppenheimer approximation breaks down, meaning higher-order terms start contributing significantly. Thus, these VBRs need to be experimentally verified before a whole experiment is constructed around laser cooling a specific species. This is especially true for a species such as RaF—working with these molecules requires significant resources that we would rather not expend if it turns out that laser cooling is actually not a possibility.

6.1 Determining branching ratios of trace isotopes

The goal of this measurement is to determine the VBRs for RaF inside the Minifridge. Typically, these measurements occur by driving the cycling transition and dispersing the decay fluorescence with a monochromator onto a camera, allowing the simultaneous collection of multiple decay wavelengths and their relative intensities. This protocol is infeasible in our setup for a variety of reasons. The strong, broadband fluorescence from the ablation process often overwhelms the molecule signal and shot-to-shot production fluctuations result in inconsistent signal strengths. On top of this, because we are working with trace materials, we are unable to average the signal from many hundreds or even thousands of ablation shots, which is a requirement to observe weak decays because of the inefficient light collection of these large monochromators.

In our previous spectroscopy of radium-containing molecules, we have developed a

fluorescence detection scheme that benefits from the fast time series data provided by a PMT, allowing us to gate out the early broadband fluorescence as well as perform real-time background subtraction without needing to average across multiple ablation shots. To adapt this method for measuring multiple decays simultaneously, we simply split the molecule fluorescence into two PMTs with a 50/50 (or dichroic) beamsplitter. By changing the optical filters in front of the PMTs, we can control which decay(s) each one detects. While an individual measurement only provides information about the ratio between two decay modes, repeated measurements with different optical filters allows for a full reconstruction of the branching pathways. Similar techniques to this work have been employed in other situations [151], although with a few differences in implementation and analysis.

Because the different decays are measured on separate devices, it is especially important to calibrate the light collection efficiencies of both PMTs to ensure the measured signal ratio is proportional to the true branching ratio. This calibration procedure is also described below.

Signal Modeling

Each PMT outputs a current which we convert to a voltage with a current preamplifier. This voltage is integrated over the length of the molecular ablation pulse to yield a signal $\tilde{\mathcal{S}}_i$, where the subscript $i = 1, 2$ is an index denoting PMT 1 or 2.

We can model the total signal from one PMT as follows:

$$\tilde{\mathcal{S}}_i = G_i L_i \left\{ \gamma_L Q_i(\lambda_L) T_i(\lambda_L) + \sum_j \gamma_j Q_i(\lambda_j) T_i(\lambda_j) \right\} . \tag{6.2}$$

The prefactor $G_i L_i$ includes the PMT gain G and the geometric (path-dependent) light collection efficiency L, neither of which depends significantly on the wavelength being measured. Since the gain and path remain largely the same over the course of the measurement, we can combine them into a single wavelength-independent prefactor φ_i. γ is the total number of photons emitted, either scattered directly by the laser off of windows or other surfaces (γ_L), or emitted by the molecules in some decay channel[1] j. These γ_j terms contain the information about the vibronic branching,

[1]Explicitly, j parameterizes all of the possible vibronic decay modes. For example, when measuring the branching ratios out of the first excited $A^2\Pi_{1/2}(v = 0)$ state of RaF, j iterates over the decays to the ground $X^2\Sigma^+(v = j)$ vibrational levels, each with an emission wavelength λ_j. Even though there is direct correspondence between j and v for a diatomic molecule, for a polyatomic molecule say with vibrational modes $v_1 v_2 v_3$ this j needs to represent all permutations of vibrational quanta.

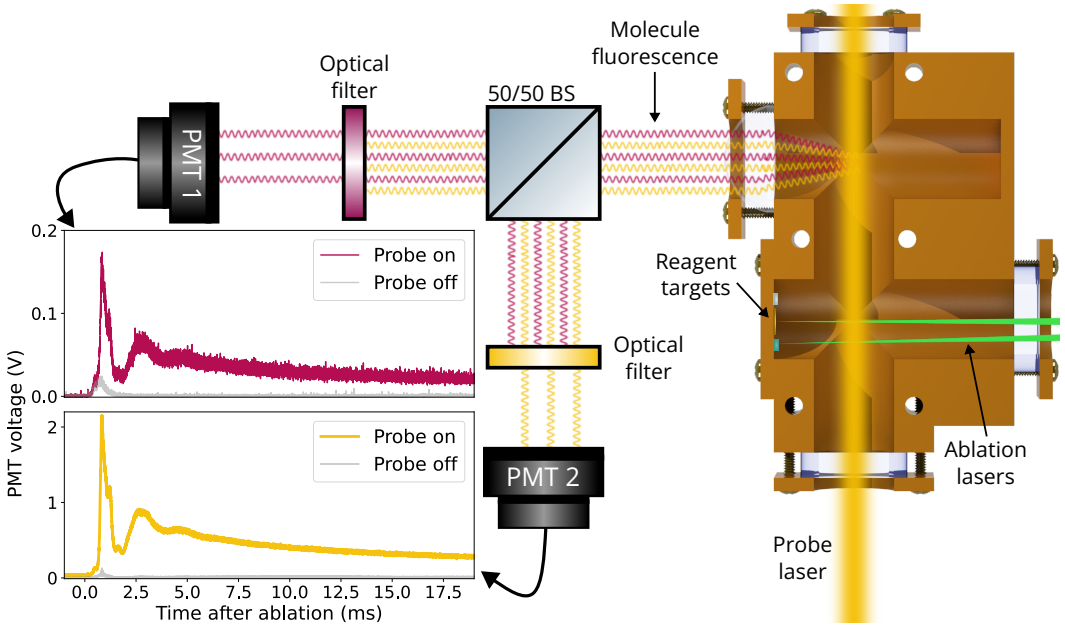


Figure 6.1: Top-down diagram of the dual-PMT setup. Red and orange wiggly lines represent fluorescence from different vibrational decay modes, originating from molecules probed inside our cryogenic buffer gas cell. Optical filtering is generally chosen to allow one decay into each PMT, but this does not need to be the case—only that the two PMTs have distinct wavelength-dependent light collection efficiencies. The plot inset is an example of a simultaneous PMT trace for a single shot in CaF, measuring the decays from $A(v' = 0)$ to $X(v'' = 0)$ and $X(v'' = 1)$ in orange and red, respectively. The raw PMT values cannot be compared directly as the gains and light collection efficiencies are different, as described in the text.

as elaborated later in Equation 6.3. Q_i and T_i are the wavelength-dependent PMT quantum efficiency and overall optical transmission, respectively. These take on values at select wavelengths of experimental interest: either that of the probe laser λ_L or the possible molecule emission wavelengths λ_j. Like the wavelength-independent prefactor, these can be combined to form a composite wavelength-dependent light collection efficiency denoted $\varepsilon_i(\lambda)$. The sum over emission channels j ensures that all photons scattered by the molecules are accounted for, but as will be shown later only a few of these terms are necessary.

Equation 6.2 can be simplified in a number of ways. Because we start recording the PMT signal one millisecond before molecule production and our probe lasers are always on, we are able to determine the laser scatter signal for this time. Given the stability of our lasers over the 20 ms molecule pulse, we can scale the signal measured in this millisecond by the length of the pulse and thus subtract the first term in brackets from our total measured signal to get a modified signal S_i. With this simplification,

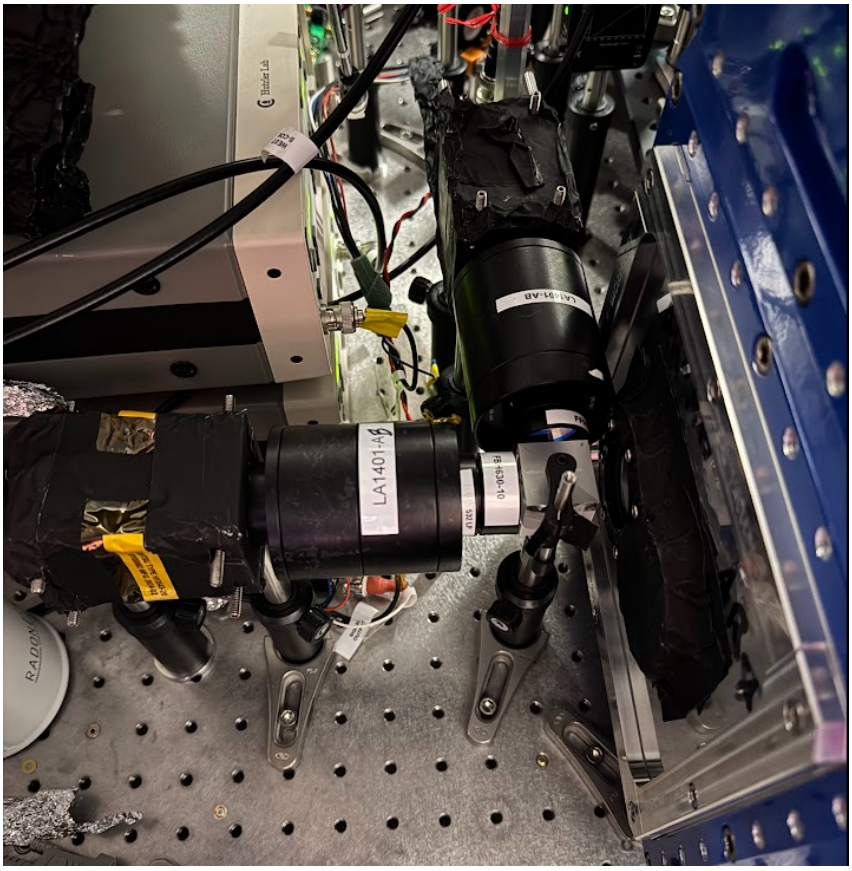


Figure 6.2: Photo of the dual-PMT implementation on the Minifridge table. In typical operation, light-blocking foil is placed all around the setup to prevent leakage from room lights and lasers. Note that the orientation of the PMT that detects the reflected fluorescence from the 50/50 beamsplitter is flipped relative to Fig. 6.1.

as well as the combined efficiencies mentioned above, we arrive at:

$$\mathcal{S}_i = \varphi_i \left\{ \gamma \sum_j b_{v'j} \varepsilon_i(\lambda_j) \right\}, \tag{6.3}$$

where we have rewritten the number of photons emitted into specific decay modes γ_j as $\gamma b_{v'j}$, with γ being the total number of photons scattered by the molecules and $b_{v'j}$ being the branching fraction into channel j out of the excited state vibrational level v'. It is worth emphasizing that γ does not possess an index as it depends on the *total* molecule fluorescence; it is not a statement about how much of this fluorescence is collected by either PMT, as this information is instead contained in the various efficiency terms.

Here we see one of the main advantages of the dual-PMT setup: for each shot, we measure *both* $\mathcal{S}_1$ and $\mathcal{S}_2$ simultaneously. The total number of scattered photons γ,

which varies wildly shot-to-shot and would be extremely difficult to measure, can thus be eliminated by dividing $\mathcal{S}_1/\mathcal{S}_2$. With this, determination of the branching ratios $b_{v'j}$ only requires knowing[2] the factors φ_i and $\varepsilon_i(\lambda_j)$ for both PMTs at all decay wavelengths λ_j. These are determined via the light collection calibration described in the next section. Once these values are known, dividing $\mathcal{S}_1$ by $\mathcal{S}_2$ yields terms that are proportional to $b_{v'j}/b_{v'j'}$, which are the relative likelihoods of decaying via two decay pathways j and j'. Using the fact that $\sum_j b_{v'j} = 1$ allows for determination of the absolute branching ratios $b_{v'j}$.

Light Collection Efficiency

When measuring a PMT signal in the absence of molecule production and *not* subtracting the laser scatter, Eq. 6.2 becomes:

$$\mathcal{S}_i = \varphi_i \varepsilon_i(\lambda_L)\gamma_L \,. \tag{6.4}$$

While the "true" number of photons scattered by the laser γ_L cannot be known, it is inherently proportional to the probe laser power $\gamma_L = \alpha P$ with some proportionality α. Assuming the beam pointing remains the same at every probe wavelength, i.e. by using a fiber-coupled laser and not changing the beam path after the fiber launch, α should be roughly the same across all measurements—we tested this is the case by varying the beam path and shape (within a reasonable range) and verified that the proportionality remained the same. Rewriting Eq. 6.4 and explicitly noting the laser power and wavelength dependence of the signal:

$$\mathcal{S}_i(\lambda_L, P) = \varphi_i \varepsilon_i(\lambda_L)\alpha P \,. \tag{6.5}$$

Thus, at a given wavelength, the slope of the signal versus laser power is the product $\varphi_i \varepsilon_i(\lambda_L)\alpha$. Since the individual efficiency terms are always multiplied together when determining branching ratios (see Eq. 6.3), it is acceptable to only know their combined value.

As long as the definition and measurement of laser power P is consistent for both PMTs across all wavelengths and powers, the proportionality α is constant, despite being unknowable. Thus, even though the term used to calculate the branching

[2] For vibrational decays that possess angular momentum selection rules, such as those involving bending modes, knowledge of the relative rotational selection rules and radiation patterns is also required. This additional factor is not relevant for diatomic molecules like the ones considered in this work.

ratios is $\varphi_i \varepsilon_i(\lambda_L)$ and not $\varphi_i \varepsilon_i(\lambda_L)\alpha$, because the determination of branching ratios requires dividing $\mathcal{S}_1/\mathcal{S}_2$, any instance of α is canceled by the division. As such, using the measured value of $\varphi_i \varepsilon_i(\lambda_L)\alpha$ in Eq. 6.3 is perfectly reasonable.

When performing this light collection efficiency calibration, it becomes apparent that most values for the combined efficiency are exceedingly small. This is because of our choice of optical filtering for the PMTs, where each one is intended to only allow light from a single molecular decay. As a result, we can often ignore all terms in Eq. 6.3 except for the one corresponding to the decay mode j that is not blocked by the filters, greatly simplifying the calculation. An example of this is provided in the worked example section below. It is important to note that this is not always the case, however; for more complicated molecules with decay channels that cannot be easily separated by filtering, the leakage light from unwanted decays needs to be considered when performing the calculations.

6.2 Worked example - RaF $A^2\Pi_{1/2}(v=0) \rightarrow X\,^2\Sigma^+(v=0,1)$ branching

Let us consider the branching ratio measurement for the $A^2\Pi_{1/2}(v=0)$ state in RaF, explicitly working through the process for determining the ratio of the decays to $X^2\Sigma^+$ $v=0$ and $v=1$ at 752 nm and 778 nm, respectively. PMT 1 is configured to observe the decays to $v=1$, using two 10-nm-bandwidth bandpass filters centered at 780 nm and one longpass filter[3] with an edge at 750 nm. PMT 2 is configured for the diagonal decay by using a single 10 nm bandpass filter[4] centered at 750 nm. Molecule excitation was performed with a Ti:sapphire laser[5] driving the ${}^PQ_{12}(0.5)$ transition at 13284.63616 cm^{-1}.

As described above, before we are able to extract a value for the relative branching we need to first calibrate the light collection efficiencies of the two PMTs. Even before this, however, we need to obtain an accurate measurement of the laser power.

Power calibrations

As probe laser power may drift over the course of the calibration, it needs to be continually monitored. This is achieved by using a beam sampler to pick off a small fraction of light which we then co-record on a power meter during all measurements. However, at different wavelengths the fraction of this pickoff light relative to the total power can change, meaning it also needs to be carefully calibrated. The pickoff-to-

[3] Thorlabs part numbers FBH780-10 and FELH0750

[4] Thorlabs FBH750-10

[5] Coherent 899

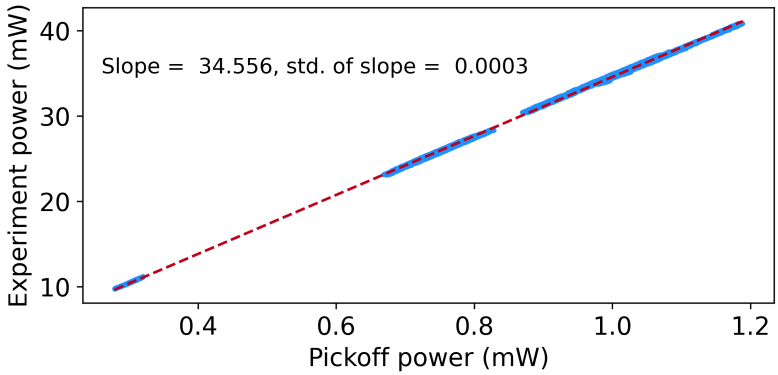


Figure 6.3: Calibrating the pickoff power for the diagonal decay light scatter measurement. The slope gives the factor that converts from measured pickoff power to true experimental laser power. DC backgrounds, such as electrical offsets or ambient light leakage, have been accounted for.

probe calibration procedure involves measuring the power on two separate meters, one at the pickoff and one right before the apparatus, over a range of input powers. From this data we can establish a relationship between the measured pickoff value and the true power entering the experiment.

This data at 752 nm, corresponding to the decay to the $v = 0$ ground state, is shown in Fig. 6.3. For 752 nm, the ratio of experimental power to measured pickoff power is 34.556; the equivalent measurement for the $v = 1$ decay at 778 nm gives a ratio of 37.392. The same laser was used as both wavelengths were within the operating range of the Ti:sapph. For both instances, measurements were also taken with the laser blocked to determine the DC background level, which we then subtract away during the real power measurements.

Light collection

Now that we have an accurate means of measuring the laser power, we are able to perform the light collection efficiency calibrations. Following Eq. 6.5, the slope of integrated PMT signal versus laser power provides the combined wavelength-independent and -dependent efficiencies. Data at four probe laser power configurations for both PMTs simultaneously are shown in Fig. 6.4. This corresponds to efficiencies $\varphi_1\varepsilon_1(752\text{ nm})\alpha = 0.028$, and $\varphi_2\varepsilon_2(752\text{ nm})\alpha = 26.679$.

Important to note for the analysis is the exceedingly small value of this efficiency for PMT 1, owing to the rejection of 752 nm light by the optical filtering. However, even though it is small, it is clearly nonzero. Another way to interpret Figure 6.4 is to say

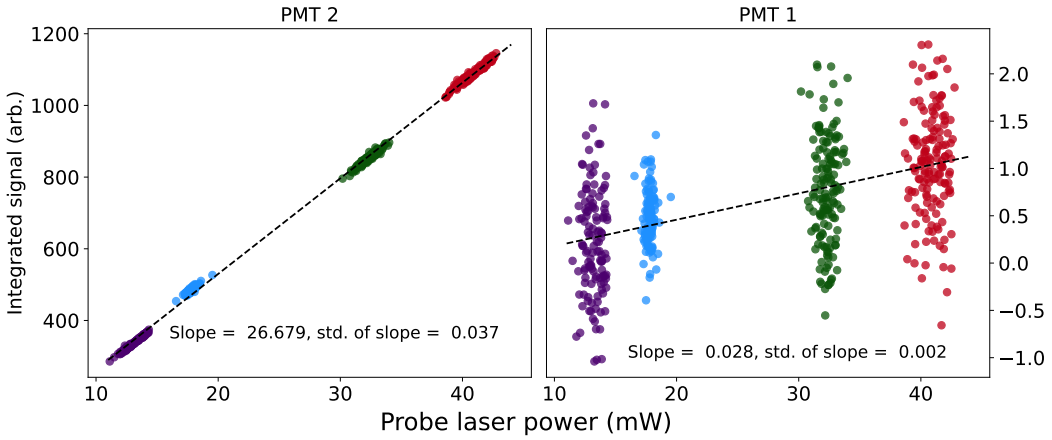


Figure 6.4: Example of the determination of the light collection efficiency for both PMTs at the on-diagonal frequency, according to Eq. 6.5. The slope gives the combined efficiency term $\varphi_i \varepsilon_i(752\text{ nm})\alpha$. Each color represents a different configuration of laser power attenuation achieved by swapping neutral density filters. The optical filters for PMT 2 should allow the on-diagonal light, while those for PMT 1 are intended to block it and only permit the light around 778 nm. Note that the laser power may vary by a significant amount within a set of data, emphasizing the need for coincident power monitoring.

that for a raw fluorescence of ~1000 in the PMT 2 channel, there is a leakage of ~1 in the integrated PMT 1 signal. Looking at the signals shown in Figure 6.6, we see that the on-diagonal integrated fluorescence is on the order of $\sim$ 1000s while the off-diagonal signal is $\sim 1 - 10$s. This implies that a non-negligible amount of the off-diagonal data is likely leakage from the $v = 0$ molecule fluorescence and cannot be ignored if we are to obtain an accurate measurement of the b_{01}/b_{00} branching ratio.

Tuning our laser to the 778 nm transition, we get $\varphi_1\varepsilon_1(778\text{ nm})\alpha = 119.85$ and $\varphi_2\varepsilon_2(778\text{ nm})\alpha = 0.016$. Unlike with the 752 nm on-diagonal leakage, the molecule signals in the $v = 1$ channel are weak enough to not expect any significant leakage contribution to the $v = 0$ integrated fluorescence. We repeated this measurement for higher-lying vibrational decays and recorded similarly small light collection efficiencies for both PMTs. This, coupled with the fact that we expect those decays to be extremely suppressed, means that the fluorescence contributions from all higher-order terms can be neglected in this measurement.

With the small terms removed, we now reduce Eq. 6.3 for each PMT to:

$$\mathcal{S}_1 = \varphi_1\varepsilon_1(752\text{ nm})\alpha\gamma b_{00} + \varphi_1\varepsilon_1(778\text{ nm})\alpha\gamma b_{01}$$
$$\mathcal{S}_2 = \varphi_2\varepsilon_2(752\text{ nm})\alpha\gamma b_{00}\,,$$

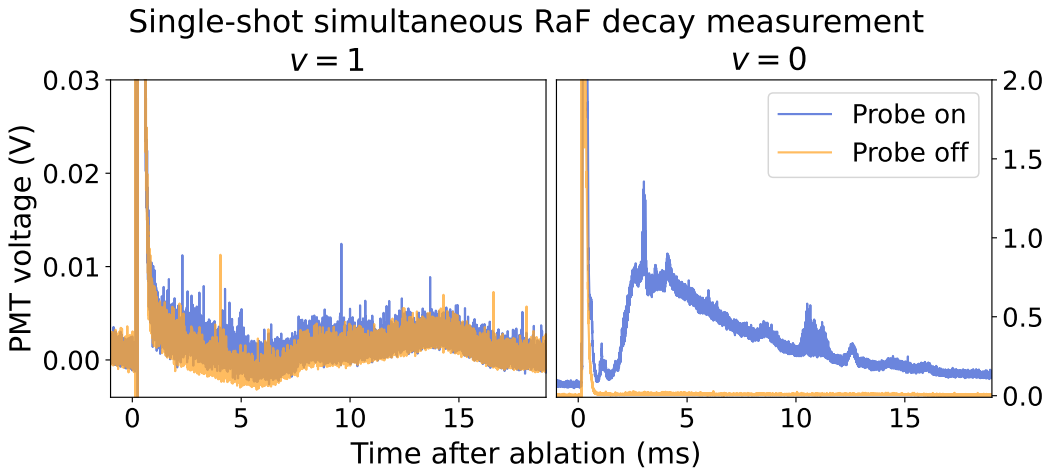


Figure 6.5: Side-by-side comparison of the raw PMT signals for one single ablation shot of the RaF $A(v = 0) - X(v = 0, 1)$ b_{01}/b_{00} branching ratio measurement. Note the dramatic difference in vertical scale, to the point where we are almost at the electrical noise floor on the $v = 1$ channel. Still, there is a discernible signal. This data will be background-subtracted and integrated to obtain the two signals $\mathcal{S}_1$ and $\mathcal{S}_2$, whose ratio relates to the ratio of VBRs, determined in Eq. 6.7 for this experimental configuration. The spikes on the $v = 0$ channel are due to laser power jitter, which does not couple into the analysis.

and the measured ratio of the two signals $\mathcal{R}$:

$$\begin{aligned}
\mathcal{R} = \frac{\mathcal{S}_1}{\mathcal{S}_2} &= \frac{\varphi_1\varepsilon_1(752\text{ nm})\alpha\gamma b_{00} + \varphi_1\varepsilon_1(778\text{ nm})\alpha\gamma b_{01}}{\varphi_2\varepsilon_2(752\text{ nm})\alpha\gamma b_{00}} \\
\frac{\mathcal{S}_1}{\mathcal{S}_2} &= \frac{\varphi_1\varepsilon_1(752\text{ nm})}{\varphi_2\varepsilon_2(752\text{ nm})} + \frac{\varphi_1\varepsilon_1(778\text{ nm})}{\varphi_2\varepsilon_2(752\text{ nm})}\frac{b_{01}}{b_{00}} \\
\frac{\mathcal{S}_1}{\mathcal{S}_2} &= \frac{0.028}{26.679} + \frac{119.85}{26.679}\frac{b_{01}}{b_{00}}\,.
\end{aligned} \tag{6.6}$$

From here we can extract the ratio of decays to the two lowest vibrational states $v = 0$ and $v = 1$ for each data point using the formula:

$$\frac{b_{01}}{b_{00}} = \frac{26.679}{119.85}\frac{\mathcal{S}_1}{\mathcal{S}_2} - \frac{0.028}{119.85}\,. \tag{6.7}$$

Now we perform the actual branching ratio measurement, which is quite simple in practice. Tuning our probe laser back to the resonance frequency to drive the $A - X$ transition, we ablate and collect the fluorescence data for a number of shots. A typical single-shot trace is shown in Fig. 6.5. Depending on the SNR and target fluctuations,

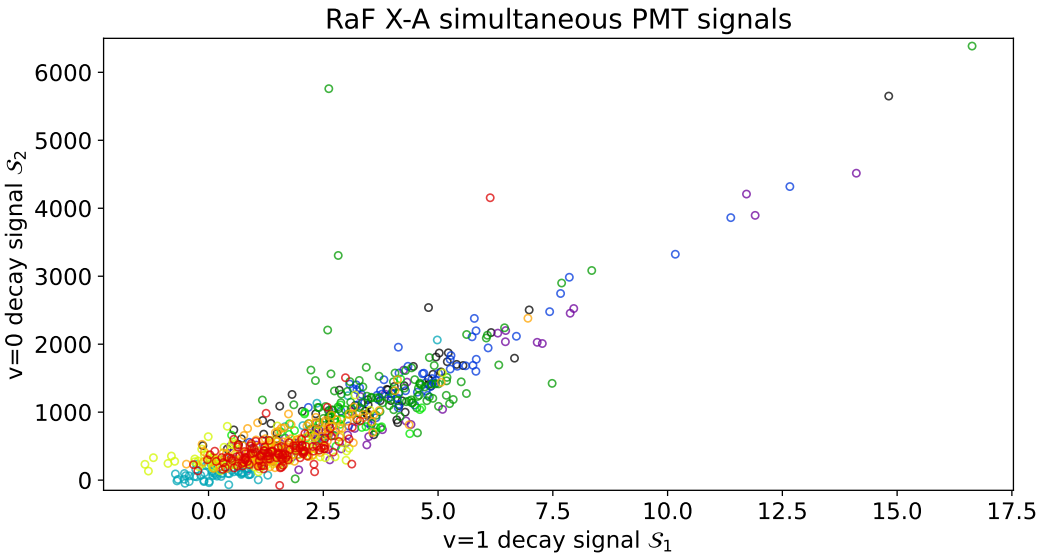


Figure 6.6: Plot of every simultaneous data point taken during the branching ratio measurement. The x-axis corresponds to PMT 1 looking at the $v = 1$ off-diagonal decay, and the y-axis is the $v = 0$ on-diagonal signal seen by PMT 2. This is before correcting for the on-diagonal leakage into the off-diagonal signal channel (see text for discussion). Each different color is a data set taken at a different probe laser power, showing how the behavior is linear with the same slope regardless of laser power.

we take anywhere from 10s to 100s of shots. Measurements are performed at a variety of probe laser powers to account for any possible power-dependent effects, as described later.

After integrating the background-subtracted fluorescence signals, we obtain the signal ratio $\mathcal{S}_1/\mathcal{S}_2$ at each individual shot, shown for the full data set in Fig. 6.6. Using Eq. 6.7 above, we use these values to obtain the measured ratio of VBRs b_{01}/b_{00} for each data point, shown in Fig. 6.7.

Cutoff analysis

Because of shot-to-shot fluctuations in our data and the weakness of the $v = 1$ decays relative to $v = 0$, it is not uncommon for certain shots to have signal in the $v = 0$ channel but not in $v = 1$ (see Fig. 6.6). We wish to reject these points in a way that is statistically motivated.

Figure 6.9 shows the method used to select the proper subset of data. A threshold is placed on the $v = 0$ decay signal, and points with integrated fluorescence below this threshold are thrown out. By varying this cutoff across the range of integrated signals for $v = 0$, we can find what value minimizes the standard error of the data.

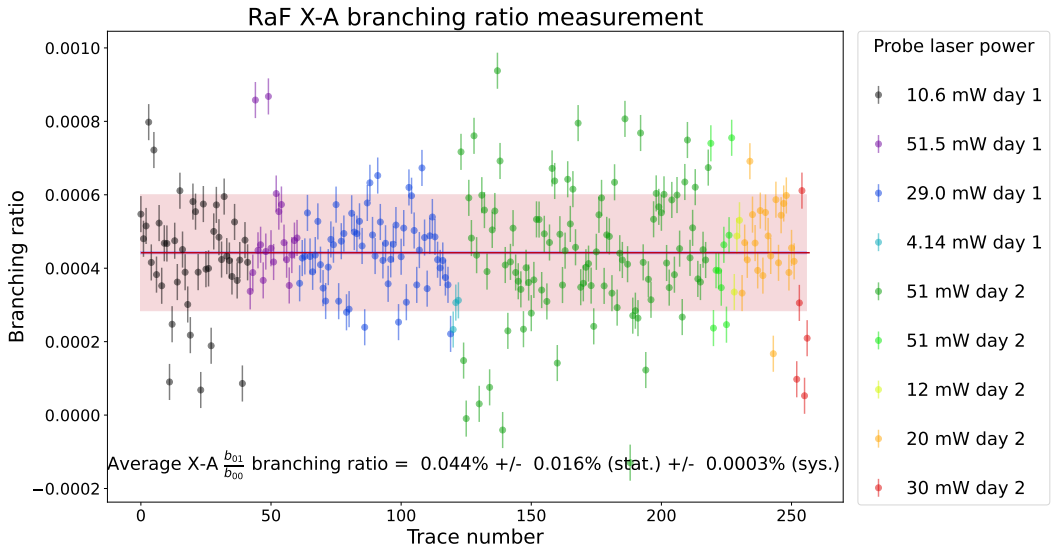


Figure 6.7: Measurement of the b_{01}/b_{00} ratio for the first excited state in RaF, yielding a value of 0.00044(16). Data was taken over the course of multiple days under different experimental conditions and remained consistent. The red horizontal line is the mean, with the shaded region indicating one standard deviation. The values shown include the correction for the leakage of the diagonal decay light into the off-diagonal channel, obtained from a linear fit as in the right side of 6.4; the uncertainty of this fit was treated as a possible systematic error and plotted here as the error bars, multiplied by 3 to give a 3σ range. The systematic uncertainty from the errors from the diagonal efficiency measurements is also included, but is smaller than the size of the points. This plot does not include every data point; see the section "cutoff analysis" for discussion on how this data was post-selected.

Standard error ($\hat{\sigma}$) was chosen as our statistic as opposed to standard deviation (σ) as it is an estimator of how close the sample VBR is to the true VBR, while standard deviation simply describes the spread of the data. In this situation, the two are related by[6] $\hat{\sigma} = \frac{\sigma}{\sqrt{n}}$.

6.3 Benchmarking

To test the validity of our method, we performed the above process on species whose branching ratios had previously been determined via other methods, or for which we had the capacity to measure ourselves in a complementary apparatus. For the following discussion, it is assumed that we are considering the VBRs out of the excited state origin, i.e. $A(v' = 0)$ or $\tilde{A}(000)$. In the case of diatomic molecules $b_{v'v''}$ remains the notation, but later for polyatomic molecules a single number is insufficient to represent the three components of v'', so instead we will label the branching with the

[6]When the sample size n is small, the formula for the unbiased estimator is used instead [154].

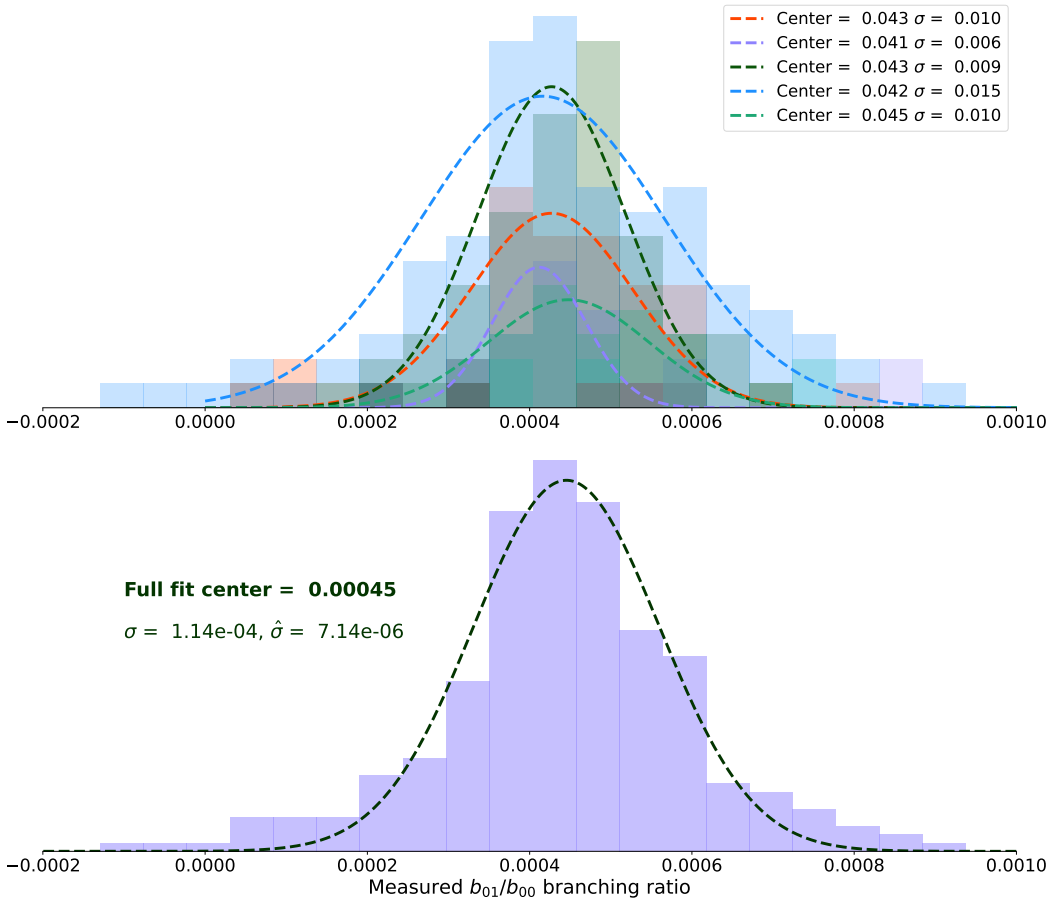


Figure 6.8: Histogram of all the data taken in the RaF X-A b_{01}/b_{00} branching ratio measurement, after applying the signal cutoff. Top: Each power plotted separately. If enough points for a power remained, the set was fit to a gaussian distribution, with resulting center and standard deviation shown. Bottom: All powers summed together in a single histogram, where the gaussian fit results are printed in the plot. From the standard deviation σ, the standard error $\hat{\sigma}$ is calculated.

ground vibrational state configuration $(v_1 v_2 v_3)$.

First, we compared against calcium fluoride (CaF), a widely used molecule in direct laser cooling owing to its favorable VBRs, and one that we can produce in the Minifridge in large quantities. Initially, CaF was appealing because its b_{02} branching ratio was predicted to be a similar magnitude to our measured b_{01} in RaF [155], so it should serve as a good test of our methods at these scales. Interestingly, despite the many experiments working with CaF and the fact that the branching to the $v = 2$ state needed to be repumped to trap these molecules, no measurement of b_{02} existed. We therefore measured it ourselves using the supersonic beam source and monochromator provided by Tim Steimle, an apparatus which has performed

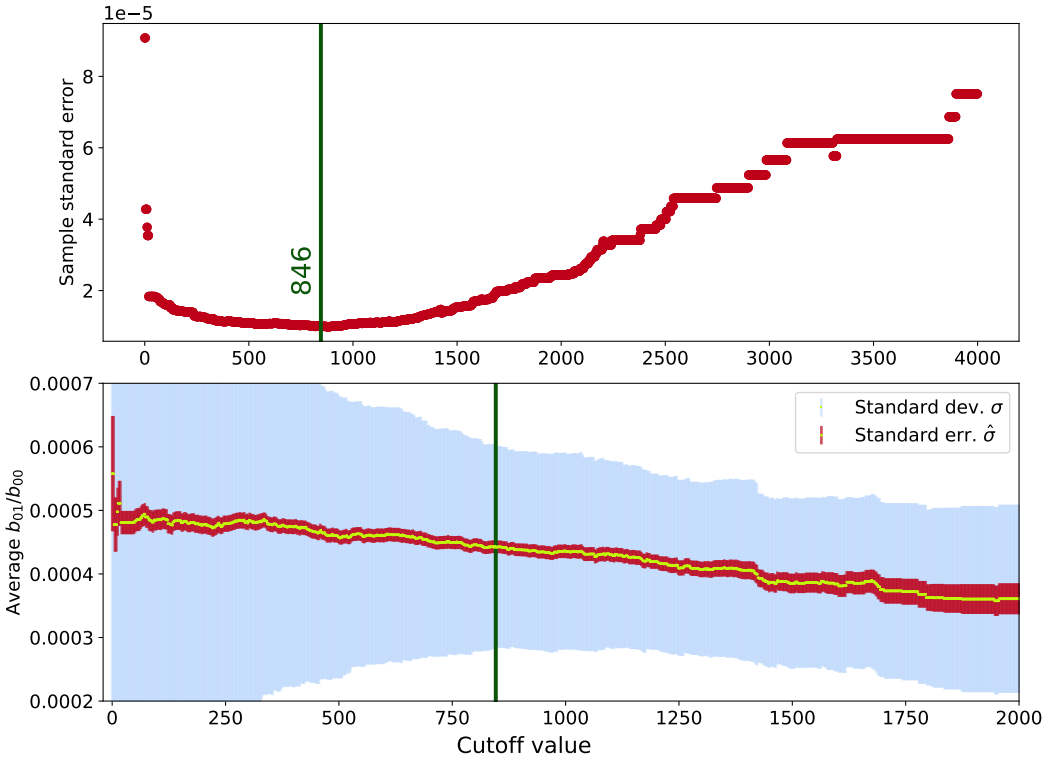


Figure 6.9: Picking a cutoff for the full dataset shown in Fig. 6.6. The top plot shows the minimum of the standard error for the sample, achieved at a threshold value of 846 (vertical line). The piecewise-looking jumps at the right are caused by a lack of data points between these high cutoff values. Bottom shows the mean of the b_{01}/b_{00} ratio (green center line) as a function of the cutoff, with the standard error at each point given as the red error bars and the 1σ standard deviation by the light blue span.

dispersed laser-induced fluorescence (DLIF) on numerous molecules in its lifetime[7].

In this supersonic source we also performed a measurement of b_{01} in CaF, through which we identified a problem with these dispersed fluorescence measurements originating from the hardware we were using. Detection of the dispersed photons was performed with an ICCD, which had a noticeable and complicated saturation behavior when exposed to large signals, such as the bright diagonal decay in CaF. Because of this, the measured intensities of the $v = 0$ decay were anomalously low, leading to branching ratios b_{01}/b_{00} and b_{02}/b_{00} which we estimate to be around $50 - 100\%$ larger than the true values. We verified this through multiple measurements at various microchannel plate gain settings, and noticed that as we decreased the gain and brought the detector further from saturation the measured ratio would trend lower. Unfortunately, we could not tune this gain arbitrarily low as other unrelated issues

[7] Measurements performed by Phelan Yu.

would creep in, and we were thus not able to obtain accurate values of b_{01}/b_{00} and b_{02}/b_{00}. However, because this measurement detects all decays simultaneously, we were able to extract the ratio b_{02}/b_{01}, which, because these decays are weaker, does not suffer from the same saturation issues.

The measurement of the CaF b_{01}/b_{00} and b_{02}/b_{00} ratios in the Minifridge mostly mimicked the measurements for RaF, where the only difference stems from the laser sources used in the light collection efficiency calibration of b_{02}. For this, we drove the $A\,^2\Pi_{1/2}(v' = 0) \leftarrow X\,^2\Sigma^+(v'' = 0)$ transition at 606 nm with our ring dye laser and configured the optical filters on the two PMTs to measure the diagonal decay as well as the decay to $X(v'' = 2)$ at $\sim$ 653 nm. Because the tuning range of the dye we used could not cover both wavelengths, for the calibrations at 653 nm we used a separate laser diode[8] to generate light at $\sim$ 658 nm. While our optical filter stack for the b_{02} PMT still admitted this wavelength, it was not initially obvious whether the higher-order wavelength-dependent effects would lead to inaccuracies, and so in a way this was also a test of how sensitive our branching ratio measurement was to wavelength offsets in the calibration process. To perform the calibrations, this diode was fiber coupled and sent through the same launch as the probe laser to maintain the same beam path and shape.

Another benchmark was performed using YbOH, whose branching ratios for the many possible decays have previously been determined to high precision [156]. This served as a both a verification as well as test of our measurement scheme on systems with a more complicated vibrational branching landscape.

We drove the cycling ${}^pQ_{12}(N'' = 1)$ and $P_1(N'' = 1)$ lines of the $\tilde{A}\,^2\Pi_{1/2}(000) \leftarrow \tilde{X}\,^2\Sigma^+(000)$ band at 577 nm and measured the decay fluorescence. As usual, one PMT was configured to detect only the diagonal decays back down to $\tilde{X}(000)$, but because of the vibrational state congestion in YbOH, it was not possible to single out any of the off-diagonal decays using the filters we had available. Instead, our filter range collected fluorescence from decays to both (200) and (12^00). Still, our measured $\frac{(200)+(12^00)}{(000)}$ branching ratio (Fig. 6.10) agrees with the previous measurement to within error, successfully demonstrating agreement with a separate measurement protocol, this time performed by a different group entirely. We also examined the branching ratios to the dominant decay pathways (100) and (02^00) and found a similar agreement, with results summarized in Table 6.1.

[8] Thorlabs L658P40.

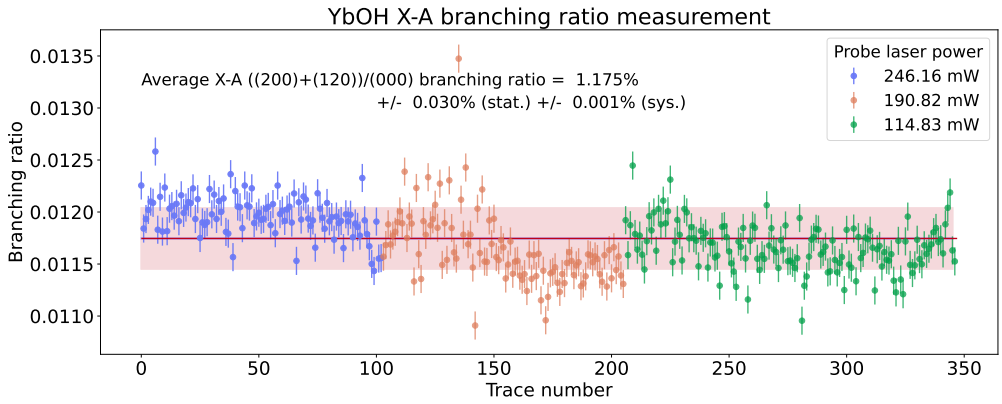


Figure 6.10: Analogous plot to Figure 6.7 but for the YbOH $\tilde{A}(000)$ state decaying to $\tilde{X}(200)$ and $(12^{2,0}0)$. A slight trend seems visible in the data but appears to correlate with shot number more than laser power, as the measured values are relatively continuous at the switching points between data sets. We observed trends like this in a handful of measurements, but were unable to pin down an unambiguous cause as there was no way to force it to occur or not. Still, with enough data, the average seems to converge to a value that agrees with other measurements to within our experimental uncertainty.

	CaF		**YbOH**		
Branching	DLIF[†]	This method	Branching rel. to (000)	DLIF[‡]	This method
b_{01}/b_{00}	2.48(3)	1.6(2)%	(100)+(020)	10.56(71)%	10.33(25)%
b_{02}/b_{00}	0.089(8) %	0.052(9)%	(200)+(120)	1.08(8)%	1.18(3)%
b_{02}/b_{01}	3.5(3)	3.3(7)%			

Table 6.1: Branching ratio benchmarking test results for CaF and YbOH. For both molecules, values recorded are for decays out of the ground vibrational level of the first excited $^2\Pi_{1/2}$ state. [†]The CaF DLIF values were taken by Phelan Yu on our supersonic beam source, and the values for YbOH are taken from [156]. As explained in the text, the supersonic DLIF values taken suffer from saturation on the b_{00} decay mode, resulting in an artificially larger value. The ratio of the two weaker decays b_{02}/b_{01} should not be affected in the same way, or at least not by as much. For the DLIF method, this last value was determined directly from signal ratios of the b_{01} and b_{02} decays, while for our PMT-based method it was inferred by taking the ratio of the first two lines. [‡]Errors for the YbOH measurement were determined by propagating the published single-state 1σ errors in [156]. Only the values for the (02^00) and (12^00) were used, as the (02^20) and (12^20) were not measured using DLIF; their values will factor into our measurement, but are predicted to be inconsequentially small at our uncertainty levels.

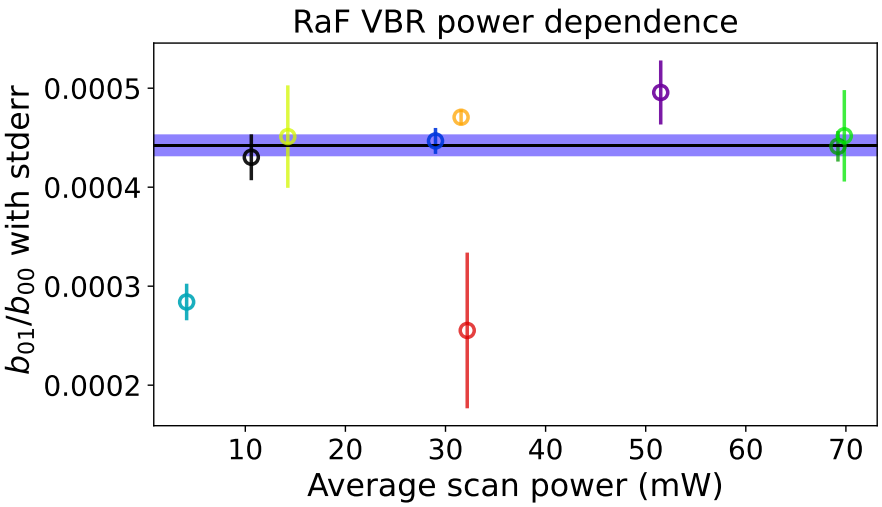


Figure 6.11: Measured b_{01}/b_{00} ratio for the RaF $A - X$ band as a function of input laser power, demonstrating approximately no correlation between the extracted value with laser power. The purple horizontal span represents the standard error of the full sample, taken as $\hat{\sigma} = \frac{\sigma}{\sqrt{n}}$ for n data points. Both apparent outliers on the low side had ≤ 5 data points after the cutoff was applied. Error bars represent the standard error of each individual sample. Some of the samples had few data points, so an unbiased estimator of the standard deviation was used [154].

One concern we had was whether the probe laser would scatter nonresonantly off of dust produced in the ablation and lead to an elevated b_{00} signal. To test this, each time we performed the branching ratio measurement, we took data at a number of different probe laser powers. This has the advantage of testing not just for dust scatter, but for any other sort of nonresonant probe laser scatter that only occurs after ablation. Recall that we measure the laser scatter off of the optics and cell for 1 ms before ablation so that we can subtract it away, meaning any uncorrected signal caused by probe laser scatter must occur because of features in the ablation. Normally this ablation-correlated excess signal would be indistinguishable from molecule fluorescence, but because the branching ratios are power-independent, we can plot the measured $b_{0j}/b_{0j'}$ at different powers and check for any residual correlation.

Most measurements showed no power correlation in the branching ratios, shown in Figure 6.11 for the RaF b_{01}/b_{00} measurement. Sometimes, when producing lots of molecules such as with CaF or YbOH, we did observe a quasi-linear power dependence. Rather than originating from some sort of dust, however, we attribute this to a nonlinear response in the PMT or current preamplifer, as when we turned the gain down and operated further from the overload value this effect vanished.

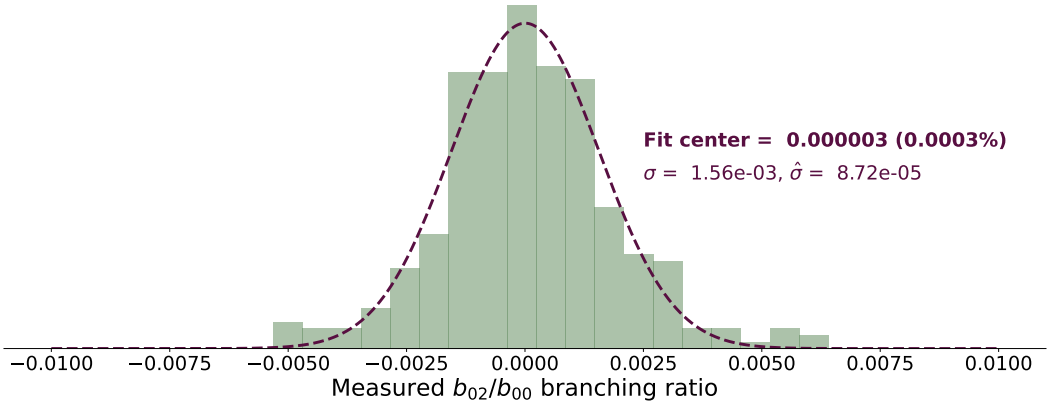


Figure 6.12: Measurement of the b_{02}/b_{00} branching ratio for RaF. The results are consistent with zero, with larger error bars than previous measurements owing to the reduced measurement sensitivity at these wavelengths and the fewer data points taken. None of the single-shot data showed any signal in the $v = 2$ decay channel.

6.4 RaF $A^2\Pi_{1/2}(v = 0) \rightarrow X\,^2\Sigma^+(v = 0, 2)$ branching

Once a repump laser is introduced to plug the $v = 1$ decays, the next limiting factor to the photon budget is the b_{02} branching from $A(v = 0)$ to $X(v = 2)$. This decay is expected to be even further suppressed relative to the $v = 1$ decay, following the trend for all other alkaline earth monofluorides. However, it is still worth verifying this fact and confirming that b_{02} is not anomalously large in RaF. It is also interesting to see just how low our signal floor can go for these trace isotope branching ratio measurements by attempting to observe a decay that is expected to be extremely weak—predictions range from $< 0.001\%$ [49] to "0%" [148]. At these levels, even the current state-of-the-art would not be able to resolve these decays.

Results for this measurement are shown in Figure 6.12. To summarize, we were unable to observe any decays from $A(v' = 0)$ to $X(v'' = 2)$. This is not too surprising, as we were already operating very close to the signal floor just to be able to detect the $X(v'' = 1)$ decays (see Fig. 6.5). Even after examining each individual shot, we found no unambiguous single-shot traces showing fluorescence from this decay pathway.

As an independent measurement, this results in a vibrational branching of $b_{02}/b_{00} = 0.0000(16)$, or $0.00(16)\%$, consistent with zero. The larger error bars follow from the reduced efficiency $\varphi\varepsilon(806\text{ nm})$ of our detection scheme at this wavelength (recall Eq. 6.3), effectively lowering our sensitivity to the branching ratio b_{02}. We also took less data, since at no point did we observe an off-diagonal signal, and we did not wish to burn through our trace quantity of radium just to achieve a $n^{-1/2}$ reduction in the statistical uncertainty.

The above is not to say that we cannot set a more stringent limit than the 1σ value of $b_{02}/b_{00} < 0.00156$; by using our measurement of b_{01}/b_{00} as a prior, we can make a claim as to the largest $v = 2$ signal $\mathcal{S}_1$ that we *should* have observed given the magnitude of the on-diagonal signal $\mathcal{S}_2$, where $\mathcal{S}_1$ and $\mathcal{S}_2$ refer to the off-diagonal and diagonal decay signals, respectively, as in the worked example above (Section 6.2).

For the b_{01}/b_{00} measurement, we had (Equation 6.2):

$$\begin{aligned}\frac{\mathcal{S}_1}{\mathcal{S}_2} &= \frac{\varphi_1\varepsilon_1(752\text{ nm})}{\varphi_2\varepsilon_2(752\text{ nm})} + \frac{\varphi_1\varepsilon_1(778\text{ nm})}{\varphi_2\varepsilon_2(752\text{ nm})}\frac{b_{01}}{b_{00}} \\ \frac{\mathcal{S}_1}{\mathcal{S}_2} &= \beta + \varepsilon b_1\,, \end{aligned} \tag{6.8}$$

where in the bottom line we cleaned up some of the cumbersome terms, combining the first into a constant β referring to the degree of $\mathcal{S}_2$ light bleed, and the efficiency ratio into a more compact ε, and the ratio of VBRs into $b_1 \coloneqq b_{01}/b_{00}$.

Doing the same for the measurement of $b_2 \equiv b_{02}/b_{00}$ we have:

$$\begin{aligned}\frac{\mathcal{S}'_1}{\mathcal{S}_2} &= \frac{\varphi'_1\varepsilon'_1(806\text{ nm})}{\varphi_2\varepsilon_2(752\text{ nm})}\frac{b_{02}}{b_{00}} \\ \frac{\mathcal{S}'_1}{\mathcal{S}_2} &= \varepsilon' b_2\,, \end{aligned} \tag{6.9}$$

where the primes simply indicate that the values listed refer to the b_2 measurement, for reasons that become clearer below. Note that there is no leakage signal term in this equation—we observed no amount of $v = 0$ light bleed on the $v = 2$ detection PMT.

From here, we can claim an upper limit to b_2 based on our SNR of the $v = 2$ measurement given by the standard deviation $\sigma_{\mathcal{S}'_1}$ of $\mathcal{S}'_1$. Rearranging Eq. 6.4:

$$b_2 < \frac{\sigma_{\mathcal{S}'_1}}{\varepsilon'\mathcal{S}_2}\,,$$

Which we can relate to our signals $\mathcal{S}_2$ from the earlier measurement to obtain:

$$b_2 < \frac{\sigma_{\mathcal{S}'_1}}{\mathcal{S}_1}\left(\frac{\beta + \varepsilon b_1}{\varepsilon'}\right)\,. \tag{6.10}$$

The terms in the parentheses are all measured constants from either the calibration procedure or obtained from the branching ratio determination in Section 6.2. The strongest limit on b_2 is set by taking the largest measured $\mathcal{S}_1$ signal from the b_1 measurement. Essentially, we are saying that previously we observed signals as large as $\mathcal{S}_1$ for similar values of $\mathcal{S}_2$, and finding what value of b_2 we should expect at this level, accounting for the relative scaling between the two efficiencies.

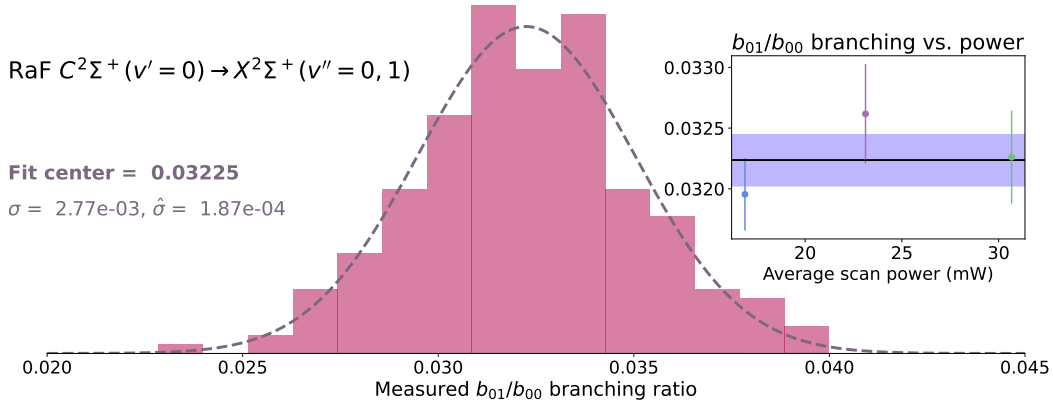


Figure 6.13: Similar branching ratio plots as above but for the measurement of b_{01}/b_{00} for the $C\,^2\Sigma^+_{1/2} \rightarrow X\,^2\Sigma^+_{1/2}$ band in RaF. Inset emphasizes the lack of dependence of the resulting value on the probe laser power, as expected. See Figures 6.8 and 6.11 for more details.

Doing so yields $b_2 \equiv b_{02}/b_{00} < 0.00032$, or $b_{02}/b_{00} < 0.032\%$. This is below the results for the b_{01}/b_{00} measurement, as expected from trends in similar molecules, although not significantly lower on account of the limited wavelength-dependent efficiency and number of data points.

6.5 RaF $C^2\Sigma^+(v=0) \rightarrow X\,^2\Sigma^+(v=0,1)$ Branching

Using our setup, it was straightforward to also measure the same b_{01}/b_{00} ratio for the $C-X$ band of RaF. While of only moderate interest as a laser cooling transition itself, owing to the fact that branching to the intermediate $A\,^2\Pi$ states is unavoidable, this excited $C\,^2\Sigma$ state will likely be used for repumping in order to reserve the A state for cycling[9]. In this case, favorable VBRs are still desirable to avoid losing the molecule to a dark state in the repumping process, but much less critical than for a cycling transition.

This measurement was performed exactly as the equivalent measurement for the $A-X$ band, just with different optical filtering. A ring dye laser was used to excite the $C \leftarrow X$ transition at 602 nm, and the same laser was used to perform both wavelength calibrations at 602 and 618 nm.

Before this measurement, this band had actually not been observed in high resolution, so we had to locate a line ourselves. Using our previously published [84] medium-resolution data for the $C(0) \leftarrow X(1)$ transition coupled with the $C(0) - X(0)$ band

[9]As more lasers connect different ground states to the same excited level, say the cycling A state in this case, the scattering rate decreases, lowering the effectiveness of the laser cooling.

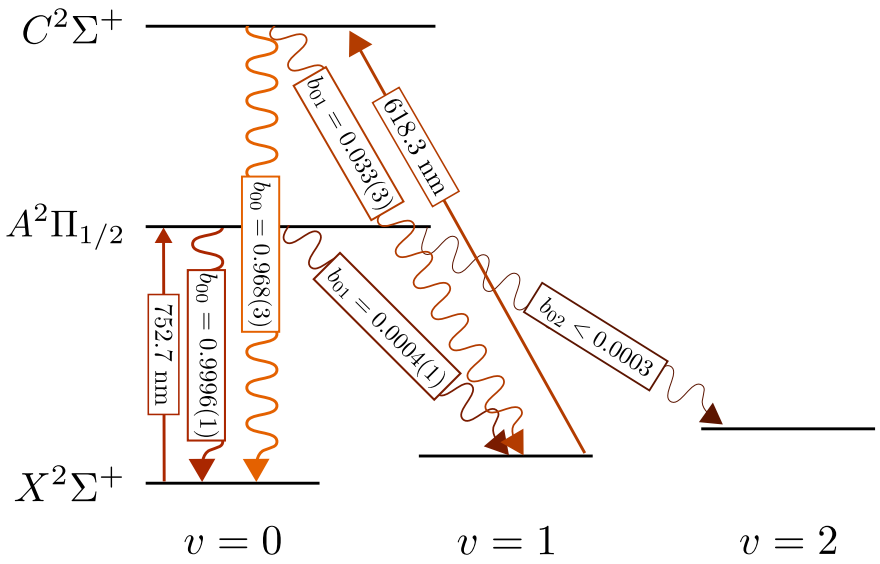


Figure 6.14: Level diagram summarizing our measurements of the vibrational branching ratios $b_{v'v''}$ in RaF. Also shown are the wavelengths for the laser cooling line at 752.7 nm and $v'' = 1$ vibrational repump line at 618.3 nm.

measured at ISOLDE [50], we found a line after a bit of searching at 16611.6393 cm^{-1}, which we thought should be near the band head. As we later learned through more spectroscopy, the band head assignment was redder than expected by around 2 cm^{-1}, and we actually performed this whole measurement using a ${}^{R}R_{11}(N'' = 8)$ line. This is quite high-J for our apparatus, meaning we were probing significantly fewer molecules than if we used a lower-N line, owing to the relative Boltzmann occupations of the rotational levels at 7 K.

Results are summarized in Figure 6.13. Given the value measured, and assuming the trend holds as one goes to increasingly higher vibrational decays, we likely ought to be able to detect the RaF $C(0) - X(2)$ decay as well and measure the b_{02}/b_{00} ratio.

6.6 Results and interpretation

The results obtained for the vibrational branching ratios of RaF are summarized in Figure 6.14.

To the best of our knowledge, these measurements demonstrate that the RaF $A\,{}^2\Pi_{1/2} - X\,{}^2\Sigma^+$ band is the most diagonal transition ever observed in a molecule to date. The closest we were able to find was the $A\,{}^1\Pi - X\,{}^1\Sigma^+$ band in AlF, with a measured branching[10] $b_{01}/b_{00} = 0.73(10)\%$ [157]—one order of magnitude larger. It is worth

[10] Note that their reference uses the notation A_{01}/A_{00}, where A is used equivalently to our b.

noting, however, that the significantly larger mass of RaF and the lower energy of its photon cycling transition means that slowing RaF requires around 20 times more photons than for AlF, assuming the same initial velocity.

With the high resolution spectroscopy of the cycling and repump transitions performed in Section 5.6, a pathway now exists to cool RaF with just two to three total lasers; despite the numerous complexities owing to its radioactivity, RaF promises a straightforward pathway to laser cooling.

These results also help to explain why we initially had so much difficulty detecting the $A - X$ band; while these vibrational branching ratios spell good news for eventual laser cooling, they definitely complicated our off-diagonal detection scheme. Even in these branching measurements the largest signals in the off-diagonal channel were only barely visible by eye, despite the strong diagonal fluorescence (see Fig. 6.5). This also could be a significant reason as to why we have still yet been unable to unambiguously locate the $\tilde{A} - \tilde{X}$ band in RaOH, despite searching the full uncertainty range a number of times[11]. The $C - X$ band for both molecules always had better SNR, and now we have a better understanding as to why.

[11]This only offers a partial explanation, as we have also tried searching by driving the $\tilde{A}(100) - \tilde{X}(000)$ band and detecting the diagonal fluorescence, which should be quite strong. Of course, with extremely diagonal VBRs, this excitation should also be quite weak.

Chapter

VII

Studies on other atoms and molecules

Throughout the life of the Minifridge, myriad species have been produced and studied optically to varying extents. While the previous chapters have detailed the more comprehensive and novel studies, there were many technical breakthroughs made during the prototyping process which we would be remiss to exclude.

This chapter covers work that spanned many years and was motivated by scientific objectives that were often disjoint. As such, it will be organized purely by the species studied, with the idea that relevant context and motivation will be provided in the respective sections.

7.1 Barium-containing

Barium served as our main prototyping species for optimizing production of radium-containing molecules early on. As the next heaviest alkaline earth element, it should behave chemically similar to radium in many ways, apart from the radiolysis effects discussed in Section 5.2 and the existence of its excited 5d orbital which lies below the first excited 6p orbital.

We worked with either pure barium metal or barium chloride liquid solution. When epoxying the pure metal to our target plates, we noticed that in typical atmospheric

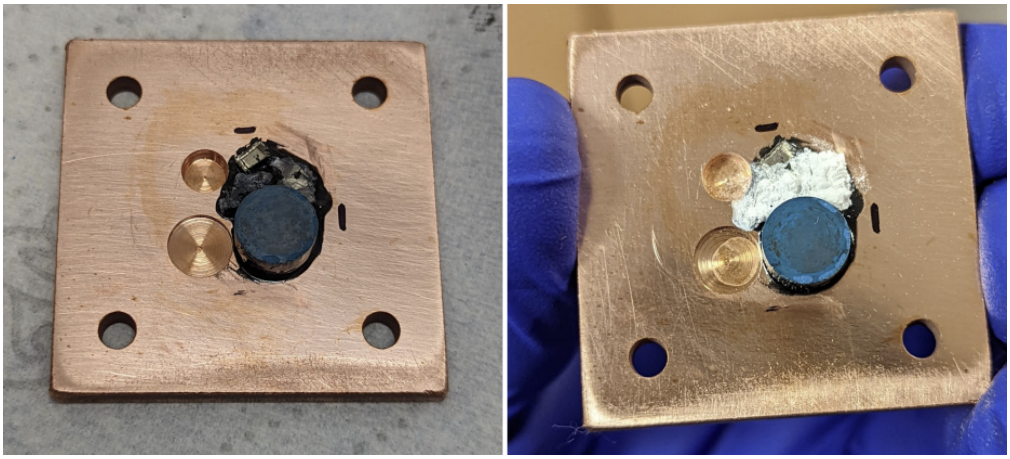


Figure 7.1: Before (left) and after (right) photos of epoxying on a chunk of pure barium metal (right above dark blue circular co-target). Even though the metal had a protective oxide layer, the presence of water vapor in the air resulted in the formation of $Ba(OH)_2$ powder, the majority of which was no longer rigidly attached to the target plate.

conditions the metal would dramatically decompose into barium hydroxide $Ba(OH)_2$, spewing loose powder on the target surface (Fig. 7.1). We remedied this for future test runs by coating the metal in a layer of Apiezon N vacuum grease to block the majority of water vapor from contacting the metal, and have not had an issue since.

The following two subsections report on the lessons we learned that allowed us to more efficiently produce the molecules BaOH and BaF, in preparation for RaOH and RaF. Experimentally, barium molecules present a slight complication due to having such low-energy first excited states, with transitions in the range of 820 nm; most of the tunable laser systems we had available to us operated at shorter wavelengths than this, so we often had to probe transitions that were not the main line to the first excited state.

BaOH

Given our restrictions in handling of our radium solution, we needed an efficient way of producing RaOH while ablating two separate targets, as described in detail in Chapter 5. Previous experiments in the group had produced YbOH via this so-called double ablation, but not in any optimized way and not as efficiently as a combined Yb + $Yb(OH)_3$ pressed powder target [62].

As a first baseline for observing BaOH in the Minifridge, we made a pressed powder co-target out of copper (II) hydroxide, $Cu(OH)_2$, with 5% polyethylene glycol

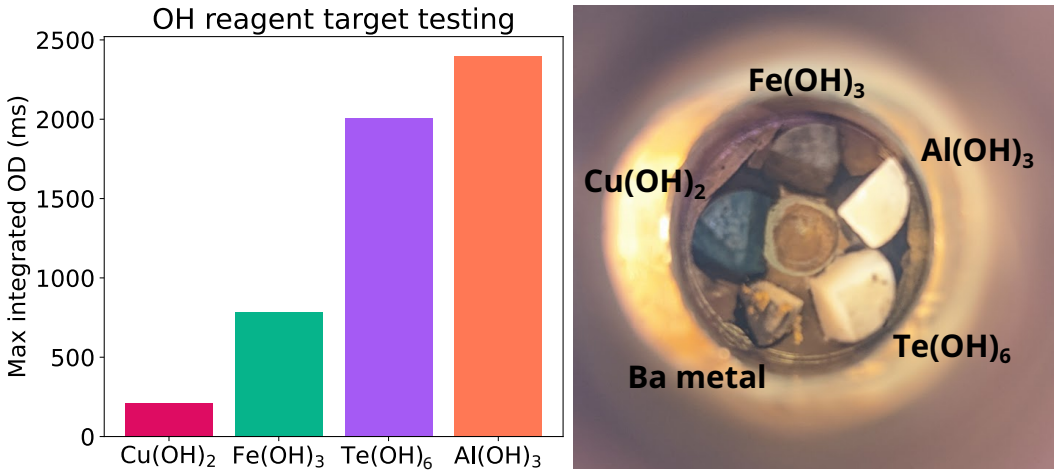


Figure 7.2: Reagent co-target testing to identify a suitable solid-state hydroxide source. Because the data was not taken in a rigorously systematic way, the bars show only the maximum signals achieved with each reagent; the telluric acid ($Te(OH)_6$) and aluminum hydroxide targets performed roughly equally. Aluminum hydroxide is significantly cheaper and possesses no safety hazards, making it the easy choice.

by mass as a binder[1]. Simultaneous ablation of a chunk of barium metal with this copper co-target yielded absorption signals on the BaOH $\tilde{A}\,^2\Pi_{3/2} \leftarrow \tilde{X}\,^2\Sigma^+$ line at 12043.493 cm^{-1} (830 nm, driven by a Coherent 899 Ti:Sapph). Peak absorption dips were only $\sim$ 3%, corresponding to a maximum molecule density of roughly 5×10^7 cm^{-3}, or approximately 10^9 total molecules if we assume a roughly uniform distribution throughout the cell.

We then set out to test various different hydroxyl-containing pressed powder reagents. Figure 7.2 details the results of a test comparing simultaneous ablation of barium metal with $Cu(OH)_2$, $Fe(OH)_3$, $Te(OH)_6$ and $Al(OH)_3$. The tests unambiguously demonstrated that $Al(OH)_3$ was the most successful reagent, as it performed similarly to telluric acid but at a fraction of the cost and handling hazards.

Production of BaOH using all of these co-targets benefitted from the use of chemical enhancement. Unlike our mechanism for enhancing the production of other species, we drove the $^1P_1$ transition in atomic barium at 18060.2610 cm^{-1} rather than the $^3P_1$ line at 12636.623 cm^{-1}, entirely due to the available laser systems at the time. Even still, the enhancemet factor achieved from sending in roughly 200 mW of this 553.7 nm light was around 15, meaning our signals were approximately 15 times larger with enhancement than without.

[1]Sometimes, our pressed powder targets would crumble or break apart when removed from the dye press. Addition of PEG helped maintain the cohesion, although not dramatically.

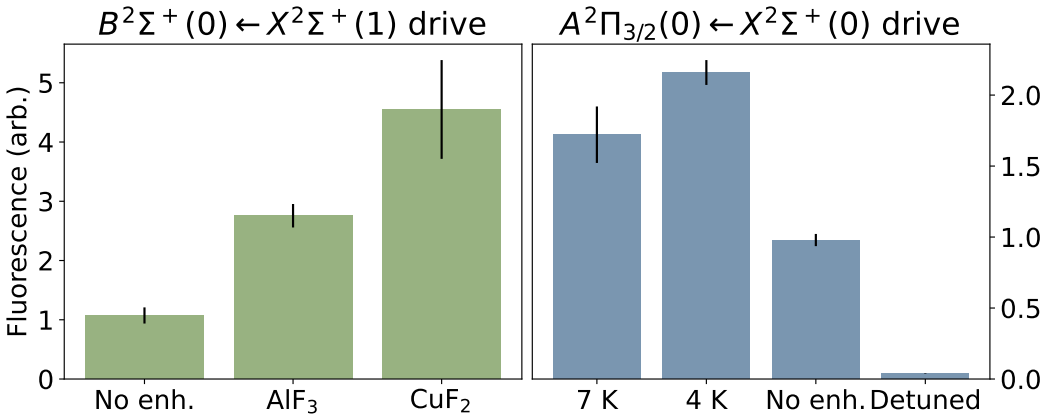


Figure 7.3: Testing various configurations for producing BaF. Data between the two plots are normalized to the "No enh." signal, referring to molecule production without enhancement light. The left data focused on co-ablation targets, where the line driven was at 13, 573.9648 cm^{-1} [159], where we detected the diagonal decays down to $X(0)$. Data for the right was obtained by driving the line at 12262.835 cm^{-1} [160] and detecting the off-diagonal decays to $X(1)$. Normally this detection scheme is weak, but BaF is suitable non-diagonal such that many of the decays are to this $X(1)$ state.

BaF

Whereas hydroxide-containing molecules have been produced using solid-state reagents in our lab before, fluorine molecules are almost always made via reactions of a metal with some fluorinated gas such as SF_6 or NF_3 [158]. Fluorinated ceramic sputtering targets exist, such as AlF_3 or CaF_2, but this does not solve our problem of how to make RaF, as we are unable to acquire a starting material made from a radium fluoride ceramic.

We tested two solid-state fluorine reagent sources: a dense AlF_3 ceramic sputtering target and a pressed powder of CuF_2, similar to how we made the hydroxide targets above. For each we also tested with and without chemical enhancement to show that, contrary to what others have shown with gas-phase reagents, these solid-state fluorine targets produced more molecules when we used chemical enhancement light, albeit with a lesser enhancement factor than for the hydroxides.

From these tests, we concluded that copper fluoride CuF_2 pressed powder targets performed the best at producing monofluoride molecules. This may be slightly counterintuitive, as the aluminum fluoride ceramic is an incredibly dense ablation target with many more fluorines per unit volume. However, we have noticed in the past that these pressed powders tend to rank among the best co-targets, perhaps by

providing some co-localized helium buffer gas that is released in the ablation process.

These measurements produced ever-so-slightly larger signals when operating at 4 K versus 7 K. We believe this to be a consequence of either not optimizing the helium properly for this data set, or by using a solid metal target as our barium source. When running with a trace, drop cast target, we almost always produce more molecules when operating at 7 K.

7.2 Calcium-containing

Like barium, the alkaline earth element calcium is another proxy for radium. It has the significant advantage over barium that many calcium-containing molecules have been studied exceptionally well, whereas even for basic transitions in BaF/BaOH we were running into problems resulting from a lack of existing spectroscopy. The molecules it produces also tend to have more similar VBRs to radium than barium-containing molecules do, allowing us to better understand the relative signal sizes we should expect. Last, calcium molecules have higher-energy transitions, which are more convenient from the perspective of our tunable laser systems.

Being so much lighter than radium, however, means that the chemistry to form calcium molecules is less analogous than for barium. Because of the much weaker spin-orbit interaction in calcium, driving the $^3P_1$ transition requires significant amounts of power at 657 nm, definitely more than we can produce without a dedicated laser system. We also lacked a way of generating light at 422 nm for the $^1P_1$ line, meaning for none of the calcium tests were we able to correlate our signals with chemical enhancement.

All of our calcium-containing molecules were produced by ablating a CaF_2 ceramic sputtering target, either on its own (to produce CaF) or with a reagent co-target described below. We performed a significant amount of tests on CaF, including attempts at photon cycling and two-photon spectroscopy inside the cryogenic buffer gas cell. Unfortunately, we were unable to see success with either of these two methods, for reasons we believe to be related to molecular state remixing from collisions with the helium buffer gas. CaF was used to benchmark the RaF branching ratio measurements, as described in Chapter 6.

The following subsections describe our tests to identify suitable reagent co-targets for making other types of radium-containing molecules.

$CaNH_2$

As we neared our first result demonstrating production of RaOH, we started to think about what sorts of other radium-containing molecules would be both interesting and feasible. From an EDM standpoint, one of the fundamental limitations of alkaline earth monohydroxides is the lifetime of the excited bending mode where the measurement takes place, typically $\lesssim 1$ s. While not a limitation in a beam measurement, where the coherence is almost always capped by the transit time, next-generation experiments utilizing trapped polyatomic molecules will benefit from science states with significantly longer lifetimes. Keeping with the metal-plus-pseudohalogen moiety, alkaline earth monoamines with the formula MNH_2 are an improvement over hydroxides because their parity doublets arise from very low-lying rotational states with radiative lifetimes $\gtrsim 100 - 1000$ times longer than the excited bending mode of a MOH molecule [161, 162]. They also benefit from the same advantages of the hydroxides, including potential laser-coolability [163]. $RaNH_2$, which combines the monoamine structure with the advantages of a heavy nucleus, has the potential to be an extremely sensitive species for future EDM searches.

As alkaline earth monoamines are only one atom larger than the monohydroxides, the naïve thought would be that they can be produced using similar means. Of course, this claim needs to be verified. It is generally found that going from a MF to MOH structure results in order-of-magnitude smaller signals, and a similar trend has been observed anecdotally from MOH to MNH_2 in the limited number of studies on these molecules[2]. Given our RaF/RaOH signals, this reduction would put us slightly above the signal floor, meaning detection of $RaNH_2$ is theoretically possible. However, in all experiments on MNH_2 molecules, gas-phase ammonium (NH_3) was used as the reagent; to be compatible with our target production protocol for radioactive species, we need to identify a suitable solid-state reagent.

Primary amines are molecules with the structure RNH_2, and thus are a logical source of -NH_2 ligands. Like always happens when trying to produce a new molecule, this new class of reagents presented its own set of challenges. Primary amines are relatively common biologically, but often in complex aromatic molecules—we have had good luck using simpler reagents to produce other molecules, so these more complicated ones were ignored for our initial round of testing[3]. Nitrogen-containing compounds

[2]This assertion comes from our own experience producing molecules in our supersonic beam source and is not rigorously quantified.

[3]Many primary amines and their salts are members of the psychoactive or opioid class of alkaloids, which (understandably) complicates their use as a molecular precursor.

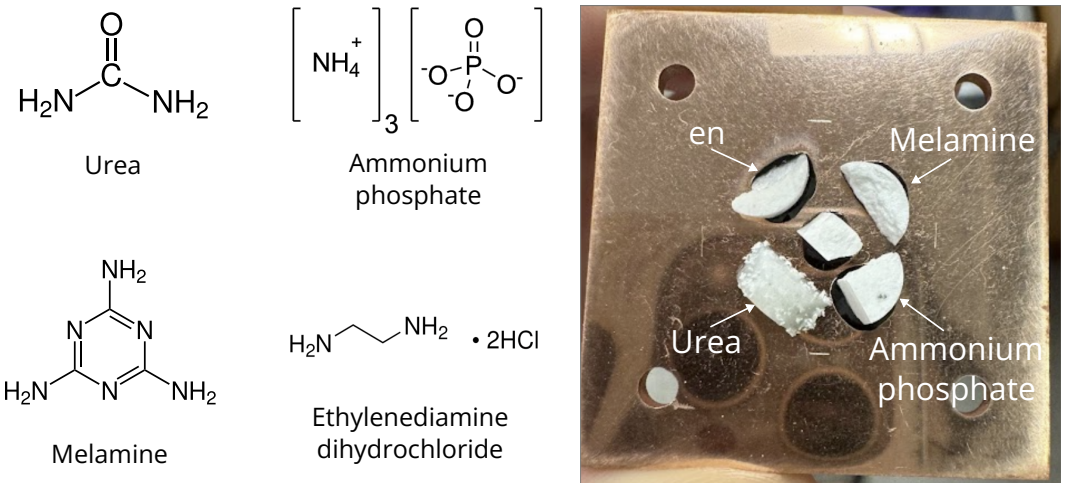


Figure 7.4: Left: chemical structures of the reagents tested for producing $CaNH_2$. Right: the target plate used for amine reagent testing, showing the four different pressed powders. Ethylenediamine is commonly abbreviated to en when represented as a ligand. The target at the very center is the CaF_2 sputtering target used as a source of calcium atoms. One point of note is the extra crystals on the edges of the urea target—these were not present when the powder was initially pressed, but did not seem to drastically alter the structure or quality of the target as a reagent.

also have a tendency to be reactive, often with an explosive or acutely toxic flair, which further restricted the set of usable molecules.

In searching for primary amine sources that are solid, relatively unreactive, simple, and acquirable, we identified four candidates for production testing: urea, ammonium phosphate, melamine, and ethylenediamine dihydrochloride (abbreviated "en" as a ligand). Their chemical structures are shown in Figure 7.4. We also purchased guanidine nitrate, but it was not tested as it did not arrive in time. All materials were acquired as powders or salts; no additional mortaring or ball-milling was performed to uniformize the different materials, so the grain size between the targets definitely varies. They were each pressed at ~1 GPa in an 8 mm die press for ~30 min, and no unusual behavior was observed during the pressing process.

Thanks to its existing spectroscopy and convenient transition wavelengths for dye lasers, $CaNH_2$ was identified as a suitable species to prototype solid-state monoamine production in the Minifridge. Previous high-resolution spectroscopy published in [164] identified a transition out of the ground state at 630.04 nm, corresponding to the $\tilde{B}\,^2B_1 \leftarrow \tilde{X}\,^2A_1$ transition (for details on the term symbols for asymmetric top molecules, see [165]). To confirm this in our apparatus, we scanned around this

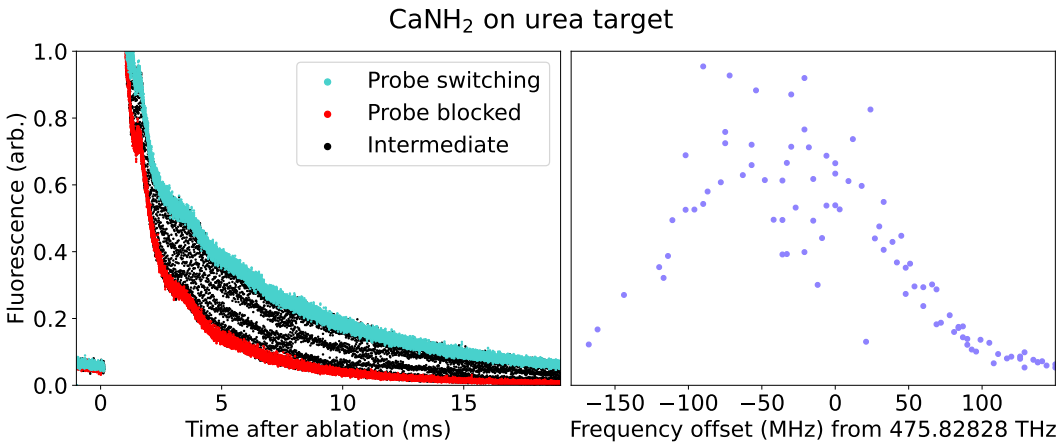


Figure 7.5: Single shot and scanning data for $CaNH_2$ while ablating the urea co-target, which seemed to yield the best signals. Left: Demodulated single-shot data showing the excess PMT signal when the CW light is on, corresponding to molecule fluorescence. Right: Scan around the resonant frequency reported in [164] for the $\tilde{B}\,^2B_1 \leftarrow \tilde{X}\,^2A_1$ transition in $CaNH_2$.

wavelength region using a CW dye laser[4] and detected the off-diagonal fluorescence to the Ca-N stretch at 653 and the in-plane bending mode at 656 nm. Single-shot and scanning data are shown in Figure 7.5.

Once we located the transition, we began comparing the signals by co-ablating different reagents. This data is summarized in Figure 7.6. In all configurations, the best signals resulted from co-ablation of urea, regardless of operating temperature. However, the relative shot-to-shot fluctuations of the urea signals were also the worst, potentially hinting at the need to grind down the reagent to a smaller particle size before pressing. Another point of note is that the ethylenediamine was undoubtedly the worst, despite being "simpler" than melamine.

Interestingly, the signals seemed much stronger when operating at 4 K, which is contrary to what we see for most other molecules we produce. A potential reason for this could be the further compression of the rotational distribution by going from 7 K to 4 K, as depicted in Chapter 4. Asymmetric top molecules have many more low-lying rotational states than diatomic or linear triatomic molecules owing to their two additional moments of inertia. This provides more states into which to distribute the rotational population.

One downside of testing production on $CaNH_2$ is our lack of a strong $^3P_1$ enhancement laser. As such, we are unable to determine whether solid-state monoamine

[4]Coherent 699 configured with Rhodamine 640 dye.

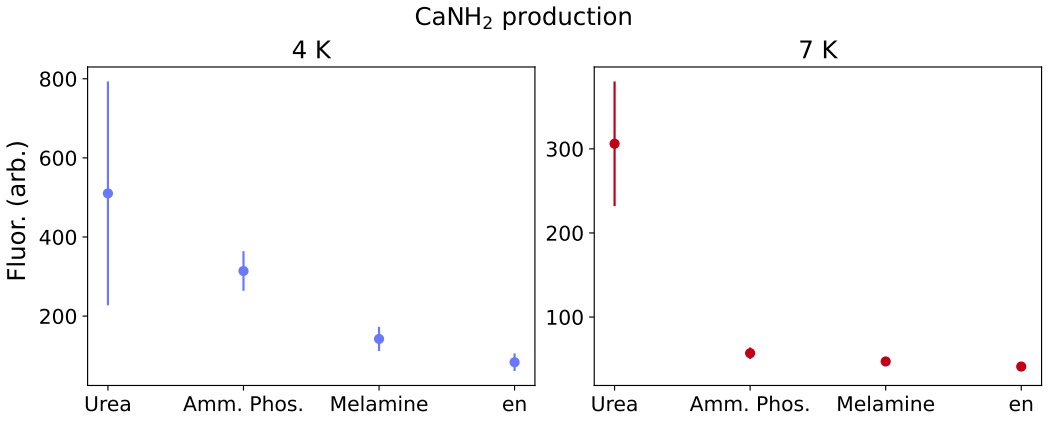


Figure 7.6: Averaged $CaNH_2$ fluorescence signals as a function of ablated reagent, at two different operating temperatures. In both cases, the urea co-target is the most successful. Error bars are the standard deviation of the sample values for each co-target.

reagents benefit from chemical enhancement in the same way that solid-state halogen and hydroxide co-targets do. However, it has been demonstrated in [164] that enhancement improved production of $CaNH_2$ with a gas-phase ammonia reagent, which would hint that it is also beneficial for these solid-state targets.

We concluded the monoamine testing here, as the theory for the $RaNH_2$ electronic energies was not yet precise enough to warrant an efficient survey scan. It is worth emphasizing that, in stark contrast with the -OH reagents, which all tend to produce signals on a roughly similar order, the variation in production of $-NH_2$ molecules is highly reagent-dependent. Given this, it is definitely worth exploring more reagent options before attempting to produce a molecule from a trace isotope such as radium. It is also unclear how chemical enhancement will affect the production, and whether the effect is similar for different reagents.

CaCl & CaI

Given the intense fluorescence signals we were able to consistently obtain for RaF, it became apparent that other radium halides should be not only feasible to make, but potentially straightforward. In fact, this is what we observed when first producing RaCl as described in section 5.7. However, that discussion ignored the process of identifying a suitable co-target for chloride molecule production. Just like with the monoamines, calcium was chosen as the production proxy because of the existing spectroscopy of Ca-halogen molecules and the convenient transition wavelengths for dye laser operation.

We produce RaF via co-ablation of radium and copper (II) fluoride. Because of the significant chemical toxicity of all of the copper halides, rather than use the analogous copper molecules to source chloride, bromide, and iodide ligands, we instead opted to first test silver halides AgX, where X = (Cl, Br, I) as the co-targets. Additionally, lanthanide trichloride targets $NdCl_3$ and $PrCl_3$ were made as we already had a stock of these chemicals for other purposes[5]. For all of these targets, ≈ 200 mg of powder was pressed in an 8 mm die press for 30 minutes at 1 GPa; no additives were used, just the chloride (or iodide) powders.

Lanthanide trichlorides

Neodymium (III) chloride and praseodymium (III) chloride exhibit striking pink and green coloration[6], respectively, as seen in Fig. 7.7a. Unfortunately, we did not appreciate how extremely water-soluble these compounds were. Test pressings developed a sticky surface layer due to overnight exposure to atmospheric water vapor but otherwise seemed stable. When we attempted to epoxy them onto a radium plate, however, the targets completely melted during the overnight curing process, destroying the Yb metal as well and seeping into the fluoride and hydroxide co-targets (see 7.7b).

Whether the additional decomposition was caused by the increased airflow in our isotope handling lab or from some reaction with the epoxy/catalyst is undetermined; these chemicals were never used again for targets. Because of the potential risks associated with attempting to install this plate, it was disposed of as radioactive waste and remains the only target plate that never made it to molecule production. From this point on, we adhered to a more rigorous procedure of testing the stability of any new chemical under our target production protocol before using it with radium.

Silver halides

Following the dramatic failure of the lanthanide chlorides, it was appealing to switch to the silver halides as they are extremely *insoluble* in water. Test targets were pressed out of AgCl and AgI powders, but not AgBr as it was on back order for a few months during the time of these tests. The new targets exhibited behaviors that we had

[5]When we were considering ways to increase the radium drop cast target adhesion, we acquired these lanthanide chlorides as they are notoriously sticky.

[6]This coloration also has the unusual property where it only appears in the right lighting conditions—under fluorescent room lighting, the targets appeared greyish-white, but when moved to an area with even indirect sunlight would immediately turn these vivid colors.

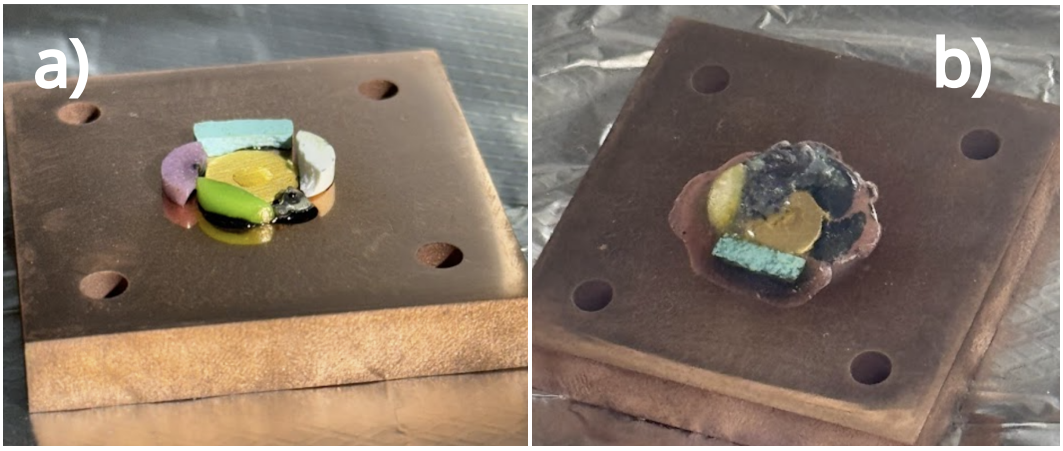


Figure 7.7: Before-and-after overnight drying of the lanthanide trichloride co-targets on a radium-containing target plate. Note that the photos are inverted from left to right; the blue CuF_2 target is visible on both panels. a) $PrCl_3$ can be seen in bright green (bottom left) and $NdCl_3$ in pink (left). The stickiness is partially observable as a sheen on the targets. b) Next morning, the lanthanides had completely melted, leaving a liquid layer on the surface of the target plate. The drop cast radium was partially covered and the plate was deemed unsafe to install, rendering it radioactive waste.

not encountered before in a pressed powder: rather than flake and crumble upon attempts to cut them into smaller pieces, they were able to bend like a soft metal. We also overlooked their tendency to corrode metals, as they were quite detrimental to the die press, leading to significant rust buildup on the steel that required a lot of scraping to remedy.

Silver halides are famous for their unique photosensitivity, capable of decomposing in the presence of ambient light. To verify that this photosensitivity would not impact the structural integrity of pressed powder silver halide targets, we have placed one target each of AgCl and AgI in the windowsill of our student office, which receives indirect sunlight. After over a year of light exposure, the targets are still rigidly attached and visibly unchanged.

Similar to $CaNH_2$, a CaF_2 sputtering target was used to source the calcium atoms. For each halide, we probed the $A\,^2\Pi_{1/2}(v=0) \leftarrow X\,^2\Sigma^+(v=0)$ transition using a 50 kHz repetition rate pulsed dye laser and detected the off-diagonal fluorescence to the $X\,^2\Sigma^+(v=1)$ state. The pulsed dye laser was chosen for this application because of its large linewidth $\Delta\nu \sim 0.07$ cm^{-1} relative to the published transition precisions of 0.1 cm^{-1} [166, 167]. For CaCl, the probe transition is listed at 16094.8 cm^{-1} (~621 nm) with a corresponding off-diagonal decay at 15727.3 cm^{-1} (~635.8 nm). For CaI, the

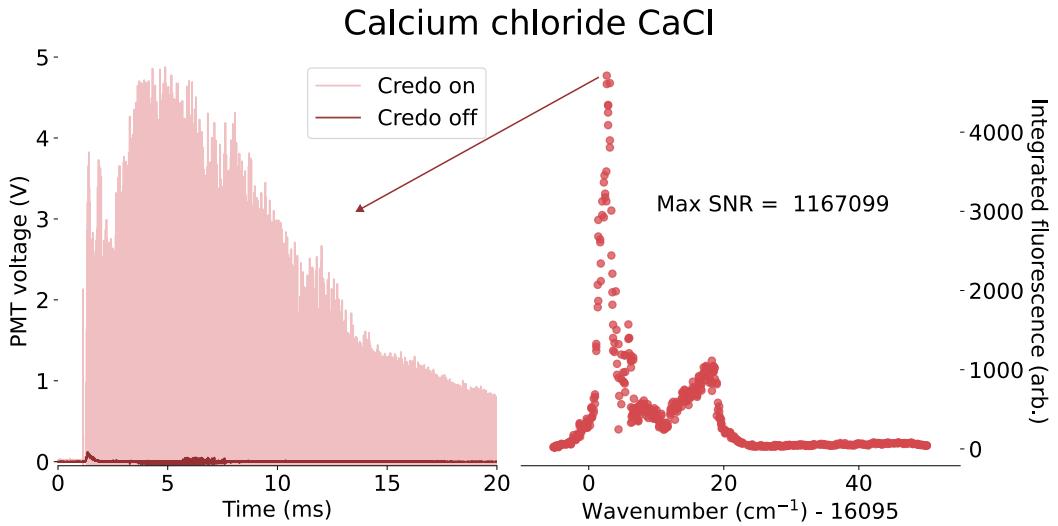


Figure 7.8: Single-shot and scan data for pulsed dye excitation of calcium chloride, produced by co-ablating a calcium fluoride sputtering target with a pressed powder of silver chloride (AgCl). The single-shot data corresponds to the point on the scan with the largest integrated signal. Signal-to-noise ratio for this point is included inset in the scan trace.

probe transition is listed as 15588.4 cm^{-1} (~641 nm) with a decay at 15349.7 cm^{-1} (~651 nm). Data for these scans are shown in Figures 7.8 and 7.9. Single-shot SNR on the band head was incredibly high, exceeding 200,000 for CaI and 1,000,000 for CaCl, giving us confidence that these reagents would be sufficient for producing radium halides. This is without any form of chemical enhancement, which was demonstrated to be effective for radium chloride, meaning we still have potential to produce another additional order-of-magnitude number of molecules.

Given the success of the silver halides for CaCl and CaI, it is natural to be curious about using AgF for production of CaF and RaF. Unfortunately, the trend of extreme insolubility reverses for AgF, which is ~ 10^7 times more soluble in water than AgI [168]. Given our experience with the highly soluble lanthanide chlorides, and since we already had a working source of fluorine atoms in CuF_2, we decided to forego trying AgF as a reagent.

7.3 Uranium oxide

In preparation for eventually trying to observe neptunium-containing molecules (see the following Section 7.4) and other exotic transuranic species, we wanted to test our production and detection scheme on some reasonably similar molecule. Some of the more promising and interesting neptunium-containing candidates were neptunium

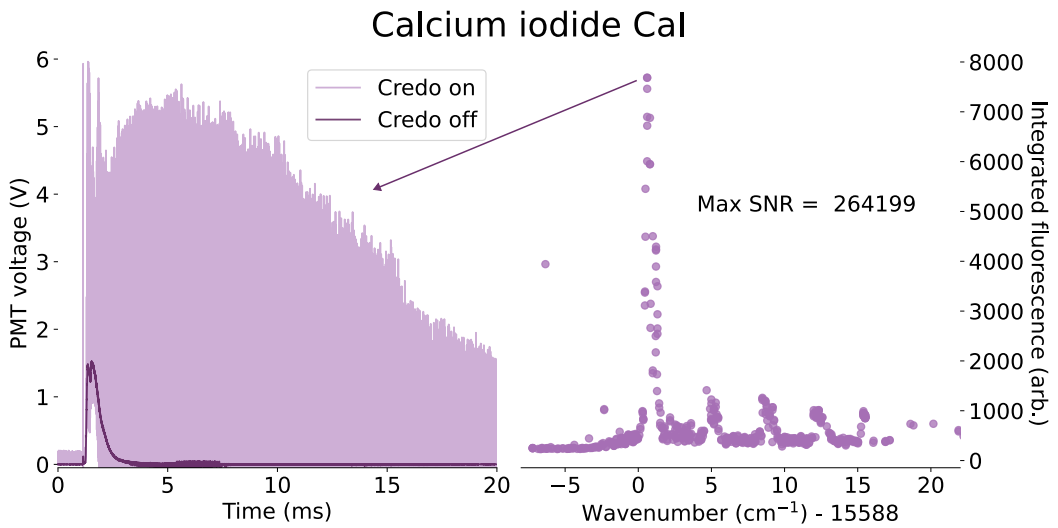


Figure 7.9: Single-shot and scan data for pulsed dye excitation of calcium iodide, produced by co-ablating a calcium fluoride sputtering target with a pressed powder of silver iodide (AgI). The single-shot data corresponds to the point on the scan with the largest integrated signal. Signal-to-noise ratio for this point is included inset in the scan trace.

oxide (NpO) or dioxide (NpO_2), in part because the solid-state actinide oxides are relatively well-understood relative to other actinide compounds.

Previous sections have discussed how we prototype our production and detection protocols using lighter elements in the same column, owing to the similar chemistry within a periodic group. For the actinides, particularly elements from thorium to neptunium, this chemical similarity begins to break down dramatically. The easiest way to see this is by looking at the term symbol of the elements: for example, all alkaline earth elements including radium, barium, and calcium have the exact same $^1S_0$ ground state configuration, leading to their formation of very similar types of molecules. The next-heaviest element in the neptunium group is promethium, with a $^6H_{5/2}$ ground state; contrast this with the $^6L_{11/2}$ ground state of neptunium, where the two differ by four units of orbital angular momentum. On top of this, promethium is the second-lightest element (after technitium) which has no stable isotopes, and sees no justification for its industry-scale production or purification, making its acquisition just as difficult as (if not greater than) that for neptunium.

Uranium, however, has a $^5L_6$ ground state, and is acquirable in quantities amenable for prototyping. In addition, because of the practical uses of uranium, many uranium-containing molecules have also been studied spectroscopically, including uranium monoxide (UO) [169, 170] and uranium dioxide (UO_2) [171]. Even though not a direct

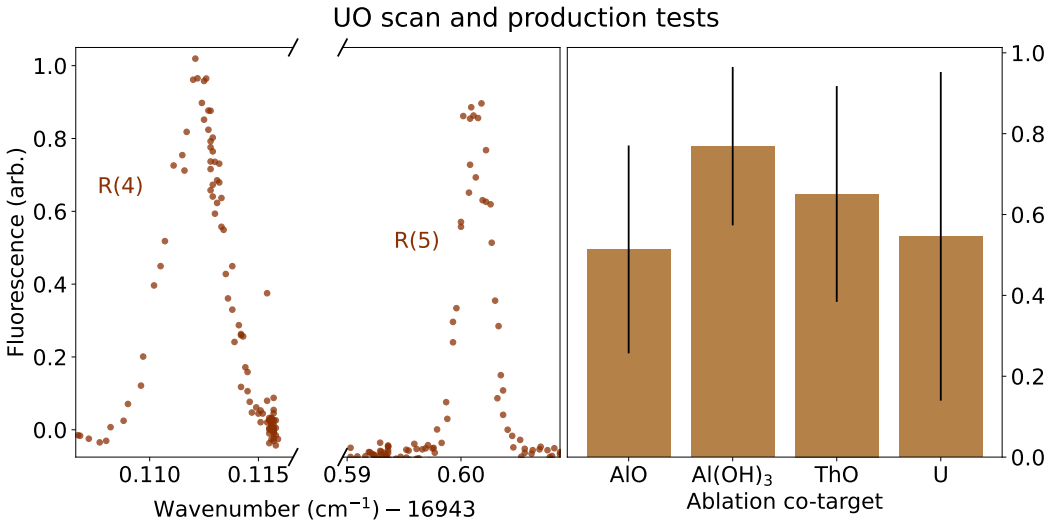


Figure 7.10: Left: Fluorescence scans of some lines in uranium monoxide (see text for details), showing two lines recorded at high resolution. Right: Tests of various ablation co-targets in producing UO. The co-targets are: alumina ceramic, aluminum hydroxide pressed powder targets, thoria ceramic, and none. In the no co-target example, we believe the oxygens to be sourced from the extreme degree of oxidation of the pure uranium metal.

parallel to neptunium, it seemed like uranium was the best we could do.

Production of uranium molecules followed from ablation of a piece of uranium metal, either on its own or with one of a number of co-targets. Initial tests focused on demonstrating and optimizing production of UO, as we have found diatomic molecules much simpler to work with and because nice high-resolution spectroscopy on this molecule already existed, whereas for UO_2 the lines present near wavelengths that were accessible with our existing laser systems were only known to low resolution. We drove what have been previously observed to be strong lines at 16943.109 cm^{-1} and 16943.590 cm^{-1}, corresponding to $R(4)$ and $R(5)$ transitions out of the ground electronic $X(1)4$ state to the excited [16940]5 level[7] [170]. To probe these transitions, we used our ring cavity dye laser and detected the off-diagonal fluorescence to the $v'' = 1$ vibrational level of the ground state, at a wavelength of ≈ 622 nm.

The results of these tests are summarized in Figure 7.10. Notably, the strong SNR of

[7]The complicated structures of these molecules give rise to these unconventional term symbols. In this representation, the rightmost number for both levels labels the internuclear-axis-projected electronic angular momentum Ω. The number in parentheses (n) labels the state as the n^{th} state with this Ω, starting from 1. Therefore, $X(1)4$ is the ground (X) state, which is the 1$^{\text{st}}$ state with $\Omega = 4$. The number in brackets refers to the energy in cm^{-1} from the ground state where an excited level was observed, in lieu of giving it a more rigorous assignment when not enough is known about the molecule.

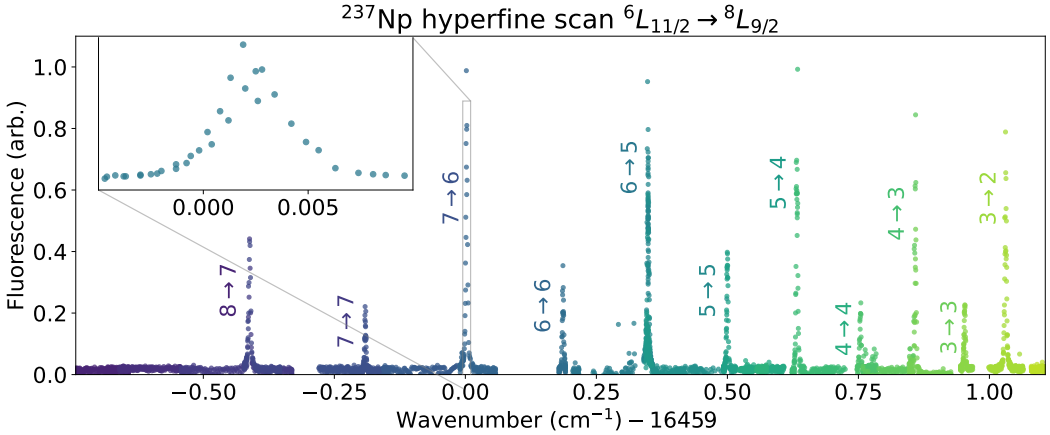


Figure 7.11: Scan of the hyperfine lines on the ^{237}Np ($I = 5/2$) $^6L_{11/2} \rightarrow {}^8L_{9/2}$ transition at 607.5 nm. Lines are labeled by the ground and excited hyperfine sublevels $F'' \rightarrow F'$. Only the $\Delta F = -1, 0$ transitions were observed, as the $\Delta F = +1$ transitions are expected to be a factor of 10 weaker. Inset shows typical line shapes for each of these transitions.

these lines, which we were also able to observe in absorption, implied that successful production should also be feasible in the structurally similar molecule NpO.

7.4 Neptunium

Laser spectroscopy on transuranic-containing molecules in the gas phase is not just sparse, it is nonexistent. Given our developments on producing radioactive molecules safely and in high enough concentrations to measure rotationally resolved spectra, we are in a unique position to advance the understanding of many of these understudied species.

The most straightforward transuranic molecule for us to start with would be one containing a radionuclide with a long half-life, as this drastically mitigates the hazards associated with its radioactivity without us having to engineer anything. Neptunium-237, with its half life of 2.14 millions years, fits this criterion. In addition, it decays via the U-233 chain, meaning there is no radon produced as a daughter nuclide.

To develop our capabilities for producing and studying increasingly exotic species, we received a custom-made pressed powder target containing neptunium from Richard Wilson at Argonne National Laboratory. The target composition is 7.4 mg of ^{237}Np (total activity 5.2 μCi) in the form of NpO_2 mixed into roughly 90 mg of potassium chloride (KCl) to increase the volume. Unlike our other pressed powder targets, this was formed using a 4 mm die press.

Our first measurements focused on testing this target to characterize the production of neptunium atoms. We drove the ^{237}Np $^{6}L_{11/2} \rightarrow {}^{8}L_{9/2}$ transition at 607.5 nm and performed a scan over the many hyperfine sublevels, shown in Fig. 7.11. Relative to the published line list from the 1970's [172], we observed all of these lines to be red-shifted by roughly 22.49 GHz, indicating a systematic offset present in these older values.

At the time of this writing, the work on neptunium is active and ongoing, with the goal of eventually moving to study neptunium-containing molecules for the first time.

Chapter

VIII

Magnetic shielding

Paramagnetic molecules (such as RaF, RaOH, and YbOH) possess a permanent magnetic dipole moment, which in the ground $\Lambda = 0$ state is largely given by the intrinsic magnetic moment (spin) of the valence electron, on the order of $\mu_{\text{mol}} \sim \mu_B$. EDM-style measurements involve orienting the molecules using an external electric field, which will also orient them relative to any external magnetic fields that may be present in the experimental region. Interactions of these external magnetic fields $B(t)$ with the magnetic dipole of the molecule will induce a precession of the electron spin, and this precession leads to a phase accumulation of the molecular wavefunction[1]:

$$\Delta\phi^B = \frac{\mu_{\text{mol}}}{\hbar} \int_0^\tau B(t)dt \,, \tag{8.1}$$

for an interaction time τ. If we only consider the contribution from static fields, or those which vary on timescales much slower than that of the measurement[2], we get:

$$\Delta\phi^B = \frac{\mu_{\text{mol}} B\tau}{\hbar} \,.$$

[1] In an EDM measurement the electron is prepared in a spin-up and spin-down superposition, where the energy separation between these two states interacting with the external magnetic field gives rise to this phase accumulation.

[2] Fields which vary at a faster rate are essentially averaged over in the integral and contribute negligibly to the false EDM signal. On top of this, these oscillatory fields are largely blocked by the electrically conductive vacuum chamber which surrounds the molecules.

The sign of this phase accumulation flips when the molecular spin is inverted relative to the external magnetic field B.

Compare this with the phase accumulation due to a permanent CP-violating electromagnetic moment, such as the electron electric dipole moment d_e interacting with a molecular effective electric field $\mathcal{E}_{\text{eff}}$:

$$\Delta\phi^{\mathcal{E}} = \frac{d_e \mathcal{E}_{\text{eff}} \tau}{\hbar} .$$

Inverting the molecular dipole the orientation of d_e relative to $\mathcal{E}_{\text{eff}}$, and thus this phase acquired also changes sign under inversion. Experiments measuring an EDM project out the phase accumulated in the two molecule orientations to extract the underlying CP-violating moment (d_e in the above example).

The consequence of $\Delta\phi^B$ is simple but profound: the interaction of a quasi-static magnetic field with a paramagnetic molecule can mimic the effect caused by a permanent CP-violating electromagnetic moment. While they can be isolated from each other by, for example, comparing their behavior under inversion of the molecular dipoles, there can still be higher-order effects that can lead to systematic errors. Furthermore, any sort of magnetic field noise or inhomogeneity can lead to decoherence of the wavefunction and a reduction in sensitivity. Any experiments attempting to measure these sources of new physics thus need to control the magnetic fields present in the experimental region to prevent decoherence or measurement of a false EDM signal. Several ideas have arisen recently to overcome this limitation, either by careful selection of field-insensitive molecular transitions [116], or by implementing a measurement scheme that does not require alignment of the molecules in the lab frame [43]. Even so, uncontrolled magnetic fields will couple into the magnetic moment of the molecule at some order and ultimately contribute to the experimental noise floor.

Any compass will elucidate the fact that magnetic fields exist everywhere; even with no field-generating object or appliances nearby, the Earth still contributes to the magnetic background at the level of ~ 0.5 Gauss (G), varying slightly around the world[3]. One may think of simply measuring the value of this background field at the experimental location and accounting for it as contributing to some global phase offset in all future measurements; unfortunately, this logic fails for a handful of reasons. At the most basic level, Earth's magnetic field itself is not constant, varying throughout the day

[3]It is convention within the field of AMO to use units of Gauss as opposed to the SI unit Tesla (T), where 1 T $\equiv 10^4$ G. This is partly historical, and partly because magnetic phenomena affecting molecules often occur at small field values, making it a more natural unit to describe these quantities.

as much as ±0.2% due to thermal changes in the solar wind [173] and as much as 10s of percent over years to decades [174]. Practically, as will be described later, the interaction of magnetic fields with magnetically susceptible metals is incredibly complex to predict, where magnetic field lines can be redirected in unexpected ways, even by materials which themselves do not generate significant fields. As most experiments are comprised of many metallic parts, this leads to an experimental environment which is sensitive to any changes of external magnetic fields, either originating from the Earth or any other magnetic items nearby, and is also sensitive to the positioning of the experimental components themselves, as these will interact with and modify any ambient fields.

Rather than understand and account for the background magnetic field, experiments opt to reduce it as much as possible, with the idea that at a low enough level any unexpected fields will contribute negligibly to the total noise compared to other sources. The use of the word "reduce" rather than "eliminate" is subtle, and adumbrates the main challenge underscoring magnetic shielding: the non-existence of magnetic charges (monopoles) means that magnetic fields cannot terminate. In this sense, mitigation of static magnetic fields is entirely unlike that for electric fields. Whereas the charge rearrangement inside a conducting material will block electric fields as well as oscillating electromagnetic fields (assuming the material is thicker than the skin depth [175]), magnetic fields can only be redirected using materials with a high magnetic permeability, or shimmed by the application of counter-propagating fields. The former method is typically referred to as "magnetic shielding" because these high-permeability enclosures shield an interior experimental region from the external fields.

While not the subject of this work, it is worth a brief discussion on the advantages and limitations of using field-generating coils for magnetic field attenuation. Three pairs of coils, one for each spatial dimension, allow for the homogenization (shimming) of the background fields, simply by generating magnetic fields opposite to the ones measured in the experimental region. A main advantage of this method is its tunability; by adjusting the current driving each coil, the shimming field can be changed quickly and precisely to meet the exact needs of the setup. Active feedback with in-situ field measurement further allows for the compensation of changing background levels, and with careful experimental design can be incorporated into the measurement scheme. Without any sort of feedback, this method becomes highly sensitive to changes in the background level, as the field cancellation using coils is an additive pro-

cess ($B_{\text{experiment}} = B_{\text{background}} + B_{\text{coils}}$) rather than an attenuation of the background level ($B_{\text{experiment}} = \frac{B_{\text{background}}}{S}$, where S is the "shielding factor" of a magnetic shield assembly, discussed later). A further limitation arises when the experimental region is large; fields generated by magnetic coils vary as $B(r) \sim 1/r^3$ for a distance r from the coil, meaning that controlling the uniformity becomes significantly more challenging as the shimmed area increases. Uniformity is improved when the coils sit further from the region of interest, but this requires driving them with increasingly higher currents, which at a certain point introduces a number of experimental challenges. See the footnote[4] for the author's perspective on magnetic field mitigation using coils versus shields. In our case, complete shimming with coils is incompatible with our experimental design, as our beam region is quite large and would thus require many pairs of high-current coils to address the magnitudes, gradients, and higher-order curvatures of the background fields. Furthermore, we are unable to measure the field at the location of the molecules, as any magnetic field sensor sufficiently close to the experiment would disturb the measurement. Thus, our only option is to attenuate the fields as much as possible with magnetic shielding.

The principle of magnetic shielding is simple: by surrounding the region of interest with a high-magnetic-permeability material, incident magnetic fluxes preferentially travel through this material and out the other side, rather than penetrating into the interior region. The total field inside the experiment is thus reduced not by counteracting the background, but by redirecting it, a concept represented visually in Figure 8.1. In this way, the shields can be thought of as a path of lesser "magnetic resistance" than the air—an analogy with a mathematical basis, as described in Section 8.1.

Before beginning our discussion on the theory and implementation of magnetic shielding, let us first consider some experimentally relevant values to establish an approximate desired background level for a typical EDM experiment. An upper limit on the acceptable phase accumulation noise during a measurement is $\Delta\phi^B < \pi/4$, as

[4] Many people have asked for my input on magnetic shielding design. My answer always starts the same way: if you can get away with just using coils, do it. Magnetic shielding, which might seem simpler to implement as it just involves setting up some static enclosure, presents many engineering challenges that will be discussed throughout this chapter. It is my firm belief that these challenges outweigh those associated with designing shimming coils for most modern setups, and that magnetic shields should only be implemented in experiments that need to protect a large (many cm or larger) area, or in the case where there is no way to engineer a sufficient degree of feedback to allow the coils to keep up with changes in the background field level.

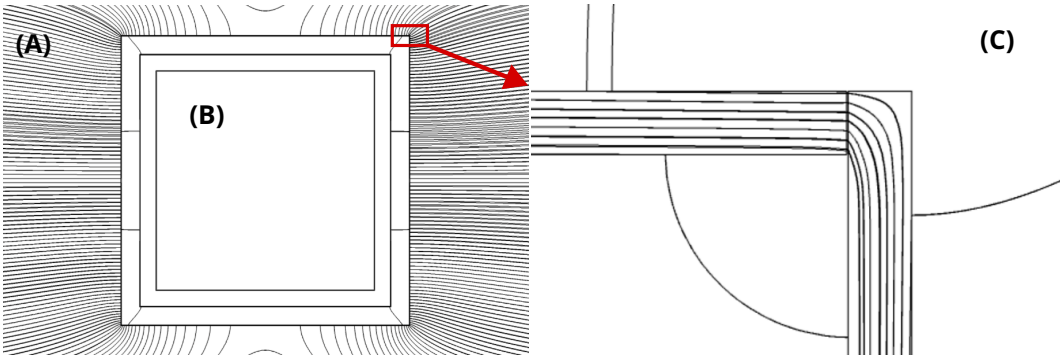


Figure 8.1: Representation of the principle of magnetic shielding, using simulations from a three-layer nested square shield design. Region (A) is outside of the shields and (B) is inside (where the experiment would occur). The lines incident from the edges of the image represent the ambient magnetic field lines, defined in this simulation to be applied from left to right, which preferentially travel through the high permeability material rather than inside to the experimental region. A zoom-in on the thin shielding material in (C) shows a densely-packed collection of field lines, owing to the fact that they do not terminate, but rather travel through the shields and out to the other side. A few lines are visible representing field leakage through the outer layer of shields, but these are further redirected by the subsequent layer.

around this point (and beyond) the contrast drops sharply[5]. Assuming a molecule with $\mu_{\text{mol}} \approx \mu_B$, interacting with a field B for a time τ, we have:

$$\Delta\phi^B \approx \frac{\mu_B B \tau}{\hbar} < \pi/4\,. \tag{8.2}$$

As a function of evolution time τ, an approximate maximum allowed ambient B field is given in Figure 8.2.

For a beam experiment, such as the one our lab is constructing to measure the nuclear MQM using YbOH [44, 177], a typical transit time is on the order of a few milliseconds. Thus, the uncontrolled ambient magnetic field must be on the order of a few 10s of μG or below, meaning we need to attenuate the background field by a factor of 10^4 or greater.

8.1 Shielding in theory

The attenuation factor of magnetic shields is called the shielding factor S, which is given as the ratio of the external magnetic field to the field inside the shields, which for

[5] EDM measurements are performed in the regime that is linearly sensitive to $\Delta\phi^{\mathcal{E}}$—this occurs when a (controlled) magnetic field applies a phase $\phi = \pi/4 \times (2n + 1)$, as this means the phase accumulated is now at the maximum of the slope of the contrast fringes, rather than at the nodes, where the sensitivity to $\Delta\phi^{\mathcal{E}}$ would be quadratic instead. Any (uncontrolled) phase shift on the level of $\pi/4$ or greater will essentially "wash out" any ability to resolve a signal. See [176] for a good discussion.

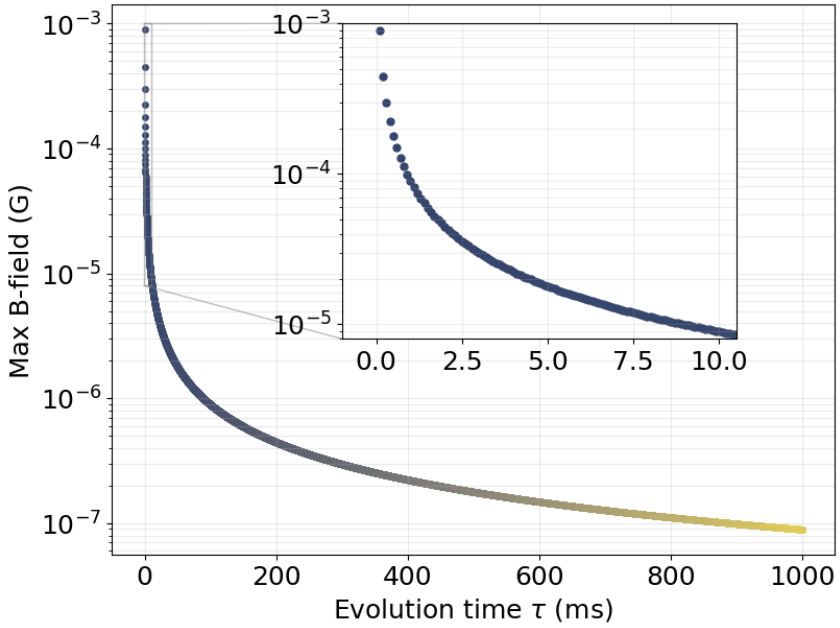


Figure 8.2: Approximate maximum acceptable background magnetic field levels for an EDM-style measurement as a function of evolution time τ. The magnetic dipole moment of the molecular state undergoing the measurement was taken to be μ_B. The inset shows the limits for shorter times, of particular relevancy to molecular beam experiments.

our purposes we desire to be $S \equiv B_{\text{ext}}/B_{\text{int}} \gtrsim 10^4$. Later this will also be represented using magnetic fluxes Φ instead of magnetic fields B, but the two expressions are interchangeable in this application[6].

Analytical formulations for the shielding factor exist only for spherical or long cylindrical geometries. Given that we intend to shield a beam, a cylindrical shield is the more natural shape for our purposes[7]. Considering first the transverse shielding factor S^T, referring to the ability to attenuate fields that are normal to a plane containing the cylinder axis, it can be shown that for a single cylindrical shield [179]:

$$S^T \approx 1 + \frac{\mu_r t}{2R}\,, \tag{8.3}$$

where $\mu_r = \frac{\mu}{\mu_0}$ is the relative permeability of the shield material, assumed to be $\mu_r \gg 1$, t is the thickness of the shield walls, and R is the average radius of the shields. In this approximation, $t \ll r$ (thin shields) is also assumed.

[6]This is valid since what we call the magnetic field B is actually the magnetic flux density, meaning if we integrate B over some area we get the flux Φ, leading to an analogous expression for S just with $B \to \Phi$

[7]The shielding factor for a spherical shield, while not discussed herein, is related to the transverse shielding factor of a cylinder by a factor of 2/3 [178]

The axial shielding factor S^A, describing the attenuation of fields incident parallel to the cylinder axis, is much harder to calculate even approximately. For a long cylinder that is enclosed at the ends, it is given by [179]:

$$S^A \approx 1 + S^T \times \mathfrak{f}\,(a, \alpha, \beta)\ , \tag{8.4}$$

where $\mathfrak{f}\,(a, \alpha, \beta)$ is a function of the cylinder length-to-diameter ratio $a \equiv L/R$ and two geometry-dependent constants α and β that pertain to the surface charge amount and distribution on the endcaps of the shields. For completeness, $\mathfrak{f}\,(a, \alpha, \beta)$ can be written:

$$\mathfrak{f}\,(a, \alpha, \beta) \coloneqq \frac{2K}{1 + a + \alpha a^2/3}\ ,$$

for a function K given by:

$$K \coloneqq (1 + \frac{1}{4a^3})\beta - \frac{1}{a} + 2a\left\{\ln\left[a + (1 + a^2)^{1/2}\right] - 2\left[(1 + \frac{1}{a^2})^{1/2} - \frac{1}{a}\right]\right\}\ .$$

Experiments have measured $\alpha \approx 0.85$ and $\beta \approx 1.83$, with values that are roughly consistent across changes to a [179]. In this formalism, a maximum axial shielding factor is attained for a length-to-diameter ratio $a \approx 5.5$.

The shielding factor may be improved by picking a material with a large μ_r. These materials tend to be comprised of iron-nickel alloys, such as mu-metal with $\mu_r \approx 5{\times}10^4$, or metglas with $\mu_r \approx 10^6$; while it may seem like metglas is strictly better owing to its much larger permeability, its extreme thinness and lower magnetic saturation point (described later) make it not so clear of a choice.

As can be seen in 8.3, S grows linearly with the shield thickness t. Superlinear growth, on the other hand, occurs when additional layers are added, rather than simply making the shields thicker. An intuitive understanding of this behavior can be attained via the magnetic circuit interpretation of magnetic shielding [180], called so because the equations governing magnetostatics directly parallel those for electrical currents:

$$\begin{aligned}
\mathbf{B} = \mu\mathbf{H} \quad &\Longleftrightarrow \quad \mathbf{J} = \sigma\mathbf{E} \\
\nabla \cdot \mathbf{B} = 0 \quad &\Longleftrightarrow \quad \nabla \cdot \mathbf{J} = 0 \\
\nabla \times \mathbf{H} = 0 \quad &\Longleftrightarrow \quad \nabla \times \mathbf{E} = 0\ ,
\end{aligned}$$

where bolds were used to represent vectors, matching the convention that is typically used when presenting these equations. In this formalism, the electric current is replaced by the magnetic flux:

$$I = \int \mathbf{J} \cdot \hat{\mathbf{n}}\, dA \quad \Longrightarrow \quad \Phi = \int \mathbf{B} \cdot \hat{\mathbf{n}}\, dA\ ,$$

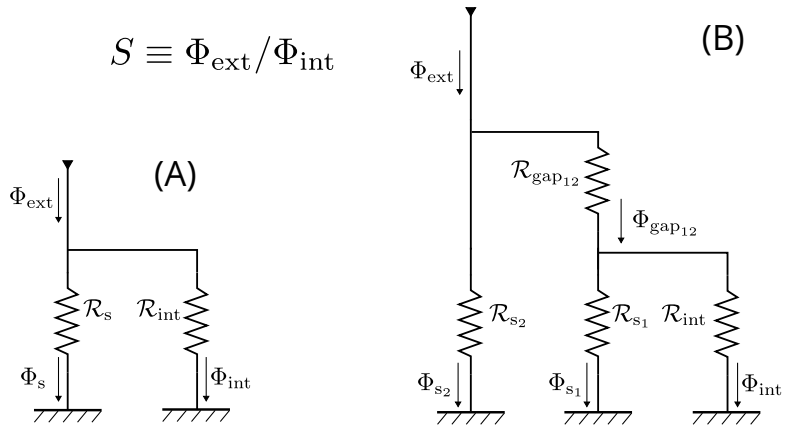


Figure 8.3: Diagrammatic representation of the principle of magnetic circuits, showing the advantage of adding additional shielding layers in attenuating an external magnetic flux Φ_{ext}. (A) shows the analogous magnetic circuit for a single layer of magnetic shielding, while (B) shows the circuit for a two-layer magnetic shield separated by a gap. The pattern may be repeated for arbitrarily many shield layers. Subscript s denotes the shield, with a further subscript indicating which shield, following the notation that the numbering increases from the inner layer outwards. "gap" refers to the air gap between the shielding layers, and "int" to the interior region where the experiment takes place.

and electrical resistance has an analogue in the magnetic reluctance $\mathcal{R}$:

$$R = \frac{V}{I} \quad \Longrightarrow \quad \mathcal{R} = \frac{\mathcal{F}}{\Phi}\,,$$

for a magnetomotive force $\mathcal{F}$. The punchline to this is that magnetic fluxes can be imagined as currents, and materials treated as "magnetic resistors" defined by their reluctance $\mathcal{R} \equiv \frac{l}{\mu_r A}$ for a length l and cross-sectional area A. A material with high relative permeability thus possesses a low magnetic reluctance, more easily allowing the transmission of magnetic fluxes than air or other materials.

This framework, illustrated diagrammatically in Fig. 8.3, provides intuition for the use of multiple, nested shield layers. Air gaps between successive layers act as strong resistors of magnetic flux, with reluctances that add in parallel. The benefit to this is that by using the distributing the same quantity of shielding material—which tends to be expensive and cannot be made arbitrarily thick—into more layers rather than in a single thicker layer allows for a multiplicative increase in the shielding. Calculating the shielding factor with this method agrees with the result reached through a magnetostatic treatment of the full system, demonstrating that the magnetic circuit approach is both qualitatively and quantitatively rigorous [180].

The full shielding factor for a set of n nested shields each with average radius R can be determined recursively from the equation [179]:

$$\begin{aligned} S^T_{\text{tot}} \approx 1 &+ \sum_i^n S^T_i + \sum_i^{n-1} \sum_{j>i}^n S^T_i S^T_j \left[1 - \left(\frac{R_i}{R_j}\right)^2\right] \\ &+ \sum_i^{n-2} \sum_{j>i}^{n-1} \sum_{k>j}^n S^T_i S^T_j S^T_k \left[1 - \left(\frac{R_j}{R_k}\right)^2\right] \left[1 - \left(\frac{R_i}{R_j}\right)^2\right] \\ &+ [\ldots] \\ &+ \prod_i^{n-1} S^T_n S^T_i \left[1 - \left(\frac{R_i}{R_{i+1}}\right)^2\right], \end{aligned} \tag{8.5}$$

where each S_i is given by Eq. 8.3. An analogous form of Eq. 8.5 can be established for the axial shielding factor by replacement of $S^T \to S^A$ and $(R_i/R_j)^2 \to L_i/L_j$ for a shield length L.

8.2 Shielding in reality

While Eq. 8.5 provides the shielding factor for an idealized cylindrical shield, a number of practical considerations lead to necessary deviations from this ideal. These non-idealities, as well as their qualitative effects on the shielding, will be discussed in this section, but quantitative determination of their effects requires simulation.

One fundamental limitation is the need for optical and vacuum access; the molecular beam and probe lasers originate from outside the shielding region[8] and need some way of entering it. Thus, the shields require apertures. An analytical formulation of the effects of circular apertures on spherical shields exists in [181], which, for practical purposes, reaches one main qualitative result: apertures reduce the shielding factor in a manner proportional to their size and angle relative to the background field, with the largest reduction occurring for fields incident normal to the aperture. Given the futility of achieving a quantitative result for any real-world configuration, the best guiding principle is that apertures should be as small as necessary for the application at hand.

Because these shields need to surround some experimental region, they must be made of multiple parts that are assembled together. This introduces a number of design challenges. In general, magnetic shielding materials are thin and therefore

[8] These elements are large and often made of magnetic components, so there is no straightforward way to design a fully enclosed magnetically shielded region for this type of experiment.

not load-bearing, meaning they need a way of mounting to some structural frame. This mounting necessarily requires additional apertures to pass the frame legs, on top of needing to accommodate the experimental apparatus inside. In addition, the shield plates need a way of joining together such that they maintain good magnetic contact—as will be shown later, small gaps at the connecting points between plates leads to large reductions in the shielding factor.

Shields are made of magnetic materials, which are susceptible to saturation and magnetization, as well as loss of magnetic properties due to mechanical shock and deformation. High-permeability alloys tend to saturate in modest magnetic fields, after which point they lose their ability to magnetically shield. This requires using materials only where they will not saturate, often by restricting the more sensitive components to the inner layers of the nested shields. As a first pass of preventing saturation, we have some large magnetic coils with side length around 10 feet wound around the entire experiment to shim Earth's field, reducing the background level at the outer layer of the shields to ~mG.

As the shields will naturally magnetize in the presence of any fields, they periodically need to be degaussed, or demagnetized. This involves fully saturating the shields with a strong AC magnetizing field, which is then slowly ramped down to zero [182, 183]. An intuitive picture of how this works is the following: First, the AC saturating field repeatedly flips the orientation of the microscopic magnetic domains within the shield. As the field decreases in amplitude, certain regions of the shields are no longer saturated and essentially lock their orientation in place. If the field ramps down slowly enough, the distribution of these magnetic domain orientations is random, leading to a net zero remanent magnetization of the shield.

Degaussing requires the ability to saturate the entire shield simultaneously with an applied AC magnetic field. This is nontrivial. Typically, degaussing coils are wound around the shield plates to drive sufficient fields through them. Extreme care must be taken as to the design of this degaussing circuit to prevent regions of destructive field interference, which would not fully saturate the shields and instead lead to them becoming magnetized. In particular, for a cylindrical shield geometry, this becomes extremely complicated at the endcap regions.

In order to simplify the construction, which reduces the likelihood that the handling process destroys the magnetic grain alignment, and to facilitate a straightforward degaussing protocol, we opted for a rectangular prism geometry rather than a cylindrical one. This change, coupled with all of the other nonidealities described in this section,

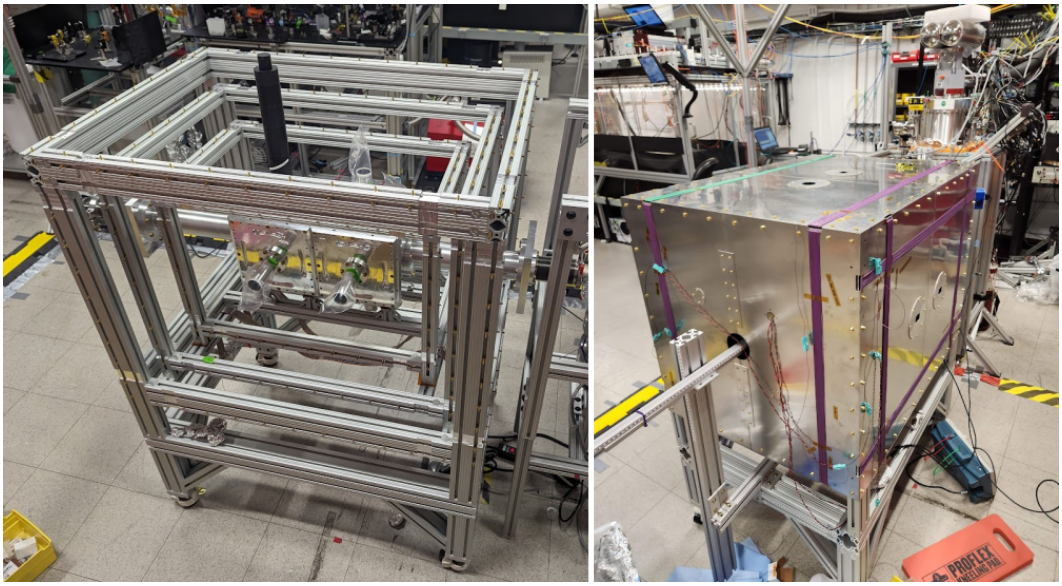


Figure 8.4: Photos of the shield assembly before and after installation of the three layers of mu-metal magnetic shields. Left shows the nested frame, while right shows the completed setup with degaussing coils.

mean that the behavior can only be roughly approximated by analytical theory, and instead must be simulated using finite element methods. Simulations for our shielding design are described later in Section 8.4.

8.3 Design

The magnetic shields we designed for the MQM measurement in YbOH are comprised of three nested layers of 0.062" (1.575 mm) thick mu-metal mounted to an 80/20 T-slotted aluminum frame. The inner layer (layer 1) measures 18" x 18" x 28" long. The middle layer is 24" x 24" x 34", and the outer layer (layer 3) is 30" x 30" x 40". The frame was designed to minimize the need for apertures in the shields, where inner layer frame legs rest on the successive outer layer. This means that the framing legs do not penetrate all shield layers, only the one which they support.

All components holding the shield plates or used inside the shielded region are made of a nonmagnetic aluminum 6061 or brass (copper C260) alloy. No steel parts are used, as even the "nonmagnetic" 316LN produces a measurable magnetic field on the order of > 1000 μG. Before any fastener is used on the shielding setup, it is brought near a sensitive magnetometer[9] in a smaller, commercial "zero gauss" chamber made of three layers of cylindrical mu-metal[10]. This magnetically quiet environment allows

[9] Mag-13 MS100 with PSU1 from Bartington

[10] MuMETAL zero gauss chamber, 6 in. diameter from Magnetic Shield Corp.

for the testing of magnetic parts to ~ 1 μG levels. Despite alloys of aluminum and brass being nominally nonmagnetic, we still test every part, as inevitably some parts within a batch actually are noticeably magnetic. In this setup, we observed firsthand the challenges of magnetic shielding; waving a pair of steel scissors one foot away from the zero gauss chamber produced measurable magnetic signals on the inside, and an office chair needed to be moved more than five feet away to prevent its interference with the measurement.

Brass set screws are affixed into the 80/20 frame at designated locations that match a hole pattern on the shield plates. These holes are numerous but small; numerous to keep the plates rigidly pressed against the frame[11], but small to maintain a large shielding factor by minimizing aperture sizes. The side plates are slid onto the set screws and fastened in place by tightening brass nuts onto the set screws using nonmagnetic beryllium copper wrenches.

Each large side plate is made of a single piece of mu-metal. The smaller side plates, corresponding to the ends of the rectangular prism, as well as the bottom plates are split down the middle into two pieces. For the endcaps, this is because the shields will need to be assembled while the beamline is connected to the science chamber inside the shield region, which would be topologically impossible if they were comprised of just one sheet of mu-metal with a central bore for the beamline. For the bottom plates this is due to the frame legs getting in the way. Small holes line the joining region of these parts, allowing for the fastening of mu-metal strips that improve the magnetic contact between the two halves.

For optical access, all side plates have bores at the locations of laser access. These bores were designed larger than necessary but with a hole pattern surrounding them so that additional mu-metal adapter pieces may be mounted to reduce them to the exact size needed at a later time. To make these adapter pieces, we water jet them from a larger 12” x 12” sheet of annealed mu-metal, as the water jetting process does not heat or disturb the parts too much to ruin their magnetic properties.

The plates themselves are not symmetric, but rather extend a few mm on two of their sides. When assembled in the correct order, this means that all plates overhang a little on two of their neighboring faces, leading to additional magnetic overlap[12]. Without

[11] These shield plates, being thin and large, are susceptible to warping. We found that a large number of mounting holes helped to prevent any deformations in the plates.

[12] This design feature, while well-intentioned, is a practical nuisance. Given that later simulations demonstrated that covering of the corners with metglas takes care of any poor overlap, this was not necessary.

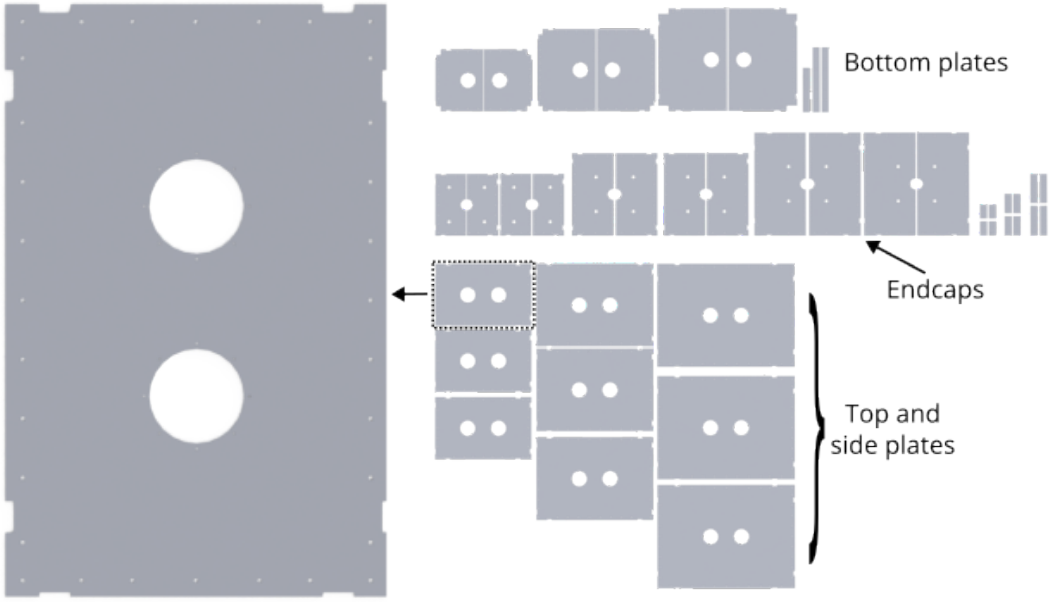


Figure 8.5: Rendering of all of the shield plates, with an example plate expanded (left) to show detail. Central bores in each plate allow laser or vacuum access, while small holes lining the perimeter are used for mounting to the aluminum frame. Slits near the corners are where the degaussing coils are wound. The shields are slightly asymmetric, as seen by the depth of these slits—the top and left edges of the enlarged shield have slightly deeper slits, indicating that the plates are longer in these dimensions, allowing them to overhang on the neighboring plates to cover the corners better when fully assembled. The small pieces on the bottom plates and endcaps are used to connect between the split plates to ensure magnetic contact.

some feature like this, all plates would meet at their interior corners and have no actual overlap with one another.

To further increase the magnetic contact and overlap between pieces, metglas strips are used liberally at any location where the magnetic continuity is suspect, such as at all corners and joining regions between plates. The flexibility of metglas allows its use as a patch, with kapton tape securing it in place.

Degaussing circuit

Saturating the entire shield simultaneously requires the application of fields that circulate around the shield so as not to lead to regions of destructive interference. This is achieved by the use of coils that generate fields that circulate the frame in two directions, one in a plane parallel to the ground, and one in a plane perpendicular to it. Figure 8.6 demonstrates the direction of the applied degaussing field, showing how only two opposing faces need coils in two axes, while every other face only requires

coils in one axis.

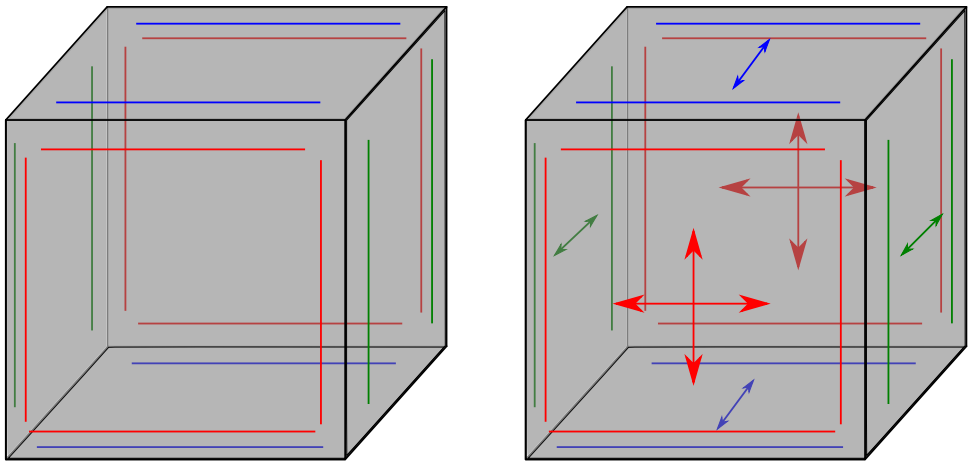


Figure 8.6: Diagrammatic representation of the degaussing coils for a single layer of the shielding, using a simplified cube as a stand-in for the rectangular prism of the shield. Each colored line is a coil wound 24 times around the plate at those locations. The resulting fields generated by sending AC current through these wires are shown as arrows on the right, where circulating paths around the shields in two directions allow for full saturation of all plates simultaneously.

Each plate is slotted around the corners to hold wires for generating degaussing fields. The degaussing coils are comprised of 24 turns of 26AWG wire. For all plates besides the bottom, these coils are manually wound onto the plate and rest there permanently; because the bottom plates are made of two pieces, and the degaussing pathway necessitates coils that span the entire length of the plates, these ones are instead made of 25-strand ribbon cables that are fed into 24-port IDC connector plugs, with one input wire and output wire not used in the connection[13]. The ribbon cables are connected in such a way that the IDC connector turns the cable into a coil, by connecting each wire to the subsequent one on the next turn.

Each of these coils is connected in series to all of the other coils, illustrated in Figure 8.7. All three layers of shielding are also connected in series, and the total resistance of the circuit was measured to be $\sim 400\ \Omega$, primarily limited by the non-gold-coated crimp leads used to connect the coils together. These IDC connectors allow for the disconnection of coils from each other when the plates are assembled and disassembled,

[13]This is because, in the current design, either the endcaps or the bottom plate need to have detachable coils to generate fields in the proper direction. If the endcap plates were designed such that they were split along the other axis, this would not be necessary, as fields in both directions could be generated by winding permanent coils around the separate halves, rather than coils that span between the two parts of the split plates.

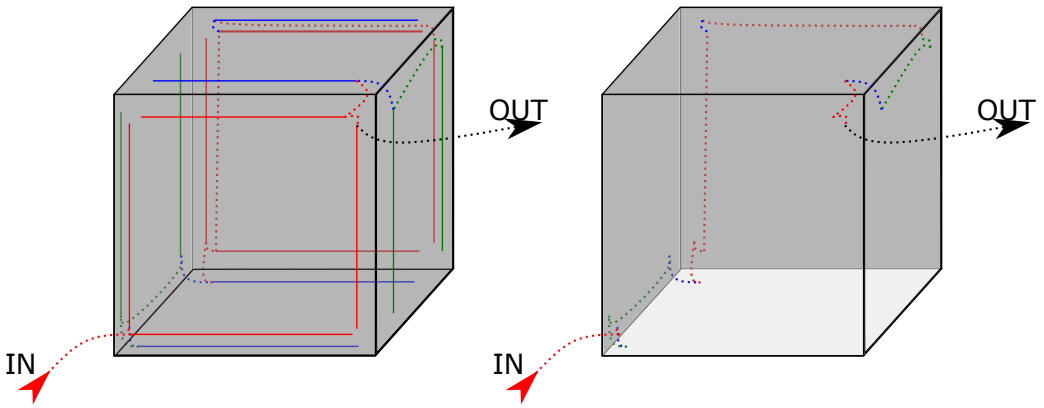


Figure 8.7: Attempt at representing the connecting wires diagrammatically with dotted lines. The right figure shows just these connecting wires. Once the current reaches OUT, it returns via the same connectors back to the IN. Colors of the dotted lines attempt to show the color of the coil which the line is connecting to.

and also contain the wires returning the current after it has traveled through all the coils, simplifying the design and number of connections needed. Any wires that span across the plates to connect coils, such as are needed on a few of the faces, are made from twisted pairs of input and output wires to ensure that there is no average direct current near the shields that could magnetize them. A total of 1768 meters of wire was used for the entirety of the coils.

Measurements by others in the group demonstrated that degaussing the shields after a long period of time improved the shielding by a factor of 22.5.

8.4 Simulations

Given the practical limitations of experiments, the only way to quantitatively predict the performance of a magnetic shield is to simulate it. The above design was motivated by months[14] of finite-element method simulations performed using COMSOL multiphysics, some of which will be described below.

Before proceeding, it is worth emphasizing that one of the biggest challenges with using a software such as this is that the computation happens inside a black box, with minimal way of knowing whether the numbers spit out at the end make any sense without a comparison to some known system. We used simulations as a relative metric to compare between different configurations, but hazard against using any of the values shown here as absolute.

[14] This work coincided with the outbreak of the COVID-19 pandemic, where the mandatory work-from-home provided a fitting environment for performing these time-consuming magnetic simulations.

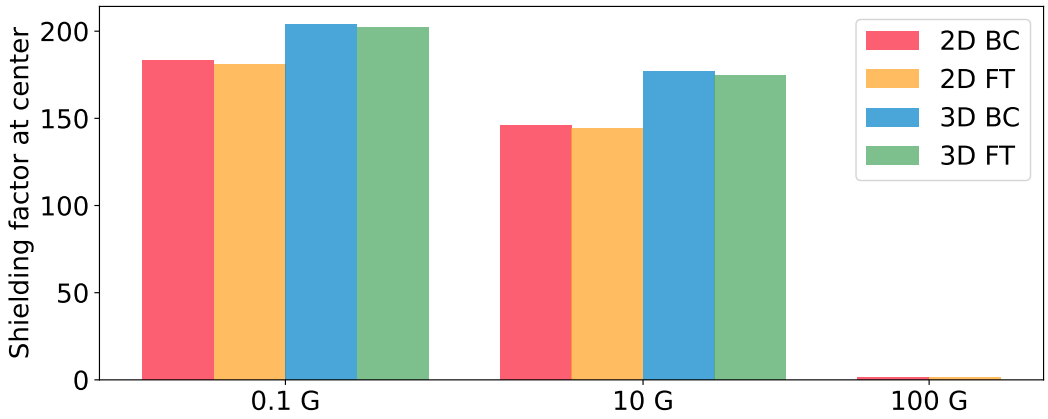


Figure 8.8: Comparing different simulation setups to test their consistency using a dummy 24" x 24" (x 48" for 3D) model shield. 2D and 3D refer to the dimensionality of the simulation, with 2D simulations being considerably simpler and faster to implement. BC refers to "boundary conditions," where the shields are modeled in COMSOL as infinitely thin sheets and the effects caused by their finite thickness are handled by the magnetic shielding module. FT means "finite thickness," where the shields were modeled as magnetic materials with an explicitly constructed thickness to benchmark the BC module within COMSOL. The comparisons were performed at a range of applied magnetic fields to test whether they would capture saturation behaviors—the 3D simulation would not converge at 100 G due to a lack of computer memory.

The first simulation worth mentioning is actually one that we performed quite late in the course of this work, involving comparing the results obtained from COMSOL through different solving methods. As our simulations moved from 2D to 3D and became more faithful representations of the design we were aiming to implement, the time and memory required for the program to reach a solution crept higher and higher, until we would either run out of memory or reaching convergence would take upwards of 52 hours.

Figure 8.8 shows the results of these consistency checks for a few configurations. While there is a systematic offset between the shielding factors achieved for 2D versus 3D simulations, the magnitude between them is close enough to use the (much simpler) 2D modules for many of the checks we wanted to perform. Of course, for any checks of the shielding behavior as a function of position along the molecule beam axis, a 3D simulation is required.

Very early on we simulated the performance of a square prism versus a cylinder to motivate our choice of the former over the latter; while rectilinear geometries are generally easier to work with, we wanted to ensure that the change would not drasti-

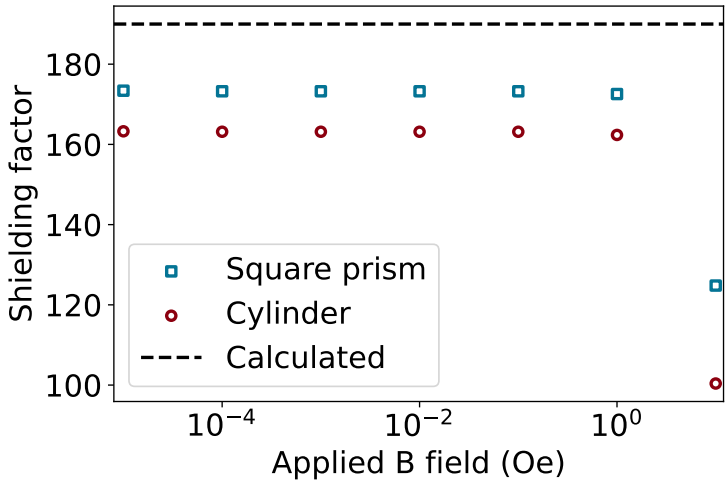


Figure 8.9: Comparison of shielding factors at the center of a 4-foot-long single-layer magnetic shield, with thickness 2 mm and no apertures, as a function of applied magnetic field in Oersteds, where in free space 1 Oe ≡ 1 G. The square prism shape has other side lengths of 2 feet each, while the cylinder was chosen such that the diameter fully enclosed the square, meaning $2R = 2\sqrt{2}$. As such, the cylinder shielding is slightly worse than the square prism, likely owing to its larger size. The calculated value comes from using Eq. 8.3 for this cylindrical geometry, using $\mu_r \approx 8 \times 10^4$. Discrepancies between this calculation and the simulation are likely due to slight variations in the permeabilities used in the simulations, which were taken from the $B - H$ curve provided from the mu-metal manufacturer.

cally alter the shielding factor over the better-understood cylinders. Figure 8.9 shows that the two geometries behave qualitatively similar to our level of simulation. Many simulations (not shown) were also performed to test the shielding ability as a function of position along the molecular beam, which implied that the magnetic field in our region of interest maintained an acceptable level[15].

One of the more important realizations we achieved through simulations was the impact on gaps in the assembly, and the degree to which these can be mitigated. Our square shields join at corners, where imperfections in the edges of the mu-metal plates make good magnetic contact at these corners challenging. Figure 8.10 shows the large impact on the shielding factor at the center of a single-layer square shield, even for gaps as small as a fraction of a millimeter. Given the futility of achieving perfect contact at the corners, we needed another idea as to how to mitigate this reduction in shielding ability.

[15] For our experiment, we intend to have an interaction length of roughly 20 cm in the middle of the shields, which are roughly 4 ft long. All of our simulations showed that this smaller subset of the total shield length did not deviate too much from the value at the very center.

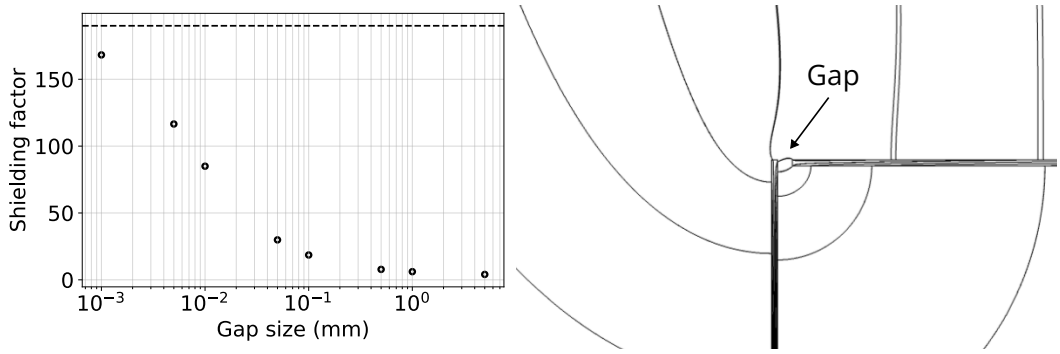


Figure 8.10: Plot of the simulated shielding factor for a 2' x 2' 2D square shield with thickness 2 mm, given an applied external field of 100 mG (below the saturation value). The dotted lines show the asymptotic value with no gap. The shielding factor quickly drops to under 10% of its starting value with a gap on the order of just 0.1 mm. The photo on the right shows the simulated field lines near one of these corner gaps, where the leakage into the shielded region is represented by the lines in the bottom right quadrant.

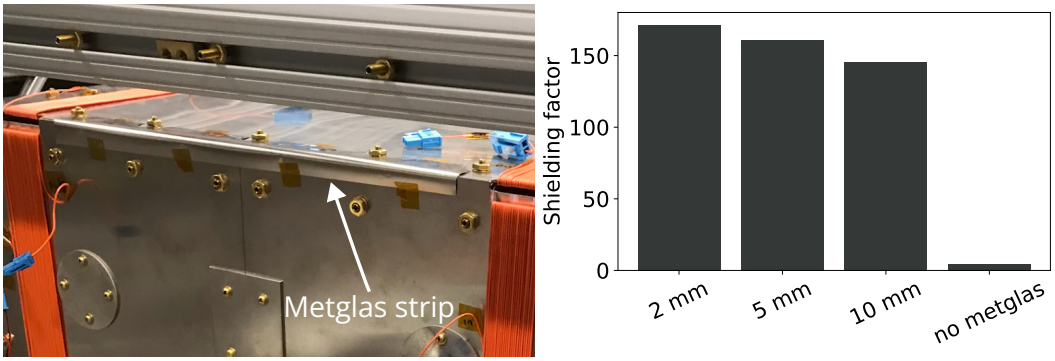


Figure 8.11: Simulation of the effect of adding a metglas strip to cover an underlying gap in the corner assembly, for the same 2D test geometry as in the previous plots. Left is a photo of what this strip might look like in practice. The plot on the right shows the shielding factor when using a strip like this to cover a gap between the plates, showing that even when the gaps get quite large this covering returns much of the shielding ability. "no metglas" refers to the shielding factor of a 2 mm gap without metglas, to show that the shielding depends strongly on its addition.

We simulated the use of metglas strips to cover these corner gaps, which proved to be very effective at recovering the loss of shielding even as the gap size approached unreasonably large values (Fig. 8.11). Similar simulations (not shown) demonstrated that the shielding factor was not sensitive to the amount of metglas overlap on the plates; as long as the gap is fully covered, and the metglas maintains good magnetic contact with the mu-metal plates, the shielding behavior returned.

Full 3D simulations of the final shield design, assuming no gaps in the assembly but

with the bores for laser and vacuum access, yielded a predicted shielding factor of $S^T_{\text{sim}} \approx 2 \times 10^5$ and $S^A_{\text{sim}} \approx 5 \times 10^4$; for a cylinder of roughly similar dimensions, the calculated shielding factors are $S^T_{\text{calc}} \approx 2.7 \times 10^5$ and $S^A_{\text{calc}} \approx 6 \times 10^4$. Of course, these are highly optimistic predictions, and it is expected that real-world shielding setups will perform at least an order-of-magnitude worse than these simulations.

"What is behind me still remains ahead of me."

— László Krasznahorkai, *Satantango*

Chapter

IX

Future prospects

It is an exciting time for radioactive molecules. The developments described herein have laid the groundwork for the tabletop production and study of a whole class of previously underutilized species, with a number of potential future directions all within reach in the Minifridge.

Our recent investigations of radium fluoride have demonstrated its superlative vibrational branching ratios and mapped out all of the necessary transitions to perform laser cooling; assuming the appropriate apparatus exists, there is nothing hindering the first laser cooling of a heavy, radioactive molecule. While it is not possible in the current iteration of the Minifridge, as the high density of the helium buffer gas leads to rotational-state-changing collisions and ruins the closed cycling loop, we are actively collaborating with the Doyle group at Harvard and Garcia Ruiz group at MIT to build a beam source specifically for this purpose.

Locally, we are looking to extend our work on RaOH, whose polyatomic structure combined with the octupole-deformed radium nucleus promises one of the best possible systems in the search for new physics. Other experiments in our group have been pushing the boundaries of sensitivity using stable YbOH molecules, with these techniques being directly portable to an experiment on RaOH. We are developing the necessary laser systems to perform the broadband survey spectroscopy on the $\tilde{A} - \tilde{X}$ laser cooling band, which we will then characterize in a manner similar to RaF,

including determination of the vibrational branching ratios. Once we achieve this, Eq. 1.1 implies that just a handful (< 10) of trapped RaOH molecules has the potential to set new limits on the value of the eEDM[1]; using ^{225}RaOH allows for a possible orders-of-magnitude improvement in the space of Schiff moment measurements[2].

This last point merits some discussion. In this work, we have largely ignored the isotopes ^{225}Ra and ^{223}Ra, of interest for future Schiff moment and MQM measurements, respectively. Their comparatively shorter half lives ($\sim$ 14.8 d and $\sim$ 11.4 d, respectively), as well as drastically greater acquisition costs relative to ^{226}Ra precluded them from the R&D process. For a future measurement, these properties represent open challenges. While not incompatible with the drop casting protocol developed in Chapter 5, their greater specific activities would lead to a significantly higher personnel handling dose at similar nuclide quantities to what we used for radium-226, and their half lives would require all measurements—including testing and troubleshooting—to occur quickly enough so as not to lose a substantial amount of material to decay. To mitigate this latter difficulty, several facilities around the world with the current or projected ability to produce these species, including FRIB, TRIUMF, CERN, and more, are building infrastructure to support these types of experiments.

In the spirit of keeping these experiments on the tabletop, without the need for isotope harvesting from a beam facility, an alternative way of sourcing these shorter-lived isotopes involves their extraction as daughters from large quantities of parent materials, in a way that enables "offline" production of the desired isotope without the need for a repeated external supply. Thorium-229, an isotope of particular interest lately due to its recently measured nuclear clock transition [185–187], decays into radium-225 and is a daughter nuclide of uranium-233 (and, by extension, americium-241). Because of its scientific relevancy, as well as its nuclear-medicine-relevant actinium-225 daughter, thorium-229 will undoubtedly see heightened purification efforts from uranium-233 samples worldwide, making it an accessible source of radium-225. With ten milligrams of starting material, an offline source of thorium-229 will reach a steady-state concentration of $\sim$ 50 ng of radium-225 after two months—not a massive amount by any stretch of the imagination, but definitely a quantity that, if extracted, could be combined with our efficient production and detection methods to study molecules containing this isotope. An apparatus such as the Minifridge, with its quick thermal cycling time, would be an ideal candidate for prototyping these new methods

[1] Assuming a coherence time $\tau \sim 750$ ms and a value $\mathcal{E}_{\text{eff}} \approx 50$ GV/cm taken from [184].

[2] Values for the intrinsic Schiff moment sensitivity of ^{225}Ra taken from [41] and molecular parameters from [119].

for sourcing some of the trickier isotopes.

The species-agnostic methodology of the Minifridge opens the door to the study of entirely new classes of molecules beyond what we produced in this work. We have demonstrated such strong signals across virtually all diatomic molecules that, with the right theory guidance, any optically-addressible Ra–X molecule should be straightforward to make and observe. This ranges from a systematic study of the monohalogens, which are all predicted to be laser-coolable [148], to the first laser spectroscopy of a dually radioactive molecule such as RaT (Ra^3H). If we instead steer our gaze to the next-next-generation of EDM experiments, we might consider more complicated molecules such as $RaNH_2$ [188], which from a practical perspective would only require a few further optimizations of $CaNH_2$ production (see Chapter 7.2) and a slightly narrower theory uncertainty window in which to search.

As much as we love radium, the versatility of this approach would be wasted if we neglected the many other radionuclides. At the time of this thesis writing we are working on producing and detecting a number of atoms and molecules, some that are only new to us, and others that are new to spectroscopy entirely. Our ongoing study of neptunium marks the first spectroscopic investigation of a transuranic element at cryogenic temperatures. Predictions for the energies of NpO and NpO_2 [189], coupled with our demonstrated production of UO (Chapter 7.3), put the first laser spectroscopy of *any* transuranic-containing molecule within reach. Given the macroscopic quantities of the long-lived ^{237}Np isotope ($\sim$ few mg), we envision producing enough molecules to detect some of these NpO or NpO_2 lines in absorption, allowing the use of our white light laser and high-resolution spectrometer setup to map out multiple lines at once without having to scan for the resonance [190]; for molecules such as these with zero preexisting spectroscopy, this presents a massive experimental simplification and saves a significant amount of time, two crucial factors when working with exotic species.

In fact, there are so many possibilities as to where to go from here that we are almost paralyzed for choice. At the ultraheavy regime, americium-241 may be acquired in quantities large enough to mimic any of the work performed on neptunium-237. Moving even further beyond, curium, berkelium, and californium all have half-lives that would enable their use in the Minifridge and, depending on the production and purification timelines at the National Isotope Development Center, are sourcable in quantities large enough to perform atomic spectroscopy. While less massive, protactinium has recently emerged as a curiosity for a number of reasons, owing to its still-undetermined bonding characteristics [53, 191, 192] and potential nuclear parity

doublet [41], making it interesting to both chemistry and fundamental physics.

We will conclude the discussion here, for attempting to further expound on the exciting opportunities available to us could drag on seemingly indefinitely, and this text has grown long enough as it is. Whatever your intention for reading to this point, we hope this thesis has served as a source of both information and inspiration, and that the enthusiasm and care with which we regard this work have been felt.

Bibliography

[1] Xing Fan, TG Myers, BAD Sukra, and G Gabrielse. "Measurement of the electron magnetic moment". In: *Physical review letters* 130.7 (2023), p. 071801.

[2] Pekka Pyykko and Jean Paul Desclaux. "Relativity and the periodic system of elements". In: *Accounts of Chemical Research* 12.8 (1979), pp. 276–281.

[3] Gordon Arrowsmith-Kron, Michail Athanasakis-Kaklamanakis, Mia Au, Jochen Ballof, Robert Berger, Anastasia Borschevsky, Alexander A Breier, Fritz Buchinger, Dmitry Budker, Luke Caldwell, et al. "Opportunities for fundamental physics research with radioactive molecules". In: *Reports on progress in physics* 87.8 (2024), p. 084301.

[4] Jens Erler and Matthias Schott. "Electroweak precision tests of the Standard Model after the discovery of the Higgs boson". In: *Progress in Particle and Nuclear Physics* 106 (2019), pp. 68–119.

[5] Laurent Canetti, Marco Drewes, and Mikhail Shaposhnikov. "Matter and Antimatter in the Universe". In: *New Journal of Physics* 14.9 (2012), p. 095012.

[6] Gerhart Lüders. "Proof of the TCP theorem". In: *Annals of Physics* 2.1 (1957), pp. 1–15.

[7] Georges Aad, Tatevik Abajyan, Brad Abbott, Jalal Abdallah, S Abdel Khalek, Ahmed Ali Abdelalim, R Aben, B Abi, M Abolins, OS AbouZeid, et al. "Observation of a new particle in the search for the Standard Model Higgs boson with the ATLAS detector at the LHC". In: *Physics Letters B* 716.1 (2012), pp. 1–29.

[8] Serguei Chatrchyan, Vardan Khachatryan, Albert M Sirunyan, Armen Tumasyan, Wolfgang Adam, Ernest Aguilo, Thomas Bergauer, Marko Dragicevic, Janos Erö, Christian Fabjan, et al. "Observation of a new boson at a mass

of 125 GeV with the CMS experiment at the LHC". In: *Physics Letters B* 716.1 (2012), pp. 30–61.

[9] David JE Marsh. "Axion cosmology". In: *Physics Reports* 643 (2016), pp. 1–79.

[10] Tatsumi Aoyama, Toichiro Kinoshita, and Makiko Nio. "Theory of the anomalous magnetic moment of the electron". In: *Atoms* 7.1 (2019), p. 28.

[11] Timothy Chupp and Michael Ramsey-Musolf. "Electric dipole moments: a global analysis". In: *Physical Review C* 91.3 (2015), p. 035502.

[12] Iosif B. Khriplovich and Steve K. Lamoreaux. *CP Violation Without Strangeness: Electric Dipole Moments of Particles, Atoms, and Molecules*. Berlin, Heidelberg: Springer, 1997. ISBN: 978-3-642-60838-4. DOI: 10.1007/978-3-642-60838-4.

[13] ACME Collaboration Andreev V. 1 5 5 Ang DG 1 DeMille D. acme@ physics. harvard. edu 2 d Doyle JM 1 Gabrielse G. 1 3 Haefner J. 1 Hutzler NR 1 4 Lasner Z. 2 Meisenhelder C. 1 O'Leary BR 2 Panda CD 1 West AD 2 6 6 West EP 1 6 6 Wu X. 1 2. "Improved limit on the electric dipole moment of the electron". In: *Nature* 562.7727 (2018), pp. 355–360.

[14] Malika Denis, Pi AB Haase, Rob GE Timmermans, Ephraim Eliav, Nicholas R Hutzler, and Anastasia Borschevsky. "Enhancement factor for the electric dipole moment of the electron in the BaOH and YbOH molecules". In: *Physical Review A* 99.4 (2019), p. 042512.

[15] Jacob Baron, Wes C Campbell, David DeMille, John M Doyle, Gerald Gabrielse, Yulia V Gurevich, Paul W Hess, Nicholas R Hutzler, Emil Kirilov, Ivan Kozyryev, et al. "Methods, analysis, and the treatment of systematic errors for the electron electric dipole moment search in thorium monoxide". In: *New Journal of Physics* 19.7 (2017), p. 073029.

[16] Konstantin Gaul and Robert Berger. "Ab initio study of parity and time-reversal violation in laser-coolable triatomic molecules". In: *Physical Review A* 101.1 (2020), p. 012508.

[17] Tanya S Roussy, Luke Caldwell, Trevor Wright, William B Cairncross, Yuval Shagam, Kia Boon Ng, Noah Schlossberger, Sun Yool Park, Anzhou Wang, Jun Ye, et al. "An improved bound on the electron's electric dipole moment". In: *Science* 381.6653 (2023), pp. 46–50.

[18] Yohei Ema, Ting Gao, and Maxim Pospelov. "Standard model prediction for paramagnetic electric dipole moments". In: *Physical review letters* 129.23 (2022), p. 231801.

[19] JM Pendlebury, Samer Afach, Nicholas J Ayres, Charles A Baker, Gilles Ban, Georg Bison, Kazimierz Bodek, Martin Burghoff, Peter Geltenbort, Katie Green, et al. "Revised experimental upper limit on the electric dipole moment of the neutron". In: *Physical Review D* 92.9 (2015), p. 092003.

[20] BW Filippone. "Worldwide search for the neutron EDM". In: *arXiv preprint arXiv:1810.03718* (2018).

[21] LI Schiff. "Measurability of nuclear electric dipole moments". In: *Physical Review* 132.5 (1963), p. 2194.

[22] Amar Vutha. "What is a Schiff moment anyway?" In: *arXiv preprint arXiv:2601.07217* (2026).

[23] WC Griffith, MD Swallows, TH Loftus, MV Romalis, BR Heckel, and EN Fortson. "Improved limit on the permanent electric dipole moment of Hg 199". In: *Physical review letters* 102.10 (2009), p. 101601.

[24] VA Dzuba, VV Flambaum, JSM Ginges, and MG Kozlov. "Electric dipole moments of Hg, Xe, Rn, Ra, Pu, and TlF induced by the nuclear Schiff moment and limits on time-reversal violating interactions". In: *Physical Review A* 66.1 (2002), p. 012111.

[25] VV Flambaum, D DeMille, and MG Kozlov. "Time-reversal symmetry violation in molecules induced by nuclear magnetic quadrupole moments". In: *Physical Review Letters* 113.10 (2014), p. 103003.

[26] CJ Ho, J Lim, BE Sauer, and MR Tarbutt. "Measuring the nuclear magnetic quadrupole moment in heavy polar molecules". In: *Frontiers in Physics* 11 (2023), p. 1086980.

[27] VV Flambaum and AJ Mansour. "Enhanced magnetic quadrupole moments in nuclei with octupole deformation and their CP-violating effects in molecules". In: *Physical Review C* 105.6 (2022), p. 065503.

[28] SA Murthy, D Krause Jr, ZL Li, and LR Hunter. "New limits on the electron electric dipole moment from cesium". In: *Physical review letters* 63.9 (1989), p. 965.

[29] Jochen Erler, Noah Birge, Markus Kortelainen, Witold Nazarewicz, Erik Olsen, Alexander M Perhac, and Mario Stoitsov. "The limits of the nuclear landscape". In: *Nature* 486.7404 (2012), pp. 509–512.

[30] Aage Niels Bohr and Benjamin Roy Mottelson. "Collective and individual-particle aspects of nuclear structure". In: *Dan. mat. fys. Medd.* 27.CERN-57-38 (1953), pp. 1–174.

[31] David Verney. "History of the concept of nuclear shape". In: *The European Physical Journal A* 61.4 (2025), p. 82.

[32] P Möller, Arnold John Sierk, Takatoshi Ichikawa, and Hiroyuki Sagawa. "Nuclear ground-state masses and deformations: FRDM (2012)". In: *Atomic Data and Nuclear Data Tables* 109 (2016), pp. 1–204.

[33] RR Chasman. "Superdeformed and hyperdeformed banana shaped nuclides near A= 190". In: *Physics Letters B* 266.3-4 (1991), pp. 243–248.

[34] Peter Möller, Ragnar Bengtsson, BG Carlsson, Peter Olivius, T Ichikawa, H Sagawa, and A Iwamoto. "Axial and reflection asymmetry of the nuclear ground state". In: *Atomic Data and Nuclear Data Tables* 94.5 (2008), pp. 758–780.

[35] Liam Paul Gaffney, Peter A Butler, Marcus Scheck, Adam B Hayes, Frederik Wenander, Michael Albers, Beyhan Bastin, Christopher Bauer, Andrey Blazhev, Sabine Bönig, et al. "Studies of pear-shaped nuclei using accelerated radioactive beams". In: *Nature* 497.7448 (2013), pp. 199–204.

[36] Hans-Jürgen Wollersheim, H Emling, H Grein, R Kulessa, RS Simon, C Fleischmann, J De Boer, E Hauber, C Lauterbach, C Schandera, et al. "Coulomb excitation of 226Ra". In: *Nuclear Physics A* 556.2 (1993), pp. 261–280.

[37] Bing-Nan Lu, Jie Zhao, En-Guang Zhao, and Shan-Gui Zhou. "Multidimensionally constrained relativistic mean field model and applications in actinide and transfermium nuclei". In: *Physica Scripta* 89.5 (2014), p. 054028.

[38] V Spevak, N Auerbach, and VV Flambaum. "Enhanced T-odd, P-odd electromagnetic moments in reflection asymmetric nuclei". In: *Physical Review C* 56.3 (1997), p. 1357.

[39] BGC Lackenby and VV Flambaum. "Time reversal violating magnetic quadrupole moment in heavy deformed nuclei". In: *Physical Review D* 98.11 (2018), p. 115019.

[40] VV Flambaum. "Spin hedgehog and collective magnetic quadrupole moments induced by parity and time invariance violating interaction". In: *Physics Letters B* 320.3-4 (1994), pp. 211–215.

[41] Jaideep Taggart Singh. "A new concept for searching for time-reversal symmetry violation using Pa-229 ions trapped in optical crystals". In: *Hyperfine Interactions* 240.1 (2019), p. 29.

[42] O Dragoun, M Rysavy, and C Günther. "Multipole character of the proposed 220 eV transition in Pa 229". In: *Physical Review C* 47.2 (1993), p. 870.

[43] Chi Zhang, Phelan Yu, Arian Jadbabaie, and Nicholas R Hutzler. "Quantum-enhanced metrology for molecular symmetry violation using decoherence-free subspaces". In: *Physical Review Letters* 131.19 (2023), p. 193602.

[44] Ivan Kozyryev and Nicholas R Hutzler. "Precision measurement of time-reversal symmetry violation with laser-cooled polyatomic molecules". In: *Physical review letters* 119.13 (2017), p. 133002.

[45] JFC Cocks, PA Butler, KJ Cann, PT Greenlees, GD Jones, S Asztalos, P Bhattacharyya, R Broda, RM Clark, MA Deleplanque, et al. "Observation of octupole structures in radon and radium isotopes and their contrasting behavior at high spin". In: *Physical review letters* 78.15 (1997), p. 2920.

[46] Ronald Fernando Garcia Ruiz, R Berger, J Billowes, CL Binnersley, ML Bissell, AA Breier, AJ Brinson, K Chrysalidis, TE Cocolios, BS Cooper, et al. "Spectroscopy of short-lived radioactive molecules". In: *Nature* 581.7809 (2020), pp. 396–400.

[47] SM Udrescu, AJ Brinson, RF Garcia Ruiz, K Gaul, Robert Berger, Jonathan Billowes, CL Binnersley, ML Bissell, Alexander A Breier, Katerina Chrysalidis, et al. "Isotope shifts of radium monofluoride molecules". In: *Physical Review Letters* 127.3 (2021), p. 033001.

[48] M Athanasakis-Kaklamanakis, SG Wilkins, P Lassègues, L Lalanne, JR Reilly, O Ahmad, M Au, SW Bai, J Berbalk, C Bernerd, et al. "Radiative lifetime of the A Π 1/2 2 state in RaF with relevance to laser cooling". In: *Physical Review A* 110.1 (2024), p. L010802.

[49] Silviu-Marian Udrescu, Shane G Wilkins, AA Breier, M Athanasakis-Kaklamanakis, Ronald Fernando Garcia Ruiz, Mia Au, Ivana Belošević, Robert Berger, ML Bissell, CL Binnersley, et al. "Precision spectroscopy and laser-cooling scheme of a radium-containing molecule". In: *Nature Physics* 20.2 (2024), pp. 202–207.

[50] Michail Athanasakis-Kaklamanakis, SG Wilkins, LV Skripnikov, Á Koszorús, AA Breier, O Ahmad, Mia Au, SW Bai, I Belošević, Justus Berbalk, et al. "Electron correlation and relativistic effects in the excited states of radium monofluoride". In: *Nature communications* 16.1 (2025), p. 2139.

[51] SG Wilkins, SM Udrescu, M Athanasakis-Kaklamanakis, RF Garcia Ruiz, M Au, I Belošević, R Berger, ML Bissell, AA Breier, AJ Brinson, et al. "Observation of the distribution of nuclear magnetization in a molecule". In: *Science* 390.6771 (2025), pp. 386–389.

[52] Nicholas R Hutzler, Hsin-I Lu, and John M Doyle. "The buffer gas beam: An intense, cold, and slow source for atoms and molecules". In: *Chemical reviews* 112.9 (2012), pp. 4803–4827.

[53] Richard E Wilson, Stephanie De Sio, and Valérie Vallet. "Protactinium and the intersection of actinide and transition metal chemistry". In: *Nature Communications* 9.1 (2018), p. 622.

[54] Polly L Arnold, Michał S Dutkiewicz, and Olaf Walter. "Organometallic neptunium chemistry". In: *Chemical Reviews* 117.17 (2017), pp. 11460–11475.

[55] Aaron Dotter, Brian Chaboyer, Darko Jevremović, Veselin Kostov, E Baron, and Jason W Ferguson. "The Dartmouth stellar evolution database". In: *The Astrophysical Journal Supplement Series* 178.1 (2008), pp. 89–101.

[56] Patrick François, Francesca Matteucci, Roger Cayrel, Monique Spite, François Spite, and Cristina Chiappini. "The evolution of the Milky Way from its earliest phases: Constraints on stellar nucleosynthesis". In: *Astronomy & Astrophysics* 421.2 (2004), pp. 613–621.

[57] Nami Mowlavi and G Meynet. "Aluminum 26 production in asymptotic giant branch stars". In: *Astronomy and Astrophysics, v. 361, p. 959-976 (2000)* 361 (2000), pp. 959–976.

[58] Brandt AL Gaches, Stefanie Walch, Stella SR Offner, and Carsten Münker. "Aluminum-26 enrichment in the surface of protostellar disks due to protostellar cosmic rays". In: *The Astrophysical Journal* 898.1 (2020), p. 79.

[59] Tomasz Kamiński, Romuald Tylenda, Karl M Menten, Amanda Karakas, Jan Martin Winters, Alexander A Breier, Ka Tat Wong, Thomas F Giesen, and Nimesh A Patel. "Astronomical detection of radioactive molecule 26AlF in the remnant of an ancient explosion". In: *Nature Astronomy* 2.10 (2018), pp. 778–783.

[60] Leonid V Skripnikov. "Nuclear magnetization distribution effect in molecules: Ra+ and RaF hyperfine structure". In: *The Journal of Chemical Physics* 153.11 (2020).

[61] Ronald Fernando Garcia Ruiz, ML Bissell, Klaus Blaum, A Ekström, N Frömmgen, G Hagen, M Hammen, K Hebeler, JD Holt, GR Jansen, et al. "Unexpectedly large charge radii of neutron-rich calcium isotopes". In: *Nature Physics* 12.6 (2016), pp. 594–598.

[62] Arian Jadbabaie. "Measuring Fundamental Symmetry Violation in Polyatomic Molecules". PhD thesis. Californai Institute of Technology, 2023.

[63] John M. Brown and Alan Carrington. *Rotational Spectroscopy of Diatomic Molecules*. Cambridge: Cambridge University Press, 2003. ISBN: 9780521810098. DOI: 10.1017/CBO9780511814808.

[64] Philip R. Bunker and Per Jensen. *Molecular Symmetry and Spectroscopy*. 2nd ed. Ottawa: NRC Research Press, 1998. ISBN: 9780660175195.

[65] Peter F. Bernath. *Spectra of Atoms and Molecules*. Oxford: Oxford University Press, 2005. ISBN: 9780195177599.

[66] Eizi Hirota. *High-Resolution Spectroscopy of Transient Molecules*. Topics in Current Physics. Berlin: Springer, 1985. ISBN: 9783540151500.

[67] KPAH Huber. *Molecular spectra and molecular structure: IV. Constants of diatomic molecules*. Springer Science & Business Media, 2013.

[68] David Robert Bates, Kathleen Ledsham, and Alan Lawther Stewart. "Wave functions of the hydrogen molecular ion". In: *Philosophical Transactions of the Royal Society of London. Series A, Mathematical and Physical Sciences* 246.911 (1953), pp. 215–240.

[69] Chaoqun Zhang, Nicholas R Hutzler, and Lan Cheng. "Intensity-borrowing mechanisms pertinent to laser cooling of linear polyatomic molecules". In: *Journal of Chemical Theory and Computation* 19.13 (2023), pp. 4136–4148.

[70] Chaoqun Zhang, Phelan Yu, Chandler J Conn, Nicholas R Hutzler, and Lan Cheng. "Relativistic coupled-cluster calculations of RaOH pertinent to spectroscopic detection and laser cooling". In: *Physical Chemistry Chemical Physics* 25.47 (2023), pp. 32613–32621. DOI: 10.1039/D3CP04040B.

[71] Jinchun Xie and Richard N Zare. "Selection rules for the photoionization of diatomic molecules". In: *The Journal of chemical physics* 93.5 (1990), pp. 3033–3038.

[72] NJ Fitch and MR Tarbutt. "Laser-cooled molecules". In: *Advances in atomic, molecular, and optical Physics* 70 (2021), pp. 157–262.

[73] Adam L Shaw, Zhuo Chen, Joonhee Choi, Daniel K Mark, Pascal Scholl, Ran Finkelstein, Andreas Elben, Soonwon Choi, and Manuel Endres. "Benchmarking highly entangled states on a 60-atom analogue quantum simulator". In: *Nature* 628.8006 (2024), pp. 71–77.

[74] Loic Anderegg, Nathaniel B Vilas, Christian Hallas, Paige Robichaud, Arian Jadbabaie, John M Doyle, and Nicholas R Hutzler. "Quantum control of trapped polyatomic molecules for eEDM searches". In: *Science* 382.6671 (2023), pp. 665–668.

[75] *Caltech Radiation Safety Training and Reference Manual*. https://safety.caltech.edu/documents/14140/radiation_safety_taining_and_reference.pdf.

[76] G Belier, J Aupiais, Goedele Sibbens, Andre Moens, and David Vanleeuw. "High-precision spontaneous fission branching-ratio measurements for Pu 240, 242 and Cf 252 isotopes". In: *Physical Review C* 98.3 (2018), p. 034612.

[77] David E Alburger. "Beta Decay of N 16". In: *Physical Review* 111.6 (1958), p. 1586.

[78] *NRC Basic Health Physics - Shielding Radiation*. https://www.nrc.gov/docs/ml1122/ML11229A721.pdf.

[79] International Atomic Energy Agency. *Analytical Methodology for the Determination of Radium Isotopes in Environmental Samples*. Tech. rep. IAEA/AQ/19. Vienna: International Atomic Energy Agency, Dec. 2010. URL: https://www-pub.iaea.org/MTCD/Publications/PDF/IAEA-AQ-19_web.pdf.

[80] https://www.chemlin.org/isotope/radium-226. Accessed: 2026-03-03.

[81] *The 2007 Recommendations of the International Commission on Radiological Protection.* ICRP Publication 103. Ann. ICRP 37 (2-4). 2007.

[82] *1991 International Symposium on Radon and Radon Reduction Technology*. EPA/600/9-91/037. Philadelphia, PA, USA: U.S. Environmental Protection Agency, 1991.

[83] Cornelius Keller, Walter Wolf, and Jashovam Shani. "Radionuclides, 2. Radioactive elements and artificial radionuclides". In: *Ullmann's Encyclopedia of Industrial Chemistry* (2000).

[84] Chandler J Conn*, Phelan Yu*, Madison I Howard, Yuxi Yang, Chaoqun Zhang, Arian Jadbabaie, Aikaterini Gorou, Alyssa N Gaiser, Timothy C Steimle, and Lan Cheng. "Production and spectroscopy of cold radioactive molecules". In: *arXiv preprint arXiv:2508.08368* (Accepted in *Science* 2026). DOI: 10.48550/arXiv.2508.08368.

[85] Thorsten Köhler, Krzysztof Góral, and Paul S Julienne. "Production of cold molecules via magnetically tunable Feshbach resonances". In: *Reviews of modern physics* 78.4 (2006), pp. 1311–1361.

[86] Niccolo Bigagli, Weijun Yuan, Siwei Zhang, Boris Bulatovic, Tijs Karman, Ian Stevenson, and Sebastian Will. "Observation of Bose–Einstein condensation of dipolar molecules". In: *Nature* 631.8020 (2024), pp. 289–293.

[87] Raymond E March. "Quadrupole ion traps". In: *Mass spectrometry reviews* 28.6 (2009), pp. 961–989.

[88] Vaishnavi Rajagopal, Chris Stokes, and Alessandra Ferzoco. "A linear ion trap with an expanded inscribed diameter to improve optical access for fluorescence spectroscopy". In: *Journal of The American Society for Mass Spectrometry* 29.2 (2017), pp. 260–269.

[89] Richard Bing-Shiun Tsai, Lewis RB Picard, Xiangkai Sun, Yuan Le, Kon H Leung, and Manuel Endres. "Gate-based Readout and Cooling of Neutral Atoms". In: *arXiv preprint arXiv:2603.21643* (2026).

[90] Michael Drewsen. "Ion coulomb crystals". In: *Physica B: Condensed Matter* 460 (2015), pp. 105–113.

[91] Barbara J Garrison and R Srinivasan. "Laser ablation of organic polymers: Microscopic models for photochemical and thermal processes". In: *Journal of Applied Physics* 57.8 (1985), pp. 2909–2914.

[92] Salvatore Amoruso, Riccardo Bruzzese, Nicola Spinelli, and Raffaele Velotta. "Characterization of laser-ablation plasmas". In: *Journal of Physics B: Atomic, Molecular and Optical Physics* 32.14 (1999), R131–R172.

[93] Roman Krems, Bretislav Friedrich, and William C Stwalley. *Cold molecules: theory, experiment, applications*. CRC press, 2009.

[94] JF Barry, DJ McCarron, EB Norrgard, MH Steinecker, and D DeMille. "Magneto-optical trapping of a diatomic molecule". In: *Nature* 512.7514 (2014), pp. 286–289.

[95] Nickolas H Pilgram. "Production and Characterization of Ytterbium Monohydroxide (YbOH) for Next-Generation Parity and Time-Reversal Violating Physics Searches". PhD thesis. California Institute of Technology, 2023.

[96] Chandler Conn. *Minifridge Part Files*. 2025. URL: https://github.com/Chandler-Conn/Minifridge-Part-Files (visited on 05/25/2026).

[97] Thomas R Roberts and Stephen G Sydoriak. "Thermomolecular pressure ratios for He 3 and He 4". In: *Physical Review* 102.2 (1956), p. 304.

[98] J-G Wang, JD Tandy, and PF Bernath. "High-resolution laser excitation spectroscopy of the A 2Π (000)-X 2Σ+(000) transition of BaOH". In: *Journal of Molecular Spectroscopy* 252.1 (2008), pp. 31–36.

[99] Nick Vogeley, Bernd Bauerhenne, and Daqing Wang. "Hydrodynamic effects in cryogenic buffer gas cells: design insights from hybrid simulations". In: *New Journal of Physics* 27.11 (2025), p. 113205.

[100] ED Marquardt, JP Le, and Ray Radebaugh. *Cryogenic Material Properties Database Cryogenic Material Properties Database*. 2000.

[101] JP Elchert. "Cryogenic multilayer insulation theory and an analysis of seams under a variety of assumptions". In: *Thermal and Fluids Analysis Workshop (TFAWS)*. GRC-E-DAA-TN60172. 2018.

[102] Wesley C Campbell. "Magnetic trapping of imidogen molecules". PhD thesis. Harvard University, 2008.

[103] RF Robbins and PR Ludtke. "Review of static seals for cryogenic systems". In: *Journal of Spacecraft and Rockets* 1.3 (1964), pp. 253–259.

[104] Sanjay Nakhate, Timothy C Steimle, Nickolas H Pilgram, and Nicholas R Hutzler. "The pure rotational spectrum of YbOH". In: *Chemical Physics Letters* 715 (2019), pp. 105–108.

[105] Arian Jadbabaie, Nickolas H Pilgram, Jacek Kłos, Svetlana Kotochigova, and Nicholas R Hutzler. "Enhanced molecular yield from a cryogenic buffer gas beam source via excited state chemistry". In: *New Journal of Physics* 22.2 (2020), p. 022002.

[106] Nickolas H Pilgram, Arian Jadbabaie, Yi Zeng, Nicholas R Hutzler, and Timothy C Steimle. "Fine and hyperfine interactions in 171YbOH and 173YbOH". In: *The Journal of Chemical Physics* 154.24 (2021).

[107] Yi Zeng. "Progress toward precision measurements using polyatomic molecules". PhD thesis. California Institute of Technology, 2024.

[108] Nickolas H Pilgram, Arian Jadbabaie, Chandler J Conn, and Nicholas R Hutzler. "Direct measurement of high-lying vibrational repumping transitions for molecular laser cooling". In: *Physical Review A* 107.6 (2023), p. 062805. DOI: 10.1103/PhysRevA.107.062805.

[109] Hans Karlsson and Ulf Litzén. "Revised Ba I and Ba II wavelengths and energy levels derived by fourier transform spectroscopy". In: *Physica Scripta* 60.4 (1999), pp. 321–328.

[110] VS Burakov, NV Tarasenko, and NA Savastenko. "Plasma chemistry in laser ablation processes". In: *Spectrochimica Acta Part B: Atomic Spectroscopy* 56.6 (2001), pp. 961–971.

[111] Zitian Ye. "Working with a Cryogenic Buffer Gas Cell: Metastable Helium Dynamics and Radium Spectroscopy". Senior Thesis. California Institute of Technology, 2024.

[112] SS Hodgman, RG Dall, LJ Byron, KGH Baldwin, SJ Buckman, and AG Truscott. "Metastable helium: A new determination of the longest atomic excited-state lifetime". In: *Physical review letters* 103.5 (2009), p. 053002.

[113] Adele Basturk. "Enhancing Molecular Yields of Cold, Gas-Phase Alkaline-Earth Monofluorides Beyond Universal Density Constraints in a Cryogenic Buffer Gas Cell". Senior Thesis. California Institute of Technology, 2025.

[114] M Athanasakis-Kaklamanakis, G Peng, S Li, H Septien-Gonzalez, C Debavelaere, AD White, S Popa, J Lim, BE Sauer, and MR Tarbutt. "Slowing YbF molecules using radiation pressure". In: *Physical Review Research* 7.4 (2025), p. 043235.

[115] Zack D Lasner, Alexander Frenett, Hiromitsu Sawaoka, Loïc Anderegg, Benjamin Augenbraun, Hana Lampson, Mingda Li, Annika Lunstad, Jack Mango, Abdullah Nasir, et al. "Magneto-optical trapping of a heavy polyatomic molecule for precision measurement". In: *Physical Review Letters* 134.8 (2025), p. 083401.

[116] Yuiki Takahashi, Harish D Ramachandran, Arian Jadbabaie, Yi Zeng, Chi Zhang, and Nicholas R Hutzler. "Engineered Molecular Clock Transitions for Symmetry Violation Searches". In: *arXiv preprint arXiv:2508.06787* (2025).

[117] TA Isaev, Steven Hoekstra, and Robert Berger. "Laser-cooled RaF as a promising candidate to measure molecular parity violation". In: *Physical Review A—Atomic, Molecular, and Optical Physics* 82.5 (2010), p. 052521.

[118] AN Petrov and LV Skripnikov. "Energy levels of radium monofluoride RaF in external electric and magnetic fields to search for P-and T, P-violation effects". In: *Physical Review A* 102.6 (2020), p. 062801.

[119] Tianxiang Chen, Chaoqun Zhang, Lan Cheng, Kia Boon Ng, Stephan Malbrunot-Ettenauer, Victor V Flambaum, Zack Lasner, John M Doyle, Phelan Yu, Chandler J Conn, et al. "Relativistic exact two-component coupled-cluster study of molecular sensitivity factors for nuclear Schiff moments". In: *The Journal of Physical Chemistry A* 128.31 (2024), pp. 6540–6554. DOI: 10.1021/acs.jpca.4c02640.

[120] Victor V Flambaum. "Enhanced nuclear Schiff moment and time-reversal violation in Th 229-containing molecules". In: *Physical Review C* 99.3 (2019), p. 035501.

[121] Stefan Brünner. “Study of radon adsorption on activated carbon for a purification system in XENON1T”. PhD thesis. Karl-Franzens-Universität Graz, 2013.

[122] Mingyu Fan, Craig A Holliman, Anna L Wang, and Andrew M Jayich. “Laser cooling of radium ions”. In: *Physical Review Letters* 122.22 (2019), p. 223001.

[123] Dmitry Budker, Derek F Kimball, and David P DeMille. *Atomic physics: an exploration through problems and solutions*. Oxford University Press, 2004.

[124] ND Scielzo, JR Guest, EC Schulte, I Ahmad, K Bailey, DL Bowers, RJ Holt, Z-T Lu, TP O’Connor, and DH Potterveld. “Measurement of the lifetimes of the lowest P 1 3 state of neutral Ba and Ra”. In: *Physical Review A—Atomic, Molecular, and Optical Physics* 73.1 (2006), p. 010501.

[125] John S Forsythe and DJT Hill. “The radiation chemistry of fluoropolymers”. In: *Progress in polymer science* 25.1 (2000), pp. 101–136.

[126] Jean-Paul Jay-Gerin. “Fundamentals of water radiolysis”. In: *Encyclopedia* 5.1 (2025), p. 38.

[127] Digby D Macdonald, George R Engelhardt, and Andrei Petrov. “A critical review of radiolysis issues in water-cooled fission and fusion reactors: Part I, Assessment of radiolysis models”. In: *Corrosion and Materials Degradation* 3.3 (2022), pp. 470–535.

[128] Dileep Mampallil and Huseyin Burak Eral. “A review on suppression and utilization of the coffee-ring effect”. In: *Advances in colloid and interface science* 252 (2018), pp. 38–54.

[129] Klaus Dreisewerd. “The desorption process in MALDI”. In: *Chemical reviews* 103.2 (2003), pp. 395–426.

[130] Bertha Herse. *Candy Making and the Effects of Heat upon Sugar*. Bachelor’s thesis, Oregon Agricultural College. June 1910.

[131] Richard W Hartel and AnnaKate Hartel. *Candy bites: The science of sweets*. Springer, 2014.

[132] Kauko K Mäkinen. “Sugar alcohols, caries incidence, and remineralization of caries lesions: a literature review”. In: *International journal of dentistry* 2010.1 (2010), p. 981072.

[133] Keiichiro Urabe, Hitoshi Muneoka, Sven Stauss, Osamu Sakai, and Kazuo Terashima. “Laser absorption spectroscopy diagnostics of helium metastable atoms generated in dielectric barrier discharge cryoplasmas”. In: *Japanese Journal of Applied Physics* 54.10 (2015), p. 106101.

[134] Kazuo Minami, Yutaka Yamanishi, Chikara Kojima, Masako Shindo, and Osamu Ishihara. “Very slowly decaying afterglow plasma in cryogenic helium gas”. In: *IEEE transactions on plasma science* 31.3 (2003), pp. 429–437.

[135] U Dammalapati, K Jungmann, and L Willmann. "Compilation of spectroscopic data of radium (Ra I and Ra II)". In: *Journal of Physical and Chemical Reference Data* 45.1 (2016).

[136] Bodhaditya Santra, Umakanth Dammalapati, Alexander Groot, K Jungmann, and Lorenz Willmann. "Absolute frequency measurement of the 7s^2 ^1 S _0– 7s7p^1 P _1 transition in^225 Ra". In: *arXiv preprint arXiv:1409.8659* (2014).

[137] M Fan, Roy A Ready, H Li, S Kofford, R Kwapisz, CA Holliman, MS Ladabaum, AN Gaiser, JR Griswold, and AM Jayich. "Laser cooling and trapping of 224 Ra+". In: *Physical Review Research* 5.4 (2023), p. 043201.

[138] VS Letokhov. "Saturation spectroscopy". In: *High-Resolution Laser Spectroscopy*. Springer, 2005, pp. 95–171.

[139] EJ Salumbides, KSE Eikema, W Ubachs, U Hollenstein, H Knöckel, and E Tiemann. "The hyperfine structure of 129 I 2 and 127 I 129 in the B band system". In: *Molecular Physics* 104.16-17 (2006), pp. 2641–2652.

[140] Timothy C Steimle, Colan Linton, Ephriem Tadesse Mengesha, Xilin Bai, and Anh T Le. "Field-free, Stark, and Zeeman spectroscopy of the A 2 Π 1/2-X 2 Σ+ transition of ytterbium monohydroxide". In: *Physical Review A* 100.5 (2019), p. 052509.

[141] S Kinsey-Nielsen, CR Brazier, and PF Bernath. "Rotational analysis of the B 2Σ+–X 2Σ+ transition of BaOH and BaOD". In: *The Journal of chemical physics* 84.2 (1986), pp. 698–708.

[142] David A Dixon, David Feller, and Kirk A Peterson. "A practical guide to reliable first principles computational thermochemistry predictions across the periodic table". In: *Annual reports in computational chemistry*. Vol. 8. Elsevier, 2012, pp. 1–28.

[143] Andraž Kocjan, Kristoffer Krnel, and Tomaž Kosmač. "The influence of temperature and time on the AlN powder hydrolysis reaction products". In: *Journal of the European Ceramic Society* 28.5 (2008), pp. 1003–1008.

[144] TG Tiecke. "Properties of potassium". In: *University of Amsterdam, The Netherlands, Thesis* (2010), pp. 12–14.

[145] Gordon WF Drake. *Springer handbook of atomic, molecular, and optical physics*. Springer Science & Business Media, 2007.

[146] A Lagerqvist. "A band-system of radium chloride". In: *Arkiv Fysik* 6 (1952).

[147] TA Isaev, AV Zaitsevskii, A Oleynichenko, E Eliav, AA Breier, TF Giesen, RF Garcia Ruiz, and R Berger. "Ab initio study and assignment of electronic states in molecular RaCl". In: *Journal of Quantitative Spectroscopy and Radiative Transfer* 269 (2021), p. 107649.

[148] Yuliya Osika, Yong-Chang Han, and Maksim Shundalau. "Theoretical insights into the spectroscopic properties and prospects for the direct laser cooling of the radium monohalides". In: *Nonlinear Phenomena in Complex Systems* 27.1 (2024), pp. 78–96.

[149] Christopher C Parker, Sarah Pascoe, Aleš Chodacki, Joe M O'Sullivan, Josep R Germá, Charles Gillies O'Bryan-Tear, Trond Haider, and Peter Hoskin. "A randomized, double-blind, dose-finding, multicenter, phase 2 study of radium chloride (Ra 223) in patients with bone metastases and castration-resistant prostate cancer". In: *European urology* 63.2 (2013), pp. 189–197.

[150] Benjamin L Augenbraun, Loïc Anderegg, Christian Hallas, Zack D Lasner, Nathaniel B Vilas, and John M Doyle. "Direct laser cooling of polyatomic molecules". In: *Advances in Atomic, Molecular, and Optical Physics* 72 (2023), pp. 89–182.

[151] SF Vázquez-Carson, Q Sun, J Dai, D Mitra, and T Zelevinsky. "Direct laser cooling of calcium monohydride molecules". In: *New Journal of Physics* 24.8 (2022), p. 083006.

[152] RJ Hendricks, DA Holland, Stefan Truppe, BE Sauer, and MR Tarbutt. "Vibrational branching ratios and hyperfine structure of 11BH and its suitability for laser cooling". In: *Frontiers in Physics* 2 (2014), p. 51.

[153] Nathaniel B Vilas, Paige Robichaud, Christian Hallas, Grace K Li, Loïc Anderegg, and John M Doyle. "An optical tweezer array of ultracold polyatomic molecules". In: *Nature* 628.8007 (2024), pp. 282–286.

[154] John Gurland and Ram C Tripathi. "A simple approximation for unbiased estimation of the standard deviation". In: *The American Statistician* 25.4 (1971), pp. 30–32.

[155] Valentina Zhelyazkova. "Laser cooling of CaF molecules". PhD thesis. Imperial College London, 2014.

[156] Benjamin Augenbraun. "Methods for Direct Laser Cooling of Polyatomic Molecules". PhD thesis. Harvard University, 2022.

[157] Stefan Truppe, Silvio Marx, Sebastian Kray, Maximilian Doppelbauer, Simon Hofsäss, Hanns Christian Schewe, Nicole Walter, Jesús Pérez-Ríos, Boris G Sartakov, and Gerard Meijer. "Spectroscopic characterization of aluminum monofluoride with relevance to laser cooling and trapping". In: *Physical Review A* 100.5 (2019), p. 052513.

[158] Xiangyue Liu, Weiqi Wang, SC Wright, Maximilian Doppelbauer, Gerard Meijer, Stefan Truppe, and Jesús Pérez-Ríos. "The chemistry of AlF and CaF production in buffer gas sources". In: *The Journal of Chemical Physics* 157.7 (2022).

[159] Joost WF van Hofslot, Izabella E Thompson, Anno Touwen, Nithesh Balasubramanian, Roman Bause, Hendrick L Bethlem, Anastasia Borschevsky, Ties H Fikkers, Steven Hoekstra, Steven A Jones, et al. "2D transverse laser cooling of a hexapole focused beam of cold BaF molecules". In: *Communications Physics* (2026).

[160] Timothy C Steimle, Sarah Frey, Anh Le, David DeMille, David A Rahmlow, and Colan Linton. "Molecular-beam optical Stark and Zeeman study of the A 2 Π–X 2 Σ+(0, 0) band system of BaF". In: *Physical Review A—Atomic, Molecular, and Optical Physics* 84.1 (2011), p. 012508.

[161] Benjamin L Augenbraun, John M Doyle, Tanya Zelevinsky, and Ivan Kozyryev. "Molecular asymmetry and optical cycling: laser cooling asymmetric top molecules". In: *Physical Review X* 10.3 (2020), p. 031022.

[162] Nicholas R Hutzler. "Polyatomic molecules as quantum sensors for fundamental physics". In: *Quantum Science & Technology* 5.4 (2020), p. 044011.

[163] Alexander Frenett, Zack Lasner, Lan Cheng, and John M Doyle. "Vibrational branching fractions for laser cooling of nonlinear strontium-containing molecules". In: *Physical Review A* 110.2 (2024), p. 022811.

[164] Sean Burchesky. "Engineered Collisions, Molecular Qubits, and Laser Cooling of Asymmetric Top Molecules". PhD thesis. Harvard University, 2023.

[165] Philip R Bunker and FA Matsen. *Molecular symmetry and spectroscopy*. American Institute of Physics, 1979.

[166] Allan E Parker. "Band systems of MgCl, CaCl and SrCl". In: *Physical Review* 47.5 (1935), p. 349.

[167] A.B. Darji and S.P. Vaidya. "Band spectrum of CaI molecule in the region 6610-6175 Å (A and B systems)". In: *Indian J. Pure Appl. Phys.* 923.11 (1973).

[168] MFC Ladd and WH Lee. "The solubilities of some inorganic halides". In: *Transactions of the Faraday Society* 54 (1958), pp. 34–39.

[169] Xi-Lin Bai, Xue-Dong Zhang, Fu-Qiang Zhang, and Timothy C Steimle. "Laser-induced fluorescence experimental spectroscopy and theoretical calculations of uranium monoxide". In: *Chinese Physics B* 31.5 (2022), p. 053301.

[170] Jiande Han, Anh T Le, Timothy C Steimle, and Michael C Heaven. "Electronic Configuration Assignments for UO from Electric Dipole Moment Measurements". In: *The Journal of Physical Chemistry Letters* 13.46 (2022), pp. 10799–10804.

[171] Michael C Heaven. "Heavy Element Spectroscopy in the Gas Phase". In: *Annual Review of Physical Chemistry* 77 (2025).

[172] Mark Fred, Frank S Tomkins, Jean E Blaise, Pierre Camus, and Jean Verges. *Atomic spectrum of neptunium.[Tables]*. Tech. rep. Argonne National Lab., IL (USA), 1976.

[173] Ingrid Cnossen, Michael Wiltberger, and Jeremy E Ouellette. "The effects of seasonal and diurnal variations in the Earth's magnetic dipole orientation on solar wind–magnetosphere-ionosphere coupling". In: *Journal of Geophysical Research: Space Physics* 117.A11 (2012).

[174] Vincent Courtillot and Jean Louis Le Mouel. "Time variations of the earth's magnetic field-From daily to secular". In: *IN: Annual review of earth and planetary sciences. Volume 16 (A88-52285 22-46). Palo Alto, CA, Annual Reviews, Inc., 1988, p. 389-476.* 16 (1988), pp. 389–476.

[175] John David Jackson. "Classical electrodynamics 3rd edition, ed john wiley & sons". In: *Inc., New York, USA* (1998).

[176] J Baron, WC Campbell, D DeMille, JM Doyle, G Gabrielse, YV Gurevich, PW Hess, NR Hutzler, E Kirilov, I Kozyryev, et al. "The ACME collaboration: Order of magnitude smaller limit on the electric dipole moment of the electron". In: *Science* 343 (2014), pp. 269–272.

[177] Malika Denis, Yongliang Hao, Ephraim Eliav, Nicholas R. Hutzler, Malaya K. Nayak, Rob G. E. Timmermans, and Anastasia Borschesvky. "Enhanced P,T-violating nuclear magnetic quadrupole moment effects in laser-coolable molecules". en. In: *The Journal of Chemical Physics* 152.8 (Feb. 2020), p. 084303. ISSN: 0021-9606, 1089-7690. DOI: 10.1063/1.5141065. URL: http://aip.scitation.org/doi/10.1063/1.5141065 (visited on 06/23/2022).

[178] JF Hoburg. "Principles of quasistatic magnetic shielding with cylindrical and spherical shields". In: *IEEE Transactions on electromagnetic compatibility* 37.4 (1995), pp. 574–579.

[179] TJ Sumner, JM Pendlebury, and KoF Smith. "Conventional magnetic shielding". In: *Journal of Physics D: Applied Physics* 20.9 (1987), pp. 1095–1101.

[180] E Paperno and I Sasada. "Magnetic circuit approach to magnetic shielding". In: *Journal of the Magnetics Society of Japan* 24.1 (2000), pp. 40–44.

[181] Kendall F Casey. "Quasi-static electric-and magnetic-field penetration of a spherical shield through a circular aperture". In: *IEEE transactions on electromagnetic compatibility* 1 (1985), pp. 13–17.

[182] Paul Oxley. "Apparatus for magnetization and efficient demagnetization of soft magnetic materials". In: *IEEE Transactions on magnetics* 45.9 (2009), pp. 3274–3283.

[183] I Altarev, P Fierlinger, T Lins, MG Marino, B Nießen, G Petzoldt, M Reisner, S Stuiber, M Sturm, J Taggart Singh, et al. "Minimizing magnetic fields for precision experiments". In: *Journal of Applied Physics* 117.23 (2015).

[184] Anna Zakharova and Alexander Petrov. "P, T-odd effects for the RaOH molecule in the excited vibrational state". In: *Physical Review A* 103.3 (2021), p. 032819.

[185] J Tiedau, MV Okhapkin, K Zhang, J Thielking, G Zitzer, E Peik, Fabian Schaden, T Pronebner, Ira Morawetz, L Toscani De Col, et al. "Laser excitation of the Th-229 nucleus". In: *Physical Review Letters* 132.18 (2024), p. 182501.

[186] R Elwell, Christian Schneider, Justin Jeet, JES Terhune, H_W T Morgan, AN Alexandrova, HB Tran Tan, Andrei Derevianko, and Eric R Hudson. "Laser excitation of the Th 229 nuclear isomeric transition in a solid-state host". In: *Physical Review Letters* 133.1 (2024), p. 013201.

[187] I Morawetz, T Riebner, L Toscani De Col, F Schneider, N Sempelmann, F Schaden, M Bartokos, GA Kazakov, S Lahs, K Beeks, et al. "Continuous-wave nuclear laser absorption spectroscopy of Thorium-229". In: *arXiv preprint arXiv:2604.16640* (2026).

[188] Chaoqun Zhang, Xuechen Zheng, Junzi Liu, Ayush Asthana, and Lan Cheng. "Analytic gradients for relativistic exact-two-component equation-of-motion coupled-cluster singles and doubles method". In: *The Journal of Chemical Physics* 159.24 (2023).

[189] Attila Kovács and Ivan Infante. "Theoretical study of the electronic spectra of neutral and cationic NpO and NpO2". In: *The Journal of Chemical Physics* 143.7 (2015).

[190] Ashay N Patel, Madison I Howard, Timothy C Steimle, and Nicholas R Hutzler. "Rapid, Broadband, Optical Spectroscopy of Cold Radicals". In: *arXiv preprint arXiv:2505.03650* (2025).

[191] John M Wills and Olle Eriksson. "Actinide ground-state properties, theoretical predictions". In: *Los Alamos Science* 26 (2000), p. 128.

[192] Gabriel F de Melo and David A Dixon. "Protactinium and Actinium Monohydrides: A Theoretical Study on Their Spectroscopic and Thermodynamic Properties". In: *The Journal of Physical Chemistry A* 126.36 (2022), pp. 6171–6184.

Chapter

A

Radium SOP

Below is a reproduction of the current version of our radium-226 Standard Operating Procedure (SOP). The point of this document is twofold. First, we used it to develop our workflow and safety procedures in cooperation with our radiation safety office to gain regulatory approval to start working with radium. Just as importantly, it serves as a reference for existing and new project members to ensure that everyone is following safe and approved handling protocols.

Significant contributions to this SOP were made by Nick Hutzler and me. Much of the content was established via discussions with our radiation safety officer Haick Issaian and our radiochemical collaborator Alyssa Gaiser.

> Disclaimer: This is **not** our complete SOP for working with radioactive materials—some general, university-specific details are contained elsewhere. Projects working with radioactive material should always be discussed and developed with the relevant safety office and regulatory agency, and performed under expert supervision.

Attempts were made to merge the formatting of the original document with this thesis layout.

A.1 Overview

We perform spectroscopy on cryogenically-cooled Ra-226 atoms and molecules containing this atom. Many isotopes of the Radium nucleus, including Ra-226, have several interesting scientific properties, including a large charge resulting in highly relativistic electron motion in the atom, and a static octupole deformation in the nucleus. These effects directly lead to significant enhancements in the sensitivity of the atom, and molecules containing the atom, to fundamental symmetry violations. The techniques that we have developed in our lab put us in a unique position to study these species at high resolution and using a very small-scale apparatus. Our goal is to perform spectroscopic studies on a variety of Ra-226-containing molecular species, and demonstrate a new approach which would be applicable to even shorter-lived species which could be obtained at future isotope facilities.

A high-level overview of the experimental approach is listed below. Details are contained in later sections.

1. Deposit a thin layer of $RaCl_2$ or $Ra(NO_3)_2$ on a piece of metal or ceramic by dropping $RaCl_2$ or $Ra(NO_3)_2$ solution on the material until all of the liquid is evaporated. This will be the **target**. Targets could also be purchased, or consist of other solid Ra-226-containing materials without the need for local handling.

2. Install the target into a few-inch-scale copper box, called the **cell**, which will be fully sealed with indium apart from a single 1/8" tube brazed to the cell.

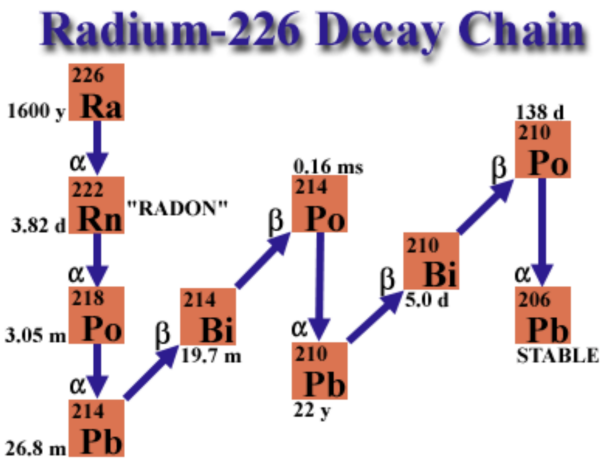
3. Install the cell in a vacuum chamber, called the **chamber**, which will cool the cell to around 4 K. Connect the cell outlet to a gas line which runs via a feedthrough to the exterior of the chamber. Note that the chamber will not be exposed to the contents of the cell as the cell is sealed apart from the cell outlet, which does not meet the interior of the chamber.

4. Pump out the cell via a gas handling system. There will be cold traps and charcoal filters between the cell feedthrough outlet and the vacuum pump.

5. Pump out the chamber and activate the cryogenic refrigerator to cool the cell to 4 K.

6. Back-fill the cell with ~100 mTorr (never more than 10 Torr) of He-4.

7. Ablate the target and perform laser spectroscopy.



Nuclide	Activities after 30 d:
Ra-226	370.0e3 Bq
Rn-222	368.3e3 Bq
Po-218	368.3e3 Bq
Pb-214	368.3e3 Bq
Bi-214	368.3e3 Bq
Po-214	368.3e3 Bq
Pb-210	769.1 Bq
Bi-210	553.9 Bq
Po-210	28.27 Bq
At-218	73.67 Bq

Figure A.1: Left: decay chain of Ra-226, taken from `https://www.nist.gov/image-23773`. Right: Activity of all daughter nuclides after starting from 10 μCi radium-226. Taken from `https://www.wise-uranium.org/rcc.html`.

8. When the target is no longer useful, for example because it has been ablated away, then warm up, permanently seal the cell and dispose of the cell and remaining target. Ablation byproducts of the target will still be contained in the cell, but may no longer be experimentally useful. We expect targets to be useful for no more than typically one month.

A.2 Summary of Hazards

We generally handle Ra-226 in quantities of 10 microCuries (uCi), which is equivalent to 10 micrograms, or $2.7 \cdot 10^{16}$ Ra-226 atoms. We also purchase solid forms of Ra-226 and portion it out into samples ranging from 10 to 200 uCi. The primary hazards are therefore solid contamination due to Ra-226 and its decay products, along with gaseous Rn-222 emitted from the decay of Ra-226. The mitigation of these hazards is discussed in detail in this SOP and the appendices, but here we give a summary and overview.

Ra-226 has a half-life of 1,600 years and decays via alpha emission to Rn-222. Thus the primary safety concern for radiation exposure is if the radium is inhaled or ingested, as clothing and dead outer layers of skin are sufficient to attenuate these alphas (see for example "Health Physics" by Cember.) Specific scenarios and effective dose calculations are provided in a later section, but to summarize, it would take ingestion of an entire ~10 uCisample, or aspiration of the entire sample through an N95 mask, to exceed ICRP maximum recommended dose limits for occupational exposure.

Rn-222 has a half-life of 3.8 days and decays via alpha emission to a chain of short-

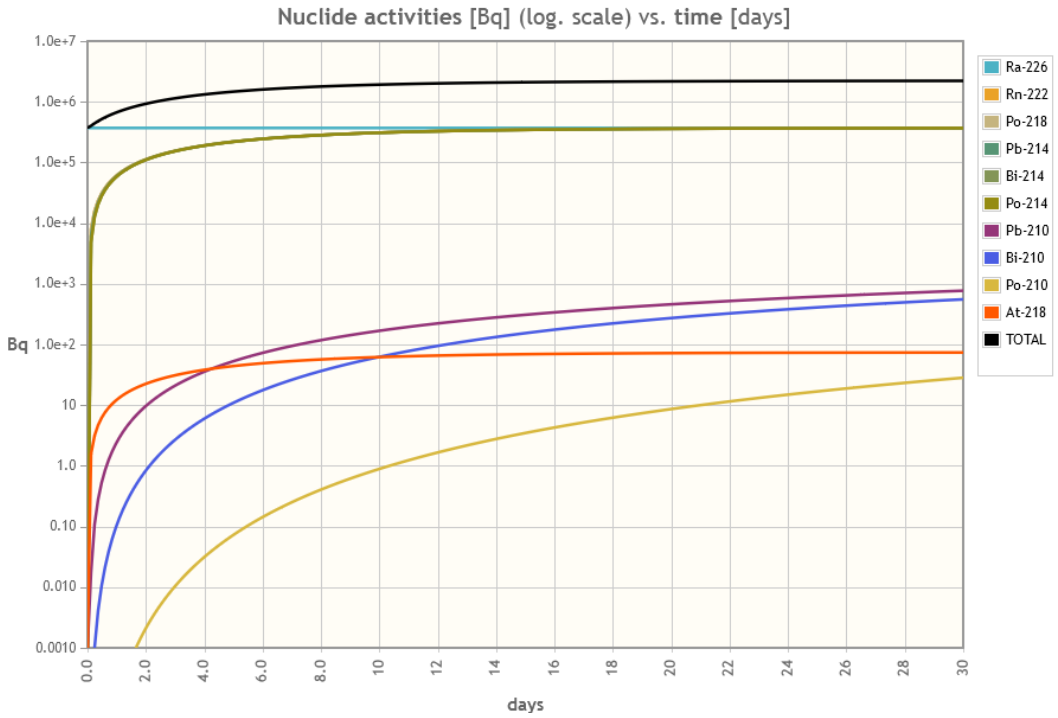


Figure A.2: Activity of 10 microCi Ra-226 (pure sample at t=0) versus time over one month, log scale. From `https://www.wise-uranium.org/rcc.html`

lived (<1 hour) alpha-, beta-, and gamma-emitting progeny before reaching Pb-210, which has a 22 year half-life and is therefore effectively stable on the time scales of our experimental work. The primary safety concern with Rn-222 is that it is gaseous at room temperature and can therefore be inhaled. Specific scenarios and effective dose calculations are provided in a later section, but a summary is that even a catastrophic (but realistic) scenario where the entire radioactive sample is released into the room and there is a complete failure of the ventilation system, the equilibrium Rn-222 density is below the OSHA limits for occupational exposure on a one year time scale, and would require several weeks of exposure to meet ICRP maximum recommended dose limits for occupational exposure.

A.3 Target Preparation

There are two forms of Ra-226 that we purchase. From Eckert & Ziegler, we acquire Ra-226 in the form of $RaCl_2$ solution dissolved in 0.5 or 5 mL of 0.1 M HCl (item number 8226[1]). From the Department of Energy National Isotope Development Center, we acquire $Ra(NO_3)_2$ solid salt in 1 mCi quantity, which we then dissolve and

[1]https://www.ezag.com/home/products/isotope_products/isotrak_calibration_sources/standardized_solutions/calibrated_solutions/single_nuclide_solutions/

aliquot into smaller containers. In order to turn the Radium into an experimentally useful form, we will evaporate the entire quantity of a single vial out of solution onto what we call the "target" plate, which will then be sealed to our cryogenic cell. This process will occur in a fume hood.

In order to improve both the surface adhesion and uniformity of the finished target, we dissolve around 1 mg of xylitol in the solution before drop casting. The full details of this procedure, as well as the rationale behind it, are described in [84].

Target preparation tests with barium analogs are always performed prior to changing the chemical form or composition of the radium targets, modifying the dropcast methods, or introducing new additives or substrates. In initial development, testing was conducted with solutions of $BaCl_2$, the closest chemical analogue to the commercially available chloride salts (product 35584-AP from Alfa Aesar, diluted to match the concentration of $RaCl_2$ that we receive). Identical end-to-end tests of drop casting, target loading, and ablation were performed with $Ba(NO_3)_2$ prior to work with $Ra(NO_3)_2$ salt sourced from DOE. Full test runs with barium analogs are similarly performed when introducing new additives or substrates to the target protocol.

The target plate begins as a 1.5"x1.5" plate made from Copper alloy C10100. Many different protocols have been tested to produce the best targets, so we will only describe the current method that has been used on the most recent target runs in this SOP. A piece of 1mm thick pure gold foil (product AA11391FF from Thermo Fisher) is hole-punched to produce a 5/16" diameter gold disc, which is then epoxied onto the center of the copper plate. Gold is used to minimize any reaction between the radioactive solution and the surface material. Even though copper should theoretically not react with weak hydrochloric or nitric acid, we have noticed that radiolytic reactions with the radium solution are quite dramatic and difficult to control.

Using a pipette, individual microliter-sized drops of the solution are added onto the gold. The plates sit on a hot plate set to 80°C to speed up evaporation of the solution without boiling. Once the solution has evaporated onto the target plate, another drop is added and the process repeated until the entire solution has been used. This is performed in a radiation-appropriate environment, with precautions taking place as needed at the consultation of EHS. All open radioactive materials are handled inside an absorbent pad-lined fume hood to ventilate radon and capture accidental spills. Stock solutions containing radium salts will be stored behind lead shielding to minimize radiation exposure.



Figure A.3: Images: Left: A target plate showing the central gold disk and a droplet of radium solution on top after it has fully dried (the current protocol). Right: An older target protocol, where the blue coloration in the middle is the result of radiolytic reactions between a radium chloride solution and the copper surface, likely forming copper (II) chloride dihydrate.

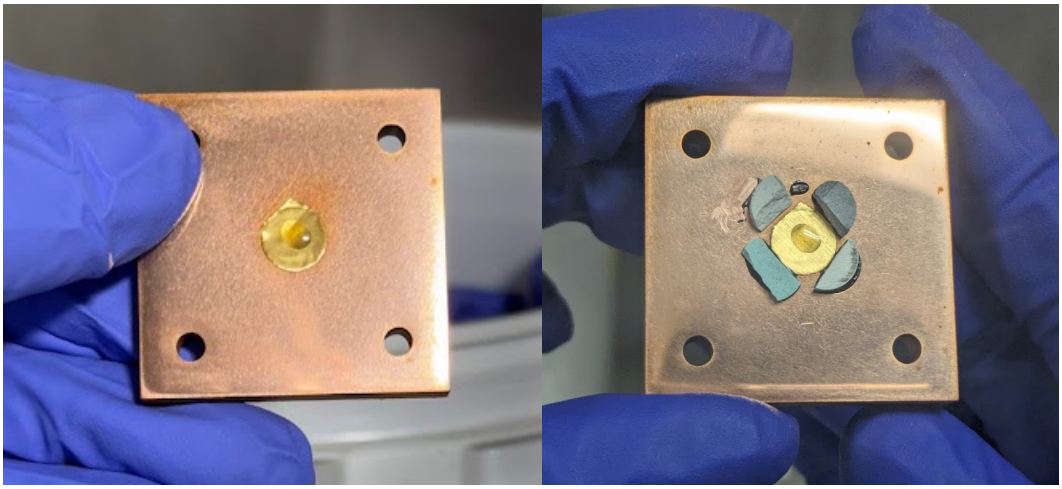


Figure A.4: Images: the same target plate, before and after the addition of the ablation co-targets. Left: the xylitol-doped radium nitrate solution is fully evaporated in the center of the gold foil, even though it looks like a liquid droplet (the plate is being held vertically and the material does not move). Right: the ablation co-targets. Clockwise from top: Yb metal chunk, Yb powder-doped $Al(OH)_3$, $Al(OH)_3$, CuF_2, and $Al(OD)_3$.

Following the evaporation of all of the material, we then epoxy the ablation co-targets on the target plate. These co-targets contain the reagents which we react with the Ra atoms to form molecules, and typically are either $Al(OH)_3$ for making RaOH, $Al(OD)_3$ for making RaOD, or CuF_2 for making RaF.

A separate method of target production involves depositing the radium solution

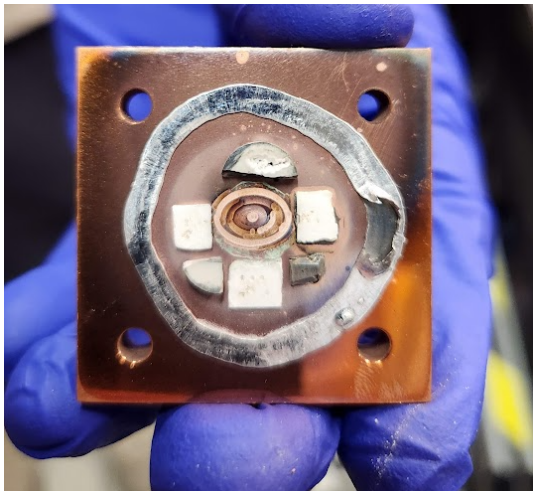


Figure A.5: Image: A barium test target featuring many different alumina porosities. The center is a typical drop cast target, and the white pieces are different types of alumina. Any dark coloration is the result of the ablation process. The metallic ring surrounding the targets is the indium seal, which is explained in the following section.

directly onto a piece of alumina ceramic. We purchase alumina of various porosities ranging from 36% to non-porous and use pieces of them as we would use the gold foil for the drop cast substrate. Distributing the material inside the ceramic has the advantage of dramatically increasing the number of useful atomic ablation shots before needing to move the ablation laser.

After this, the targets are ready to be sealed to the cell as described in the next section.

Solution volumes utilized during the dropcast should not exceed 1 mL, to avoid taking excessive time for drop casting and solution evaporation. To reduce the total time of the evaporation process when the solution volume exceeds 1 mL, larger solutions can be "pre-evaporated" to a final volume of ~0.5 mL before being added to the target plate. This pre-evaporation follows a protocol given to us by a nuclear chemistry group at Johannes Gutenberg University Mainz. To do this, the full solution (5 mL in the example below) is added to a PTFE beaker and placed closely under a heat lamp, where it slowly evaporates to the final volume.

The pre-evaporation rate for a $BaCl_2$ test solution was one hour per mL of solution, meaning the total evaporation time for the largest volume Radium solution should be around five hours. The activity of all daughter species produced by Radium decay during a timeframe similar to this is plotted below:

The total activity of Rn-222 after eight hours, which is assuming the evaporation process takes much longer than expected, is 587 nCi (22 kBq). This would motivate

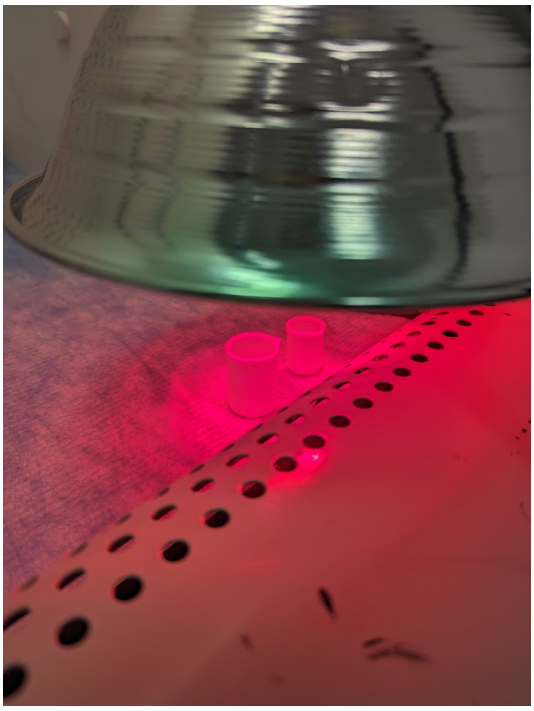


Figure A.6: Image: two PTFE (Teflon) beakers of barium chloride solution during a test of the pre-evaporation protocol. Teflon is slippery and thus prevents any sticking of radium to the walls of the beakers, and because it is resistant to the hydrochloric acid in the solution. Based on our tests, the pre-evaporation process reduces the volume from 5 mL to 0.5 mL in around 3.5-4 hours, and will reduce the necessary handling time of the radioisotope by 90%.

performing the evaporation in a radiation-approved fume hood or vented glove box to achieve a background radon level of <0.1 pCi/L, which is an order-of-magnitude below the EPA-recommended level. With 370,000 Rn-222 atoms being produced per second from radium decay, this corresponds to production of $1.38*10^{-17}$ L/s of radon gas. The dynamics of small quantities of gas in a fume hood are difficult to predict, but we can make some scaling arguments. Fume hoods certified by Caltech must have an ANSI/ASHRAE 110 rating of 4.0 AU 0.1 or less[2]. This means that for a release rate of 4 L/min of gas in the fume hood under normal use, a person operating at the hood would experience 0.1 ppm of the gas or less. Approximating all gases as ideal and noting the specific activity of radon[3], we can estimate an upper bound on the radon activity experienced just outside the fume hood in the ANSI/ASHRAE 110 (meaning 4 L/min release rate) test to be 200 mCi/L. By scaling this 4 L/min release rate down to our extremely low radon release rate of $1.38*10^{-17}$ L/s, we would expect only $3.15*10^{-5}$ pCi/L in the region just outside the fume hood, a value much smaller than the EPA-recommended background level.

A.4 Preparation and Installation of Cell and Chamber

Once the target is prepared, for example by the procedure described above or by purchasing a target made by a third party, it is installed in the cell.

[2] https://www.dir.ca.gov/title8/5154_1.html
[3] https://www.ncbi.nlm.nih.gov/books/NBK158787/table/T23/

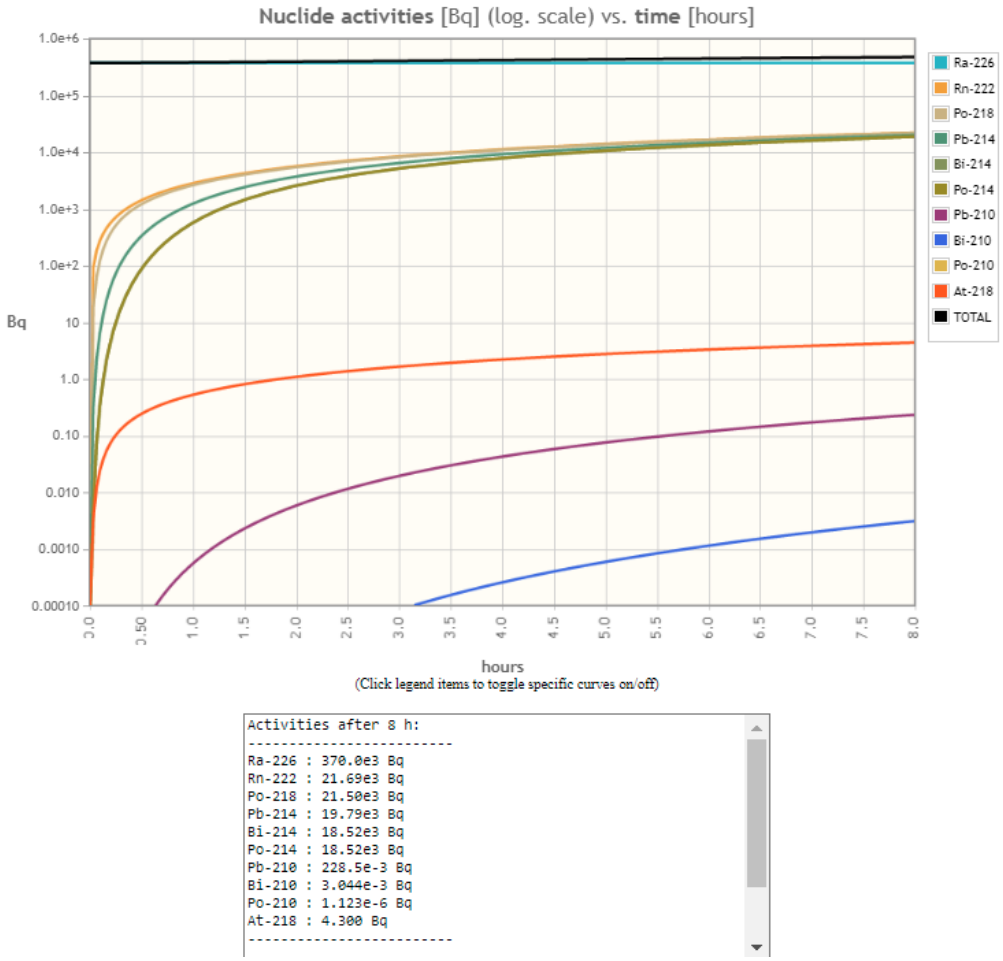


Figure A.7: Figure from `https://www.wise-uranium.org/rcc.html`

Description of cell and sealing process

The cell is a copper enclosure that allows for target storage and laser access at cryogenic temperatures. We have used a few different designs for the cell; the current design measures 2”x2.5”x3.5” with one 1.25” diameter cylindrical bore through the long axis and two 0.75” diameter bores intersecting it. Copper plates, including the target plate described above, and optics are mounted to the sides of the cell at these holes with a leak-tight indium wire seal.

Indium is a soft metal that easily bonds to metals and glass when compressed and retains its malleability at cryogenic temperatures, making it the standard for cryogenic vacuum applications. We create a vacuum seal by forming a ring of indium wire that is slightly larger in diameter than the bores in the cell and placing this ring between the cell and the plate or optic to be attached. By tightening screws on the copper mounting plates, the indium is compressed and bonds to both the cell and the attached part,

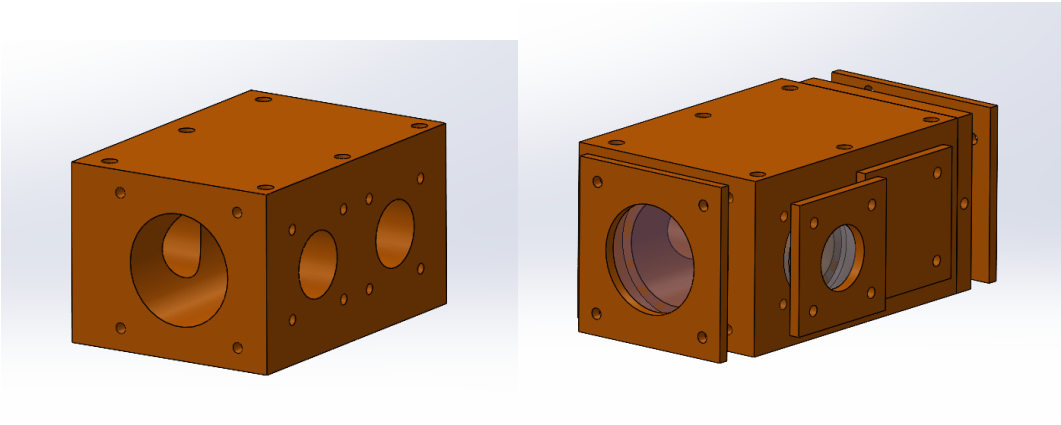


Figure A.8: Images: 3D rendering of the cell before (left) and after (right) mounting of various attachments. The bores that create the internal cavity are visible as the three large through-holes on the left image. The target plate is the featureless plate visible on the right side of the right image.

creating a leak-tight seal even at cryogenic temperatures[4].

We have measured the leak rate of this indium-sealed cell by using a helium leak-checker to be $5.9*10^{-10}$ mbar l/s, which implies a "flow" into the cell of $1.5*10^{10}$ helium atoms/s and is analogous to a gap of just 5 nm[5]. The actual leak rate for Radon in the experiment will be even lower for a few reasons. First, radon is larger and less permeable than helium[6]. Second, the cell will be at cryogenic temperatures, so most radon will freeze before encountering an indium seal.

Before assembly, we paint part of the interior of the cell with an ultra-low reflectance black paint (formerly Alion MH2200, now owned by Huntington Ingalls Industries – Mission Technologies). This paint is airbrushed on the interior of the cell that is visible to the fluorescence collection part of the experiment in order to reduce the background light scatter visible on the photomultiplier tube.

"Full assembly" of the cell consists of all of the windows, target plate, and gas line being assembled. This includes all gas lines which will ultimately reside inside the chamber, including the cell cold trap (see Section A.5) and a cap on the gas line to prevent radon escaping. The gas lines are bent into the correct shape during this stage. The target plate is installed last, after every other component has been assembled and inspected.

[4]https://ntrs.nasa.gov/api/citations/19890013479/downloads/19890013479.pdf

[5]https://www.leybold.com/en-us/knowledge/vacuum-fundamentals/leak-detection/definition-and-measurement-of-vacuum-leaks

[6]https://www.sciencedirect.com/science/article/pii/S0168900210001099

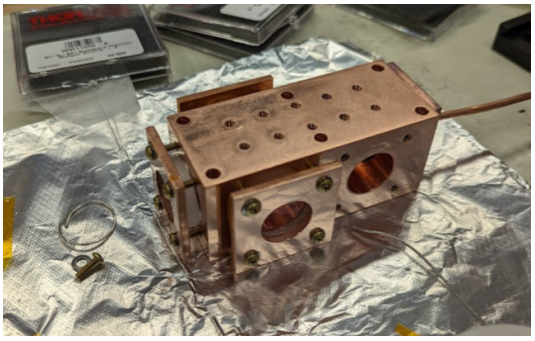


Figure A.9: Photo: Midway through the assembly process of an older cell version. Copper flanges are used to hold the windows in place. Indium wire can be seen on the left of the photo (above the screw on the table), as well as pressed between the left window and the cell. The uncovered hole visible on the right of the cell is where the target plate would mount. The helium cell outlet is extending to the right of the photo.

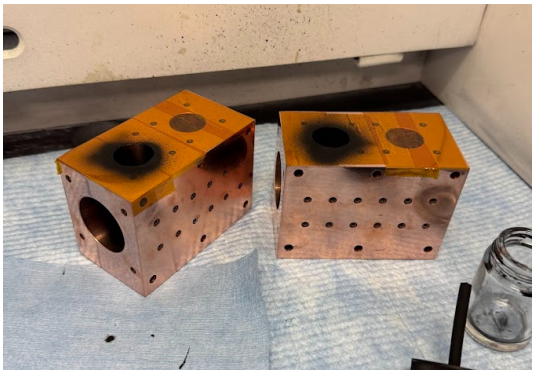


Figure A.10: Photo: two cell bodies immediately after painting. They will dry in a fume hood for 24 hours before being handled. On both, the paint was airbrushed through the hole on the left of the top surface, creating a very dark interior region.

Once the cell has been fully assembled, it is leak-checked with a helium leak-checker to ensure that the seals are functioning properly. We use a liquid nitrogen cold trap between the cell (see Section A.5) and the leak checker to freeze out the small amount of Radon that will be produced during the leak checking process, which typically takes less than 20 minutes. The sealed cell will then be mounted to the 4 K stage of the cryostat, described in the next section.

A.5 Description of the Cryostat

The cryostat used for this research consists of a Sumitomo RDK-205D closed cycle helium cold head mounted to an Ideal Vacuum cube assembly, which in the lab is referred to as "MiniFridge," and is located in Downs-Lauritsen 127. We refer to components of this cryostat in terms of three "stages," denoted by the temperature

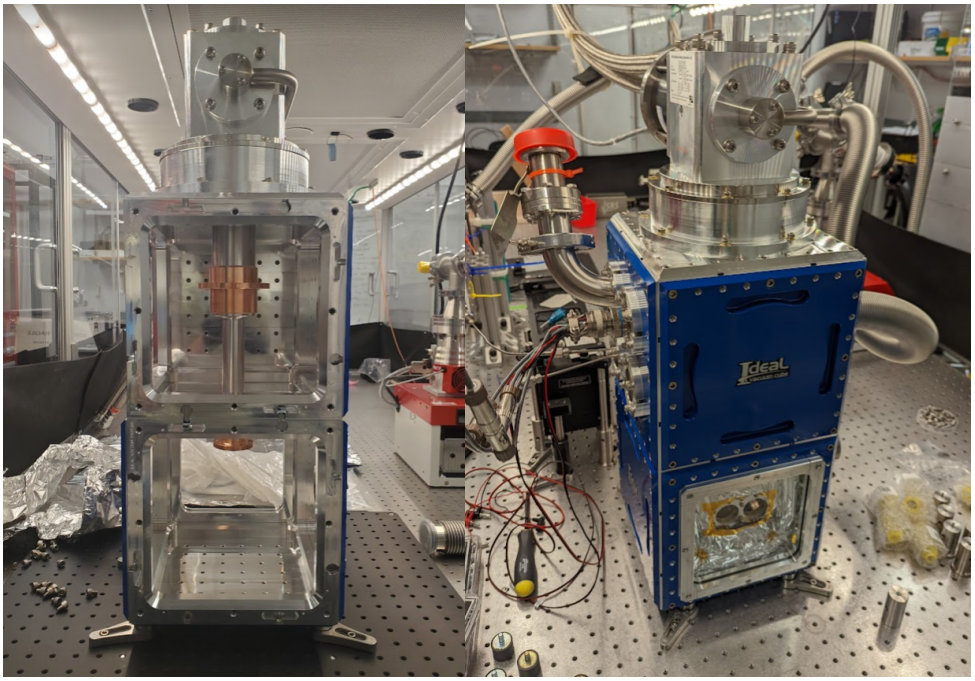


Figure A.11: Photos: Right: A completed cryostat with all components in place, ready to take data. The 300 K stage is the blue layer, with part of the 30 K stage visible through the window on the bottom. Left: An early step in the construction where the 30 K and 4 K copper sections of the cold head are visible. The 30 K section is the portion slightly up from center, and the 4 K section is just below the joining segment of the two cube frames.

that the components in that stage experience:

- 300 K stage: the outer chamber and all components that are mounted directly to it, such as vacuum feedthroughs. Everything within the 300 K stage is under vacuum, and everything outside of it is in atmosphere.
- 30 K stage: a layer of aluminum mounted to the 30 K section of the cold head, which surrounds and shields the 4 K stage from black body radiation from the 300 K stage.
- 4 K stage: the cell and related components that are attached to the 4 K section of the cold head.

Gas Handling System

A gas line exterior to the chamber is connected to the cell outlet via vacuum feedthroughs in the 300 K stage. This line allows us to pump out the cell to vacuum–because the cell

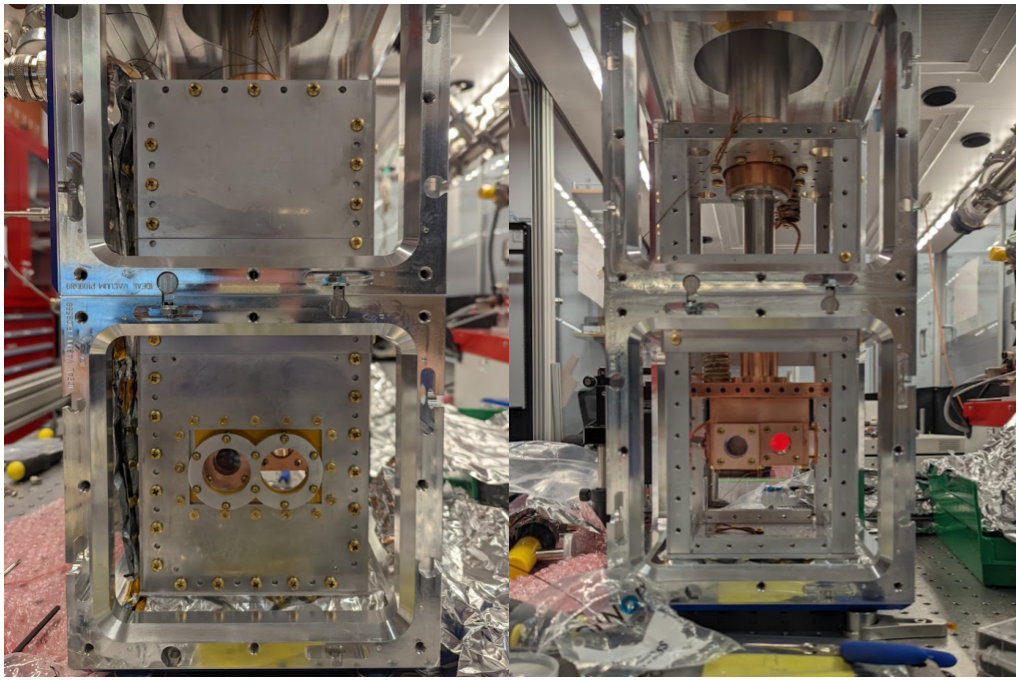
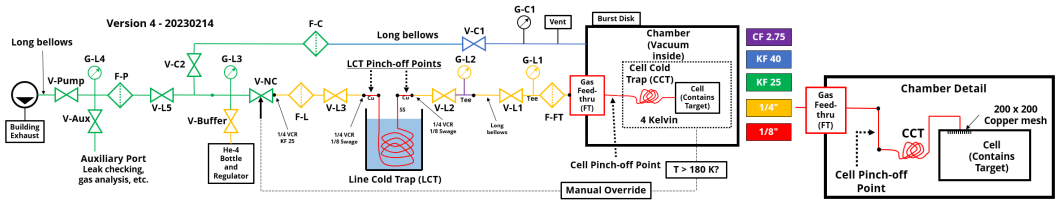


Figure A.12: Right: The 4 K stage sitting within a partially-assembled 30 K stage. The cell is visible as the bottom copper part. The cell window on the left allows for laser access to the target, and the window on the right allows for laser access to the plume of atoms and molecules produced by laser ablation. Left: The completed 30 K stage as it surrounds the 4 K stage. Windows allow laser access through the 30 K stage to the cell.

is sealed from the rest of the cryostat, we need to pump on it separately. We also use the line to introduce controlled amounts of helium. A sketch of the full gas handling layout is below (see Figure 5.3 in the main thesis document for an additional view).



- The box labeled “Chamber” is the vacuum chamber.
- Items are labeled as **V**alves, **F**ilters, **G**auges, and usually indicated whether they are on the Gas **L**ine or **C**hamber pumping portions.
- The “Cell” contains the radium.
- The cold traps are coils of ” gas lines submerged in liquid nitrogen. The Line Cold Trap (LCT) is located in the room and can be used while the experiment

is running. The CCT is inside the vacuum chamber and will be cryogenically cooled by the refrigerator, but can also be submerged in liquid nitrogen during cell installation, pump out, and leak checking.

- Feed-thru (FT) is the cell feedthrough outlet, which brings the gas lines from inside to outside of the chamber.
- "Pinch-off Points" are locations where we may use a tube pinch-off tool to cut and seal the gas lines during cell changes or disposal, or otherwise seal the gas line using a VCR plug.
- Filters (diamonds with dashed internal lines) are activated charcoal in-line filters, which filter[7] up to 90% of radon at room temperature and 99% at 0°C, with the exception of F-FT, which is a particulate filter.
- "T > 180 K?" is a temperature sensor relay which will send a logical high signal if the temperature of the cell is above 180 K. This will trigger the shutting of a normally-closed (NC) valve.
- Everything which has a reasonable chance of encountering radon gas, in particular everything between V-L3 and the cell, will be all metal.

The gas handling system is fully installed and leak-checked before the cell is installed. The chamber side of the feed-thru can be plugged to enable leak-checking.

A.6 Cell installation

The installation of the cell involves a one-time procedure to get the cell and chamber to typical operating conditions. As per the cell assembly procedure, the assembled cell will also have a (capped) gas line on it.

1. This procedure requires two people, one of whom is an observer.
2. Ensure that the 180 liter LN_2 dewar in the lab is at least 25% full.
3. Ensure that the gas handling system outside of the chamber is fully assembled and leak-checked.
4. Ensure that the radon monitor is active.

[7] https://pure.mpg.de/rest/items/item_2044321_2/component/file_2044320/content

5. Ensure that a radiation meter is measuring a space near the chamber.
6. Ensure that the LCT is filled.
7. Ensure that the leak checker is hooked up to the auxiliary port and powered on, but not pumping.
8. Pump out the gas handling system apart from the gas feed-thru and the chamber.
    a. Turn off the vacuum pump.
    b. Make sure that the turbo in the vacuum pump is spun down.
    c. Open V-Pump, V-L5, V-Aux, V-C2, V-Buffer, V-NC, V-L3, V-L2.
        i. In other words, open all valves apart from V-C1, V-L1.
    d. Turn on the vacuum pump.
9. Ensure that the cap on the cell assembly is secure.
10. Mount the cell to the 4 K stage.
11. Gently adjust the gas line into place, so that it is ready to be attached to the feedthrough on the vacuum side.
12. Submerge the CCT in liquid nitrogen. Make sure it stays filled until it is time to remove it.
13. Close V-L1, V-L2, V-L3, V-NC.
14. Ensure the LCT is filled, and that it remains filled until noted otherwise.
15. Remove the cap from the cell fill line and attach it to the feedthrough. **This step should be done quickly as radon gas may be leaking out of the tube** (though not at a rate which is of concern; see below.)
    a. If for some reason the attachment to the feedthrough fails, re-attach the cap.
    b. If this step instead succeeds, be sure to dispose of the cap as contaminated waste.
16. Ensure that the LCT and CCT are filled.
17. Ensure that V-C1, V-C2 are closed.

18. Open V-NC.
19. Slowly pump out the cell and gas line by slowly opening V-L3, V-L2, V-L1.
    a. The gas line should be already pumped out by the earlier steps.
20. Start pumping with the leak checker.
21. Once the pressure is low enough to leak-check, close V-pump
22. Leak-check the entire gas line to confirm that the new connections are leak-tight. Note that the chamber will be open at this point, so ensure that the internal gas connections and the cell are leak-checked again.
23. Close V-L1, V-L2, V-L3, V-NC to isolate the cell from the rest of the gas handling system.
    a. Put red tape around V-L1, V-L2, V-L3, V-NC, and ensure that V-NC is overridden to be closed, until the chamber is cold.
24. Remove the LN2 container from the CCT.
25. Leave a piece of clean aluminum foil under the cell.
26. Assemble the 30 K shield and vacuum chamber.
27. Pump out the chamber and check for leaks in the vacuum chamber.
    a. Ensure that V-NC, V-L3, V-L2, V-L1 are closed
    b. Turn off the vacuum pump and wait for the turbo to spin down.
    c. Set the leak checker to stop pumping (though it can be left on).
    d. Open V-Pump, V-Aux, V-L5, V-C2, V-C1
    e. Turn on the vacuum pump
    f. Once the pressure is low enough to leak-check, close V-Pump
    g. Leak check the entire vacuum chamber and all vacuum lines connecting to it.
28. Turn on the refrigerator, and set it to keep the cell temperature below 130 K.
29. At this point, the LCT can be allowed to empty.

From this point onward, unless the cell is closed off from the rest of the gas handling manifold, the cell and chamber will always be at low pressure (<1 Torr) and low temperature (<130 K), with the pressure inside the cell resulting from any helium that we flowed in. Occasionally we will need to reintroduce helium, and that process is described in a later section.

Note that the cell cold trap being filled during initial pump-out is a safety redundancy, and is not likely to be needed. Assume that the sealed cell and gas line have reached steady-state and conservatively contains a density of $2*10^{10}$ cm^{-3} radon atoms (see "Radon" section). The diffusion coefficient of radon in air[8] is around 0.1 cm^2/s. Assume that the cap is taken off and the tube exposed for one second before being attached to the next tube. During that second, ~0.1 cm of the length of the tube will diffuse into the air, which is a volume of 0.5 uL, 10^7 radon atoms, and an activity of 21 Bq or 570 pCi. If this fills the optics table enclosure, which has a volume of around 5,000 L, this corresponds to around 0.1 pCi/L and is likely not a concern. However, the cold trap will still be used as an extra line of defense, especially until everything is leak-checked.

A.7 Experimental Operation and Procedures

Once the cell is prepared, installed, and leak checked, typical daily operating procedures ("data taking") will consist of the following steps.

1. Check chamber pressure to ensure that it is <1 mTorr.
2. Ensure that the Radon monitor is active.
3. Turn on the refrigerator and wait for the cell to cool to 4 K.
4. Visually check the gas and vacuum manifold for damage, loose fittings, and condensation.
5. Visually inspect the cell for cracks or gaps. Visual access will be limited but the windows should be clearly visible.
    a. If a crack or gap is observed, pump out all of the cell helium using the "Cell Helium Pressure Change Procedure," and then begin the "Cell and Target Disposal Procedure."

[8] `https://www.nrc.gov/docs/ML2007/ML20070G506.pdf` Table II

   b. Cracks or gaps will also be observable as an increased rate of helium loss from the cell, visible on the cell pressure gauge.
   c. Set cell helium pressure using the "Cell Helium Pressure Change Procedure" if needed.

6. Perform research measurements. This will involve ablating the target with a 532 nm nanosecond pulsed YAG with up to 100 mJ of energy, shining resonant lasers through the cell, and measuring either absorption or fluorescence. These measurements will go on typically for hours, but will be concluded before personnel leave for the day.

   a. During measurements, the cell pressure may need to be adjusted using the "Cell Helium Pressure Change Procedure".

7. When measurements are concluded, go through the "Daily Shutdown" procedure

Cell Helium Pressure Change Procedure

1. Ensure that valves V-C1,V-C2, V-L1, V-L2 are closed.
2. Ensure that the LCT is filled with LN2, and that it remains filled until mentioned otherwise.
3. Ensure that the cell is at cryogenic temperatures, <10 K, so that Radon gas is unlikely to ever leave the cryogenic region.
4. Ensure that the Radon monitor is active.
5. Visually inspect the gas lines for damage, possible leaks, condensation, or obstructions.
6. Open V-L2, V-L3, V-NC.
7. Change the helium cell pressure with the following procedure.

   a. Ensure that V-L1 is closed.
   b. Adjust valves V-Pump, V-L5, V-NC, V-L3, V-L2 as needed to either raise or lower the pressure at G-L2 such that when it is opened to the cryogenic gas manifold the result will be approximately the desired pressure. Do not adjust V-L1 during this step.

c. Ensure that V-L3 is closed.

d. Ensure that the LCT is filled with LN2.

e. Once pressures on G-L2 have stabilized, close V-L2.

f. Slowly open V-L1, wait for pressures on G-L1 and G-L2 to stabilize, then close V-L1.

    i. Note that this procedure uses the space between V-L1 and V-L2 as a load-lock to introduce helium without exposing LCT to radon. Since the cell is cold, this is a redundancy.

g. V-L1 and V-L2 should not be opened at the same time during this procedure.

8. Repeat steps outlined in 8 as necessary to achieve desired cell helium pressure.

    a. If the goal is to pump out the cell entirely, for example as part of cell disposal, then perform step 8 until the pressure on G-L1 is <100 mTorr, then slowly open V-L1 and V-L2 until the cell has been pumped out.

9. Ensure that V-L1, V-L2 are closed.

10. Close V-L3 to isolate LCT, which can now be allowed to warm up.

11. Open V-C1, V-C2, V-L5, V-Pump to ensure that the chamber is being pumped on.

12. Ensure that V-L1, V-L2, V-L3, V-NC are closed.

Shutdown Procedure

This procedure will be used whenever the experiment will be left unattended, either for a short period such as a meeting or a longer period such as a weekend.

1. Visually inspect the windows and gas handling lines for damage or condensation.

2. Close valves V-L1, V-L2, V-L3 to isolate the cell.

3. Manually override V-NC to keep it closed.

4. Ensure that the vacuum pump is turned on.

5. Open valves V-C1, V-C2, V-L5, V-Pump to ensure that the chamber is being pumped on.
6. Ensure that the Radon monitor is active.
7. Ensure that the compressor is set to keep the cryostat <130 K.
8. If work will be resumed within a short period of time, the procedure can stop here. If work will resume in more than a few hours, continue the following steps.
    a. Shut down lasers.
    b. Turn off the refrigerator, but ensure that it is set to keep the cell below 130 K.

A.8 Cell and Target Disposal

When the target is no longer useful, for example because all of the Ra-226 has been ablated, the entire cell will be sealed off and disposed of. As a reminder, all of the initial Ra-226 will still be in the cell, but may no longer be in an experimentally useful form (for example, deposited on surfaces with no optical access for ablation.)

Cell and Target Disposal Procedure

1. Ensure that the 180 liter LN2 dewar in the lab is at least 25% full.
2. Ensure that the Radon monitor is active.
3. Ensure that the cell is above 20 K, but below 130 K
    a. This is to ensure that helium is desorbed from the ablation targets so that helium can be efficiently removed from the cell
4. Pump the helium out of the cell using the "Cell Helium Pressure Change Procedure".
5. Close V-L1.
6. Put red tape around V-L1 to indicate that it should be closed.

7. Ensure that the LCT is still full (it should be full as a result of using the "Cell Helium Pressure Change Procedure."

8. Pump out the helium from the room-temperature gas lines. This will require opening V-Pump, V-L5, V-NC, V-L3, V-L2 (but leave V-L1 closed).

    a. As always, open the valves slowly to avoid an inrush of helium to the turbopump. If the pressure in the lines is high, spin down the turbo first.

9. Close V-NC (via manual override) and V-L1, V-L2, V-L3. Put red tape around the valves to make it clear that they should not be open until this entire procedure is completed.

    a. This step is critical, as the following steps will result in radon gas emanating from the cell.

10. Close all of the panels around the optical table, and put up signage indicating that the table is not to be used until the cell disposal procedure is complete.

11. Warm the entire chamber to at least a few degrees above the dew point in the room. This will take approximately one day.

    a. If heaters are used, ensure that a timer is set to avoid overheating.
    b. **Once the cell goes above around 200 K, radon will begin emanating down the cell fill line.** This means that V-L1, G-L1, F-FT, FT, and all gas lines inside the chamber will be exposed to radon.

12. The following steps involve opening the chamber, and removing the cell. They should be performed in one session with minimal interruptions.

13. This procedure requires two people, one of whom is an observer.

14. This procedure will require the following items:

    a. Two VCR plugs, including gaskets.
    b. J-B Weld 8267.
    c. Materials for wipe testing.

15. Visually inspect the cell to look for cracks or breaks. Visual access will be limited but cell windows should be clearly visible.

   a. If a crack or gap in the cell is observed, then reconfigure the gas and vacuum manifold so that the chamber can be pumped out through a cold trap. Take note of the location of the crack or gap and prepare Kapton tape, epoxy, or anything else which could be used to seal it once the chamber is disassembled.

16. Ensure that the LCT is full, and stays full until indicated otherwise.

17. Ensure that the LCT is filled.

18. Open V-C1, V-C2 so that the chamber can be pumped on as it warms.

19. Close V-L1, V-L2.

20. Once all of the cryogenic stages are above the room dew point, prepare to vent the chamber to atmosphere.

   a. Ensure that **all** valves are closed, including V-C1 and V-C2.
   b. Slowly open the vent valve on the vacuum chamber.

21. Ensure that V-C1, V-C2 are closed. Put red tape around the valves to make it clear that they should not be open until this entire procedure is completed.

   a. This is to add another redundancy against radon entering breathable space in the event of a failure of LCT, V-L3, F-L, and V-NC.

22. Disassemble vacuum chamber and radiation shields sufficiently to access and remove the cell, but do not disassemble any cell parts or gas lines. Perform a wipe test of the exterior of each item before removing it, and then a wipe test of the interior of the item after it is removed. Store the items on a clean, disposable surface, such as foil.

23. Visually inspect all of the windows and joints in the cell, including those without easy visual access, by using an endoscope or dentist's mirror.

   a. If a crack or gap in the cell is observed, seal it with Kapton tape, epoxy, or anything else sufficient.

24. Ensure that LCT is filled with LN2.

25. Fill CCT with LN2.

26. Remove and dispose of the cell.

    a. Line the bottom of the chamber with clean aluminum foil.
    b. Disconnect the VCR connection from the cell to the FT and immediately plug it on both sides, starting with the cell.
    c. If the disconnect and plugging fails, or is unable to be attempted, then crush the cell gas fill line close to the FT connection using a handheld vise or crimper.
        i. Disassemble the VCR connection and immediately cap the lines.
        ii. Apply J-B Weld 8267 to the cap on the cell line to prevent it ever being removed.
    d. Remove most of the screws holding up the cell, but leave enough in place for mechanical support.
    e. Remove the LN2 container around the CCT
    f. Prepare an open plastic bag ("inner bag"), and place another open bag ("outer bag") on a safe work surface.
    g. Remove the last screws holding up the cell and transfer the cell and crimped fill line to the inner bag.
    h. Seal the inner bag, then transfer the bag to the interior of the outer bag (without touching the exterior of the outer bag).
    i. Dispose of gloves, and with new gloves seal the outer bag.
    j. Place the outer bag in the radioactive waste accumulation area and bring to the isotope lab for disposal at the earliest convenience.
    k. Wipe test the clean aluminum foil lining the bottom of the chamber and dispose of it as contaminated waste.
    l. Wipe test surfaces in the chamber interior which were in the proximity of the cell.

27. If needed: remove and dispose of the LCT gas line.

    a. Ensure that the LCT is filled.
    b. Ensure that valves V-L1, V-L3 are closed.
    c. Open valve V-L2 to allow any residual gases to cold trap.

d. Close V-L2.

e. Make sure a charcoal filter fan is blowing air away from people.

f. Use hermetically sealing cold weld crimper to pinch-off the cold trap at the LCT Pinch-Off Points. As soon as each crimp is made, apply J-B Weld 8267 to the crimped ends.

g. Wait 5 minutes for the J-B Weld to harden

h. Remove and dispose of the coiled gas line in a tagged disposal bag.

28. Clean up the area

    a. Wipe test surfaces near the chamber, including high-touch surfaces such as handles on optics table panels and valves, and the radiation meter.

    b. Make sure that all contaminated materials have been properly labeled and disposed of.

    c. Check personnel for contamination.

29. Schedule a pickup for disposal of contaminated waste with EHS.

A.9 Mitigation of Contamination

Any surface which has been exposed to radium or radon above background levels should be considered contaminated.

Everything which is contaminated or either potentially contaminated should be clearly labeled.

- Some things which will be contaminated but cannot be disposed of immediately, such as portions of the gas line and the cell, should be clearly labeled at all times.
- Things which can be disposed of should be disposed of immediately. Contaminated or potentially contaminated materials should never be left anywhere apart from approved accumulation sites.

Assume that everything potentially contaminated is contaminated until proven otherwise.

All contaminated waste must be placed in clearly labeled bags which are gathered in the satellite accumulation areas. Waste should be brought to the isotope lab for disposal the day that it is generated.

All work involving the handling of potentially contaminated surfaces or materials, such as cell installation and removal, requires a "buddy system" of at least two people, at least one of whom is an "observer" who will not touch any potentially contaminated surface unless it is necessary. The main function of the observer is to provide a second line of defense against mistakes, and assist by taking notes, getting tools, monitoring cold traps/temperatures, etc. Both people must have full PPE, training, and be ready to handle contaminated materials if needed.

Procedures listed in this SOP will be treated as a checklist, and printed copies verifying the completion of the steps will be maintained. This will be one of the jobs of the observer for procedures requiring one.

Full PPE consists of safety glasses/goggles, long pants, lab coat, closed toe shoes, fit-tested P100 organic vapor/acid gas respirators, and double gloves. The inner gloves should be taped to the sleeve of the lab coat and not removed until the lab coat is removed. The outer gloves should be changed as often as needed, and routinely checked for contamination during drop casting or liquid solution work with radium Gloves should be disposed of as contaminated waste when no longer being used. Lab coats, respirators, and goggles should be checked for contamination before removing, and clothing should be checked as well after finishing work involving contaminated materials.

Regular swabs, wipes, and surveys are essential procedures for detecting and preventing the spread of contamination, especially during and following drop casting and open sample work. A portable alpha scintillator detector should be readily available during drop casting and open sample work with radium to allow for prompt checking of gloves and surfaces for contamination following material handling.

Following any drop casting and solution work with radium, swabs should be taken of gloves, clothing, and work surfaces for immediate liquid scintillation counting. Due to the short half life of radium-226 progeny, samples should be processed as soon as reasonably practical to accurately measure count rates from any potentially contaminated surface. Project members should be familiar with scintillation sample processing and operation of the liquid scintillation counter in the EHS office.

Wet Wipe Test Procedure

1. Wet a Kim Wipe with isopropanol.

2. Wipe the surface to be tested. Be sure to wipe all exposed areas.

3. Hold the wipe up to the radiation meter for at least 15 seconds.
4. Note the count rate. If it is higher than the background rate than would be expected from the Poisson statistics of the background, then the item should be considered contaminated.
5. If the item can be easily disposed of, then dispose of it.
6. If the item cannot be easily disposed of, then repeat the wipe test several times to attempt to clean the surface.
    a. If the count rate drops below the contamination threshold, then double-check by performing another thorough wipe test, as well as waving the radiation meter slowly over all areas of the surface.
    b. If the wipe tests continue to be above background, then dispose of the item.

A.10 Safety Concerns and Potential Failure Modes

Radon Hazards

Ra-226 decays into gaseous Rn-222 ("Radon"), which has a half-life of 3.8 days. 10 uCi of Ra-226 results in a flux of 370,000 radon atoms per second, not all of which necessarily end up in the gas phase, but which we conservatively assume does so. After a typical operating period of 1 month, which is much longer than the half-life of Rn-222, we expect the activity of the Radon to equal that of the Ra-226, namely 370 kBq. Using (Activity)=0.69*(Number of atoms)/(Half-life), this results in a steady-state number of 1.8e11 Radon atoms. ICRP 137[9] provides an effective dose per exposure of Rn-222 and its progeny of $1.3*10^{-5}$ (mSv/hr)/(Bq/m^3) for an indoor workplace. A good summary of radon is contained in ICRP 4836-9756-8598[10].

Assuming a cell and gas line volume of 10 cm^3 (which is conservative, as the cell itself is more like 120 cm^3), this is a number density of 1.8e10 cm^{-3}, or a pressure of 0.5 uTorr.

A general purpose cutoff for "no action needed" radon activity is 4 pCi/L = 0.15 Bq/L, according to both the EPA[11] and OSHA[12]. Using (Activity)=0.69*(Number of

[9] `https://journals.sagepub.com/doi/pdf/10.1177/ANIB_46_3-4` Table 12.7

[10] `http://www.icrpaedia.org/images/f/fd/ICRPRadonSummary.pdf`

[11] https://www.epa.gov/radon/what-epas-action-level-radon-and-what-does-it-mean

[12] OSHA Standard Interpretation 1910.1096 - Occupational exposure limits, access restrictions, and posting requirements for airborne radioactive materials, https://www.osha.gov/laws-regs/standardinterpretations/2002-12-23

atoms)/(Half-life), we find that this cutoff corresponds to 72,000 Rn-222 atoms per liter, or about 2e-15 Torr.

As a possible "worst case" scenario, consider the full release of the entire steady-state Rn-222 activity into the optics table enclosure, which is a volume of roughly 5 m^3 (5000 L). This would correspond to an activity density of 74 kBq/m^3 or 2 nCi/L. Using equation (1) from the Appendix for activity as a function of air turnover rate, and noting that our optics table has a flow rate of 500 cfm (14000 L/min), we would reach a Rn activity below 4 pCi/L after ~7 minutes. The equivalent dose rate would be (74,000 kBq/m^3) * 1.3*10^{-5} (mSv/hour)/(Bq/m^3) = 1 mSv/hr at the onset. Given the time it takes for the optics table enclosure to be pumped out of about one minute, this corresponds to an equivalent dose of around 10 uSv.

The room (Downs-Lauritsen 127) is 352 square feet with a 13 foot ceiling, for a volume of approximately 125 m^3 (125000 L). Thus, assuming another possible "worst case" scenario where the HVAC system fails, and radon gas builds up in the room over the course of days, the steady-state activity would be 370 kBq/(125 m^3) = 80 pCi/L = 3 kBq/m^3. While this is unacceptably high for our standards, it is still below the air concentration limit of 100 pCi/L set by OSHA[11] for full-time occupational exposure over the course of a year without additional respiratory protection. Using the same effective dose rate as above, this corresponds to 1 mSv/day. If the HVAC system is operating at typical flow rates, the steady-state radon activity in the room would be 0.2 pCi/L in the event that all radon emanated directly into the room, following equation (2) from Appendix, which is approximately 2 uSv/day.

Radium Hazards

Ra-226 has a half-life of 1,600 years and decays via alpha emission to Rn-222. Thus the primary safety concern for radiation exposure is if the radium is inhaled or ingested, as clothing and dead outer layers of skin are sufficient to attenuate these alphas (see for example "Health Physics" by Cember.) However, ingestion or inhalation of radium pose hazards. Since radium is chemically similar to calcium, its uptake by the body depends on its chemical form. However, ingesting radium typically results in around 20% being retained in the body and the rest excreted after a few days. The recommended committed effective dose coefficients are given in ICRP 137[13]; for inhalation of unspecified compounds it is 1.4*10^{-6} Sv/Bq, and for ingestion it is 1.3*10^{-7}

[13]https://journals.sagepub.com/doi/pdf/10.1177/ANIB_46_3-4 Table 13.7

Sv/Bq. Note that ingesting the entire 10 uCi sample of Ra-226 would result in an effective dose of 50 mSv, and breathing it in would result in 520 mSv.

All handling of radium in liquid solution will be performed in a radiation approved fume hood. Handling of solid radium after evaporation onto the target plate will occur in Downs-Lauritsen 127. The most likely mechanism for radium to leave the cell will be as particulate matter which escapes through the gas inlet; the leak-tight cell will not have any gaps through which particulate matter could escape, but particles could, for example, escape by being carried via gas flow through the gas inlet. This will be mitigated by the copper mesh on the cell interior, the particulate filter (rated to remove >95% of particles), and by wearing N95 masks (rated to remove >95% of particles) at all times when handling potentially contaminated materials. Note that ablation will likely create particulate matter, but the cell will never be opened after ablation.

A single 2 micron diameter particle of Ra-226 being inhaled into the lungs would result in a dose of 1.2 uSv, using the dose coefficient for inhalation above. If the entire 10 uCi sample was turned into particulate matter and aspirated through an N95 mask, the effective dose would be 26 mSv.

Leaks

There are several ways that leaks could introduce radon into breathable air, but all would require multiple failures. The following features are designed to prevent this:

- Keeping the cell below 130 K whenever there is radium or radon within it.
- V-NC being normally closed (that is, closed in the event of a power loss or the cell heating up).
- Making the cell and chamber vacuum tight and leak-checked.
- Using cold traps and charcoal filters.
- Exhausting the vacuum pump to the building exhaust

As an example, say that one of the windows on the cell cracked, or the cryogenic gas line developed a leak. For radon to enter breathable space, we would need the cell to warm up for at least several hours, for example due to a power failure or a failure of the compressor control system. The radon could then emanate from the cell into the

vacuum chamber. If the power was off, the radon would build up in the chamber, which would then have to have developed a leak to introduce radon into breathable space. Thus, we would need a window to crack, the chamber to warm up, and the chamber to develop a leak. Even in that case, the fraction of radon entering the room would likely be very low. However, such an outcome is possible, for example, in the event of a large earthquake which effectively destroys the chamber and cuts building power.

Forgetting to close valves or fill cold traps

There is a path where radon could emanate from the cell, down the gas handling system, and through the vacuum pump. While the pump will be exhausted to the building exhaust and not breathable space, that is still not an acceptable situation. Radon making it to the vacuum pump would require:

- The cell warming up through a failure of the compressor controls, or somebody forgetting to activate them.
- Somebody forgetting to close V-L1, V-L2, V-L3
- Overriding V-NC to stay open (without cutting power), or a failure of the control system.
- Empty LCT
- Passage of the gas through two charcoal filters

Note that our procedures require shutting these valves at the end of the day, but even if somebody completely forgot to close the valves the other systems would prevent release of radon gas into breathable or exhaust space, namely the charcoal filters, V-NC valve, and cold chamber.

Using checklists based off of the procedures in this SOP will provide additional assurance that steps are not forgotten.

Power loss

In the event of a power loss, the compressor will turn off, and the cell will start warming up. After a period of several hours, the cell will start emanating radon. However, V-NC will close if power is lost, and the vacuum pump will seal (it is backed by a

diaphragm pump, which has no conductance when not operating.) Thus, for radon to enter breathable space, we would need a leak to develop in the cell or gas handling line concurrent with the power loss, or a series of failures outlined in "Forgetting to close valves or fill cold traps."

Appendix: Room Air Exchange Data

From data in the Hutzler Lab "COVID-19 Room Descriptions and Protocols," the prep lab HVAC has a 250 cfm outflow and the optics table has a 500 cfm inflow. Assuming a uniform distribution of gas within a volume, the rate of removal due to an HVAC system can be modeled as:

$$\frac{dN}{dt} = -N\frac{Q}{V} \tag{A.1}$$

$$N(t) = N_0 e^{-\frac{Q}{V}t} \tag{A.2}$$

Where N is the amount of gas as a function of time, N_0 is the initial amount of gas, Q is the volumetric flow rate of gas due to the HVAC system, and V is the volume of the space being pulled by the HVAC.

For the case where a gas is being introduced at a constant rate within the volume, the rate of removal due to an HVAC system can be modeled as:

$$\frac{dN}{dt} = P - N\frac{Q}{V} \tag{A.3}$$

$$N(t) = P\frac{V}{Q} + e^{-\frac{Q}{V}t}(N_0 - P\frac{V}{Q}) \tag{A.4}$$

Where P is the rate of production of the gas within the entire volume.

Appendix: Radon Vapor Pressure

End of SOP

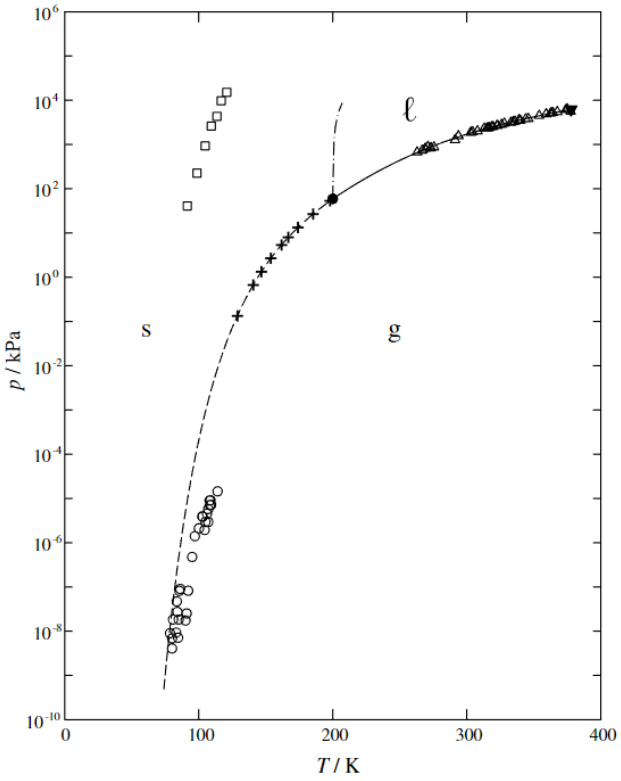


Figure A.13: The CRC Handbook lists the melting point of radon as 202 K, and the boiling point as 211 K. The `plot` at left shows the vapor pressure of Radon versus temperature (taken from `https://www.sciencedirect.com/science/article/pii/S0021961407000687`).

Chapter

B

Cell assembly guide

The following is a write-up I made to detail the cell assembly procedure, which contains some tips and tricks that others might find useful. Colorful language has been removed, but the result is still quite casual as it was written for internal circulation only.

B.1 Gather the cell parts

Acquire the cell body

If purchasing the cell from an external contracted manufacturer (such as Xometry), allow 2-3 weeks for lead time. The current cell model, as well as a dump of many of the part files used for the Minifridge, can be found at my Github https://github.com/Chandler-Conn/Minifridge-Part-Files. The design parameters are as follows:

- Process: CNC machining
- Material: C101 (probably not necessary to be this alloy, or even copper, but we haven't tested aluminum and I'm not about to take time to do that now)
- Threads and tapped holes: 34
- Inserts/threaded inserts: 34

- Tolerance: 0.005”
- Surface roughness: 0.4μm Ra (entire part)
- Certifications: Material traceability (to confirm they send us the right alloy)
- Custom notes: SEE PDF FOR SURFACE REQUIREMENTS. ALL HELICOILS TO BE INSTALLED FLUSH WITH SURFACE, NOT ABOVE.

When the cell body arrives, ensure that there are no massive dings/dents/scratches near any of the open bores and that all of the helicoils are installed properly and can accept 4-40 screws. If any of the helicoils on the sides cannot be made to work, we need to reorder and get a refund. Also, check the helicoil tabs are popped off (we can fix that easily if they aren’t).

Waterjet side plates

We should have a collection of 1/8” and 1/4” thick copper. The dxf part files are found in: [send me an email if you want the part files]. There are 6 total plates that we waterjet for each cell.

Necessary parts for one cell:

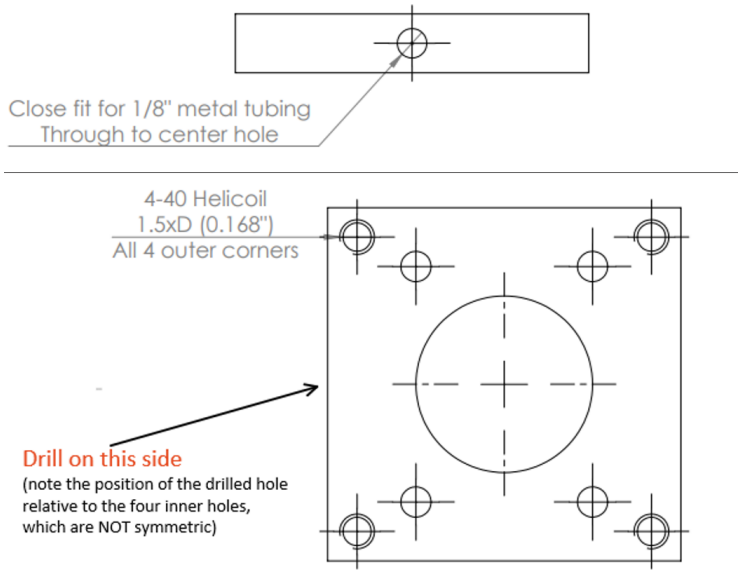
- fill line adapter: qty 1, 1/4” thick
- side blank: qty 1 of 1/4” thick
- fill line window holder: qty 1, 1/8” thick
- endpiece holder: qty 1, 1/8” thick
- window holder: qty 2, 1/8” thick

Make fill line adapter

The helium fill line part is custom since we don’t trust other people to do the brazing for us (and it would be expensive/time consuming). The reason for the adapter plate is that, if the brazing fails, we only have to trash one part of the cell rather than the whole cell body.

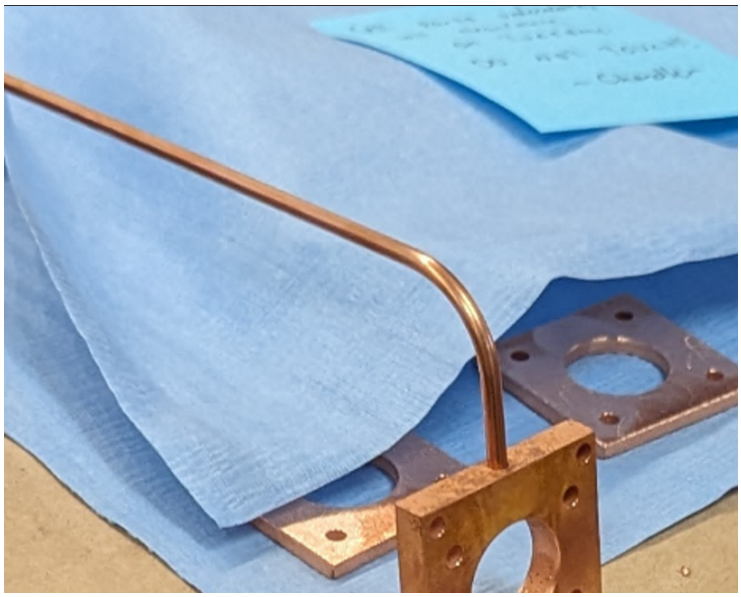
Recommended order for making fill line adapter (after waterjetting the part):

1. Drill a through hole in one side of the plate, size 30 drill (0.1285") for 1/8" copper tubing. See drawings for where to position hole.



2. Cut 16.5" of copper tubing for the fill line. I like using the thicker-walled tube, I think it's C101? OD is 1/8", easy to find on McMaster, part number 8965K22 (it's NOT the "ultra-weldable" kind or whatever, that's too thin). I prefer using the hacksaw to the tube cutter, the quality of the cut doesn't matter too much and I find the tube cutter pinches the ends together rather than cutting them.

3. Bend the tube on one end using the smallest section of the tube bender to a 90° angle, basically as close to the end as you can. This makes it so you don't have to bend this part of the tube after brazing, which is a lot harder to do. See photo for what the end of the tube should look like.



4. Braze the tube to the fill line adapter plate in the position shown above. Brazing will not be covered here! Stop asking! Get an in-person demonstration! Try not to get extra braze adhered to the front and back of the adapter plate, as this could affect its ability to seal to the cell. If you do, file it away.
5. Braze a 1/8 VCR gland with a female nut on the other end



6. Spray isopropanol through the end of the tube to ensure it goes all the way through. You might have to spray compressed air too. **Something that is likely to happen is that you accidentally seal the tube at the VCR end by using too much braze (VERY EASY TO DO! don't be hard on yourself :))**. If this is true, take the smallest possible drill bit and drill straight down the VCR gland until you punch through the clog. You'll know this is necessary to do if the chips that are coming out are the color of the braze, not copper.

7. Deburr all holes on both sides, including the big inner hole. File the edges of the square plate so that they won't cut gloves.

8. Install 4-40 helicoils in the 4 outer corners as per the diagram in step 1. Ensure that they are flush with the surface that is opposite the direction that the tube is bending. In the photo after step 3, this would be the surface that you can see. The reason for this is that we will be screwing into the fill line adapter from this side, so we want the helicoils to be accessible. Don't know how to install helicoils? Ask someone who does.

You're done with the fill line adapter part for now, even if it doesn't look finished. We will come back to it during sanding. Note: You'll finish bending the fill line roughly into place after the leak check and do the *final* adjustments after the cell is mounted in the chamber.

Sanding

This step is unfortunately crucial to the cell construction as it ensure that the surfaces are able to vacuum seal. If you don't sand properly, you will regret it during the leak check and will eventually have to do it anyways.

To save you some time, below I will list all of the parts that go into the cell and what level of sanding they need to be, in terms of final sandpaper grit. This is because some parts aren't involved in the vacuum seal, so they just need to be somewhat smooth instead of squeaky clean.

To stress: the point of sanding is so that we can get a vacuum seal on the cell. This means that for the surfaces listed with the highest grits there can be no visible scratches, dents, or dings near any of the big bores in the cell. If there are, you might need to start at 60 grit and really work the surface to get them out before continuing. If you can't, try filing them, and if that doesn't work the part should be disposed of and we should request a refund if it wasn't our fault.

Blacken the fluorescence collection region

We use Alion MH2200 to reduce light scatter behind the fluorescence collection region. (The company has since changed their name from Alion to HII – Mission Technologies Corp.)

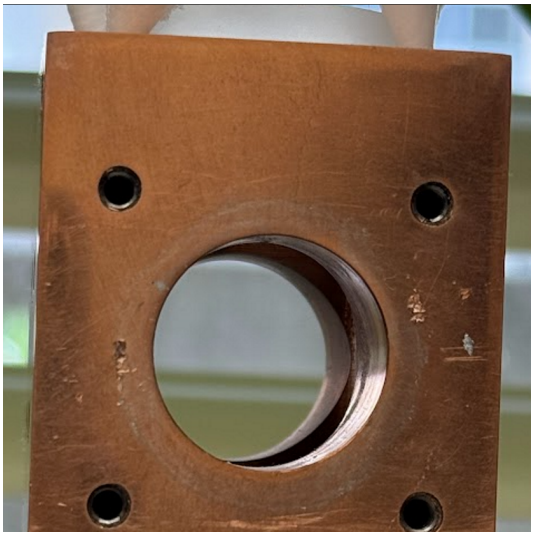


Figure B.1: These marks (left and upper-right of the bore) are examples of dings that could impact the sealing ability of the cell, and would need to be sanded/filed away completely.

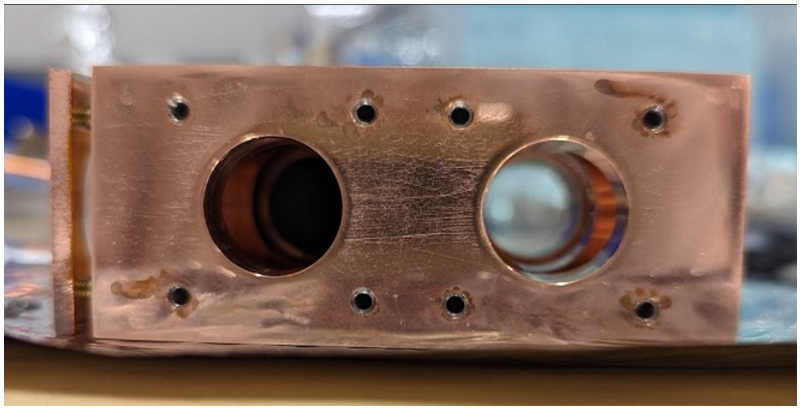


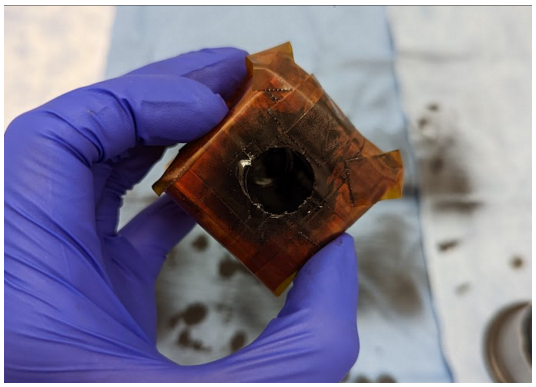
Figure B.2: These sorts of scratches (between the two bores) are the result of the sanding process and are inevitable. They won't impact the sealing of the cell in almost all cases.

Surface to be sanded	**Final grit recommendation**
Cell body sides with bores	1000 (I do 2000 because it looks impressive)
Top of cell body	600 (just needs thermal conductivity)
Bottom of cell body	200 (just needs to not be rough)
Fill line adapter plate	1000 **both sides** (make sure to sand AFTER you braze)
Side blank	1000 one side, 200 other (only one surface is vacuum sealing)
All other 1/8" holder plates	200

Table B.1: Sanding requirements for different aspects of the Minifridge cell. Note that not every surface needs to be sanded to vacuum-quality, which saves time in the process.

Using an airbrush airbrush, spray the paint as according to the normal blackening procedure through the hole opposite to the blanked off part of the cell, being sure to coat the plate and the inside of the cell on the fluorescence side.

Do not use too much paint, otherwise it will drip. Protect the outside edges of the cell from being painted by applying kapton tape around the cell bores. An example of this is below. Don't worry about the kapton residue, it doesn't ruin vacuum tightness.



Only paint the region that is "seen" by the PMT (or camera, or whatever we're using in the current year). Don't get paint on the ablation side of the cell.

Allow the paint to dry in the fume hood for 24 hours. Do not bake out the cell, even though baking is standard practice for other blackened parts; we don't care about outgassing for this application.

Make sure we have enough optics, screws, and indium wire

If any of these are getting low, order them before the next cell installation:

B.2 Assemble the cell

A note: this section was written before the cell body only had 5 open ports. Previously, the fluorescence bore went all the way through the cell, and we used a blank plate to block it off. In the following diagrams, plate/side/port #3 is not a plate anymore, but rather just a blank face on the cell.

Now we get to put everything together! Below is a what the completed cell looks like:

Part description	Quantity per cell	Part # and usual provider
VIS/NIR AR coated windows for probe beams	2	Thorlabs WG11050-AB
Wedged UVFS uncoated window for ablation	1	Thorlabs WW41050
VIS/NIR AR coated 1" focal length PCX lens for light collection	1	Thorlabs LA1951-AB
4-40 Belleville spring washers	~28	McMaster 9712K54
4-40 screws 1/2" length, brass* or 316 SS, for 5mm thick windows	~16	McMaster 94070A110 or 92185A110
4-40 screws 5/8" length, brass* or 316 SS, for lens	~4	McMaster 94070A113 or 92185A112
4-40 screws, 7/16" length, 316 SS, for 1/4" thick plates	~8	McMaster 92185A109
Indium wire, 1 mm diameter	Approx. 22" or 3 grams	Sigma Aldrich 357073 (buy the 28g)
1/8" VCR gasket	≥4 (depends on #/leak checks)	Swagelok SS-2-VCR-2

Table B.2: *brass has been the historical convention due to its thermal expansion matching copper better, but I have had bad luck torquing the 4-40 brass screws enough to get a good seal with the indium. Often the screwheads will break off which is annoying. On the other hand, using steel makes it possible to apply too much force for the windows and crack them... at the very least, always use stainless steel screws to secure the radium target plate to avoid screw breakage.

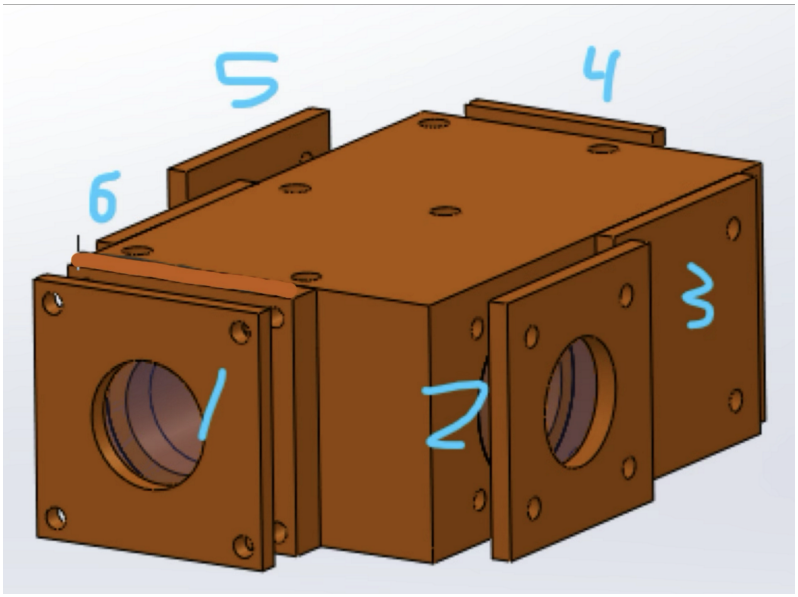


Figure B.3: Diagram of the cell with each port explicitly numbered to match those listed in Table B.4

And below is what parts are on each port on the cell. Parts are listed in order of how they go onto the cell, so inner→outer (i.e. window followed by the mount that holds the window).

Port no.	Mounted parts	Screws
1	Fill line adapter plate VIS/NIR coated window Fill line window holder	7/16” 1/2”
2	Uncoated UVFS wedged window Window holder	1/2”
3	1/8” side blank (black painted)	1/2”
4	VIS/NIR coated window Endpiece holder	1/2”
5	VIS/NIR 1” focal length PCX lens Window holder	5/8”
6	1/4” side blank (target plate)	7/16”

Table B.3: Table listing the parts attached to each cell port, accompanying the diagram B.3

How do we mount the parts? With indium wire! Indium is the state-of-the-art for vacuum sealing at cryogenic temperatures. There’s some nuance to how to make an indium seal, so have someone show you if it’s your first time. In general, you will form the indium wire into a circle to act as a sealing “gasket” once it is smooshed down.

For the blank plates (the target plate, fluorescence background plate, and fill line adapter) the size of the indium circle is not too crucial. Just make sure that it is bigger than the bore of the cell and smaller than the 4 hole pattern that holds the plate onto the cell.

When adding indium for a window, the size matters quite a bit more. The circle needs to be bigger than the bore but smaller than the diameter of the window, otherwise when you compress the window onto the indium it will slip into the bore or slip outside of the window and neither option will seal. I recommend watching someone who knows how to do it if it’s your first time, or wrapping the indium wire around a teflon tube of the proper diameter.

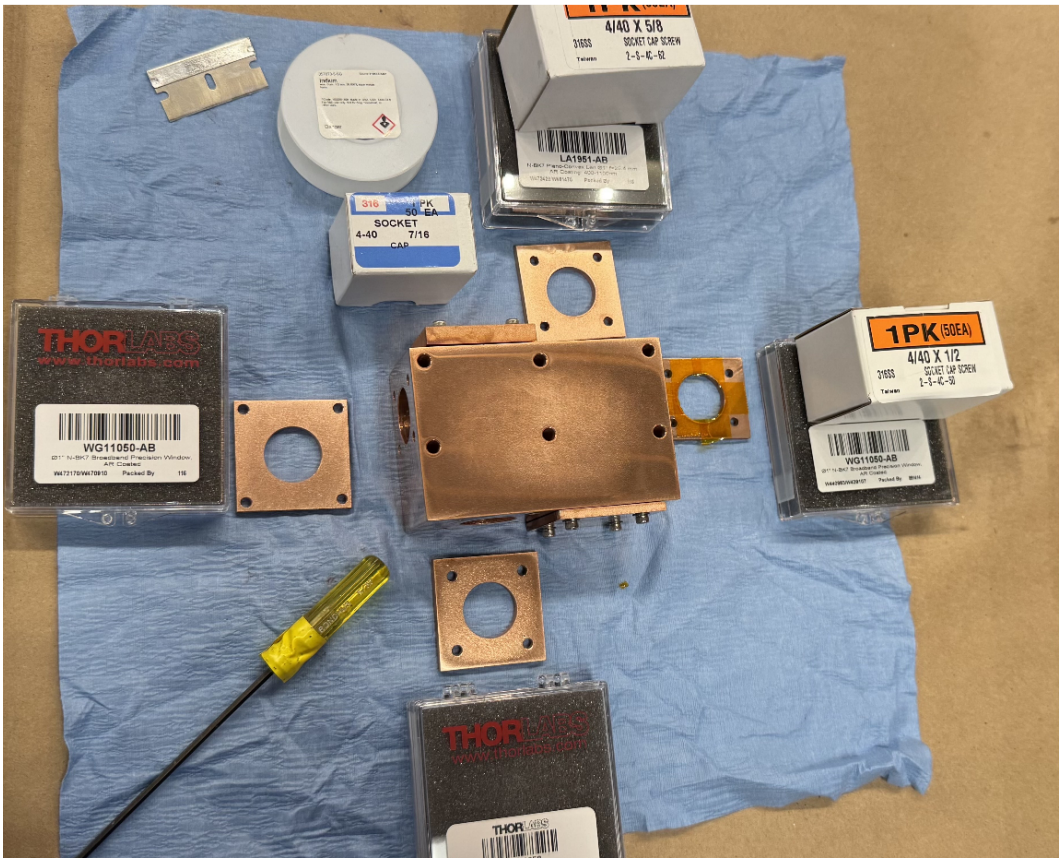


Figure B.4: All of the parts used for assembling the cell laid out prior to assembly, except for two plates already attached.

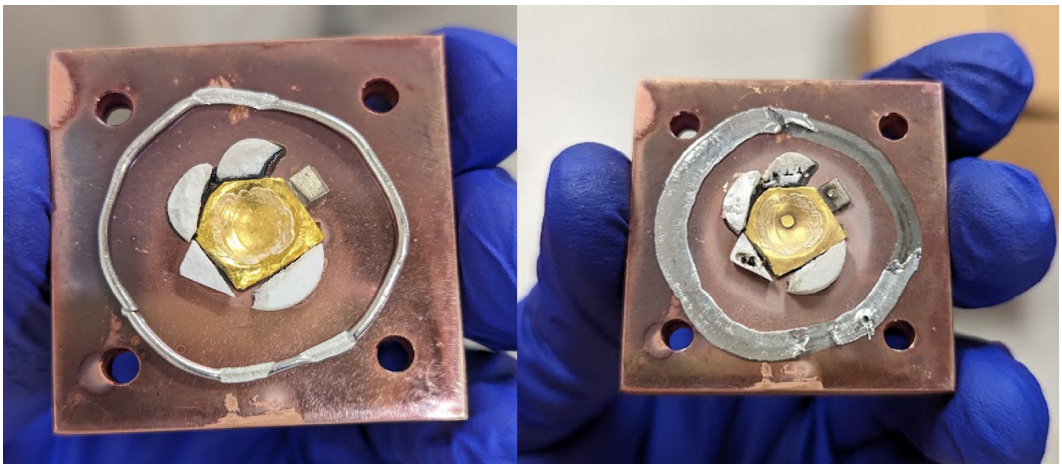


Figure B.5: Left: indium wire (mostly) pre-smoosh. Right: indium wire post-smoosh (some is missing due to coming off when I removed the plate).

When cutting the indium, use a razor blade and cut the wire at a steep angle. The goal is that you don't have a "flat" end.

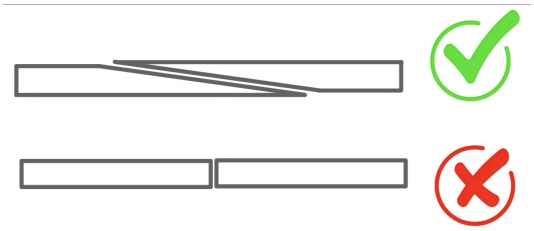


Figure B.6: How to cut indium wire to increase the contact surface area. This method increases the probability that the indium will seal properly when compressed

Above is what the two ends of the circle of indium should look like. Why is this? When you cut indium, you expose the bare metal as opposed to the passivated layer that forms after it's been exposed to air for long enough. Bare indium can stick to itself. When you cut the indium as above, there's a lot of surface area contact between the two ends of the circle and it will stick to itself easier. This helps the indium to make a good seal at the point where the two ends meet. If you don't cut the indium like this, there might be a channel that allows leakage in or out of the cell.

Indium needs to be applied at all ***vacuum sealing surfaces***, but only at these regions. There needs to be indium between the window and the cell, but not between the window holder and the window, because this is not a sealing surface. Basically, if the surface is sanded to 1000 grit, there should be indium on it.

For the window holders, you should apply kapton tape on the side that presses against the window. Obviously the kapton should not block optical access, so use a razor to cut it out of the central bore. The kapton prevents metal-on-glass contact which can scratch/crack the windows easier. Think of it like a really thin, orangeish pillow.

To actually attach things, make sure first that you're using the right length screw. The right length should have 4 – 8 threads of engagement into the helicoil—too short and it won't go in, too long and it'll bottom out in the hole. Each screw needs a belleville washer where the curvature points away from the screw head as such:

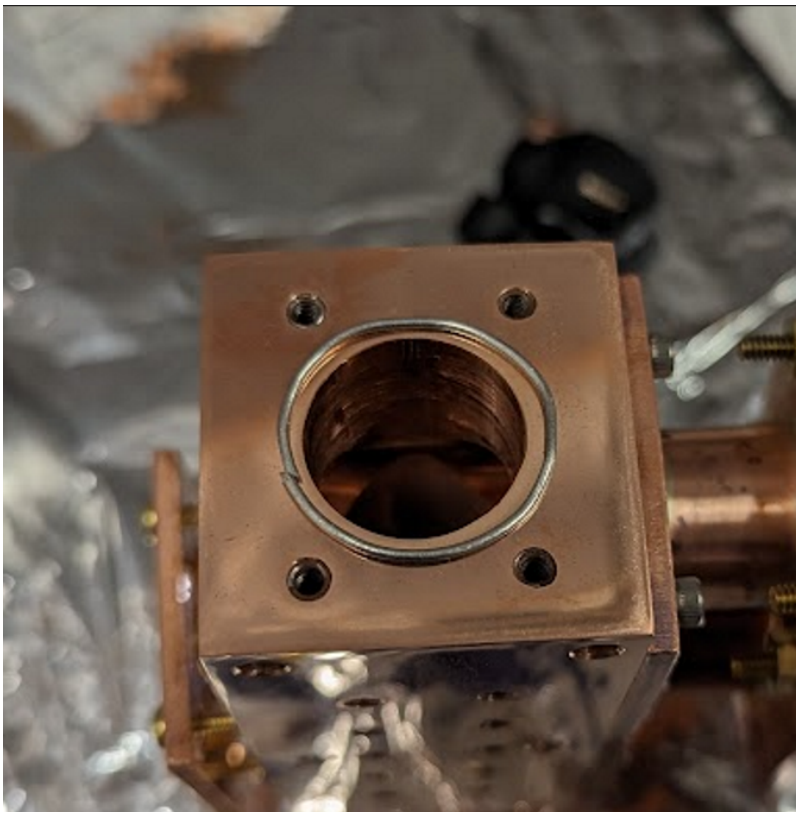
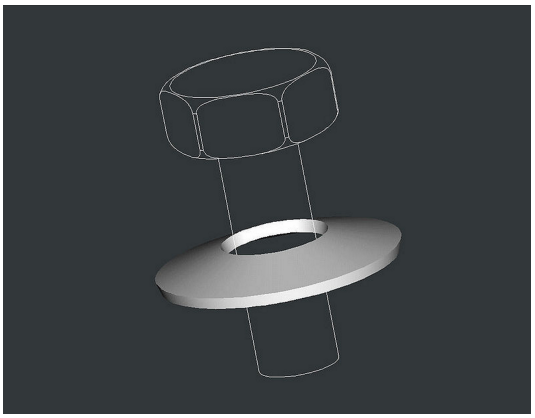


Figure B.7: Photo of an indium gasket in accordance to the cutting scheme presented in Fig. B.6. Not the best example of a good cut, but still better than just being flat!



Always tighten the screws in a star pattern. Don't overtighten on one side before doing the other screws, I generally go through the whole pattern like 6 times before it's fully tightened. Only use straight wrenches/screwdrivers, not anything with an angled handle otherwise you will apply too much torque. In my experience, tightening it basically as hard as I can get by hand with a straight wrench/screwdriver is the right tightness.

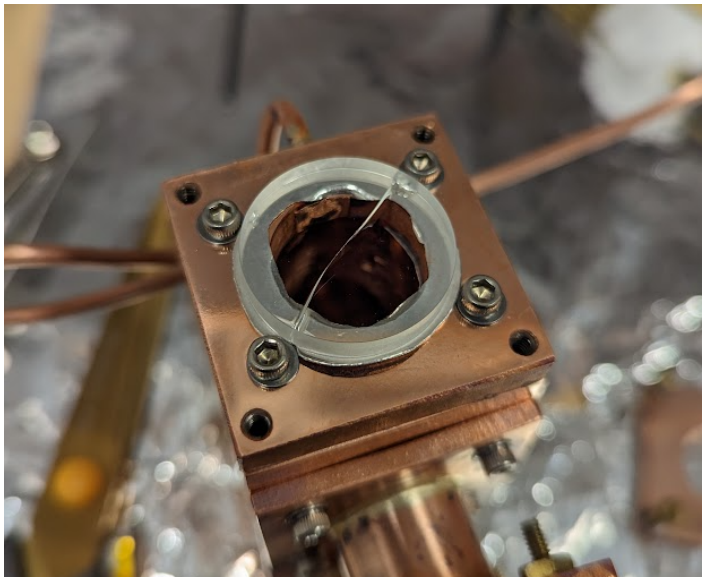


Figure B.8: It is quite easy to tell when the window is cracked.

Random tidbits:

- When attaching anything to the side, be mindful of any motion that could move the indium wiring. This is especially easy to do on the windows. Thankfully, for the windows, you can see if the indium has shifted.
- When attaching the window to the fill line adapter plate, the belleville washers that hold the adapter plate in place might sit slightly under where the window wants to go. If this happens, when you tighten down the window, it's possible that it cracks. Obviously if it cracks you should throw it away and redo the connection. If it happens twice, get rid of the belleville washer that is causing the crack, and be mindful of this region when checking for leaks as a result.
- If you smoosh the indium down and notice that it popped out from under the window, you have to redo it. Use new indium. DO NOT REUSE INDIUM WIRE IT DOESN'T WORK LIKE THAT! Take it off by hand first (if you can) and if it's really stuck scrape with a Teflon rod. Dispose of it in the "indium scraps" container, in case one of these days we decide to try and recycle it.
- Brass screws might break at the head, if so you have to remove and replace the screw.

Once the cell is assembled, it needs to be leak checked before installation. Be careful not to bend the gas line when doing this, the copper is really easy to bend especially

after it has been softened by the brazing process. If you bend it too much it might break. Make sure the gas line is always supported somehow, otherwise the weight of the adapter/bellows from the leak checker might bend it.

Perform a leak check on every port of the cell and the custom VCR connections. Leak rate should never go above $5e-9$ mbar·l/s.